
# Electrochemical Modification of Electrodes with Metal Nanoparticles

*A thesis submitted for the degree of*

*Doctor of Philosophy*

*in Physical & Theoretical Chemistry*

**Christos K. Mavrokefalos**

*St Edmund Hall*

Trinity Term 2016

*Dedicated to my parents,*

*whose love, faith and support, never wavered*

Christos K. Mavrokefalos
St. Edmund Hall, University of Oxford

Doctor of Philosophy
Trinity Term 2016

# Abstract

In this thesis, the use of boron-doped diamond and Au (111) as electrode materials with special physical and electrochemical properties was investigated in a number of electrochemical and photoelectrochemical applications. The surface chemistry of the aforementioned electrodes was modified utilising such strategies as electrochemical and hydrogen plasma treatment as well as coating treatment. Extended attention was paid to metal alloys and/or core-shell metal nanostructures. The modified surface of the diamond and Au (111) electrodes was studied using a wide spectrum of techniques. The electrochemical activity of these materials was investigated in order firstly to expand the knowledge of diamond electrochemistry and secondly to establish an understanding of how the electrochemical modification with metal nanoparticles of core-shell structure impacts their electrochemical performance.

In the first study, the nanostructuring strategies of boron-doped diamond surface with Pt-Cu and Cu nanoparticles were developed for two different applications. Pt-Cu modified diamond electrode was explored for methanol oxidation, which is of relevance to the direct methanol fuel cell. The motivation of this work was to understand how these core-shell structures on diamond compare to similar structures on other forms of carbon. The second objective was the development of a simple Cu-modified diamond electrode that can be used as a sensitive non-enzymatic amperometric glucose sensor.

The second work involves two fundamental electrochemical studies. The first one reports the overpotential growth of Pd metallic nanoparticles on Au (111). For the first time, this study contradicts the classical theories for electrochemical nucleation and growth which proceed only by the fresh reduction of ions. It demonstrates that electrochemical nucleation and growth at the early stages is overpotential dependent and in fact proceed also by the aggregation of small clusters through surface diffusion when deposited at relatively higher overpotentials. The second study reports the influence of two dissimilar surface terminations of diamond: hydrophobic H-terminated and hydrophilic O-terminated. The latter work provides a useful insight of how the chemical terminations of diamond with electrodeposited Pd nanoparticles impact their overall electrochemical performance.

The third project extends the discussion on the study of the diamond electrodes modified with core-shell metal nanoparticles along with two different chemical terminations. In this work, a H-terminated diamond electrode was modified with Pd-Sn nanoparticles and an O-terminated diamond electrode was electrochemically modified with Pd-Ni nanoparticles. The enhanced electrodes' performance with regard to the ethanol electrooxidation reaction was demonstrated.

The fourth study reports on the development of a novel photocatalyst comprised of $Cu_2O$ nanoparticles coated with Ni supported on boron-doped diamond electrodes, of relevance to water splitting and $CO_2$ reduction reactions. Similarly to the previous works, an insight is provided on how a co-catalyst contributes not only to the protection of semiconductor materials from self-photo-corrosion issues in aqueous solutions, but also to improved stability and enhanced photoelectrochemical performance.

Overall, the electrochemical and photoelectrochemical performance of the boron-doped diamond and Au (111) electrodes for sustainable energy applications is reported in this thesis.

## Acknowledgements

First and foremost, an incredibly big thank you and my sincere gratitude must go to my supervisors, Professor John S. Foord and Richard G. Compton, for taking me on as a DPhil student in their groups. From an academic point of view, their mentorship, scientific knowledge and hours devoted to sharing their experience in electrochemical studies with me have been invaluable throughout these years. Besides their supervision, a huge thank you for their continuous support, inspiration and great sense of humour.

I would like to thank Dr. Geoffrey Nelson, Dr. Robert Jacobs and Prof. Jingping Hu for sharing their knowledge and helping me with their profound experience in electrochemistry as well as surface analysis, each one in their field of expertise especially during the first year of my studies. I would like to thank especially Dr. Ashley Shepherd not only for her scientific and academic help but also for her support on career and future advice. Special thanks must also go to Dr. Emina Hadzifejzovic and Dr. Maksudul Hasan for the excellent collaboration and endless discussions on my personal and professional development.

I am happy and lucky at the same time to have met and worked with such people in the Foord and Compton groups and therefore I thank all of them, past and present. I am especially grateful to Céline, Lulu, Patrick, Tony, Sirikarn and Inga for their friendship and help with my work. I would like to separately thank Johanna for her support and our interesting and concurrently thought-provoking discussions.

I would also like to thank my college friends, Andreas, Rita, Stefano, Anna and Lisa with whom I shared a lot of moments and made me to have a pleasant DPhil experience in Oxford.

A big thank you must go to Elena Tobolkina for her support and company during my ups and downs as well as for her constant motivation towards the end of my doctoral studies.

An important part of my life are my fifteen years close friends and their families, which live and work in Greece and never forgot about me no matter how many miles away I am from them. I would like to individually thank, Spiros Papailiopoulos, Tsvetan Tomy Bankov, Dimitris Oikonomou and Giorgos Pyrris for their endless support, motivation, advice and attitude. I thank them for being fellow travellers on this journey, especially for the last three years.

Finally, words fail to adequately describe my feelings and express my boundless gratitude to the reason I am who I am. This is the standard and guide in my life, my parents, Konstantinos Mavrokefalos and Stamatia Markou. These are the persons who built my character, equipped me with real life values and taught me to have persistence, tenacity and belief. They showed me what the family standard is and they are my mentors in life. Without them, I would not have been able to be here. I thank them for their love and true belief in me. Last but not least, I cannot forget my brother, Michail Mavrokefalos for his real and endless love, as well as his faith in me too.

## Relevant Publications

[1] **Electrochemical aspects of Pt-Cu and Cu modified boron-doped diamond**
**Christos K. Mavrokefalos**, Geoffrey W. Nelson, Christopher G. Poll, Richard G. Compton, John S. Foord
Phys. Status Solidi A 212, No. 11, 2559-2567 (2015)

[2] **Overpotential dependent electrochemical growth of Pd nanoparticles from surfactant free electrolyte with enhanced electrocatalytic properties**
Maksudul Hasan, **Christos K. Mavrokefalos**, Worawut Khunsin, Stefan A. Maier, James F. Rohan, John S. Foord
Submitted to Journal of Catalysis (2016) – Elsevier

[3] **Electrochemical modification and surface pre-treatment of boron-doped diamond electrodes with Pd and Pd-Sn nanoparticles for ethanol electrooxidation**
**Christos K. Mavrokefalos**, Maksudul Hasan, Worawut Khunsin, Stefan A. Maier, Richard G. Compton, John S. Foord
Accepted to Electrochimica Acta (2017) – Elsevier

[4] **Enhanced mass activity and stability of Pd-Ni nanoparticles on boron-doped diamond electrodes for direct alcohol fuel cells applications**
**Christos K. Mavrokefalos**, Maksudul Hasan, Worawut Khunsin, Richard G. Compton, John S. Foord
Ready for submission to Journal of the Electrochemical Society (2016) – ECS, after the 230$^{th}$ ECS Meeting in October 2016

[5] **Electrochemical deposition of $Cu_2O$ nanoparticles on boron-doped diamond as photocathode for solar hydrogen generation**
**Christos K. Mavrokefalos**, Maksudul Hasan, Michael Schmidt, James F. Rohan, Richard G. Compton, John S. Foord
Accepted to Applied Surface Science (2017) – Elsevier

[6] **Electrochemically embedded plasmonic sandwich $Cu_2O$ thin film as efficient photocathode for solar water splitting**
Maksudul Hasan, **Christos K. Mavrokefalos**, James F. Rohan, John S. Foord
In preparation

[7] **Electrochemically deposited Cu nanoflowers as efficient photocathode for solar water splitting**
Maksudul Hasan, **Christos K. Mavrokefalos**, James F. Rohan, John S. Foord
In preparation

[8] **Fabrication of noble metals shell on Ni nanowire arrays by autocatalytic chemical process: excellent electrocatalytic properties**
Maksudul Hasan, **Christos K. Mavrokefalos**, James F. Rohan, John S. Foord
Forthcoming

[9] **Electrochemical reduction of $CO_2$ on diamond electrodes for valuable resources**
Emina Hadzifejzovic, **Christos K. Mavrokefalos**, Maksudul Hasan, John S. Foord
Forthcoming

## Table of Contents

Abstract ..... i
Acknowledgements ..... ii
Relevant publications ..... iv
Glossary ..... x
List of most common abbreviations used ..... xii
List of figures ..... xiii
List of tables ..... xix

**Chapter 1: Introduction ..... 20**
**1.1** Electrode materials ..... 20
1.1.1 Diamond ..... 20
1.1.1.1 General overview ..... 20
1.1.1.2 Structure and general properties ..... 21
1.1.1.3 Synthetic diamond and its application in electrochemistry ..... 23
1.1.1.4 Growth techniques of diamond ..... 26
1.1.1.4.1 A short introduction ..... 26
1.1.1.4.2 High Pressure High Temperature (HPHT) technique ..... 27
1.1.1.4.3 Chemical Vapour Deposition (CVD) technique ..... 29
1.1.2 Complementary Metal Oxide Semiconductor (CMOS) ..... 32
**1.2** Surface modifications with metal nanoparticles ..... 32
**1.3** Scope of the thesis ..... 33
**1.4** Bibliography ..... 35

**Chapter 2: Experimental theories and techniques ..... 45**
**2.1** Surface and structure analysis techniques ..... 45
2.1.1 Scanning Electron Microscopy (SEM) ..... 45
2.1.2 X-ray Diffraction (XRD) ..... 47
**2.2** X-ray spectroscopies ..... 48
2.2.1 X-ray Photoelectron Spectroscopy (XPS) ..... 48
2.2.1.1 XPS fundamentals ..... 49
2.2.1.2 XPS instrumentation ..... 51
2.2.1.3 XPS spectral features ..... 52
2.2.1.3.1 Main photoelectron lines ..... 52

2.2.1.3.2 Auger peaks ..... 54
2.2.1.3.3 Shake-up satellites ..... 54
2.2.1.3.4 Multiplet splitting ..... 56
2.2.1.3.5 Plasmons ..... 56
2.2.2 Energy-dispersive X-ray Spectroscopy (EDS, EDX or XEDS) ..... 57
**2.3** Electrochemical methods ..... 58
2.3.1 Electrochemical fundamentals ..... 58
2.3.1.1 Electrochemical equilibrium ..... 58
2.3.1.2 Faradaic and non-faradaic processes ..... 60
2.3.1.2.1 Capacitative current and the double layer ..... 61
2.3.1.2.2 Faradaic process ..... 62
2.3.1.3 Mass transport ..... 64
2.3.1.3.1 Diffusion ..... 64
2.3.1.3.2 Convection ..... 65
2.3.1.3.3 Migration ..... 65
2.3.1.4 Diffusion to macroelectrodes ..... 66
2.3.2 Electrochemical techniques ..... 66
2.3.2.1 Cyclic voltammetry ..... 66
2.3.2.2 Chronoamperometry ..... 69
2.3.2.3 Electrochemical Impedance Spectroscopy (EIS) ..... 71
**2.4** Bibliography ..... 72

**Chapter 3: Pt-Cu and Cu modified boron-doped diamond electrodes for methanol electrooxidation and glucose sensing ..... 75**
**3.1** Introduction ..... 75
**3.2** Aims of the project and principal outcomes ..... 78
**3.3** Experimental section ..... 79
3.3.1 Chemical reagents ..... 79
3.3.2 Equipment and experimental set-up ..... 79
3.3.3 Fabrication and working electrodes ..... 80
**3.4** Results and discussion ..... 81
3.4.1 Oxidation of methanol using Pt-Cu modified diamond ..... 81
3.4.1.1 Morphology and XPS characterisation of the deposits on BDD ..... 81
3.4.1.2 Voltammetric characterisation ..... 85

3.4.1.2.1 Electrodeposition of the electrodeposits ..... 85
3.4.1.2.2 Electrochemical activity of the electrocatalysts ..... 87
3.4.1.3 Evaluation of Pt-Cu electrocatalysts preparation conditions on methanol oxidation characteristics ..... 91
3.4.2 Cu/BDD electrodes for glucose sensing ..... 94
3.4.2.1 Amperometric detection of glucose with Cu/BDD electrodes ..... 99
3.4.2.2 Stability and anti-interference test ..... 101
**3.5** Conclusions ..... 102
**3.6** Bibliography ..... 103

**Chapter 4: Electrochemical modification of Au (111) and diamond electrodes with Pd nanoparticles for ethanol electrooxidation ..... 110**
**4.1** Introduction ..... 110
**4.2** Aims of the project and principal outcomes ..... 113
**4.3** Experimental section ..... 114
4.3.1 Chemical reagents ..... 114
4.3.2 Equipment and experimental set-up ..... 114
4.3.3 Fabrication and working electrodes ..... 116
4.3.3.1 Modification of Au (111) electrodes ..... 116
4.3.3.2 Modification of diamond electrodes ..... 117
**4.4** Results and discussion ..... 118
4.4.1 Overpotential dependent growth of Pd for ethanol electrodeposition ..... 118
4.4.1.1 Electrochemical deposition of Pd ..... 118
4.4.1.2 Characterisation of Pd nanoparticle deposits by cyclic voltammetry in aqueous acidic electrolyte ..... 123
4.4.1.3 Growth mode and structural characterisation of Pd nanoparticle deposits ..... 125
4.4.1.4 Electrocatalytic performance of Pd nanoparticles ..... 132
4.4.2 Oxidation of ethanol using Pd modified diamond ..... 139
4.4.2.1 Morphology and XPS characterisation of the deposits on boron-doped diamond electrodes ..... 139
4.4.2.2 Voltammetric characterisation ..... 143
4.4.2.2.1 Electrodeposition of the electrocatalysts ..... 143
4.4.2.2.2 Electrochemical activity of the electrocatalysts ..... 144
4.4.2.3 Evaluation of Pd electrocatalysts preparation conditions on ethanol oxidation

characteristics....146
4.4.2.4 Amperometric response of the catalysts in ethanol....148
**4.5** Conclusions....149
**4.6** Bibliography....151

**Chapter 5: Electrochemical modification and surface pre-treatment of diamond electrodes with Pd-Sn and Pd-Ni nanoparticles for ethanol electrooxidation....159**
**5.1** Introduction....159
**5.2** Aims of the project and principal outcomes....161
**5.3** Experimental section....162
5.3.1 Chemical reagents....162
5.3.2 Equipment and experimental set-up....162
5.3.3 Fabrication and working electrodes....163
5.3.3.1 Modification of HBDD electrodes....163
5.3.3.2 Modification of BDD electrodes....164
**5.4** Results and discussion....165
5.4.1 Oxidation of ethanol using Pd-Sn nanoparticles on hydrogen terminated diamond electrodes....165
5.4.1.1 Morphology and XPS characterisation of the deposits on HBDD....165
5.4.1.2 Voltammetric characterisation....169
5.4.1.2.1 Electrodeposition of the electrocatalysts....169
5.4.1.2.2 Electrochemical activity of the electrocatalysts....170
5.4.1.3 Evaluation of Pd-Sn electrocatalysts preparation conditions on ethanol oxidation characteristics....174
5.4.1.4 Tafel analysis of Pd-Sn electrocatalysts....178
5.4.1.5 Amperometric response of the catalysts in ethanol....181
5.4.2 Oxidation of ethanol using Pd-Ni nanoparticles on oxygen terminated diamond electrodes....182
5.4.2.1 Morphology, EDX and XPS characterisation of the deposits on BDD....182
5.4.2.2 Voltammetric characterisation....187
5.4.2.2.1 Electrodeposition of the electrocatalysts....187
5.4.2.2.2 Electrochemical activity of the electrocatalysts....188
5.4.2.3 Evaluation of Pd-Ni electrocatalysts preparation conditions on ethanol oxidation characteristics....192

5.4.2.4 Tafel analysis of Pd-Ni electrocatalysts ..... 195
5.4.2.5 Amperometric response of the catalysts in ethanol ..... 196
**5.5** Conclusions ..... 197
**5.6** Bibliography ..... 199

**Chapter 6: Electrochemical modification of diamond electrodes with $Cu_2O$ for water splitting and $CO_2$ reduction ..... 207**
**6.1** Introduction ..... 207
**6.2** Aims of the project and principal outcomes ..... 210
**6.3** Experimental section ..... 211
6.3.1 Chemical reagents ..... 211
6.3.2 Equipment and experimental set-up ..... 211
6.3.3 Fabrication and working electrodes ..... 212
**6.4** Results and discussion ..... 214
6.4.1 Solar hydrogen generation using $Cu_2O$ cubical particles coated with NiO ..... 214
6.4.1.1 Structural and XPS characterisation of the deposits on BDD ..... 214
6.4.1.2 Photoelectrochemical measurements of different photocathodes ..... 217
6.4.1.3 Stability tests of different photocathodes ..... 220
6.4.1.4 Amperometric photostability of different photocathodes ..... 223
6.4.1.5 Electrochemical impedance ..... 226
6.4.2 $CO_2$ reduction using electrodeposited Ni and $Cu_2O$ nanoparticles ..... 230
6.4.2.1 Structural and XPS characterisation of the deposits on BDD ..... 230
6.4.2.2 Photoelectrochemical measurements of different photoelectrodes ..... 233
**6.5** Conclusions ..... 237
**6.6** Bibliography ..... 238

**Chapter 7: Overall Conclusions ..... 245**
**7.1** Thesis conclusions ..... 245
**7.2** Bibliography ..... 248

# Glossary

Where appropriate, symbols are defined in terms of the generic species *i* or the reduction

$A + e^- \rightleftharpoons B$

## Roman Symbols

| Symbol | Definition | Units |
|---|---|---|
| $A$ | Electrode area | $cm^2$ |
| $A_d$ | Double layer area | $cm^2$ |
| $C_i$ | Concentration of species *i* | mol $cm^{-3}$ |
| $C_d$ | Differential capacitance | μF $cm^{-2}$ |
| $C_p$ | Droplet concentration | mol $cm^{-3}$ |
| $D_i$ | Diffusion coefficient of species *i* | $cm^2$ $s^{-1}$ |
| $d$ | Density | g $mL^{-1}$ |
| $E^0$ | Standard electrode potential | V |
| $E_f^{\ominus}$ | Formal potential | V |
| $E_{1/2}$ | Half wave potential | V |
| $F$ | Faraday constant ≈ 96485 | C $mol^{-1}$ |
| $G$ | Gibbs Energy | J $mol^{-1}$ |
| $I$ | Current | A |
| $I_{A/C}$ | Anodic/ Cathodic current | A |
| $i_p$ | Peak Current | A |
| $i_{ss}$ | Steady State Current | A |
| $j$ | Flux | mol $cm^{-2}$ $s^{-1}$ |
| $k_0$ | Standard electrochemical rate constant | cm $s^{-1}$ |
| $k_B$ | Boltzmann constant ≈ 1.381 x $10^{-23}$ | J $K^{-1}$ |
| $k_{red/ox}$ | Rate constant for reduction/ oxidation | cm $s^{-1}$ |
| $M$ | Mass | g |
| $N_A$ | Avogadro constant ≈ 6.022 x $10^{23}$ | $mol^{-1}$ |
| $n$ | Total number of electrons transferred | Dimensionless |
| $n'$ | Number of electrons transferred before the rate determining step | Dimensionless |
| $R$ | Gas constant ≈ 8.314 | J $K^{-1}$ $mol^{-1}$ |

| | | |
|---|---|---|
| $r$ | Electrode radius | cm |
| $r_0$ | Microelectrode radius | cm |
| $T$ | Temperature | K |
| $T$ | Time | s |
| $V$ | Volume | mL |
| $\upsilon(x)$ | The solution velocity in the $x$ direction | cm $s^{-1}$ |
| $x$ | Displacement of a species | cm |
| $z_i$ | The charge of a species $i$ | C |

## Greek Symbols

| Symbol | Definition | Units |
|---|---|---|
| $\alpha$ *and* $\beta$ | Butler-Volmer transfer coefficients | *Dimensionless* |
| $\alpha_{A/B}$ | Activities of species A and B | *Dimensionless* |
| $\gamma_{A/B}$ | Activity coefficients of species A and B | *Dimensionless* |
| $\eta$ | Overpotential | *V* |
| $\eta_i$ | Viscosity | *Pa* $s^{-1}$ |
| $v$ | Scan Rate | *V* $s^{-1}$ |
| $\Phi_{(m)/(s)}$ | Electrical potentials of the electrode and solution | *V* |

## List of most common abbreviations used

| | |
|---|---|
| **AC** | Alternating current |
| **B.E.** | Binding energy |
| **BDD** | Boron-doped diamond |
| **CMOS** | Complementary metal oxide semiconductor |
| **CV** | Cyclic voltammetry |
| **CVD** | Chemical vapour deposition |
| **DAFC** | Direct alcohol fuel cell |
| **DL** | Double layer |
| **DMFC** | Direct methanol fuel cell |
| **EAS** | Electrochemical surface area |
| **EDS** | Energy-dispersive spectroscopy |
| **EDX** | Energy-dispersive X-ray spectroscopy |
| **EIS** | Electrochemical impedance spectroscopy |
| **FAT** | Fixed analyser transmission |
| **HBDD** | Hydrogen terminated boron doped diamond |
| **HPHT** | High pressure high temperature |
| **IHP** | Inner Helmholtz plane |
| **LOD** | Limit of detection |
| **NPs** | Metal nanoparticles |
| **OBDD** | Oxygen terminated boron doped diamond |
| **OHP** | Outer Helmholtz plane |
| **PBS** | Phosphate buffer solution |
| **SEM** | Scanning electron microscopy |
| **SLJ** | Semiconductor-liquid junction |
| **SSA** | Specific surface area |
| **UHV** | Ultra-high vacuum |
| **V** | Volt |
| **XEDS** | X-ray energy dispersive spectroscopy |
| **XPS** | X-ray photoelectron spectroscopy |
| **XRD** | X-ray diffraction |

## List of Figures

**Figure 1-1** Various types of diamond: (a) the core of BPM 37093 found 50 light years away from Earth[4]. (b) Centenary diamond, the largest flawless and colourless diamond[5]. (c) SEM image of a boron-doped diamond (blank sample). (d) Black boron-doped diamond squares. (p. 21)

**Figure 1-2** 3D diamond structure[7]. (p. 22)

**Figure 1-3** Representation of the energy diagram of selected states in the band gap of diamond[8]. (p. 23)

**Figure 1-4** Cyclic voltammograms of water electrolysis in 0.5M $H_2SO_4$ of two boron-doped polycrystalline films (B:PCD-NRL and B:PCD-USU, one single crystal boron doped diamond (B:H-SCD) and one undoped diamond (H-SCD)[32]. (p. 25)

**Figure 1-5** Schematic representation of the carbon phase diagram[2]. (p. 26)

**Figure 1-6** Image of a belt press[63]. (p. 28)

**Figure 1-7** Schematic example of a Belt type HPHT press[64]. (p. 28)

**Figure 1-8** Image of the BARS apparatus[63]. (p. 29)

**Figure 1-9** Examples of some of the most common types of low pressure CVD reactors. (a) Hot filament, (b) NIRIM type microwave plasma reactor, (c) ASTEX type microwave plasma reactor and (d) DC arc jet (plasma torch). (p. 31)

**Figure 1-10** Schematic diagram of the physical and chemical processes during diamond CVD growth[79]. (p. 31)

**Figure 2-1** (a) Schematic diagram of the basic components of SEM[1] and (b) SEM image of a bare BDD electrode. (p. 46)

**Figure 2-2** Schematic representation of Bragg's law[4]. (p. 47)

**Figure 2-3** (a) Schematic illustration of the XPS process, where photoionisation of an atom by the emission of 1s electron from the K shell occurs and (b) Image of an XPS instrument[7]. (p. 49)

**Figure 2-4** Schematic illustration of an Auger emission process[7]. (p. 50)

**Figure 2-5** Schematic diagram of XPS with a X-ray source and hemispherical analyser, reprinted from[8]. (p. 51)

**Figure 2-6** An example of a typical survey spectrum showing the appearance of XPS and Auger peaks, adapted from personal experiments of an electrode consisted of $Cu_2O$/Au (111). (p. 53)

**Figure 2-7** Shake-up structure in Cu 2p spectra of copper (II) hydroxide ($Cu(OH)_2$, top) and copper (II) oxide (CuO, bottom)[15]. (p. 55)

**Figure 2-8** π-bond shake-up satellite for the C 1s photoelectron peak, obtained from[16]. (p. 55)

**Figure 2-9** Multiplet splitting peaks of the $La(OH)_3$, obtained from[17]. (p. 56)

**Figure 2-10** Plasmon loss structure in a spectrum of aluminium metal, obtained from[18]. (p. 57)

**Figure 2-11** Helmholtz double layer model, taken from[20]. (p. 61)

**Figure 2-12** Linear diffusion to a macroelectrode. (p. 66)

**Figure 2-13** Cyclic voltammetry potential waveform varied with time during a cyclic voltammogram. (p. 67)

**Figure 2-14** (a) A 'reversible' system, (b) a 'quasi-reversible' system and (c) an 'irreversible' system[19]. (p. 68)

**Figure 2-15** (a) The dependence of potential vs time of a chronoamperometric measurement, (b) the dependence of concentration with the distance of the electrode and the change of it over time and (c) resulting chronoamperogram current as a function of time[20]. (p. 70)

**Figure 2-16** Nyquist plot of an EIS measurement, obtained from[33]. (p. 71)

**Figure 3-1** Schematic presentation of a Direct Methanol Fuel Cell (DMFC)[21]. (p. 76)

**Figure 3-2** Schematic representation of a glucose meter[45]. (p. 78)

**Figure 3-3** (a) SEM image of Cu deposited on BDD electrodes, (b) Pt on BDD and (c) Pt-Cu deposited on BDD, respectively through chronoamperometry at -0.8V for the Cu and -0.3V for the Pt, respectively. (p. 82)

**Figure 3-4** (a) XPS spectra of wide scans of the Cu/BDD, Pt/BDD and Pt-Cu/BDD, respectively. (b) Typical Cu 2p peaks of Cu and Pt-Cu modified BDD catalysts, respectively. (c) Typical Pt 4f peaks of Pt and Pt-Cu modified BDD catalysts, respectively. (p. 84)

**Figure 3-5** (a) Cyclic voltammogram of bare BDD in a solution containing 5mM $CuSO_4 \cdot 5H_2O$ in 1M $H_2SO_4$ at scan rate of 0.1 V/s (inset: chronoamperogram of Cu deposition in 5mM $CuSO_4 \cdot 5H_2O$ in 1M $H_2SO_4$ on bare BDD at constant potential of -0.8V). (b) Cyclic voltammogram of bare BDD in a solution containing 1M $H_2SO_4$ and 5mM $K_2PtCl_6$ respectively at scan rate of 0.1 V/s (inset: chronoamperogram of Pt deposition in 5mM $K_2PtCl_6$/1M $H_2SO_4$ on bare BDD at constant potential of -0.3V). (p. 85)

**Figure 3-6** (a) Cyclic voltammogram and (b) linear sweep voltammogram of the Cu, Pt and Pt-Cu deposited on BDD, respectively in 1M $H_2SO_4$ solution at scan rate of 0.1 V/s. (p. 90)

**Figure 3-7** Galvanic replacement or transmetallation. (p. 91)

**Figure 3-8** (a) Cyclic voltammograms of Pt and Pt-Cu modified BDD in 0.5M $H_2SO_4$ and 1M $CH_3OH$ at scan rate of 0.1 V/s. (b) Cyclic voltammogram of Pt and CuPt modified BDD in 0.5M $H_2SO_4$ and 1M $CH_3OH$ at scan rate of 0.1 V/s. (p. 93)

**Figure 3-9** (a) Cyclic voltammogram of Cu modified BDD in 0.1M KOH at scan rate 0.1 V/s. (b) Cyclic voltammograms of bare BDD in the absence and presence of 10mM glucose, Cu/BDD in the absence and presence of 10mM glucose in 0.1M KOH at scan rate of 0.1 V/s. (p. 95)

**Figure 3-10** Cyclic voltammograms of Cu modified BDD in PBS at (a) scan rate 0.025 V/s, (b) 0.05 V/s, (c) 0.1 V/s, (d) 0.15 V/s, (e) 0.2 V/s and (f) 0.25 V/s in the absence and presence of 1, 2.5, 5 and 10mM glucose respectively. (p. 98)

**Figure 3-11** (a) Amperometric responses of Cu/BDD in 0.1M KOH between the concentrations range of 1μM and 10μM, (b) 10μM and 100μM, (c) 0.1mM and 1mM and (d) 80nM. Inset shows the current vs concentration plot. (p. 100)

**Figure 3-12** (a) Stability test of the Cu/BDD in 0.1M KOH in the presence of 10μM glucose at +0.4V for 1800 sec and (b) anti-interference property of the Cu/BDD in the presence of 0.1mM glucose, 20μM UA and AA, respectively at +0.4V. (p. 101)

**Figure 4-1** (a) Cyclic voltammetry of the Au (111) substrate recorded in deaerated 0.1M HCl solution containing 10 mM $PdCl_2$ scanned negatively from OCP with a scan rate of 0.005 V/s (initial/conditioning: +0.79$V_{RHE}$, 10s), the upper potential limit was selected at 1.3$V_{RHE}$ and reverse potential at +0.52$V_{RHE}$ (F), +0.32$V_{RHE}$ (E), +0.12$V_{RHE}$ (D), -0.002$V_{RHE}$ (C) and -0.08$V_{RHE}$ (B), where

A represents the voltammogram of the substrate in 0.1M HCl electrolyte. (b) Expanded current densities within the selected potential region +0.1 to +0.6$V_{RHE}$. (p. 119)

**Figure 4-2** (a) Pd electrodeposition on a Au (111) substrate in deaerated 0.1M HCl solution containing 10 mM $PdCl_2$ (a) by liner sweep voltammetry (LSV) with a scan rate of 0.005 V/s (initial/conditioning: 0.79$V_{RHE}$, 10s); (b) by constant potential (potentiostatic) at four different potentials as marked by closed circles on LSV curve at (i) +0.54$V_{RHE}$ (small), (ii) +0.16$V_{RHE}$ (medium), (iii) +0.06$V_{RHE}$ (large) and (iv) -0.002$V_{RHE}$ (overlarge) (initial/conditioning: +0.79$V_{RHE}$, 10 s). The inset shows the time dependent current density in the shorter time scales. The legend shows the corresponding Pd deposition overpotential at +0.54$V_{RHE}$, +0.16$V_{RHE}$, +0.06$V_{RHE}$ and -0.002$V_{RHE}$. (p. 121)

**Figure 4-3** (a) Current-time transient recorded at various overpotentials vs. RHE on a Au (111) substrate in deaerated 0.1M HCl solution containing 10 mM $PdCl_2$ (initial/conditioning: +0.79$V_{RHE}$, 10s); (b) plot of current vs. time$^{-1/2}$ showing linear characteristic consistent with the Cottrell equation. The legend shows the corresponding Pd deposition potential at +0.54$V_{RHE}$, +0.16$V_{RHE}$, +0.06$V_{RHE}$ and -0.002$V_{RHE}$. (p. 122)

**Figure 4-4** Cyclic voltammetry of the Pd deposited on a Au (111) substrate at (a) +0.54$V_{RHE}$, (b) +0.16$V_{RHE}$, (c) +0.06$V_{RHE}$ and (d) -0.002$V_{RHE}$ in deaerated 0.1M $H_2SO_4$ solution shows $H_{ads}$/ $H_{abs}$/$H_{des}$ as well as Pd oxide formation/reduction peaks. CVs were recorded in static conditions with a scan rate of 0.02 V/s (initial/conditioning: +0.9$V_{RHE}$, 10s). The legend indicates the corresponding Pd deposition time. (p. 125)

**Figure 4-5** Ex-situ FEGSEM images for Pd nucleation and growth on a Au (111) substrate electrodeposited potentiostatically at (a) +0.54$V_{RHE}$, (b) +0.16$V_{RHE}$, (c) +0.06$V_{RHE}$ and (d) -0.002$V_{RHE}$ for a 433 μC cm$^{-2}$ deposition charge (0.98 monolayer equivalent). The electrolyte was made up with deaerated 0.1M HCl solution containing 0.001M $PdCl_2$. (p. 127)

**Figure 4-6** Ex-situ FEGSEM images of the Pd NPs on a Au(111) substrate as electrodeposited potentiostatically at (a) +0.54$V_{RHE}$, (b) +0.16$V_{RHE}$, (c) 0.06$V_{RHE}$ and (d) -0.002$V_{RHE}$ for a 3183 μC cm$^{-2}$ deposition charge (7.2 monolayer equivalent). The electrolyte was made up with deaerated 0.1 M HCl solution containing 0.001 M $PdCl_2$. (p. 129)

**Figure 4-7** Schematic illustration of the electrochemical growth mechanism of the Pd deposition on a Au (111) substrate when the overpotential is (i) small, (ii) medium, (iii) large and (iv) overlarge. (p. 130)

**Figure 4-8** (a) XPS and (b) XRD of Pd NPs on a Au (111) substrate for a total deposition charge of 3183 μC cm$^{-2}$. (p. 131)

**Figure 4-9** Cyclic voltammetry of Pd NPs deposited on a Au (111) substrate recorded in deaerated 5mM $K_3[FeCN]_6$ and 1M KCl electrolyte. CVs were recorded in static conditions with a scan rate of 0.05 V/s (initial/conditioning: +0.9$V_{RHE}$, 10s). Each electrode contains total Pd deposition charge of 3183 μC cm$^{-2}$ (i.e., 1.75 x 10$^{-6}$ g cm$^{-2}$). (p. 133)

**Figure 4-10** Cyclic voltammetry of Pd NPs deposited on a Au (111) substrate recorded in deaerated 0.5M KOH aqueous electrolyte. CVs were recorded in static conditions with a scan rate of 0.02 V/s (initial/conditioning: +1.0$V_{RHE}$, 10s). Electrode contains a total Pd deposition charge of 3183 μC cm$^{-2}$ (i.e., 1.75 x 10$^{-6}$ g cm$^{-2}$). (p. 134)

**Figure 4-11** Cyclic voltammetry of Pd NPs deposited on a Au (111) substrate for the electrooxidation of Ethanol in deaerated 1M EtOH and 0.5M KOH electrolyte. CVs were recorded in static conditions with a scan rate of 0.025 V/s (initial/conditioning: +0.4$V_{RHE}$, 10s). Each electrode contains total Pd deposition charge of 3183 μC cm$^{-2}$ (i.e., 1.75 x 10$^{-6}$ g cm$^{-2}$). (p. 136)

**Figure 4-12** SEM images of (a) Pd deposited on BDD electrode and (b) Pd deposited on HBDD electrode, respectively through chronoamperometry at -0.15V. (p. 141)

**Figure 4-13** (a) XPS spectra of wide scans of the Pd/BDD and Pd/HBDD, respectively. (b) Typical Pd 3d peaks of Pd modified BDD and HBDD catalysts, respectively. (p. 142)

**Figure 4-14** Chronoamperogram of Pd deposition in 1mM $PdCl_2$/0.1M HCl on bare BDD and HBDD electrodes, respectively at constant potential of -0.15V. (p. 143)

**Figure 4-15** (a) Cyclic voltammogram of Pd/BDD and Pd/HBDD (5.80 μg/cm$^2$) and (b) Linear sweep voltammograms of the Pd modified BDD and HBDD (5.80 μg/cm$^2$), respectively in 0.5M KOH solution at scan rate of 0.02 V/s (all CVs were started from open circuit potential). (p. 145)

**Figure 4-16** Cyclic voltammograms of Pd modified BDD and HBDD with 5.80 μgr/cm$^2$ (i.e., 10.52 mC/cm$^2$ charge) Pd loading, respectively in 0.5M KOH and 1M EtOH at scan rate of 0.02 V/s. Cyclic voltammograms shown here are taken after 10 cycles. (p. 146)

**Figure 4-17** Chronoamperometric response of Pd modified BDD and HBDD respectively after 5.2 mC/cm$^2$ passage of charge in 0.5M KOH and 1M EtOH at potential -0.15V. (p. 148)

**Figure 5-1** SEM images of (a) Pd deposited on HBDD electrodes and (b) Pd-Sn on HBDD through chronoamperometry at -0.15V for the Pd and cyclic voltammetry between -0.6V and +0.5V at scan rate of 0.01 V/s for the Sn. (c) Elemental mapping of Pd-Sn modified HBDD. (p. 167)

**Figure 5-2** (a) XPS spectra of wide scans of the Sn/HBDD, Pd/HBDD and Pd-Sn/HBDD, respectively. (b) Typical Sn 3d peaks of Sn and Pd-Sn modified HBDD catalysts, respectively. (c) Typical Pd 3d peaks of the Pd and Pd-Sn modified HBDD catalysts, respectively. (p. 168)

**Figure 5-3** (a) Cyclic voltammogram of bare HBDD in a solution containing 0.26M $C_2H_6O_6S_2Sn$ in 1M $CH_3SO_3H$ at scan rate of 0.01 V/s (inset: linear sweep voltammogram of bare HBDD in 0.26M $C_2H_6O_6S_2Sn$ in 1M $CH_3SO_3H$). (b) Cyclic voltammogram of bare HBDD in a solution containing 0.1M HCl and 1mM $PdCl_2$/0.1M HCl respectively at scan rate of 0.01 V/s (inset: chronoamperogram of Pd deposition in 1mM $PdCl_2$/0.1M HCl on bare HBDD at constant potential of -0.15V). (p. 170)

**Figure 5-4** Cyclic voltammogram of (a) Pd/OBDD and Pd/HBDD (5.80 μg/cm$^2$), (b) Sn/HBDD (97 μgr/cm$^2$), (c) Pd and Pd-Sn modified HBDD (2.90 μg/cm$^2$), and (d) Linear sweep voltammograms of the Pd and Pd-Sn modified HBDD (2.90 μg/cm$^2$), respectively in 0.5M KOH solution at scan rate of 0.02 V/s (all CVs were started from open circuit potential). (p. 174)

**Figure 5-5** (a, b) Cyclic voltammograms of Pd and Pd-Sn modified HBDD with 1.45 μg/cm$^2$ (i.e., 2.6 mC/cm$^2$ charge) and 2.90 μg/cm$^2$ (i.e., 5.2 mC/cm$^2$ charge) Pd loading, respectively in 0.5M KOH and 1M EtOH at scan rate of 0.02 V/s. (c) Cyclic voltammograms of Pd and Pd-Sn modified HBDD (with 5.80 μg/cm$^2$: Pd loading) in 0.5M KOH and 1M EtOH at scan rate of 0.02 V/s. (all CVs were started from open circuit potential). Cyclic voltammograms shown here are steady state taken after 10 cycles. (p. 177)

**Figure 5-6** Representation of mechanism of Ethanol Oxidation Reaction (EOR) on various Pd loadings of shell-core Pd-Sn nanostructures. (p. 178)

**Figure 5-7** Tafel plots of anodic polarisation curve for ethanol oxidation in 0.5M KOH and 1M EtOH: (a, b) of Pd and Pd-Sn modified HBDD with 1.45 μg/cm$^2$ (i.e., 2.6 mC/cm$^2$) and 2.90 μg/cm$^2$ (i.e., 5.2 mC/cm$^2$) Pd loading, respectively. (c) of Pd and Pd-Sn modified HBDD (with 5.80 μgr/cm$^2$: Pd loading). (p. 180)

**Figure 5-8** (a, b) Chronoamperometric response of Pd and Pd-Sn modified HBDD after 2.6 mC/cm$^2$ and 5.2 mC/cm$^2$ passage of charge respectively in 0.5M KOH and 1M EtOH at potential -0.15V. (p. 181)

**Figure 5-9** SEM images of (a) Ni deposited on BDD electrodes, (b) Pd on BDD and (c) Pd-Ni deposited on BDD, respectively through chronoamperometry at -1.2V for the Ni and -0.15V for the Pd, respectively. (p. 184)

**Figure 5-10** EDX spectra of (a) Ni deposited on BDD electrodes, (b) Pd on BDD and (c) Pd-Ni on BDD, respectively. (p. 185)

**Figure 5-11** XPS spectra of wide scans of the Ni/BDD, Pd/BDD and Pd-Ni/BDD, respectively. (b) Typical Ni 2p peaks of Ni and Pd-Ni modified BDD catalysts, respectively. (c) Typical Pd 3d peaks of the Pd and Pd-Ni modified BDD catalysts, respectively. (p. 186)

**Figure 5-12** (a) Chronoamperogram of bare BDD in a solution containing 10mM [$Ni(NO_3)_2 \cdot 6H_2O$] in acetate buffer at constant potential of -1.2V. (b) Cyclic voltammogram of bare BDD in a solution containing 0.1M HCl and 1mM $PdCl_2$/0.1M HCl respectively at scan rate of 0.01 V/s (inset: chronoamperogram of Pd deposition in 1mM $PdCl_2$/0.1M HCl on bare BDD at constant potential of -0.15V). (p. 187)

**Figure 5-13** Cyclic voltammograms (a and b) and linear sweep voltammogras (c and d) of the Ni/BDD (658 mC/cm$^2$), Pd/BDD (Pd loading: 2.9 (a) and 11.6 (b) μg/cm$^2$) and Pd-Ni modified BDD (Pd loading: 2.9 (a) and 11.6 (b) μg/cm$^2$, respectively), respectively in 0.5M KOH solution at scan rate of 0.02 V/s (all CVs and LSVs were started from open circuit potential). (p. 191)

**Figure 5-14** (a, b) Cyclic voltammograms of Pd and Pd-Ni modified BDD with 2.9 μg/cm$^2$ (i.e., 5.2 mC/cm$^2$ charge) and 11.6 μg/cm$^2$ (i.e., 21 mC/cm$^2$ charge) Pd loading, respectively in 0.5M KOH and 1M EtOH at scan rate of 0.1 V/s. (c) Cyclic voltammograms of Pd and Pd-Ni modified BDD (with 2.9 μgr/cm$^2$: Pd loading and various Ni loadings) in 0.5M KOH and 1M EtOH at scan rate of 0.1 V/s. (all CVs were started from open circuit potential). The subscript values in the legend in Fig. (c) show the Ni charge per 1 cm$^2$ of electrode. Cyclic voltammograms shown here are taken after 10 cycles. (p. 194)

**Figure 5-15** Tafel plots of anodic polarisation curve for ethanol oxidation in 0.5M KOH and 1M EtOH: (a, b) of Pd and Pd-Ni modified BDD with 2.9 μgr/cm$^2$ (i.e., 5.2 mC/cm$^2$) and 11.6 μg/cm$^2$ (i.e., 21 mC/cm$^2$) Pd loading, respectively. (p. 195)

**Figure 5-16** (a) Chronoamperometric response of Pd and Pd-Ni modified BDD after 5.2 mC/cm$^2$ passage of charge and (b) after 21 mC/cm$^2$ and 2.9 mC/cm$^2$ passage of charge respectively in 0.5M KOH and 1M EtOH at potential -0.15V. (p. 197)

**Figure 6-1** SEM images of (a) $Cu_2O$ modified BDD and (b) Ni(15)-$Cu_2O$/BDD electrode under the preparation conditions described in the experimental section. (p. 214)

**Figure 6-2** (a) XPS spectrum of survey of the $Cu_2O$/BDD (Inset: typical Cu 2p peak). (b) XPS spectrum of wide scan of the NiO-$Cu_2O$/BDD (Inset: typical Ni 2p peak). (c) Typical Cu 2p peaks of the $Cu_2O$ and NiO-$Cu_2O$ modified BDD, respectively. (p. 216)

**Figure 6-3** Photoelectrochemical responses of (a) bare BDD, $Cu_2O$, NiO(3)- $Cu_2O$ and NiO(6)- $Cu_2O$ modified BDD, respectively (Inset: PEC performances under non-chopped light), (b) NiO(10)- $Cu_2O$, NiO(15)- $Cu_2O$, NiO(20)- $Cu_2O$ and NiO(20)- $Cu_2O$ modified BDD, respectively (Inset: PEC performances under non-chopped light) and (c) $Cu_2O$/BDD and NiO(15)- $Cu_2O$/BDD. All the linear sweep voltammograms were conducted in 0.1M $Na_2SO_4$ electrolyte at 10 mV/s buffered at pH 6.1 under chopped AM 1.5G light illumination. (p. 220)

**Figure 6-4** Photoelectrochemical repsonses of different photoelectrodes: (a) NiO(10)-$Cu_2O$/BDD, (b) NiO(15)-$Cu_2O$/BDD, (c) NiO(20)-$Cu_2O$/BDD and (d) NiO(25)-$Cu_2O$/BDD under chopped AM 1.5G light illumination at 0.2 Hz at scan rate of 10 mV/s. (p. 222)

**Figure 6-5** Chronoamperograms of the photoelectrochemical response of the different photoelectrodes (a) NiO(10)-$Cu_2O$/BDD, (b) NiO(15)-$Cu_2O$/BDD, (c) NiO(20)-$Cu_2O$/BDD, (d) NiO(25)-$Cu_2O$/BDD

and (e) $Cu_2O$/BDD under chopped AM 1.5G light illumination at 0.2 Hz held at -0.5V under chopped light illumination for 30 min. (p. 225)

**Figure 6-6** (a) Nyquist plots of NiO(10)-$Cu_2O$/BDD, NiO(15)-$Cu_2O$/BDD, NiO(20)-$Cu_2O$/BDD and NiO(25)-$Cu_2O$/BDD photoelectrodes in dark and under AM 1.5G light illumination in 0.1M $Na_2SO_4$ electrolyte buffered at pH 6.1. (b) Mott-Schottkly plots of NiO(10)-$Cu_2O$/BDD, NiO(15)-$Cu_2O$/BDD, NiO(20)-$Cu_2O$/BDD and NiO(25)-$Cu_2O$/BDD photoelectrodes in dark in 0.1M $Na_2SO_4$ electrolyte buffered at pH 6.1. (p. 229)

**Figure 6-7** SEM images of (a) $Cu_2O$ deposited on BDD electrodes (100 μm), (b) $Cu_2O$ on BDD (20 μm) and (c) Ni deposited on $Cu_2O$/BDD, respectively through potentiostatic method at -6.6 mA for the $Cu_2O$ and -20 mA for the Ni, respectively. (p. 231)

**Figure 6-8** (a) XPS spectrum of survey of the $Cu_2O$/BDD and Ni-$Cu_2O$/BDD. (b) Typical Cu 2p peaks of the $Cu_2O$ and Ni-$Cu_2O$ modified BDD electrodes respectively. (c) Typical Ni 2p peak of the Ni-$Cu_2O$ modified BDD. (p. 232)

**Figure 6-9** Electrochemical and photoelectrochemical responses of (a) bare BDD, $Cu_2O$ and Ni(20s)-$Cu_2O$ in the presence of $CO_2$ and Ni(20s)-$Cu_2O$ modified BDD in the presence of $CO_2$ under non-chopped light, respectively. (b) $Cu_2O$, Ni(10s)-$Cu_2O$, Ni(20s)-$Cu_2O$, NiO(30s)- $Cu_2O$ and NiO(50s)-$Cu_2O$ modified BDD, respectively in the presence of $CO_2$ under non-chopped light. (c) Bare BDD, $Cu_2O$/BDD and Ni(20s)-$Cu_2O$/BDD in the presence of $CO_2$ under non-chopped light. All the cyclic voltammograms were conducted in 0.5M $KHCO_3$ electrolyte at 20 mV/s buffered at pH 6.1 under non-chopped AM 1.5G light illumination. (p. 235)

**Figure 6-10** Schematic illustration of the basic mechanism of photocatalytic reduction of $CO_2$ with $H_2O$ on a semiconductor photocatalyst[18]. (p. 237)

# List of Tables

**Table 1-1** Fundamental properties of diamond (source from[9]). (p. 22)

**Table 3-1** XPS % elemental ratio of different electrodes. (p. 83)

**Table 3-2** Pt features after electrodeposition through chronoamperometry. (p. 91)

**Table 4-1** Overpotential dependent electroactive surface area (EASA), specific surface area (SSA), ethanol electrooxidation and mass activity of Pd NPs. (p. 134)

**Table 4-2** Pd features after electrodeposition through chronoamperometry. (p. 145)

**Table 4-3** Pd features after electrodeposition through chronoamperometry. (p. 147)

**Table 5-1** Pd features after electrodeposition through chronoamperometry. (p. 178)

**Table 5-2** Pd features after electrodeposition through chronoamperometry. (p. 193)

# Chapter 1

# Introduction

## 1.1 Electrode materials

### 1.1.1 Diamond

#### 1.1.1.1 General overview

Diamond is well known as the symbol of wealth, prestige and prosperity. The exact word *diamond* comes from the ancient Greek word *adamas* (*αδάμας)* which means unbreakable, invincible or indestructible and is used exactly for the same reason as the words describe, being the hardest substance known[1,2]. It is said that diamond was first mined in India some thousands of years ago between three rivers[2]. The popularity of diamonds as gemstones rose in the 19$^{th}$ century because of the increased supply and growth in the global economy as well as due to the improved cutting and polishing techniques[3]. In the 20$^{th}$ century, the methods of grading diamonds and other gemstones was significantly developed by experts. Four characteristics were used to value them as gems. These were the carat (its weight, 1 carat=0.2 grams), the cut (its quality according to proportions, symmetry and polish), the colour (to what extent is it close to white or colourless) and finally the clarity (how free is it from inclusions)[2].

Various types and sizes of diamond are illustrated in figure 1-1. A diamond bigger than the Earth was discovered in constellation Centaurous (Figure 1-1 (a)). The Harvard-Smithsonian Centre for Astrophysics announced the discovery of this diamond known as star BPM 37093. It is believed that this is the biggest diamond in the galaxy and is fifty light years

away from Earth[4]. Figure 1-1 (b) shows another type of diamond, the Centenary Diamond, which is the largest flawless and colourless diamond known on earth and took its name from the centenary celebrations of De Beers in the end of the 19th century[5]. The De Beers is a company having a leading role in the diamond exploration, diamond mining, retail, trading and industrial manufacturing sectors[5].

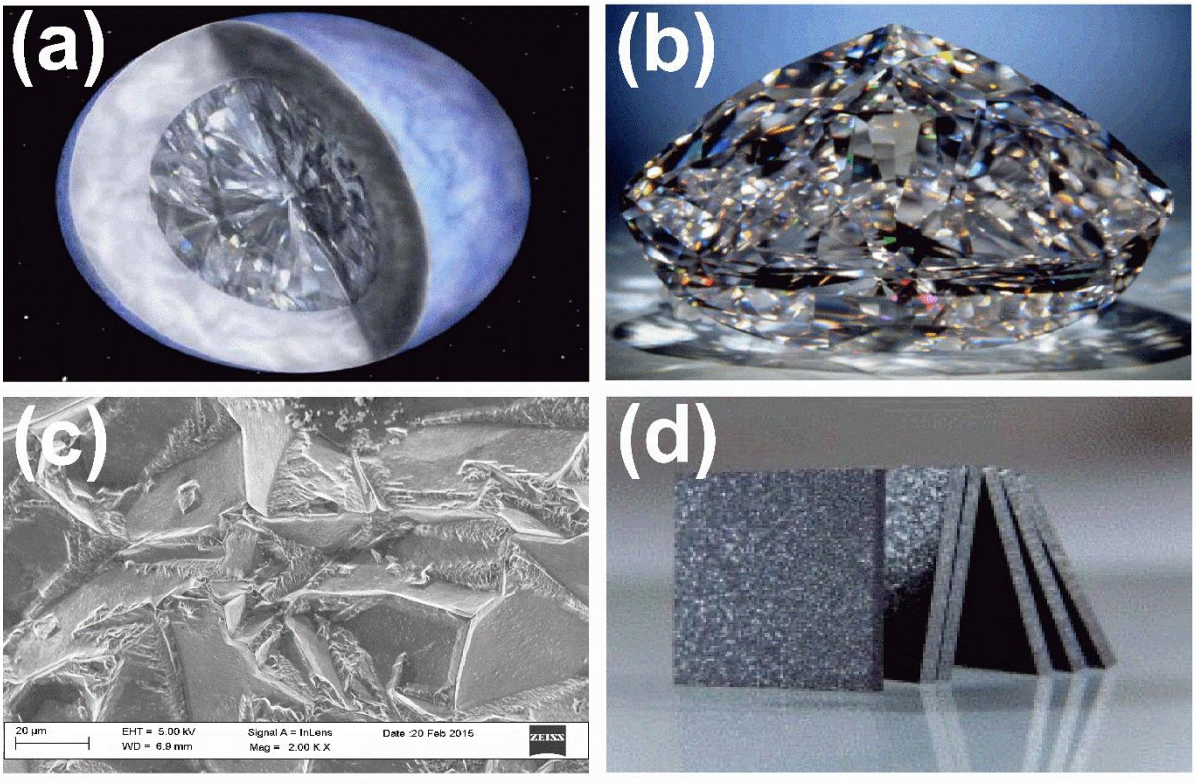


**Figure 1-1** Various types of diamond: (a) the core of BPM 37093 found 50 light years away from Earth[4]. (b) Centenary diamond, the largest flawless and colourless diamond[5]. (c) SEM image of a boron-doped diamond (blank sample). (d) Black boron-doped diamond squares.

## 1.1.1.2 Structure and general properties of diamond

Diamond is a transparent form of bonded carbon atoms in a covalent network lattice ($sp^3$). All the carbon atoms are arranged in a variation of the face-centered cubic crystal structure in this lattice (Figure 1-2). Each carbon atom is tetrahedrally surrounded by four equidistant neighbours. Furthermore, diamond contains two interpenetrating FCC lattices, which are off-set along the body diagonal by a quarter of its length[6].

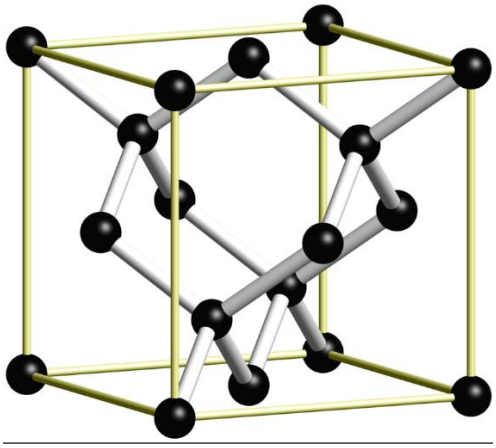

**Figure 1-2** 3D diamond structure[7].

In comparison with other carbon materials diamond possesses outstanding properties such as the high hardness ($1 \times 10^4$ kg mm$^{-2}$), high thermal conductivity (2600 W m$^{-1}$ K$^{-1}$) and high charge carrier mobilities (electron mobility: 2200 cm$^2$ V$^{-1}$ s$^{-1}$, hole mobility: 1600 (cm$^2$ V$^{-1}$ s$^{-1}$)[8]. Some of the main properties of diamond can be found in Table 1-1.

**Table 1-1** Fundamental properties of diamond (source from[9]).

| Properties | Values |
|---|---|
| Extremely high hardness (Vickers) | ca. 10000 kp m$^{-2}$ |
| High thermal conductivity | 20 W cm$^{-1}$ K$^{-1}$ at 300 K |
| Optical transparency (undoped) | λ= 2.5 μm to 230 nm |
| Large electronic bandgap (undoped) | $E_{gap}$= 5.5 eV |
| Refractive index | 2.42 at 546 nm |
| Dielectric constant | 5.6 |
| Dielectric strength | Ca. $10^8$ to $10^9$ Vm$^{-1}$ |
| Melting point | 4027 K |
| Density | 3.52 g cm$^{-3}$ |
| Chemically inert surface | Up to 850 K in air<br>Up to 2000 K in vacuum |

With a bandgap of 5.45 eV undoped diamond is an excellent insulator with resistivities of the order of $10^{20}$ (Ω cm)[8]. Due to the high resistivity, the properties of doped diamond have received increasing attention. Boron is the most common dopant used to produce conducting diamond[10]. This arises from the low charge carrier activation energy of 0.37 eV (Figure 1-3). However, controlling the level of the doping is important because high levels can lead to a

semimetal behaviour. A p-type semiconductor of boron-doped diamond can be obtained at a lower doping level of $10^{17}$-$10^{18}$ ($cm^{-3}$)[10]. Conversely, BDD with higher doping levels of around $10^{20}$ to $10^{21}$ ($cm^{-3}$) exhibits semi-metal behaviour due to overlapping of p-type holes on diamond with boron-acceptor state, which allows current to flow without thermal activation[10]. Other dopants are also possible (Figure 1-3). Nitrogen (charge carrier activation energy 1.6-1.7 eV)[10–12] and phosphorous, can provide n-type conductivity (charge carrier activation energy 0.6 eV)[12,13].

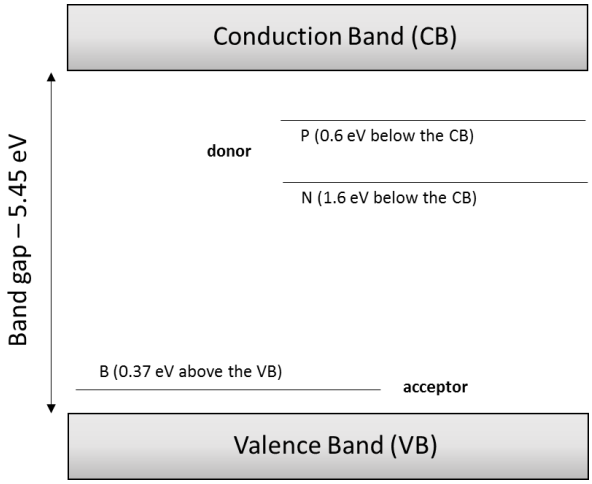


**Figure 1-3** Representation of the energy diagram of selected states in the band gap of diamond[8].

## 1.1.1.3 Synthetic diamond and its application in electrochemistry

As already discussed in section 1.1.1.2, diamond possesses outstanding properties but its application can be prohibited by the high cost as well as the dimensions and the reproducibility of natural diamond. Therefore, the development of synthetic diamond has attracted a lot of attention in the past few decades. Natural diamond is formed under extreme conditions such as high heat and pressure. Thus scientists have tried to reproduce those conditions in their labs, in attempts to fabricate a structure which is more stable than graphite.

Scientists in Sweden succeeded in fabricating synthetic diamond in 1953[14] and one year later the General Electric reported they had synthesized diamond with the belt press[15], a process further explained in the next section 1.1.1.4. In 1982, the Matsumoto group invented the first hot filament chemical vapour deposition (HFCVD) reactor which was able to deposit a high quality diamond film[16,17] and the following year, the same group reported a microwave plasma enhanced CVD (MWCVD) system[18,19]. Both these methods are explained in section 1.1.1.4.

It is of utmost importance to reproduce the conditions of diamond growth and subsequently to take advantage of some of the exceptional properties of diamond. However, various dopants can increase the overall conductivity and electrochemical properties. Various types of dopants are phosphorous[20], nitrogen[21], hydrogen[22] or sulphur[23]. Nevertheless, most of the work in diamond electrochemistry is based on boron-doped diamond materials. In this context, besides the outstanding physical properties of that kind of synthetic diamond, it exhibits excellent electrochemical properties such as chemical inertness, low capacitance, low background current (~ 10 μF $cm^{-2}$), an extremely wide potential window in aqueous solutions (see Figure 1-4), resistance to fouling and electrocorrosion in hostile environment[9,24,25]. The last two properties are especially important given that during many electrochemical measurements the electrode can be poisoned by adsorption of electrically insulating compounds on the surface[26]. It is notable additionally that reproducibility, sensitivity to various analytes and by extension the easily measurable signal response[26,27,28]. Another interesting feature is the fact that diamond electrodes exhibit stable terminations with the diamond substrate, so this interaction could be controlled by changing the chemical termination from O-terminated to H-terminated[29–31]. Hence, the electrochemical properties of diamond electrodes

are determined by the nature of the surface hydrogen termination which comes from the hydrogen rich environment during the growth and cooling process[25].

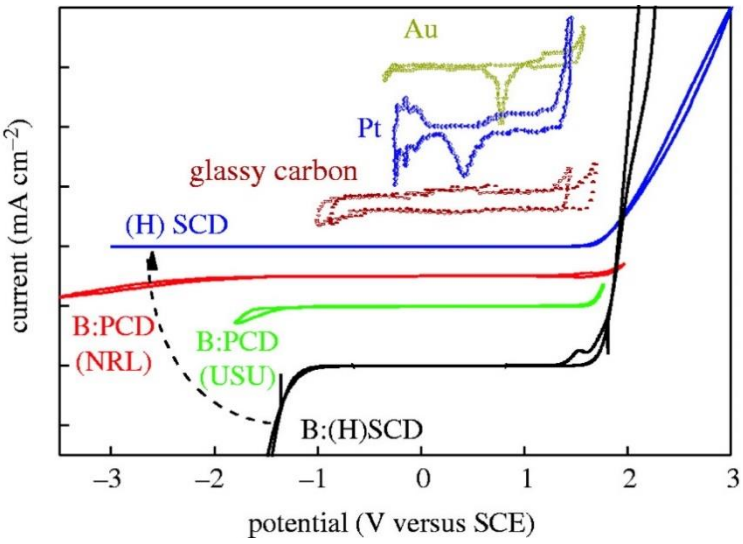


**Figure 1-4** Cyclic voltammograms of water electrolysis in 0.5M $H_2SO_4$ of two boron-doped polycrystalline films (B:PCD-NRL and B:PCD-USU, one single crystal boron doped diamond (B:H-SCD) and one undoped diamond (H-SCD)[32].

Because the special electrochemical properties of doped diamond electrodes can be used for multiple applications. Some of applications are in fuel cells[24,33], electrochemical sensors[34–36] and water treatment[37]. The boron-doped diamond electrodes more specifically have been used to the following electrochemical areas: in electroanalysis[38–42], electrosynthesis[43,44], electrocatalysis[45–47], energy harvesting[48,49] and water purification[50–52]. Currently, a remarkable number of reviews discussing the electroanalytical and electrocatalytic aspects of boron-doped diamond electrodes are available. Reviews of this type include Compton *et al.* in 2003 which gives a summary on the types of diamond electrodes, their properties and their applications in electroanalysis[9]. A more recent review from the same group is also available, examining the modification of boron-doped diamond with metal nanoparticles[53]. In addition, the Krueger *et al.* in 2012, discuss the modification strategies of detonation nanodiamond powders, their properties as well as their applications[54].

# 1.1.1.4 Growth techniques of diamond

## 1.1.1.4.1 A short introduction

The first early attempts to synthesize diamond started in 1828 by Gannal, who tried to crystallise diamond from a carbon rich solution but without success[55]. Some decades later, James Ballantyne Hannay in 1880 claimed to have synthesised diamond by heating a mixture of bone-oil, paraffin spirit and lithium in a sealed iron tube, thus creating a very high pressure. The oil vapourised and reacted with the lithium to produce carbon, which was deposited on the reactor walls[56,57]. A French chemist Henri Moissan tried a similar experiment with Hannay in 1896 but later, Sir Charles Parson, repeated both Hannay's and Moissan's experiments, with the result that after 30 years, none of these scientists had succesfully synthesised diamond. Finally, a high pressure synthesis was examined from a truly scientific viewpoint by two chemists, Gilbert Lewis and Merle Randall, who showed for the first time that diamond is unstable with respect to graphite at room temperature and atmospheric pressure. Hence, they roughly calculated that by increasing the pressure to over 10,000 atmospheres, diamond would reach the stable form[58]. Since then, more investigations and calculations have been achieved. A carbon phase diagram is shown in Figure 1-5.

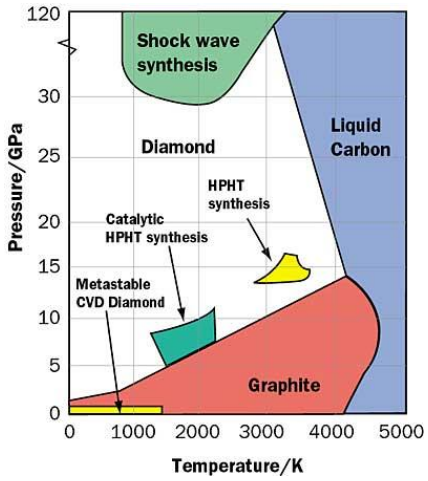


**Figure 1-5** Schematic representation of the carbon phase diagram[2].

Percy Williams Bridgman, an American physicist who won the Nobel Prize in Physics in 1946 for his work on the physics of high pressures, found that diamond cannot be formed at pressures up to 400,000 atmospheres, although the carbon phase diagram predicts diamond formation. This is due to very strong diamond bonds and at room temperatures the conversion is therefore extremely slow. A Swedish company Allmänna Svenska Elektriska Aktiebolaget (ASEA) was first to create a high-pressure synthesis of diamond in 1953[59].

The HPHT growth technique was not the only one used to produce high quality diamond industrial applications. A second method was found to enable the growth of large areas of high quality single crystal diamond on non-diamond substrates. This method is the Chemical Vapour Deposition (CVD) of diamond at reduced pressures. The earliest report concerning diamond growth from the gas phase was published by Warner von Bolton in 1911[60] who claimed that he deposited diamond from acetylene in the presence of mercury vapour at 100 °C.

### 1.1.1.4.2 High Pressure High Temperature (HPHT) technique

ASEA did not publish and patent its accomplishment, so the first publication of successful diamond high-pressure high-temperature (HPHT) synthesis was made by the General Electric Company in 1955[61]. To reproduce the conditions of diamond's birth some 150-200 km below the Earth's surface, several HPHT methods have been developed. HPHT diamond can be crystallised from metal-solvated carbon at a pressure of approximately 5-10 GPa and a temperature in the range of 1800-2300 K (see Figure 1-5)[62]. Metal catalysts are used during the fabrication and as a result contaminate the diamond lattice as it forms. The metal impurities create slight imperfections in the crystal lattice that are able to cause many flaws for electronic devices and other applications. The metal contaminations can also cause the

production of coloured diamonds. The two most common HPHT methods are the BELT system and its Russian counterpart, the BARS system.

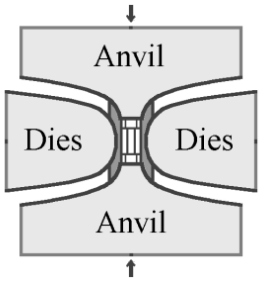


**Figure 1-6** Image of a belt press[63].

The BELT system was used by De Beers[5] and General Electric[61], amongst others and is basically a huge hydraulic press (Figure 1-6)[63]. The upper and the lower anvils supply the pressure load to a cylindrical inner cell. This internal cell is confined radially by a belt of pre-stressed steel bands. The anvils also serve as electrodes providing electrical current to the compressed cell.

Figure 1-7 gives a more detailed schematic example of a BELT[64]. High quality diamond seed crystals are placed at the bottom of the press medium. The internal part of the press is heated by a tubular, graphite heater. This generates temperatures above 1400 °C and melts the solvent metal (e.g. Fe-Co + Ti, Cu). The molten metal dissolves the high purity carbon source, which is then transported to the mode of natural diamond and precipitates.

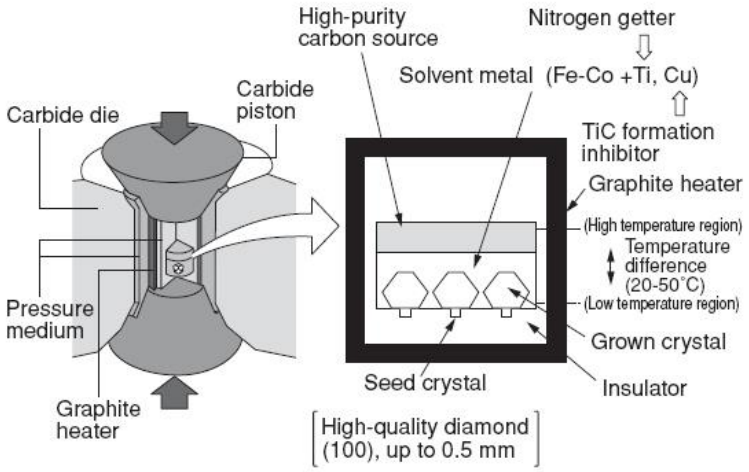


**Figure 1-7** Schematic example of a Belt type HPHT press[64].

The BARS apparatus on the other hand (Figure 1-8), is the most effective, compact and economical of all the diamond producing presses. In the center of a BARS device, there is a ceramic cylindrical "synthesis capsule" of about 2 $cm^3$ in volume. The cell is placed into a cube

of pressure-transmitting material, such as pyrophyllite ceramics. The other cavity is pressed by 8 steel outer anvils. After mounting the whole assembly is locked in a disc-type barrel with a diameter of about 1 meter. The barrel is filled with oil, which is pressurized upon heating and the oil pressure is transferred to the central cell. The synthesis capsule is heated by a coaxial graphite heater and the temperature is measured with a thermocouple[65].

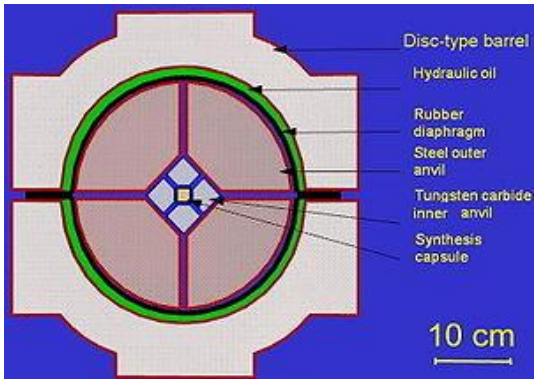


**Figure 1-8** Image of the BARS apparatus[63].

## 1.1.1.4.3 Chemical Vapour Deposition (CVD) technique

Chemical vapour deposition (CVD) production of diamonds has received a great deal of attention in Materials Sciences because it overcomes the prohibitive expense of synthesising diamonds, and therefore allows new applications of diamonds to be explored. CVD is a chemical process used mostly in the semiconductor industry in order to produce thin films. In a typical CVD, the wafer (substrate) is exposed to one or more volatile precursors which react and/or decompose on the substrate to produce the desired deposit. Frequently, volatile by-products are produced during this process which are removed by gas flow through the reaction chamber.

Diamond films can be deposited by various chemical vapour deposition (CVD) techniques, of which the most important are the arc-jet CVD[66], the hot filament CVD[16] and the microwave plasma CVD[67]. Regarding the growth procedure, a hydrocarbon-hydrogen mixture

(typically 0.1-5 % methane in hydrogen) is activated by a plasma or a thermal source, creating radicals and hydrocarbons such as acetylene. The growth species diffuse to the substrate surface (which is usually Si or W) to produce diamond via a complex growth mechanism which is very sensitive to temperature changes, pressure and gas composition. During the above procedure, boron can be added as the dopant in the gas phase mixtures, which consists of a carbon source such as methane and hydrogen as the carrier gas in order to produce a boron doped diamond[68]. In this way diamond films can display semi-metallic properties as well as electrochemical properties, supplying numerous advantages such as high overpotential for both oxygen and hydrogen evolution in aqueous media and subsequently leading to a wide potential window[69–72], very low capacitance[73] and low adsorption of contaminants leading to low fouling and high electrochemical stability (as discussed in section 1.1.1.3 of this chapter) [69,61–64]. Figure 1-9 shows further examples of some of the most common types of low pressure CVD reactors[78]. These methods for production of diamond are described in detail by Paul W. May in an article[78]. In terms of a schematic diagram of the physical and chemical processes during diamond CVD growth is given in the schematic figure (Figure 1-10)[79]. The process gases first mix in the chamber before diffusion toward the substrate surface. A hot filament provides the energy to the gaseous species. The activation causes molecules to fragment into reactive radicals and atoms, creates ions and electrons and heats the gas up to temperatures reaching a few thousand Kelvin. Beyond the activation region, these reactive fragments continue to mix and complete a complex set of chemical reactions until they strike the substrate surface. At this point the species either adsorb and react with the surface, desorb back into the gas phase or diffuse close to the surface until an appropriate reaction site is found. If the surface reaction occurs and the conditions are suitable, the growth of diamond is attained.

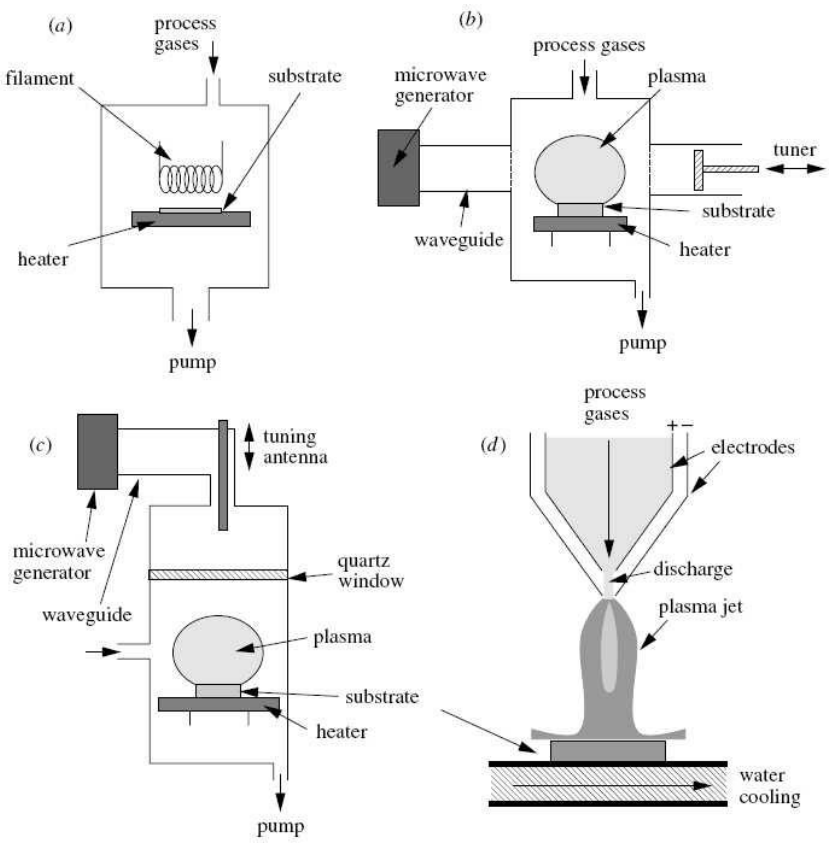


**Figure 1-9** Examples of some of the most common types of low pressure CVD reactors. (a) Hot filament, (b) NIRIM type microwave plasma reactor, (c) ASTEX type microwave plasma reactor and (d) DC arc jet (plasma torch).

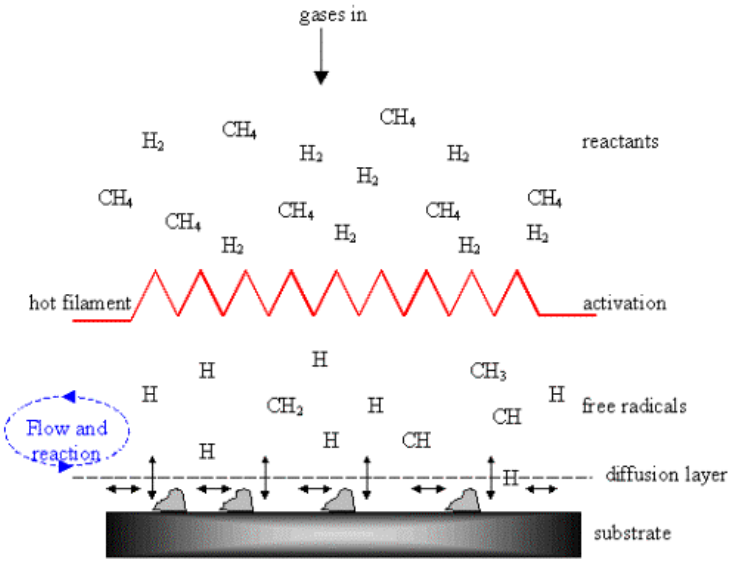


**Figure 1-10** Schematic diagram of the physical and chemical processes during diamond CVD growth[79].

### 1.1.2 Complementary Metal Oxide Semiconductor (CMOS)

CMOS (complementary metal-oxide semiconductor) is the semiconductor technology used in the transistors that are manufactured into most of today's computer microchips. Semiconductors are mostly made of silicon and germanium materials. The doped areas in these materials become full-scale conductors of either negative charge carriers (n-type transistors) or of positive charge carriers (p-type transistors). In CMOS technology, both kind of transistors are used in complementary ways to form a current gate that forms an effective means of electrical control. CMOS transistors use almost no power when not needed. However, the transistors become hot as the current direction changes more rapidly. This characteristic tends to limit the speed at which microprocessors can operate.

For the past few decades, CMOS have received huge attention due to their potential use in advanced areas of sensors, photovoltaic cells, biomedical and photocatalytic engineering[80–82]. In addition, these metal oxides of controlled micro/nano-morphologies have found significant applications such as nanomaterial synthesis, super capacitors, water purification systems and self-cleaning and self-sterilising materials[83–85].

## 1.2 Surface modification with metal nanoparticles

Exploitation of nanomaterials and nanoparticles is an area of research that is continually growing. Surface modification of conventional electrodes for enhanced current response is very important in developing a stable and highly target specific interface. Sensitivity and selectivity are the crucial issues for the development of sensors for detecting biologically active molecules. Moreover, sensitivity and selectivity are equally important to the fuel cell industry. The deposition of nanosized metal or metal oxide clusters enables improved features such as enhanced sensitivity and selectivity towards analytes which cannot be detected on the

unmodified surface[39]. Additionally, the deposition of catalytic metal nanoparticles on various carbon electrodes can increase the electrochemically active surface area, not only for a variety of electroanalytical applications, but also for adsorptive voltammetry[86].

Metal nanoparticles (NPs), on the other hand, have wide applications in different kinds of electroanalytical methods and can be used to construct novel and improved sensing devices, particularly electrochemical sensors and biosensors. Owing to their small size (in order of 1-100 nm) metal nanoparticles exhibit special chemical, physical and electronic properties. They can absorb biomolecules strongly and play an important role in the modification of electrodes to improve, performance, mass transport and biocompatibility and their electrocatalytic activities as they exhibit higher catalytic efficiency than the bulk materials. Metal nanomaterials enhance performance of the electrodes by enlarging their surface area to volume ratio[87]; large areas of deposited metal nanoparticles permit improvement of the analytical performance in terms of low detection limits especially for sensing applications.

Transition metal nanomaterials possess high catalytic activity and facilitate electron transfer for many electrochemical reactions. A wide variety of metallic nanoparticles have been studied to assess the applications of these materials. Some examples of metals studies include platinum black[88], copper[89], silver[90], palladium[91] and gold[92], all of which have exhibited good biocompatibility and enhanced performance. Nanoparticles of bismuth[93] and iridium[94] have also been synthesised recently.

## 1.3 Scope of the thesis

Boron-doped diamond has in recent years become widely used in the field of electrochemistry and is considered as one of the most promising electrode materials due to its special properties such as wide potential window, low background current, corrosion resistance

etc. The main target of this work is therefore the electrochemical modification of diamond electrodes with various transition metal nanoparticles and their use for sustainable energy applications. The vast majority of the projects were conducted on boron-doped diamond electrodes but Au (111) substrates were also used. The latter was used in a collaboration with a Marie Curie research associate. Furthermore, apart from the sustainable energy oriented projects, one project dealt with the fabrication and application of diamond electrodes in glucose sensing. More specifically, this work is mostly focused on the fabrication of core-shell structures and their metallic interaction with each other, as well as with the underlying substrate. Yet, the different chemical terminations of diamond are examined and how they can affect not only the size of the particles but also the overall electrocatalytic performance. A brief description of the projects follows.

In *Chapter 3,* the electrochemical deposition of Pt-Cu core-shell nanoparticles as well as Cu nanoparticles for the electrooxidation of methanol and glucose oxidation are developed, respectively. The data suggested that metallic interaction can be achieved through core-shell nanostructures and therefore they can offer improved electrocatalytic performance towards various analytes compared to single nanoparticle structures. Also, a low-cost material such as the Cu/BDD electrode, which can oxidise glucose effectively and thus be a promising 4$^{th}$ generation non-enzymatic glucose sensor was developed.

In *Chapter 4*, a more fundamental study is carried out. An overpotential dependent growth of Pd metallic nanoparticles on Au (111) substrates by electrodeposition from a surfactant-free "green" electrolyte is accomplished. The main aim of this work is the investigation of the nucleation and growth mechanism of nanoparticles related to the electrocatalytic performance. In addition, the Pd nanoparticles are electrodeposited on oxygen and hydrogen-terminated diamond surfaces as an effort to investigate the electrocatalytic performance of the electrocatalysts correlated to the surface termination.

*Chapter 5* further extends all of the above work. More specifically, core-shell structures and two different chemical terminations of diamond are investigated with regard to electrocatalytic activity towards ethanol electrooxidation of different core metals supported on two dissimilarly terminated surfaces. Pd was chosen to replace Pt as it is more abundant on Earth and cheaper, having similar features to the latter.

*Chapter 6* describes a novel electrode material for the application of water splitting and $CO_2$ reduction, respectively. In this work, photoactive materials consisted of Ni-$Cu_2O$ modified boron-doped diamond electrodes are fabricated and tested under solar illumination for solar hydrogen production and $CO_2$ reduction reaction, respectively. As in chapters 3 and 5, core-shell structures are examined as Ni (shell) metal was electrodeposited onto $Cu_2O$/BDD electrodes and played a role of a protective layer in order to avoid $Cu_2O$ self-photo corrosion.

# 1.4 Bibliography

1. May PW. Diamond thin films: a 21st-century material. *Philos. Trans. R. Soc. A Math. Phys. Eng. Sci*. 2000;358(1766):473–495. doi:10.1098/rsta.2000.0542.

2. http://en.wikipedia.org/wiki/Diamond.

3. http://www.theatlantic.com/magazine/archive/1982/02/have-you-ever-tried-to-sell-a-diamond/304575/.

4. http://www.dailygalaxy.com/my_weblog/2007/11/a-diamond-bigge.html.

5. http://famousdiamonds.tripod.com/centenarydiamond.html.

6. Earnshaw AA. Chemistry of the Elements. *Reed Educ. Prof. Publ. Ltd*.

7. http://tex.stackexchange.com/questions/141363/draw-a-3d-diamond-structure.

8. Kraft A, Doped Diamond : A Compact Review on a New, Versatile Electrode Material. *J. Electrochem. Sci.* 2007;2:355–385.

9. Compton RG, Foord JS, Marken F. Electroanalysis at Diamond-Like and Doped-Diamond Electrodes. *Electroanalysis*. 2003;15(17):1349–1363. doi:10.1002/elan.200302830.

10. Haenni W, Rychen P. and Comminellis C. Thin-Film Diamond Part B. *Acad. Press Semicond. Semimetals Ser. Elsevier*. 2004:149.

11. Nesladek M. Conventional n-type doping in diamond: state of the art and recent progress. *Semicond. Sci. Technol*. 2005;20(2):R19–R27. doi:10.1088/0268-1242/20/2/R01.

12. Chen Q, Gruen DM, Krauss AR, Corrigan TD, Witek M, Swain GM. The Structure and Electrochemical Behavior of Nitrogen-Containing Nanocrystalline Diamond Films Deposited From $CH_4/N_2$/Ar Mixtures. *J. Electrochem. Soc*. 2001;148(4):L4. doi:10.1149/1.1357189.

13. Eaton SC, Anderson AB, Angus JC, Evstefeeva YE, Pleskov YV. Co-doping of Diamond with Boron and Sulfur. *Electrochem. Solid-State Lett*. 2002;5(8):G65. doi:10.1149/1.1486821.

14. Karl E. Spear JPD. Synthetic Diamond: Emerging CVD Science and Technology. *Wiley*. 1994.

15. http://en.wikipedia.org/wiki/Chemical_vapor_deposition#Diamond.

16. Matsumoto S, Sato Y, Tsutsumi M, Setaka N. Growth of diamond particles from methane-hydrogen gas. *J. Mater. Sci*. 1982;17(11):3106–3112. doi:10.1007/BF01203472.

17. S. Matsumoto, Y. Sato MK and NS. Japanese Journal of Applied Physics Part 2-Letters. *Japanese J. Appl. Phys. Part 2-Letters*. 1982;21(4):L183–L185.

18. Kamo M, Sato Y, Matsumoto S, Setaka N. Diamond synthesis from gas phase in microwave plasma. *J. Cryst. Growth*. 1983;62(3):642–644. doi:10.1016/0022-0248(83)90411-6.

19. Saito Y, Matsuda S, Nogita S. Synthesis of diamond by decomposition of methane in microwave plasma. *J. Mater. Sci. Lett*. 1986;5(5):565–568. doi:10.1007/BF01728692.

20. Koizumi S, Kamo M, Sato Y, Ozaki H, Inuzuka T. Growth and characterization of phosphorous doped {111} homoepitaxial diamond thin films. *Appl. Phys. Lett*. 1997;71(8):1065–1067. doi:10.1063/1.119729.

21. Jiang N, Ito T. Electrical properties of surface conductive layers of homoepitaxial diamond films. *J. Appl. Phys*. 1999;85(12):8267. doi:10.1063/1.370668.

22. Gaudin O, Whitfield MD, Foord JS, Jackman RB. Deep level transient spectroscopy of CVD diamond: The observation of defect states in hydrogenated films. *Diam. Relat. Mater*. 2001;10(3-7):610–614. doi:10.1016/S0925-9635(00)00418-0.

23. Sakaguchi I, Gamo NM, Kikuchi Y, Yasu E, Haneda H. Sulfur: A donor dopant for n-type diamond semiconductors. *Phys. Rev. B*. 1999;60(4):R2139–R2141. doi:10.1103/PhysRevB.60.R2139.

24. Lu X, Hu J, Foord JS, Wang Q. Electrochemical deposition of Pt–Ru on diamond electrodes for the electrooxidation of methanol. *J Electroanal Chem*. 2011;654(1-2):38–43. doi:10.1016/j.jelechem.2011.01.034.

25. Nebel CE and JR. Thin-Film Diamond II. *Elsevier Acad. Press*. 2004.

26. Compton, Richard G. Craig Banks E. Understanding Voltammetry. *Imp. Coll. Press*. 2nd edition, 2011.

27. Bard A. J. and Faulkner L. R. Electrochemical Methods: fundamentals and applications. *John Wiley Sons*. 2001.

28. Wang J. Analytical Electrochemistry. *John Wiley Sons*. 2000.

29. Mehedi H, Hebert C, Ruffinatto S, Eon D, Omnes F, Gheeraert E. Formation of oriented nanostructures in diamond using metallic nanoparticles. *Nanotechnology*. 2012;23:455302. doi:10.1088/0957-4484/23/45/455302.

30. Nebel CE, Yang N, Uetsuka H, Osawa E, Tokuda N, Williams O. Diamond nano-wires,

a new approach towards next generation electrochemical gene sensor platforms. *Diam. Relat. Mater*. 2009;18(5-8):910–917. doi:10.1016/j.diamond.2008.11.024.

31. Kriele A, Williams OA, Wolfer M, Hees JJ, Smirnov W, Nebel CE. Formation of nano-pores in nano-crystalline diamond films. *Chem. Phys. Lett*. 2011;507(4-6):253–259. doi:10.1016/j.cplett.2011.03.089.

32. Nebel CE, Rezek B, Shin D, Uetsuka H, Yang N. Diamond for bio-sensor applications. *J. Phys. D. Appl. Phys*. 2007;40(20):6443–6466. doi:10.1088/0022-3727/40/20/S21.

33. Shpilevaya I, Smirnov W, Hirsz S, Yang N, Nebel CE, Foord JS. Nanostructured diamond decorated with Pt particles: preparation and electrochemistry. *RSC Adv*. 2014;4(2):531. doi:10.1039/c3ra43763a.

34. Wei M, Terashima C, Lv M, Fujishima A, Gu ZZ. Boron-doped diamond nanograss array for electrochemical sensors. *Chem. Commun. (Cambridge)*. 2009;(24):3624–6. doi:10.1039/b903284c.

35. Toghill KE, Compton RG. Electrochemical Non-enzymatic Glucose Sensors : A Perspective and an Evaluation. 2010;5:1246–1301.

36. Biosensing AG. Fabrication of Boron-Doped Diamond Nanorod Forest Electrodes and Their. 2009;3(8):2121–2128.

37. Andreozzi R. Advanced oxidation processes (AOP) for water purification and recovery. *Catal. Today*. 1999;53(1):51–59. doi:10.1016/S0920-5861(99)00102-9.

38. Tenne R, Patel K, Hashimoto K, Fujishima A. Efficient electrochemical reduction of nitrate to ammonia using conductive diamond film electrodes. *J. Electroanal. Chem*. 1993;347(1-2):409–415. doi:10.1016/0022-0728(93)80105-Q.

39. Ivandini TA, Sato R, Makide Y, Fujishima A, Einaga Y. Electroanalytical application of modified diamond electrodes. *Diam. Relat. Mater*. 2004;13(11-12):2003–2008. doi:10.1016/j.diamond.2004.07.004.

40. Dejmkova H, Scampicchio M, Zima J, Barek J, Mannino S. Determination of total phenols in foods by boron doped diamond electrode. *Electroanalysis*. 2009;21(9):1014–1018. doi:10.1002/elan.200804508.

41. Stradiotto NR, Toghill KE, Xiao L, Moshar A, Compton RG. The fabrication and characterization of a nickel nanoparticle modified boron doped diamond electrode for electrocatalysis of primary alcohol oxidation. *Electroanalysis*. 2009;21(24):2627–2633. doi:10.1002/elan.200900325.

42. Toghill KE, Wildgoose GG, Moshar A, Mulcahy C, Compton RG. Fabrication and characterization of a bismuth nanoparticle modified boron doped diamond electrode and its application to the simultaneous determination of cadmium(II)and lead(II). *Electroanalysis*. 2008;20(16):1731–1737. doi:10.1002/elan.200804277.

43. Griesbach U, Zollinger D, Pütter H, Comninellis C. Evaluation of boron doped diamond electrodes for organic electrosynthesis on a preparative scale. *J. Appl. Electrochem*. 2005;35(12):1265–1270. doi:10.1007/s10800-005-9038-2.

44. Fardel R, Griesbach U, Pütter H, Comninellis C. Electrosynthesis of trimethylorthoformate on BDD electrodes. *J. Appl. Electrochem*. 2006;36(2):249–253. doi:10.1007/s10800-005-9057-z.

45. Bian LY, Wang YH, Zang JB, Yu JK, Huang H. Electrodeposition of Pt nanoparticles on undoped nanodiamond powder for methanol oxidation electrocatalysts. *J. Electroanal. Chem*. 2010;644(1):85–88. doi:10.1016/j.jelechem.2010.04.001.

46. Harfield JC, Toghill KE, Batchelor-Mcauley C, Downing C, Compton RG. Nickel nanoparticle modified BDD electrode shows an electrocatalytic response to adenine and DNA in aqueous alkaline media. *Electroanalysis*. 2011;23(4):931–938. doi:10.1002/elan.201000658.

47. Hu J, Lu X, Foord JS, Wang Q. Electrochemical deposition of Pt nanoparticles on diamond substrates. *Phys. Status Solidi Appl. Mater. Sci*. 2009;206(9):2057–2062. doi:10.1002/pssa.200982226.

48. Ferreira NG, Mendonça LL, Airoldi VJT, Rosolen JM. Electrochemical intercalation of lithium into boron-doped CVD diamond electrodes grown on carbon fiber cloths. *Diam. Relat. Mater*. 2003;12(3-7):596–600. doi:10.1016/S0925-9635(02)00273-X.

49. Christy AYMT, Nahm KS, Hwang YJ, Suh EK, Kulandainathan MA, Premkumar T, Manuel Stephan A. Lithium insertion studies on boron-doped diamond as a possible anode material for lithium batteries. *Ionics*. 2008;14(2):163–163. doi:10.1007/s11581-008-0205-4.

50. Scialdone O, Randazzo S, Galia A, Silvestri G. Electrochemical oxidation of organics in water: Role of operative parameters in the absence and in the presence of NaCl. *Water Res*. 2009;43(8):2260–2272. doi:10.1016/j.watres.2009.02.014.

51. He X, Chai Z, Li F, et al. Advanced treatment of biologically pretreated coking wastewater by electrochemical oxidation using Ti/$RuO_2$-$IrO_2$ electrodes. *J. Chem. Technol. Biotechnol*. 2013;88(8):1568–1575. doi:10.1002/jctb.4006.

52. Schmalz V, Dittmar T, Haaken D, Worch E. Electrochemical disinfection of biologically treated wastewater from small treatment systems by using boron-doped diamond (BDD) electrodes-Contribution for direct reuse of domestic wastewater. *Water Res*. 2009;43(20):5260–5266. doi:10.1016/j.watres.2009.08.036.

53. Toghill KE, Compton RG. Metal Nanoparticle Modified Boron Doped Diamond Electrodes for Use in Electroanalysis. *Electroanalysis*. 2010;22(17-18):1947–1956. doi:10.1002/elan.201000072.

54. Krueger A, Lang D. Functionality is key: Recent progress in the surface modification of nanodiamond. *Adv. Funct. Mater*. 2012;22(5):890–906. doi:10.1002/adfm.201102670.

55. Gannal JN. *Chim. Med*. 1828;4:582.

56. Hannay JB. *Nature*. 1880;22:255.

57. Davies G. *Diamond Adam. Hilger Ltd*. 1984:43–67.

58. Lewis GN, Randall M. The Free Energy of Some Carbon Compounds. [Contribution from the Chemical Laboratory of the University of California].

59. http://en.wikipedia.org/wiki/Allmänna_Svenska_Elektriska_Aktiebolaget.

60. von Bolton WZ. *Electrochem*. 1911;17:971.

61. Bundy FP, Hall HT, Strong HM. *Nature*. 1955;176:51.

62. May PW. *Endeav. Mag*. 1995;19(3):101.

63. http://en.wikipedia.org/wiki/Synthetic_diamond.

64. http://www.diamondlab.org/80-hpht_synthesis.htm.

65. Palyanov YN, Sokol AG, Borzdov YM, Khokhryakov AF. Fluid-bearing alkaline carbonate melts as the medium for the formation of diamonds in the Earth's mantle: An experimental study. *Lithos*. 2002;60(3-4):145–159. doi:10.1016/S0024-4937(01)00079-2.

66. Windischmann H, Simpson MA. CVD diamond wafers fabricated by DC arc jet. *Isr. J. Chem*. 1998;38(1-2):51–56.

67. Liu C, Wang JH, Weng J. Growth of micro- and nanocrystalline dual layer composite diamond films by microwave plasma CVD: Influence of $CO_2$ concentration on growth of nano-layer. *J. Cryst. Growth*. 2015;410:30–34. doi:10.1016/j.jcrysgro.2014.10.040.

68. Yano T. Electrochemical Behavior of Highly Conductive Boron-Doped Diamond Electrodes for Oxygen Reduction in Alkaline Solution. *J. Electrochem. Soc*. 1998;145(6):1870. doi:10.1149/1.1838569.

69. Bouilov LL, Spitsyn BV, Krotova MD. Photoelecfrochemical properties of semiconductor diamond. *J. Electroanal. Chem.* 1987;228:19–27.

70. Marselli B, Garcia-Gomez J, Michaud PA, Rodrigo MA, Comninellis C. Electrogeneration of Hydroxyl Radicals on Boron-Doped Diamond Electrodes. *J. Electrochem. Soc*. 2003;150(3):D79. doi:10.1149/1.1553790.

71. Martin HB. Hydrogen and Oxygen Evolution on Boron-Doped Diamond Electrodes. *J. Electrochem. Soc*. 1996;143(6):L133. doi:10.1149/1.1836901.

72. Chakrapani V, Eaton SC, Anderson AB, Tabib-Azar M, Angus JC. Studies of Adsorbate-Induced Conductance of Diamond Surfaces. *Electrochem. Solid-State Lett*. 2005;8(1):E4. doi:10.1149/1.1828351.

73. Strojek JW, Granger MC, Swain GM, Dallas T, Holtz MW. Enhanced Signal-to-

Background Ratios in Voltammetric Measurements Made at Diamond Thin-Film Electrochemical Interfaces. *Anal. Chem*. 1996;68(13):2031–2037. doi:10.1021/ac9506847.

74. Vinokur N. Electrochemical Behavior of Boron-Doped Diamond Electrodes. *J. Electrochem. Soc*. 1996;143(10):L238. doi:10.1149/1.1837157.

75. Landstrass MI, Ravi KV. Resistivity of chemical vapor deposited diamond films. *Appl. Phys. Lett*. 1989;55(10):975–977. doi:10.1063/1.101694.

76. Shang F, Glennon JD, Luong JHT. Glucose oxidase entrapment in an electropolymerized poly(tyramine) film with sulfobutylether-β-cyclodextrin on platinum nanoparticle modified boron-doped diamond electrode. *J. Phys. Chem. C*. 2008;112(51):20258–20263. doi:10.1021/jp807482a.

77. Beck F, Krohn H, Kaiser W, Fryda M, Klages CP, Scha L. Boron doped diamond/titanium composite electrodes for electrochemical gas generation from aqueous electrolytes. *Electrochim. Acta*. 1998;44:525–532.

78. May PW. Diamond UK. Diamond thin films : a 21st-century material. *Phil. Trans. R. Soc. Lond. A* 2000;358:473–495.

79. http://www.chm.bris.ac.uk/pt/diamond/gustavothesis/chapter2.htm.

80. Diamanti MV, Ormellese M, Marin E, Lanzutti A, Mele A, Pedeferri MP. Anodic titanium oxide as immobilized photocatalyst in UV or visible light devices. *J. Hazard Mater*. 2011;186(2-3):2103–2109. doi:10.1016/j.jhazmat.2010.12.128.

81. Vetrivel V, Rajendran K, Kalaiselvi V. Synthesis and characterization of Pure Titanium dioxide nanoparticles by sol-gel method. *Int. J. ChemTech Res*. 2015;7(3):1090–1097.

82. Khameneh Asl S, Alavi B, Ahmadi S. The effect of highly ordered titania nanotube structures on hydrogen gas detection. *Surf. Interface Anal*. 2012;44(8):1051–1053. doi:10.1002/sia.4890.

83. Shelimov KB, Davydov DN, Moskovits M. Template-grown high-density nanocapacitor arrays. *Appl. Phys. Lett*. 2000;77(2000):1722. doi:10.1063/1.1290598.

84. Zhang Z, Shimizu T, Senz S, Gösele U. Ordered High-Density Si [100] nanowire arrays epitaxially grown by bottom imprint method. *Adv. Mater*. 2009;21(27):2824–2828. doi:10.1002/adma.200802156.

85. Kamegawa T, Shimizu Y, Yamashita H. Superhydrophobic surfaces with photocatalytic self-cleaning properties by nanocomposite coating of $TiO_2$ and polytetrafluoroethylene. *Adv. Mater*. 2012;24(27):3697–3700. doi:10.1002/adma.201201037.

86. Gan P, Foord JS, Compton RG. Ionic Liquid-Carbon Nanotube Modified Screen-Printed Electrodes and Their Potential for Adsorptive Stripping Voltammetry. *Electroanalysis*. 2014;44(0):1886–1892. doi:10.1002/elan.201400214.

87. Hrapovic S, Liu Y, Male KB, Luong JHT. Electrochemical Biosensing Platforms Using Platinum Nanoparticles and Carbon Nanotubes. *Anal. Chem*. 2004;76(4):1083–1088. doi:10.1021/ac035143t.

88. McLamore ES, Shi J, Jaroch D, Claussen JC, Uchida A, Jiang Y, Zhang W, Donkin SS, Banks MK, Buhman KK, Teegarden D, Rickus JL, Porterfield DM. A self referencing platinum nanoparticle decorated enzyme-based microbiosensor for real time measurement of physiological glucose transport. *Biosens. Bioelectron*. 2011;26(5):2237–2245. doi:10.1016/j.bios.2010.09.041.

89. Xu Q, Zhao Y, Xu JZ, Zhu JJ. Preparation of functionalized copper nanoparticles and fabrication of a glucose sensor. *Sensors Actuators B Chem*. 2006;114(1):379–386. doi:10.1016/j.snb.2005.06.005.

90. Ren X, Meng X, Chen D, Tang F, Jiao J. Using silver nanoparticle to enhance current response of biosensor. *Biosens. Bioelectron*. 2005;21(3):433–437. doi:10.1016/j.bios.2004.08.052.

91. Lim SH, Wei J, Lin J, Li Q, KuaYou J. A glucose biosensor based on electrodeposition of palladium nanoparticles and glucose oxidase onto Nafion-solubilized carbon nanotube electrode. *Biosens. Bioelectron*. 2005;20(11):2341–2346. doi:10.1016/j.bios.2004.08.005.

92. Daniel MCM, Astruc D. Gold Nanoparticles: Assembly, Supramolecular Chemistry, Quantum-Size Related Properties and Applications toward Biology, Catalysis and Nanotechnology. *Chem. Rev*. 2004;104(1):293–346. doi:10.1021/cr030698+.

93. Vajíček S, Štolcová M, Kaszonyi A, Micusik M, Alexy P, Canton P, Onyestyak G, Harnos S, Lonyi F, Valyon J. Gel-type ion exchange resin stabilized Pd-Bi nanoparticles for the glycerol oxidation in liquid phase. *J. Ind. Eng. Chem*. 2016;39:77–86. doi:10.1016/j.jiec.2016.05.010.

94. Li HB, Liu L, Ma XY. Effective Hydrogenation of Haloaromatic Nitro Compounds Catalysed by Iridium Nanoparticles Deposited on Multiwall Carbon Nanotubes. *Synth. React. Inorganic Met. Nano-Metal Chem*. 2016;46(10):1499–1505. doi:10.1080/15533174.2015.1137013.

# Chapter 2

# Experimental Theories and Techniques

This chapter explains the theoretical background of the experimental techniques employed in this thesis. These consist of scanning electron microscopy (SEM), X-ray diffraction (XRD), X-ray photoelectron spectroscopy (XPS) and energy-dispersive X-ray spectroscopy (EDS or EDX). Emphasis is given to electrochemistry, such as electrochemical fundamentals and techniques used for the investigation and characterisation of diamond and Au (111) materials.

## 2.1 Surface and structure analysis techniques

### 2.1.1 Scanning Electron Microscopy (SEM)

Scanning electron microscopy (SEM) is a type of electron microscopy that produces high-resolution images even in the 10 nm range, impossible to obtain with an optical microscope, by scanning the sample with a focused beam of electrons. The electrons interact with atoms in the sample, producing various signals that contain information about the sample's surface topography and composition. Figure 2-1 (a) shows a schematic diagram of a SEM[1,2]. After the sample is placed in a vacuum chamber, a focused beam of electrons passing through an array of lenses strike upon the surface of the working sample. The sample is irradiated by the focused beam of electrons and the latter are scattered. Electron scattering results in the production of either backscattered incident electrons from a heated filament or the emission of the secondary electrons. The backscattered electrons are diverted out of the sample due to elastic scattering whereas the secondary electrons result from the inelastic

scattering of the incident electrons beam. A final image of the surface of the sample is produced by the combination of the intensity and velocity of the electrons backscattered and emitted as described above. A typical SEM image of a bare boron-doped diamond is shown in figure 2-1 (b) where visible diamond grains are shown.

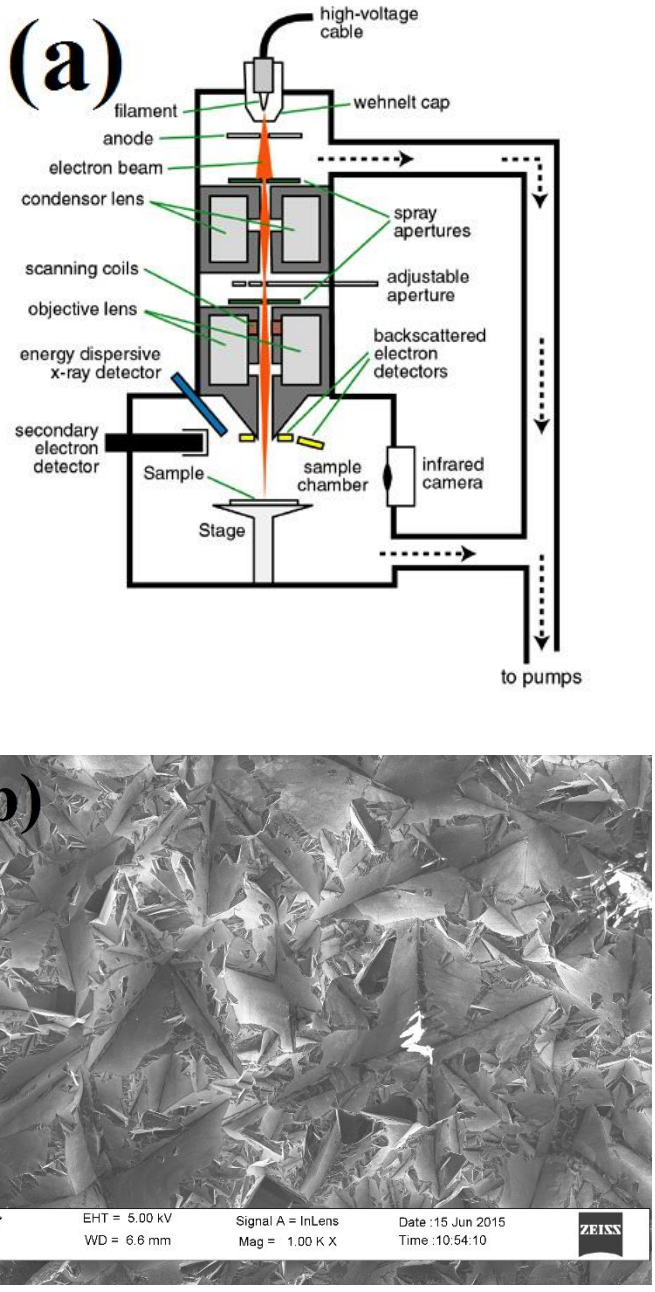


**Figure 2-1** (a) Schematic diagram of the basic components of SEM[1] and (b) SEM image of a bare BDD electrode.

## 2.1.2 X-ray Diffraction (XRD)

X-ray diffraction is a widely used technique to characterise and identify crystalline materials. An X-ray diffraction pattern can be obtained after a constructive interference of scattered X-ray beams when all the conditions satisfy Bragg's law (Equation 2-1)[3]. Figure 2-2 illustrates schematically the principle of X-ray diffraction[4].

$$2d \sin \Theta = n\lambda \qquad (2\text{-}1)$$

where $d$ is the spacing between diffracting planes, $\Theta$ is the incident angle, $n$ is the reflections order and $\lambda$ is the wavelength of the beam.

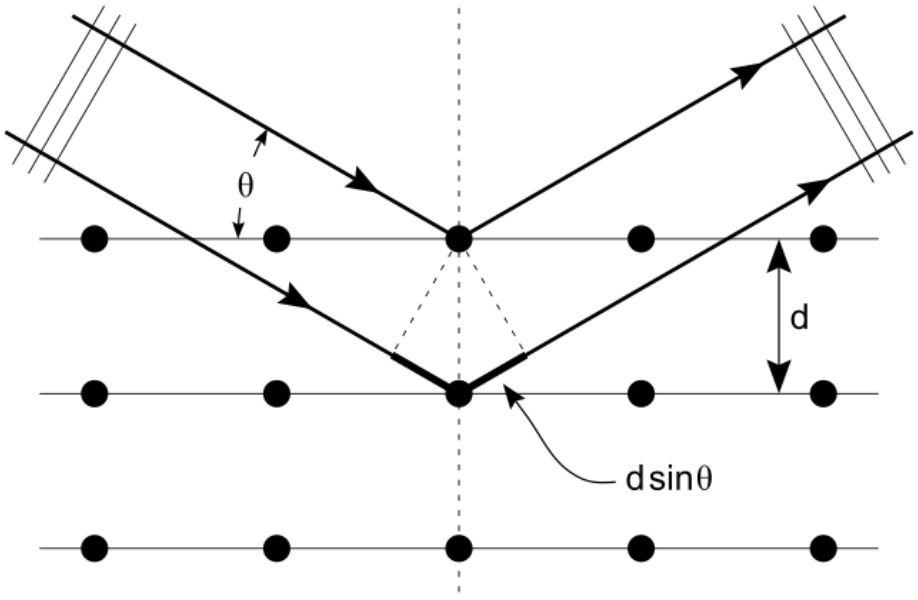


**Figure 2-2** Schematic representation of Bragg's law[4].

The incoming beam causes each atom encountered to scatter and reradiate a small portion of the beam's intensity as a spherical wave. If scatterers are arranged symmetrically with a separation $d$, these spherical waves will be synchronized (constructively) only in directions where their path-length difference $2d \sin\theta$ equals an integer multiple of the wavelength $\lambda$. In that case, part of the incoming beam is deflected by an angle $2\theta$, producing a reflection spot in the diffraction pattern.

For the purpose of this thesis and in particular for the detection of Pd nanoparticles of Chapter 4, X-ray diffraction (XRD) analysis was carried out with a Philips X'pert PW3710-MPD diffractometer using filtered Cu-Kα (λ = 1.54 Å) radiation operated at 40 kV and 40 mA. The data were analysed by X'Pert Highscore software and then were exported to OriginPro 8.5 software (OriginLab Ltd.) as described in the next sections.

# 2.2 X-ray spectroscopies

## 2.2.1 X-ray Photoelectron Spectroscopy (XPS)

X-ray photoelectron spectroscopy (XPS) is a surface-sensitive quantitative spectroscopic technique that measures the elemental composition, chemical and electronic states of the elements that exist within a material. It is also widely known by the acronym ESCA which means Electron Spectroscopy Chemical Analysis. The latter abbreviation was introduced by Kai Siegbahn's research group in order to emphasize the chemical information that this technique provides in addition to the elemental composition[5,6]. Kai Siegbahn received the Nobel Prize for Physics in 1981 in recognition of his efforts to develop XPS into a useful analytical tool[5,6]. In this work, XPS was used for the investigation of the elemental composition of metal nanoparticles supported on diamond and Au (111) electrodes. Apart from the surface composition, the main composition was the various chemical states as well as any shifts in binding energy due either to core-shell nanoparticles electronic interactions or various chemical terminations. Regarding the latter, XPS was used as a way to detect the chemical termination of diamond electrodes either with oxygen or hydrogen functionalities on the surface as shown analytically by the O 1s photoelectron peak see in Chapters 4 and 5. Basic information about XPS, XPS instrumentation and XPS spectral features follows.

## 2.2.1.1 XPS fundamentals

XPS spectra can be obtained by irradiating a surface with a beam of X-rays while simultaneously measuring the kinetic energy and number of electrons that escape from the top 0 to 10 nm of the material being analysed. Monochromatic X-rays usually Al Kα (1486.6 eV) or Mg Kα (1253.6 eV) are used to analyse the energy of the photoelectrons. Figure 2-3 (a) and (b) illustrate the XPS process as it happens by photoionization of an atom by the emission of a 1s electron and the principle scheme of an XPS instrument, respectively. The energy of the X-rays excites core electrons which then are transmitted towards the surface and then are emitted. Core electrons are referring to K shell or 1s electron (see figure 2-3 (a)). The kinetic energy of the electrons is propagated towards an electron energy analyser, an electron detector counts the number of the electrons and the resulting photoelectron spectrum is displayed as a plot of the intensity versus the electron binding energy (see figure 2-3 (b)).

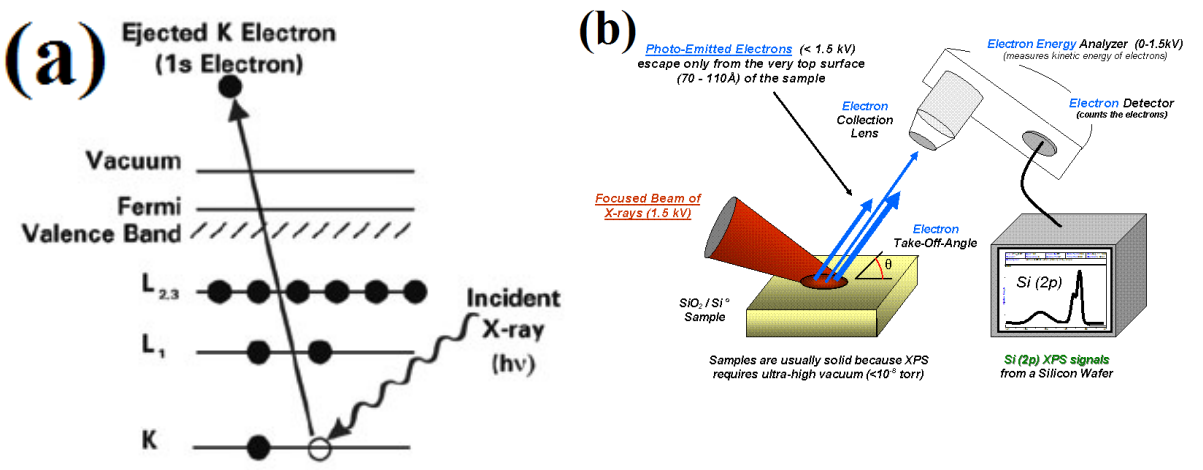


**Figure 2-3** (a) Schematic illustration of the XPS process, where photoionisation of an atom by the emission of 1s electron from the K shell occurs and (b) Image of an XPS instrument[7].

Hence, XPS is a surface-sensitive technique as only electrons from the top layers can be detected. Because the emitted electrons' kinetic energies are measured, the electron binding energy of each of the emitted electrons can be determined by using:

$$E_K = h\nu - E_B - \Phi \qquad (2\text{-}2)$$

where $h\nu$ is the photon energy, $E_B$ is the binding energy of the core level from which the electrons were emitted and $\Phi$ is the work function dependent on both the spectrometer and the material.

In addition, besides the main photoemission described above there is also another emission due to the Auger effect. Figure 2-4 shows that after the first strike at the K shell, a hole is left from the ejected electrons ($L_1$ of the figure 2-4) and another electron can fall from a higher level to the hole below. Due to the principle of energy conservation, the energy that was released can result in radiated energy or X-ray fluorescence and therefore a secondary photoemission is generated. The secondary photoemission from the energy level $L_{2,3}$ of the figure 2-4 called Auger emission.

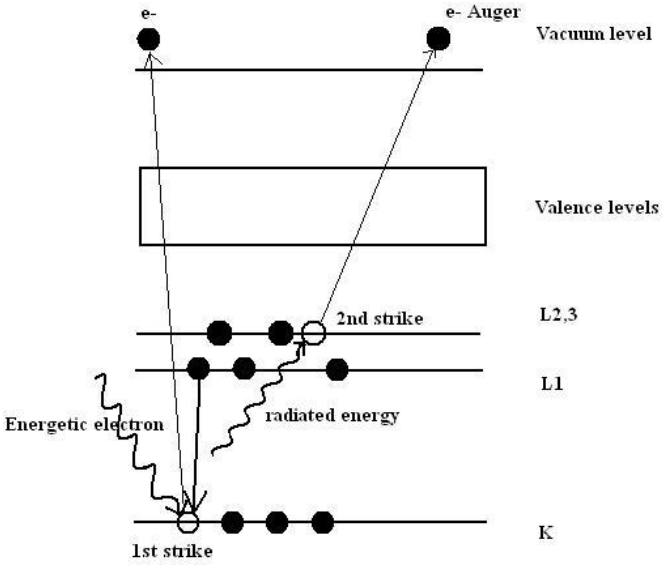


**Figure 2-4** Schematic illustration of an Auger emission process[7].

## 2.2.1.2 XPS instrumentation

XPS measurements were performed using an XPS spectrometer which works under ultra-high vacuum (UHV) between the ranges of $10^{-9}$-$10^{-10}$ Torr. The XPS spectrometer consists of various modules such as an X-ray source, an electron energy analyser and a detection system as shown in figure 2-5.

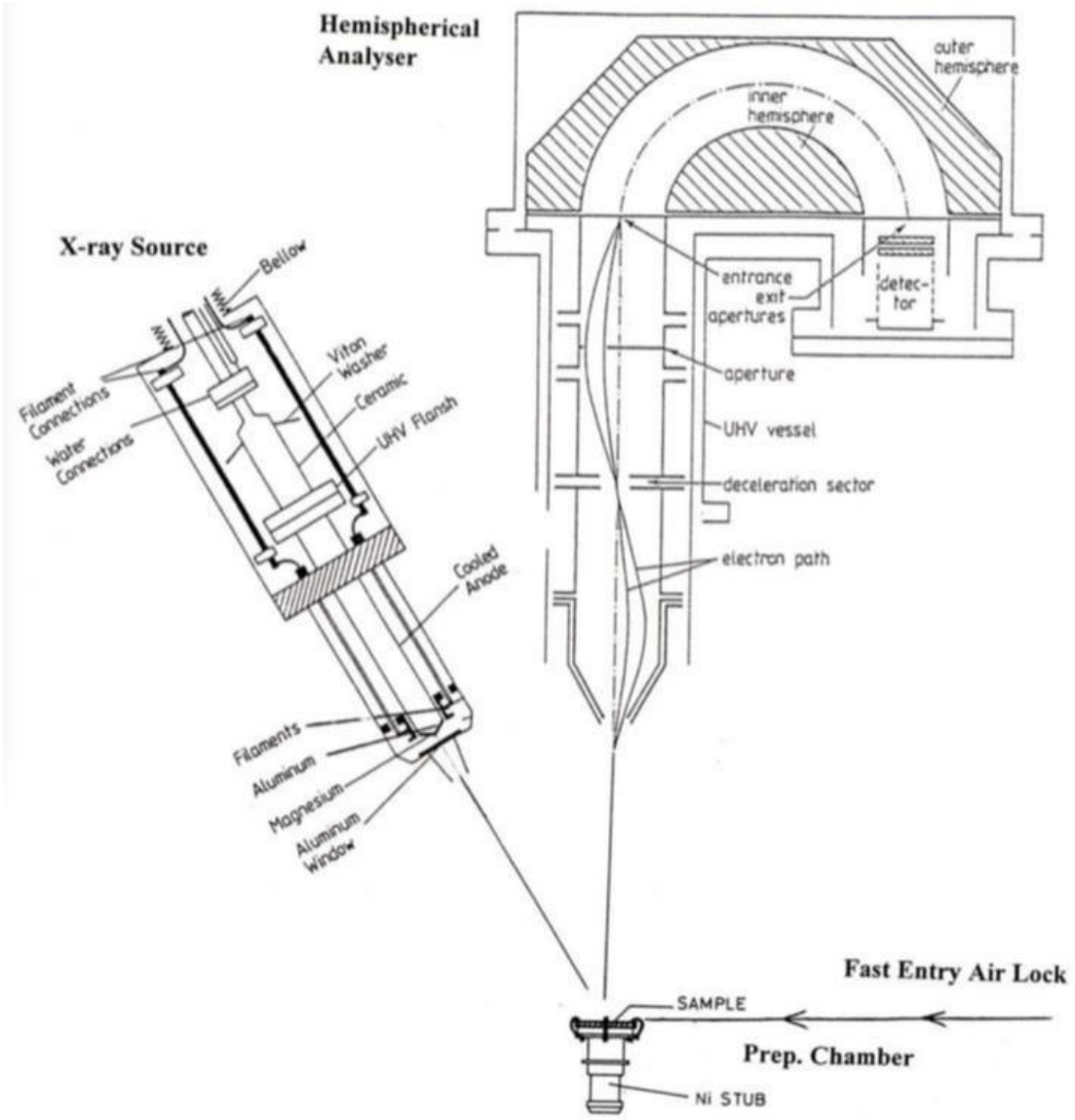


**Figure 2-5** Schematic diagram of XPS with a X-ray source and hemispherical analyser, reprinted from[8].

All the experiments in this thesis were performed under an Al Kα X-ray source (1486.6 eV), the pressure range given in section 2.2.1.2 and under a constant potential that corresponds to a fixed analyser transmission (FAT) mode. Prior to the wide survey and narrow scans of the photoelectron peaks, the sample was mounted in a preparation chamber before it was placed to the UHV chamber. When the sample was placed in the preparation chamber the pressure was atmospheric. The sample was kept in the preparation chamber until the pressure reached $10^{-6}$ Torr. After the preparation chamber, a second chamber was used in order to store the carousel with the sample(s) and then the samples were transferred to the main UHV analysis chamber using controlled arms. The pressure in the main chamber is held below $10^{-9}$ Torr and the arms are positioned around 45 degrees angle between the X-ray gun, sample and the detector. In the end, a wide survey and narrow scans are conducted with pass energy of 25 eV and 50 eV, respectively. The samples were scanned at least 5 times for the acquisition of the wide scan, and around 20 times in the regions of interest. During this time the ejected surface electrons pass through the hemispherical analyser under the FAT mode. These electrons travel to the electron detector equipped with a multi-channel plate electron multiplier. The detector processes the corresponding current from the electrons and produces an XPS spectrum which is displayed by a software. All the spectra obtained were analysed with CasaXPS software[9].

## 2.2.1.3 XPS spectral features

### 2.2.1.3.1 Main photoelectron lines

In general, a lot of spectral features are produced as a result of the elements' photoelectron peaks in addition to some unwanted features that are caused by instrumental effects. The main photoelectron lines are all the photoelectron peaks, these are intense and sharp (see an example of a survey in figure 2-6).

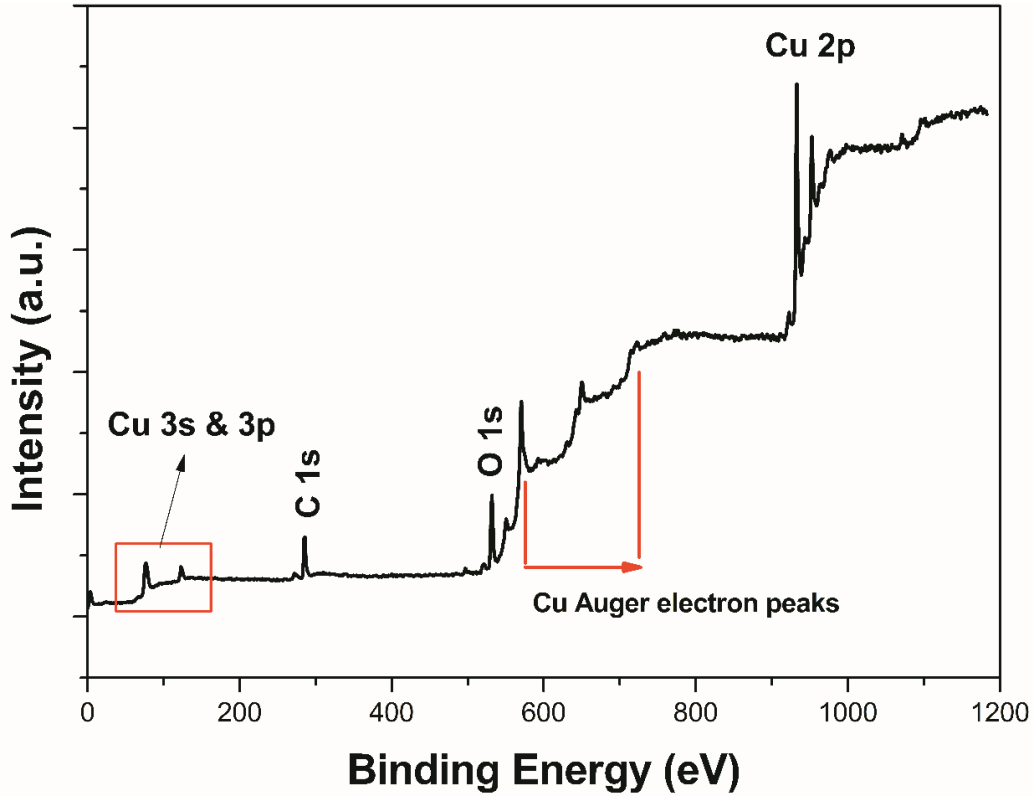


**Figure 2-6** An example of a typical survey spectrum showing the appearance of XPS and Auger peaks, adapted from personal experiments of an electrode consisted of $Cu_2O$/Au (111).

The main photoelectron lines as shown in the above figure are intense, and well-defined because the electrons are emitted from core orbitals as discussed in section 2.2.1.1 due to the lack of energy loss. Moreover, the XPS spectrum gives chemical state information from the top 20 atomic layers (few nm) of the sample surface. In this context, the term "chemical state" refers to the local bonding environment of the species in question. The latter is affected by its formal oxidation state. For example, while the binding energy of carbon C 1s electron is 284.6 eV (some also use 285 eV as the nominal value for the binding energy of the carbon), subtle but reproducible shifts in the actual binding energy can provide the chemical state information. This subtle shift is called chemical shift. A chemical shift can be caused by either initial chemical bonding before the photoelectron ejection or post-photoemission processes such as core hole screening, relaxation of photoionization and polarisation of surrounding ions[10–13].

### 2.2.1.3.2 Auger peaks

As discussed in section 2.2.1.1, an electron from a lower energy level can be excited and another electron form a higher energy level can drop down and fill the vacant core hole that the initial electron left. By doing this, energy is released and thus another electron, an Auger electron, can be ejected to the vacuum level. Consequently, there is a category of XPS spectral features which are called the Auger lines. In the photoemission spectrum, additional peaks appear which do not have the characteristics of photoemission peaks, in which kinetic energy is independent of the photon energy[14]. All these peaks are called Auger peaks (see figure 2-6). The most common types of Auger peaks are *KLL*, *LMM*, *MNN* and *NOO* series that are addressed in terms of initial and final vacancies in the Auger transition. For example, *KLL* series corresponds to the initial vacancy in the K shell and final double vacancy in the L shell. Figure 2-6 shows that apart from the main photoelectron peaks and Auger electron peaks, there are smaller peaks that represent photoexcited electron peaks from other orbitals. These peaks are referred as Cu 3s and Cu 3p peaks in the figure 2-6 of $Cu_2O$/Au (111) electrode.

### 2.2.1.3.3 Shake-up satellites

Another category of XPS spectral features is that of shake-up satellites. Shake-up satellites may occur when the outgoing photoelectron simultaneously interacts or collides with a valence electron and excites it to a higher-energy level. Then, the energy of the emitted core electron is reduced slightly, which gives a satellite structure a few electron volts below the core level position (but above on a binding-energy scale). Such features are not very common and usually the main peaks are separated from the satellites peaks by up to 15 eV. The most notable examples being the 2p spectra of the d-band metals and the bonding to anti-bonding transition of the $\pi$ molecular orbital ($\pi \rightarrow \pi^*$ transition) brought about by C 1s electrons in aromatic organics. The former is best illustrated by the Cu 2p spectrum. A strong shake-up satellite is

observed for CuO as shown in figure 2-7, but is absent for $Cu_2O$ and metallic copper. The π-bond shake-up satellite fir the C 1s photoelectron peak is shown in figure 2-8.

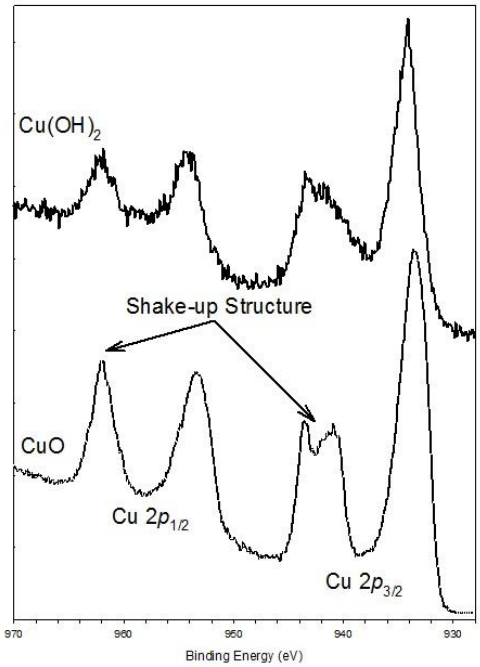


**Figure 2-7** Shake-up structure in Cu 2p spectra of copper (II) hydroxide ($Cu(OH)_2$, top) and copper (II) oxide (CuO, bottom)[15].

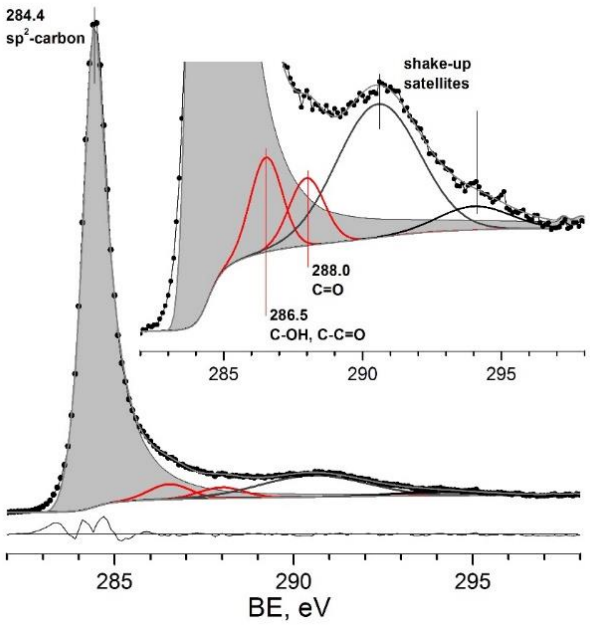


**Figure 2-8** π-bond shake-up satellite for the C 1s photoelectron peak, obtained from[16].

### 2.2.1.3.4 Multiplet splitting

Multiple splitting of a photoelectron peak occurs in compounds that have unpaired electrons in the valence band and arises from different spin distributions of the electrons of the band structure. This results in a doublet of the core level peak; multiple splitting effects are observed for La in figure 2-9. Both of the peaks in figure 2-9 belong to La $3d_{3/2}$ and La $3d_{5/2}$ component of $La(OH)_3$, respectively.

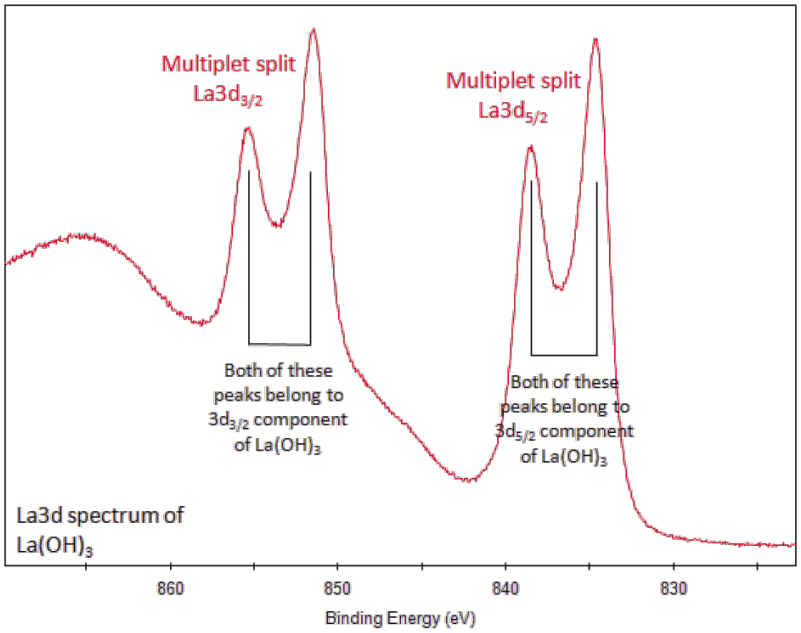


**Figure 2-9** Multiplet splitting peaks of the $La(OH)_3$, obtained from[17].

### 2.2.1.3.5 Plasmons

The final type of XPS spectral features is that of plasmon losses. These occur in both Auger and XPS spectra and are specific to clean metal surfaces. They arise when the outgoing electron excites collectively oscillations in the conduction-band electrons and thus suffers either a discrete energy loss or several discrete losses in multiples of the characteristic plasmon frequency, about 15 eV for aluminium. The characteristic plasmon loss peaks for clean aluminium are shown in Figure 2-10. The loss features described above can provide valuable information but some, as in the case of plasmons, merely serve to complicate the spectrum.

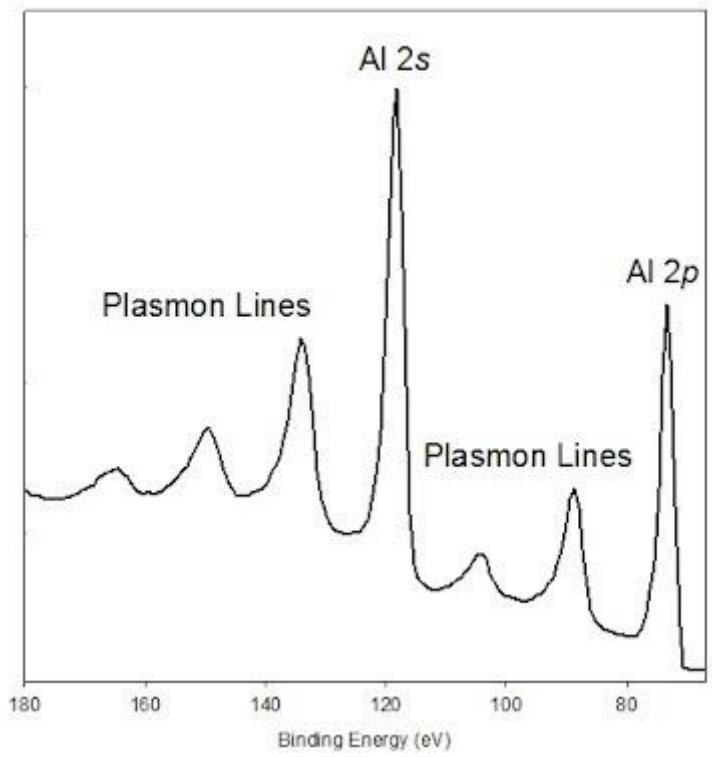


**Figure 2-10** Plasmon loss structure in a spectrum of aluminium metal, obtained from[18].

## 2.2.2 Energy-dispersive X-ray Spectroscopy (EDS, EDX or XEDS)

Sometimes this method is also called energy dispersive X-ray analysis (EDXA) or energy dispersive X-ray microanalysis (EDXMA). EDS combines the backscattered electron images obtained by SEM compositional contrast from the elements and their distribution with the XPS spectrum. Energy Dispersive Spectroscopy (EDS) allows the identification of particular surface elements and gives their relative proportions e.g. atomic %. In other words, it is an analytical technique used for the elemental analysis and chemical characterisation of a sample. The basic idea behind this technique is that information about the quantity and kinetic energy of ejected electrons is used to determine the binding energy, which is specific and characteristic to each element, of these now-liberated electrons and thus allows for the chemical

characterisation of a sample. EDS is another close relative technique of XPS and AES due to the principles for which this technique operates.

# 2.3 Electrochemical methods

This section explains the basic principles of electrochemical theory. It is separated into two subsections; one focused on electrochemical fundamentals and the second one discusses the electrochemical techniques employed in this thesis for the modification and investigation of the electrochemical properties of diamond and Au (111) electrodes.

## 2.3.1 Electrochemical fundamentals

### 2.3.1.1 Electrochemical equilibrium

Electrochemistry is generally the branch of chemistry which deals with the relations between electrical and chemical phenomena and more specifically with phenomena associated with the charge separation at electrode-electrolyte interfaces. When an electrode is immersed in a solution, there is charge separation because of electron transfer across the two phases, the electrolyte and the electrode, and a potential difference builds up at the electrode surface. Taking into account the following case of an electrochemical equilibrium between species A and B:

$$A_{(aq)} + e^-_{(m)} \rightleftharpoons B_{(aq)} \qquad (2\text{-}3)$$

where A is the oxidised form of B, the electrical potential of the electrode that is established across the electrode/electrolyte interface can be quantified by the Nernst equation[19]:

$$\Phi_{(m)} - \Phi_{(s)} = \frac{\Delta\mu^0}{F} + \frac{RT}{F} ln \frac{\alpha_A}{\alpha_B} \qquad (2\text{-}4)$$

where $\Phi_{(m)}$ and $\Phi_{(s)}$ refer to the electrical potentials (V) of the electrode and the solution, respectively, $\Delta\mu^0$ is the difference between the standard chemical potentials of species A and B (J $mol^{-1}$), $F$ is the Faraday constant (96485 C $mol^{-1}$), $R$ is the gas constant (8.314 J $K^{-1}$ $mol^{-1}$), $T$ is the temperature (K) and $\alpha_A$ and $\alpha_B$ are the activities of the oxidised and reduced species A and B, respectively (mol $kg^{-1}$).

In order for the circuit to be completed, a second electrode needs to be inserted. The role of this electrode is to be a reference electrode against the working electrode and thus the potential drop can be measured related to the reference electrode. The Nernst equation then becomes:

$$E = E^0 + \frac{RT}{F} ln \frac{\alpha_A}{\alpha_B} \qquad (2\text{-}5)$$

where $E^0$ is the standard electrode potential (V). The other terms remain the same as defined above. Due to the fact that the activities of the oxidised and reduced species are terms that are often unknown, equation 2-5 can be rewritten using the concentrations of the electroactive species:

$$\alpha_A = \gamma_A C_A \qquad (2\text{-}6)$$

$$\alpha_B = \gamma_B C_B \qquad (2\text{-}7)$$

where $\gamma_A$ and $\gamma_B$ are the activity coefficients and $C_A$ and $C_B$ are the concentrations of species, A and B, respectively (mol $cm^{-3}$). Hence, the Nernst equation becomes as follows:

$$E = E_f^{\ominus} + \frac{RT}{F} ln \frac{C_A}{C_B} \qquad (2\text{-}8)$$

where $E_f^{\ominus}$ is the formal potential (V). All other terms retain the definitions given above. Since the activities of the species A and B are proportional to their activity coefficients equation 2-8 becomes:

$$E^0 = E_f^{\ominus} + \frac{RT}{F} ln \frac{\gamma_A}{\gamma_B} \qquad (2\text{-}9)$$

Equilibrium electrochemistry deals with measurements at which the current flow is negligible. In other words, the rate of electron transfer from the electrode to species A and from species B to the electrode are equal. Non-equilibrium electrochemical conditions require the use of a third electrode which plays the role of a counter electrode since potentials are applied such that a current flow is triggered. The counter electrode is important because it prevents currents from flowing through the reference electrode. This ensures the control at the working electrode where the potentials drops as well as maintaining the composition of the reference electrode and hence not changing its potential.

Under the aforementioned conditions the current that flows through the cell causes changes in the interface (electrode/electrolyte) as well as the electrode surface concentrations of the analytes in question. Consequently, the structure of the electrode/electrolyte interface as well as the kinetics of electrochemical reactions and the ways of transport of species in the solution need to be discussed further.

## 2.3.1.2 Faradaic and non-faradaic processes

This section discusses and explains faradaic and non-faradaic charge transfer reactions. These two processes refer to whether or not electrons cross the electrode solution interface when an external potential is applied.

### 2.3.1.2.1 Capacitative current and the double layer

When an external potential is applied, a charge build-up occurs at the interface of electrode/electrolyte and ions of opposite charge accumulate near the electrode surface. The charge is usually held < 1 Å near to the electrode surface[20]. At the interface of electrode/electrolyte a double layer is formed (figure 2-11) and the interfacial system

electrode/electrolyte can be interpreted as a capacitor where a potential drop exists between the two opposite charged plates of the capacitor. This model is called Helmholtz model[21,22], but further models have been developed for the structure of the double layer[23–26].

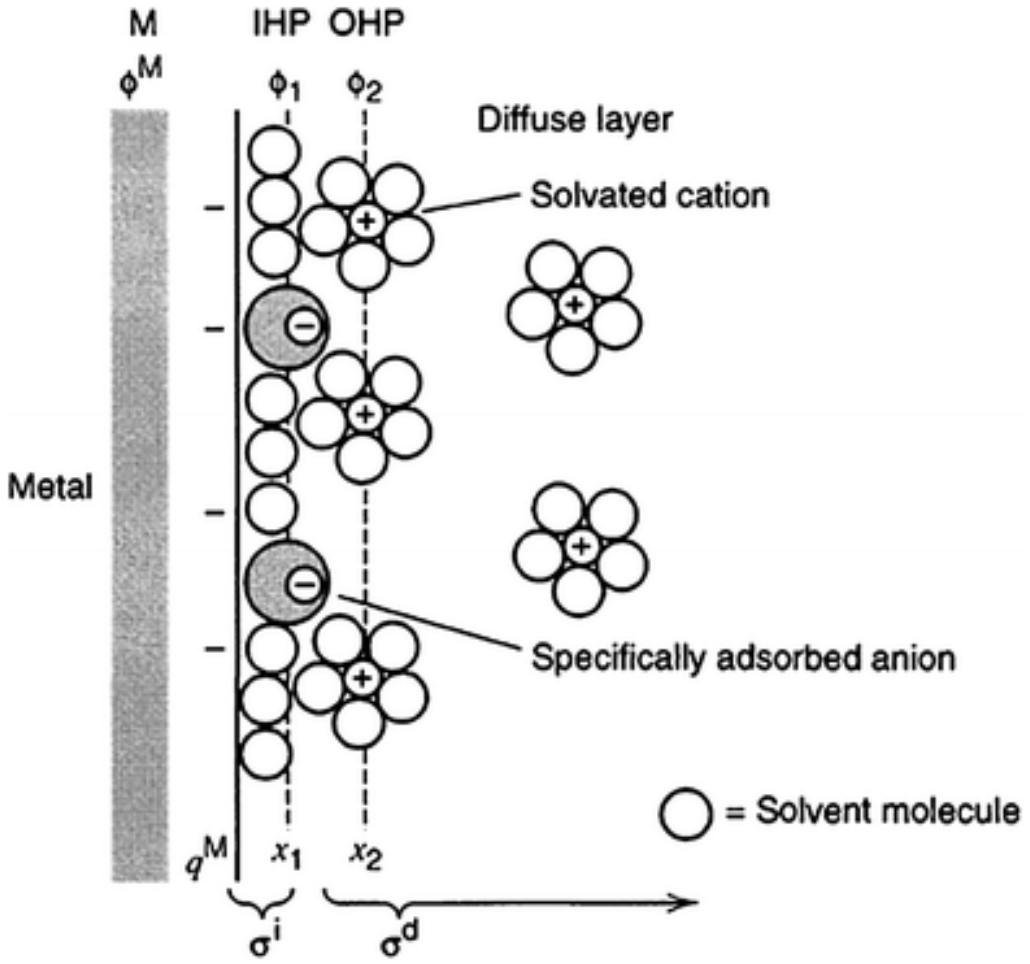


**Figure 2-11** Helmholtz double-layer model, taken from[20].

As shown in the figure 2-11, the Helmholtz double-layer model consists of two distinct layers, the Inner Helmholtz Planes (IHP) and the Outer Helmholtz Planes (OHP), respectively. The former is comprised of adsorbed ions and solvent molecules at a distance $x_1$ from the electrode surface while the latter consists of solvated ions at a distance $x_2$ from the electrode surface. The potential goes to zero when the charge density approaches the bulk solution and the potential drops approximately linearly. The existence of a double layer introduces a

capacitance in the electrochemical cell and contributes to the charging current due to ion movement. This current can be called "capacitative" and is described by

$$i = \frac{dQ}{dt} = C_d \frac{dE}{dt} = C_d A_d v \qquad (2\text{-}10)$$

where $C_d$ is the differential capacitance (μF $cm^{-2}$), $A_d$ is the double layer area ($cm^2$) and $v$ is the scan rate (V $s^{-1}$).

The double layer is closely related to the concentration of the supporting electrolyte. Given that most electrochemical experiments assume diffusion-only conditions; since electron transfer can only take place within an electron tunnelling distance from approximately 10-20 Å, the use of adequate concentration of electrolyte is crucial for a reaction to proceed. Specifically, the concentrations of the supporting electrolyte must be at least fifty times larger than any analyte concentration[27]. The double layer is compressed to the electron tunnelling distance (10-20 Å) and the bulk potential drop is available to drive the reaction when the concentration of the supporting electrolyte is restricted. Additionally, the adequate amount of supporting electrolyte reduces the solution resistivity, which provides a constant ionic strength that subsequently helps the activity coefficients (related to the concentration of species). Also, the absence of an electric field in bulk solution excludes the contribution of migration to the new transport to the electrode.

## 2.3.1.2.2 Faradaic processes

Considering the one-electron transfer of the equation 2-3 in section 2.3.1.1, the total current can be termed by

$$i = I_a + I_c = FAj \qquad (2\text{-}11)$$

where $I_\alpha$ and $I_c$ are the anodic and cathodic currents, respectively (A), $F$ is the Faraday constant, $A$ is the surface area of the electrode ($cm^2$) and $j$ is the material flux through the electrode surface (mol $cm^{-2}$ $s^{-1}$). The latter can be further expressed by

$$j = k_{red}[A]_0 - k_{ox}[B]_0 \qquad (2\text{-}12)$$

where $k_{red}$ and $k_{ox}$ are the heterogeneous rate constants for the reduction and oxidation reactions respectively (cm $s^{-1}$) and $[A]_0$ and $[B]_0$ are the surface concentrations of species A and B, respectively (mol $cm^{-3}$).

Gibbs energies are related to the heterogeneous rate constants for the reduction and oxidation reactions by Transition State Theory[19,20]. Therefore, the Butler-Volmer equation can be derived[19].

$$j = k_0[A]_0 exp\left[\frac{-\alpha F}{RT}\eta\right] - k_0[B]_0 exp\left[\frac{\beta F}{RT}\eta\right] \qquad (2\text{-}13)$$

$$\text{with } k_{red} = k_0 exp\left[\frac{-\alpha F}{RT}\eta\right] \text{ and } k_{ox} = k_0 exp\left[\frac{\beta F}{RT}\eta\right] \qquad (2\text{-}14)$$

$k_0$ is the standard electrochemical rate constant (cm $s^{-1}$), $\alpha$ and $\beta$ are the transfer coefficients (dimensionless) and $\eta$ is the overpotential (V) defined as (E - $E_f^{\ominus}$). All the other terms defined as above. If equation (2-13) is substituted into the equation (2-11), a new equation is derived that also describes the electrode kinetics as the Butler-Volmer Theory. This equation gives the Tafel Law[19]:

$$i = FAk_0\left(exp\left[\frac{-\alpha F}{RT}\eta\right][A]_0 - exp\left[\frac{\beta F}{RT}\eta\right][B]_0\right) \qquad (2\text{-}15)$$

where all the terms of the equation 2-15 have been defined above. Notably, the two terms of the equation (2-15) can be neglected when the flux depends on the rate of oxidation and reduction, respectively.

## 2.3.1.3 Mass transport

There are three ways of transport of species from bulk solution to the electrode surface. These are diffusion, convection and migration. Most electrochemical studies conventionally assume diffusion of the species exclusively, and in this section all processes are diffusion dependent. Thus, measurements are done in a way to eliminate the effects of convection and migration. An equation that describes all the contributions of the movement of species from the bulk solution to the electrode surface is given by the Nernst-Planck equation[19,20]:

$$j_i(x) = -D_i \frac{\partial C_i(x)}{\partial x} + C_i v(x) + \frac{z_i F}{RT} D_i C_i \frac{\partial \Phi_i(x)}{\partial x} \qquad (2\text{-}16)$$

where $j_i(x)$ is the flux (mol cm$^{-2}$ s$^{-1}$), $D_i$ is the diffusion coefficient (cm$^2$ s$^{-1}$), $C_i$ is the analyte concentration (mol cm$^{-3}$), $v(x)$ is the velocity of the solution in the $x$ direction (cm s$^{-1}$), $z_i$ is the charge of the species in question (C). All the rest terms have been defined above.

### 2.3.1.3.1 Diffusion

The first type of mass transport and one of the most common in electrochemical experiments is diffusion. Diffusion refers to the natural movement of species from bulk solution to the electrode surface depending on a concentration gradient. Adolf Fick deduced that the rate of diffusion is given by the change in $C_i(x)$ with respect to $x$ as formalised in Fick's First Law[19,20]:

$$j_i(x) = -D_i \frac{\partial C_i(x)}{\partial x} \qquad (2\text{-}17)$$

where $\frac{\partial C_i(x)}{\partial x}$ is the concentration gradient. The negative sign prior to the diffusion coefficient indicates that particles diffuse *down* the gradient. All the rest of the terms have been defined above.

Fick's First Law can also be expressed as a function of time and in one and three dimensions[19,20]:

$$\frac{\partial C_i}{\partial t} = D_i \frac{\partial^2 C_i}{\partial x^2} \qquad (2\text{-}18)$$

$$\frac{\partial C_i}{\partial t} = D_i \left( \frac{\partial^2 C_i}{\partial x^2} + \frac{\partial^2 C_i}{\partial y^2} + \frac{\partial^2 C_i}{\partial z^2} \right) \qquad (2\text{-}19)$$

## 2.3.1.3.2 Convection

The second form of mass transport is convection, which can be either natural or forced. During the former, the solution can be subjected to natural thermal gradients. During the latter, an external force, mechanical force can disturb the solution. The aforementioned fluxes are defined and predicted with difficult but are given by the following equation (Equation 2-20)[19,20]:

$$j_i(x) = C_i v(x) \qquad (2\text{-}20)$$

where all the terms have been defined above. In order to keep the reproducibility of the electrochemical experiments and eliminate or minimise the effect of convection, minimal time should be spent running the experiments and all vibrations should be limited or prevented. On the other hand, forced convection can be advantageous for the transport of electroactive species to the electrode surface and can easily be achieved by using a rotating disc electrode[28–30].

## 2.3.1.3.3 Migration

Migration, the 3rd form of mass transport discussed in this thesis, takes place when an electric field exists and refers to the charge transfer of species in the electrolyte. The quantification of fluxes caused by migration are given by equation (2-21)[19,20]:

$$j_i(x) = \frac{z_i F}{RT} D_i C_i \frac{\partial \Phi_i(x)}{\partial x} \qquad (2\text{-}21)$$

where all the terms are defined as above. This type of mass transport is difficult to model because the currents are complex. In experimental practice it is therefore necessary to add an inert supporting electrolyte such as KCl at concentrations at least fifty times greater than that of any analyte and its electroactive species as discussed in section 2.3.1.2.1.

### 2.3.1.4 Diffusion to macroelectrodes

In this thesis, all the electrochemical experiments have been conducted on macroelectrodes. Macroelectrodes usually have radii in the millimetre range. Due to the fact that the radius of a macroelectrode is much larger than the diffusion layer thickness, the diffusion is considered to follow a linear behaviour to the electrode surface (see figure 2-12).

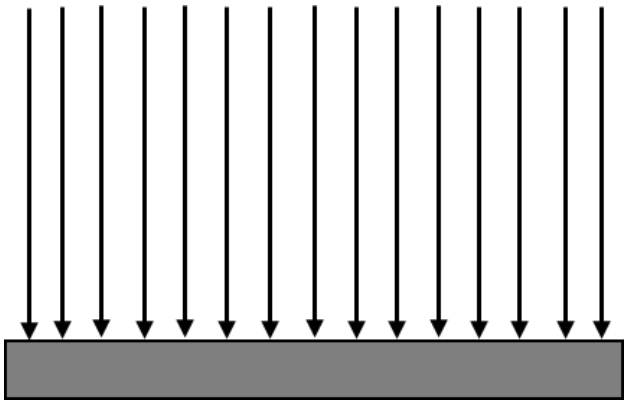

**Figure 2-12** Linear diffusion to a macroelectrode.

## 2.3.2 Electrochemical techniques

### 2.3.2.1 Cyclic voltammetry

Cyclic voltammetry (CV) is the most widely used technique for acquiring qualitative information about electrochemical reactions. The power of cyclic voltammetry results from its ability to rapidly provide considerable information on the thermodynamics of redox processes and the kinetics of heterogeneous electron-transfer reactions. During a cyclic voltammogram, the potential is varied linearly with time, at a constant scan rate (V $s^{-1}$), and is swept between

two values, $E_1$ and $E_2$. When the potential reaches $E_2$ the scan is reversed and the potential is swept back to $E_1$ as shown in figure 2-13. The current-potential graph is known as a voltammogram and is a plot of current versus the applied potential.

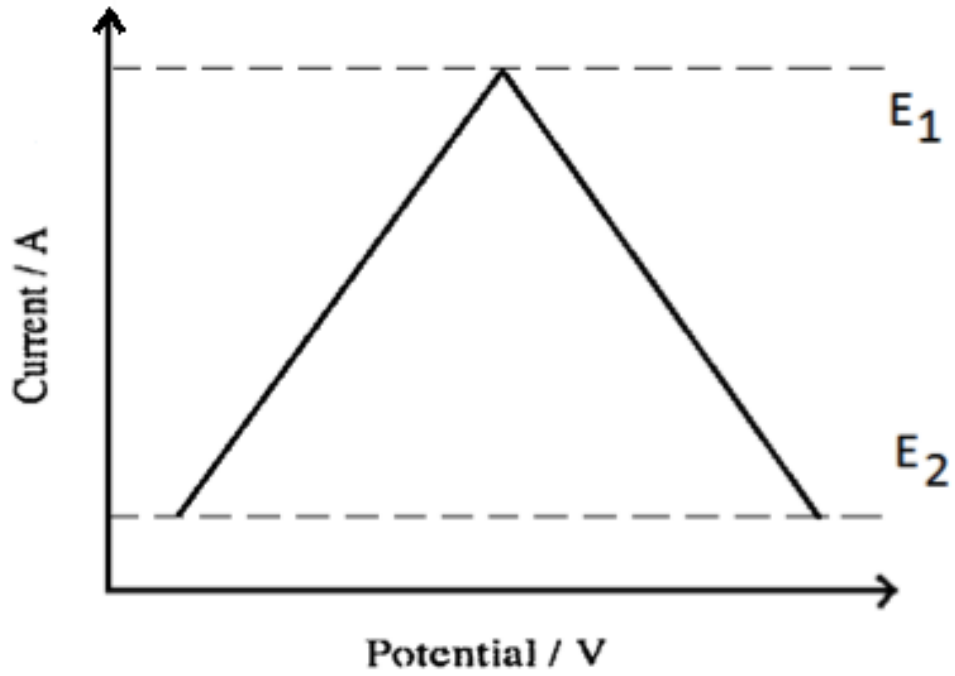


**Figure 2-13** Cyclic voltammetry potential waveform varied with time during a cyclic voltammogram.

During any voltammetric experiment, the voltammetric response of the reaction under consideration at potential $E_1$ is not yet driven because no current is produced. As the potential is scanned at higher values, electron-transfer is generated and a current flows. The electroactive species are consumed on the surface and the electrode surface concentration decreases. This has the result that the redox species need more time to travel to approach and finally reach the electrode surface.

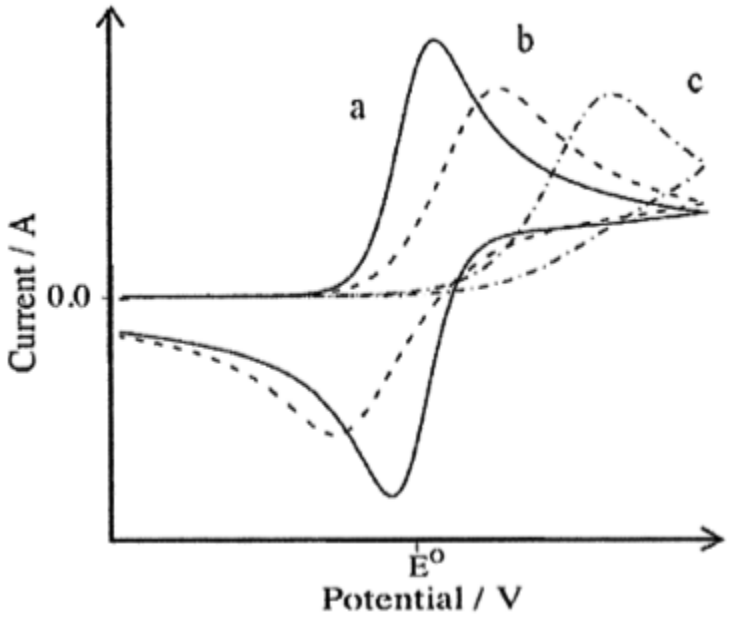


**Figure 2-14** (a) A 'reversible' system, (b) a 'quasi-reversible' system and (c) an 'irreversible' system[19].

There are three types of electrochemical systems that were first considered by Matsuda and Ayabe[20,31]; reversible, irreversible and quasi-reversible systems. In electrochemically reversible systems, the species on the electrode surface follows the Nernst equation (equation 2-5), while for an electrochemically irreversible system the reaction follows the Butler-Volmer equation (Equation 2-13). The various types of electrochemical systems are seen in the figure 2-14. One of the main characteristics of reversible systems is that the peak separation is 57 mV for a single electron transfer reaction at 25 °C[19]. An equilibrium is established at the electrode surface and low overpotentials are required in this system. For the irreversible system, the separation peak is larger and thus reflects slower electrode transfer kinetics.

In cyclic voltammetry, the current peak ($i_p$) can be used in the Randles-Sevcik equation that describes the effect of scan rate on the current peak (assuming T=25 °C). For a simple redox couple, $i_p$ depends not only on the concentration and diffusional properties of the electroactive species but also on the scan rate. The Randles-Sevcik equation for a reversible system can be defined through the following expression[19]:

$$i_p = (2.69 \text{ x } 10^5) n^{\frac{3}{2}} v^{\frac{1}{2}} A C_i D_i^{\frac{1}{2}} \qquad (2\text{-}22)$$

For the irreversible form of the above equation for electrochemically irreversible systems is given from the equations 2-23[19]:

$$i_p = (2.99 \text{ x } 10^5) n (n' + \alpha)^{\frac{1}{2}} A C_i D^{\frac{1}{2}} \qquad (2\text{-}23)$$

where *n'* is the number of electrons transferred before the rate determining step (RDS), $\alpha$ is the transfer coefficient of the RDS and all the rest of the terms were defined above.

## 2.3.2.2 Chronoamperometry

Chronoamperometry is an electrochemical technique in which the potential of the working electrode is controlled and the resulting current from faradaic processes that occur at the electrode (caused by the potential step) are monitored as a function of time (see figure 2-15 (a)). This technique was used for most of the electrodepositions reported in this thesis the results of which are discussed in the following sections. There are three ways that the potential can be generated. These are in the form of steps, pulses and waves. When the electrolyte is not stirred, the mass transport to the electrode surface is controlled only by diffusion. Given this condition, the diffusion layer can be extended over time as well as the species will be depleted on the surface. As a result, the concentration decreases with time (see relevant figure 2-15 (b)). The Cottrell equation (Equation 2-24) describes the change of the electric current with respect to time in an experiment with such controlled potential as chronoamperometry[19]. The Cottrell equation describes the case for an electrode that is planar but can also be derived for spherical, cylindrical or rectangular geometries.

$$I(t) = \frac{nFACD^{\frac{1}{2}}}{\sqrt{\pi t}} = kt^{-\frac{1}{2}} \qquad (2\text{-}24)$$

where all the terms have been previously defined.

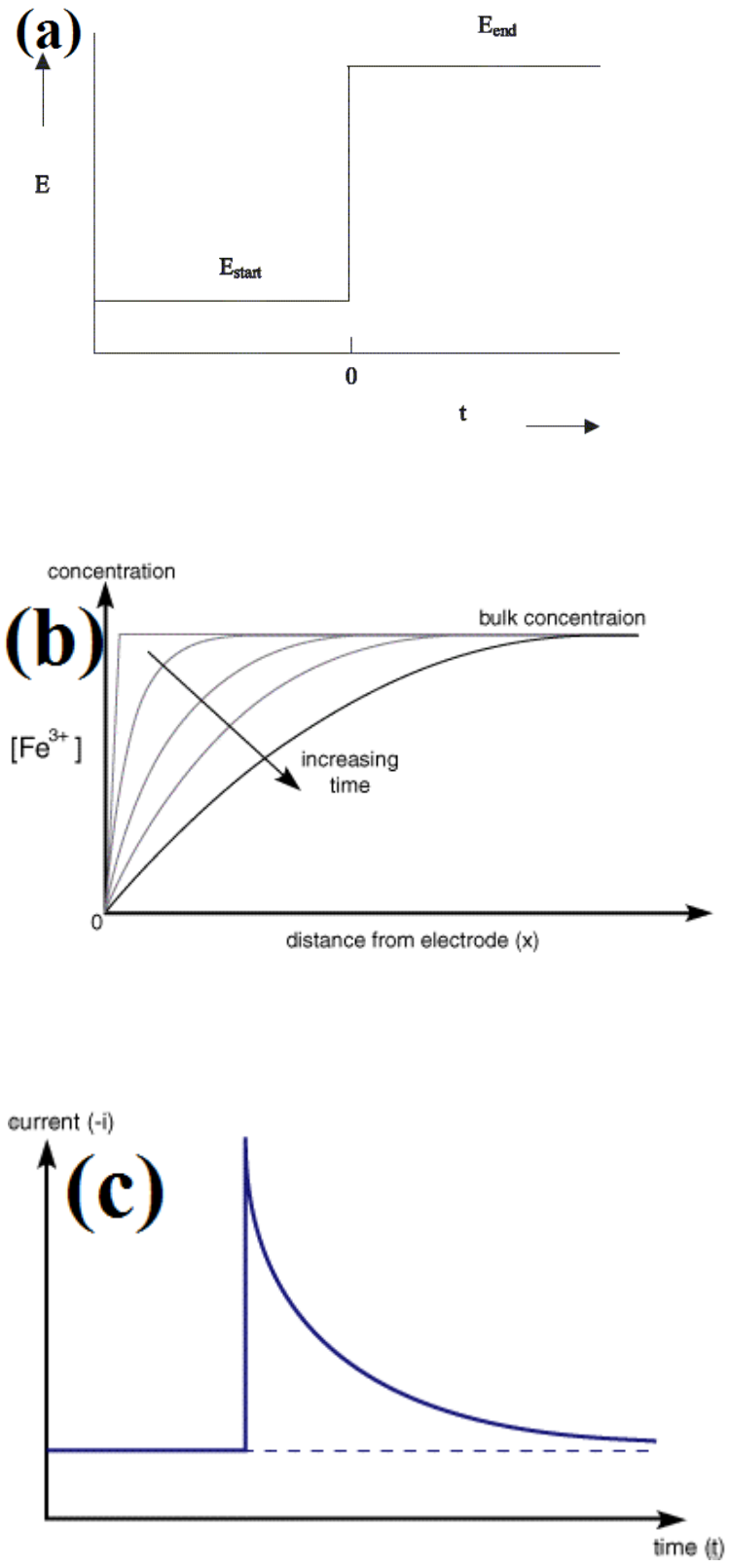


**Figure 2-15** (a) The dependence of potential vs time of a chronoamperometric measurement, (b) the dependence of concentration with the distance of the electrode and the change of it over time and (c) resulting chronoamperogram current as a function of time[20].

## 2.3.2.3 Electrochemical Impedance Spectroscopy (EIS)

Electrochemical impedance spectroscopy (EIS), also known as dielectric spectroscopy, measures the dielectric properties of a medium as a function of frequency. This theory interprets the equivalent resistance and capacitance values in terms of interfacial phenomena. EIS operates under the application of an alternating current (AC) to a working electrode and under a constant potential where the redox species can be transformed. A transient state arises at the electrode during half-period and this state changes at the second half-period[32]. The latter phenomenon takes place due to the existence of the alternating current[32]. These state changes can constantly take place over a range of AC frequencies. The data is most commonly displayed as a Nyquist plot (figure 2-16).

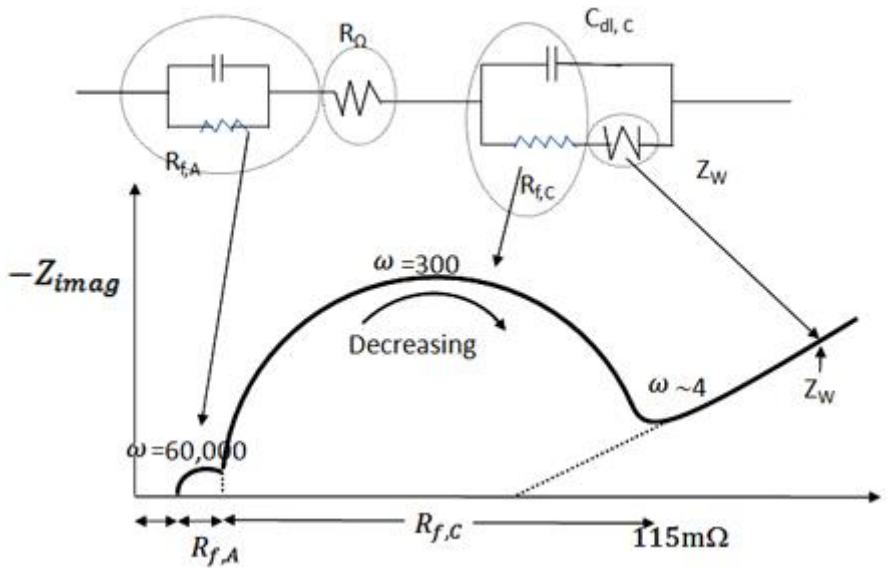


**Figure 2-16** Nyquist plot of an EIS measurement, obtained from[33].

As shown in figure 2-16, the Nyquist plot displays the imaginary (Z') *vs* real (-Z'') parts of the impedance and is interpreted by an electrical circuit model. The circuit consists of resistors and capacitors at which current is passed with the same amplitude and phase angle. Three different layers at the electrode interface can be considered. The first one is the double layer, the second the diffusion layer and the third is the bulk solution. As described in previous

sections the following phenomenon takes place under the application of alternating currents. The alternating current induces the alignment of ions and solvated ions along the electrode surface resulting the formation of double layer. Due to the latter, there is a capacitance, $C_{dl}$. During the EIS measurement a resistance is caused by the diffusion of the redox molecules of species and a second resistance is associated with solution resistance. A third resistance $Z_w$ is associated with the Warburg impedance and is attributed to the difficulty of mass transport of the redox species.

# 2.4 Bibliography

1. http://nau.edu/cefns/labs/electron-microprobe/glg-510-class-notes/instrumentation/.

2. http://mcff.mtu.edu/acmal/electronmicroscopy/FE_Form_Function.htm.

3. Warren BE, X-Ray Diffraction, Massachusetts Institute of Technology, (1990, New York).

4. https://en.wikipedia.org/wiki/X-ray_crystallography#/media/File:Bragg_diffraction_2.svg.

5. Siegbahn K, Nordling C, Johansson G, Hedman J, Heden P, Hamrin K, Gelius, U, Bergmark T, Werme L, Manne R. *ESCA applied to free molecules*; North-Holland publishing company, (1970).

6. Siegbahn K, Nordling C, Fahlman A. *Nov. Act. Uppsaliensis* (1967), 20.

7. https://en.wikipedia.org/wiki/X-ray_photoelectron_spectroscopy#/media/File:System2.gif.

8. Briggs D. & Editor. *Handbook of X-Ray and Ultraviolet Photoelectron Spectroscopy*. (Heyden, 1977).

9. http://www.casaxps.com/.

10. S. Hüfner, Photoelectron spectroscopy: principles and applications, Springer, (2003).

11. Hedin L, Johansson A. Polarization corrections to core levels. *J. Phys. B At Mol. Phys*. 2002;2(12):1336–1346. doi:10.1088/0022-3700/2/12/313.

12. Martensson N, Nilsson A. On the origin of core-level binding energy shifts. *J. Electron Spectros. Relat. Phenomena*. 1995;75(C):209–223. doi:10.1016/0368-2048(95)02532-4.

13. Pehlke E, Scheffler M. Evidence for Site-Sensitive Screening of Core Holes at the Si and Ge (001) Surface. *Phys. Rev. Letters*. 1993;71(4);2338-2341.

14. Watts JF. *An introduction to surface analysis by XPS and AES*. (New York Chichester: Wiley, 2003).

15. Biesinger MC, Payne BP, Grosvenor AP, Lau LWM, Gerson AR, Smart RSC. Resolving surface chemical states in XPS analysis of first row transition metals, oxides and hydroxides: Cr, Mn, Fe, Co and Ni. *Appl. Surf. Sci*. 2011;257(7):2717–2730. doi:10.1016/j.apsusc.2010.10.051.

16. Patil UM, Nam MS, Sohn JS, Kulkarni SB, Shin R, Kang S, Lee S, Kim JH, Jun SC. Controlled electrochemical growth of $Co(OH)_2$ flakes on 3D multilayered graphene foam for high performance supercapacitors. *J. Mater. Chem A*. 2014;2(44):19075–19083. doi:10.1039/C4TA03953J.

17. http://xpssimplified.com/elements/lanthanum.php.

18. http://xpssimplified.com/elements/aluminum.php.

19. Compton Richard G. Banks Craig E. Understanding Voltammetry. *Imp. Coll. Press*. 2nd edition, 2011.

20. Bard A. J. and Faulkner L. R. Electrochemical Methods: Fundamentals and applications. *John Wiley Sons*. 2001.

21. von Helmholtz, *Ann. Phys.* 1853;165:211

22. von Helmholtz, *Ann. Phys.* 1879;243:337

23. Gouy GJ, *J. Phys.* 1910;9

24. Gouy GJ, *Compt. Rend.*. 1910;149:654

25. Chapman DL. LI. *A contribution to the theory of electrocapillarity*. *Philos. Mag. Ser. 6*. 1913;25(148):475–481. doi:10.1080/14786440408634187.

26. Stern OZ, *Electrochem.* 1924;30;508.

27. Dickinson EJF, Limon-petersen JG, Rees N V, Compton RG. How Much Supporting Electrolyte Is Required to Make a Cyclic Voltammetry Experiment Quantitatively "Diffusional"? A Theoretical and Experimental Investigation. *J. Phys. Chem. C*. 2009;113:11157–11171.

28. Lu Y, He Q, Gasteiger H A. Probing the Lithium − Sulfur Redox Reactions: A Rotating-Ring Disk Electrode Study. *J. Phys. Chem. C*. 2014;118(1):5733–5741. doi:10.1021/jp500382s.

29. Concepcion JJ, Binstead RA, Alibabaei L, Meyer TJ. Application of the rotating ring-disc-electrode technique to water oxidation by surface-bound molecular catalysts. *Inorg Chem*. 2013;52(19):10744–10746. doi:10.1021/ic402240t.

30. Herranz J, Garsuch A, Gasteiger HA. Using rotating ring disc electrode voltammetry to quantify the superoxide radical stability of aprotic Li-air battery electrolytes. *J. Phys. Chem. C*. 2012;116(36):19084–19094. doi:10.1021/jp304277z.

31. Matsuda, H.; Ayabe, Y. Z. *Electrochem.* 1995;59:494.

32. Bagotskii VS. Fundamentals of Electrochemistry. 2nd edition. (Hoboken NJ, Wiley-Interscience, 2006).

33. nptel.ac.in/courses/103102015/fuel cell characterization/in situ characterization.html.

# Chapter 3

# Pt-Cu and Cu modified Boron-Doped Diamond electrodes for Methanol Electrooxidation and Glucose sensing

## 3.1 Introduction

Boron-doped diamond has received increasing attention since its introduction in 1987[1] as an electrode and as a catalytic support material due to its special characteristics. In comparison to other carbon materials BDD possesses outstanding properties such as: low background current, high mechanical and electrochemical stability, resistance to fouling and corrosion resistance in hostile environment; it is also available at economic cost when grown by chemical vapour deposition (CVD)[2–10]. Diamond electrodes can be modified by depositing nanosized metal or metal oxide clusters[6]. This enables improved features such as enhanced sensitivity towards analytes which cannot be detected on the unmodified surface[11], increased selectivity for electroanalytical applications, and increased surface area for adsorptive voltammetry[12]. BDD electrodes modified with catalytic metal nanoparticles are widely recognised for their electrochemical applications[2,10,13–19]. In this work, two types of modifications were explored for two different applications.

Pt-Cu modified BDD is explored for methanol oxidation, of relevance to the direct methanol fuel cell (DMFC) given schematically in figure 3-1. The DMFC is considered one of

several promising fuel cell technologies due high energy density (4.4 Wh/mL), durability and the low operational temperature (< 100 °C)[20]. The cell works by the following three reactions:

$$\text{Anode: } CH_3OH + 6OH^- \rightarrow 5H_2O + 6e^- + CO_2 \text{ (oxidation)} \qquad (3\text{-}1)$$

$$\text{Cathode: } \frac{3}{2} O_2 + 3H_2O + 6e^- \rightarrow 6OH^- \text{ (reduction)} \qquad (3\text{-}2)$$

$$\text{Overall: } CH_3OH + \frac{3}{2} O_2 \rightarrow 2H_2O + CO_2 \qquad (3\text{-}3)$$

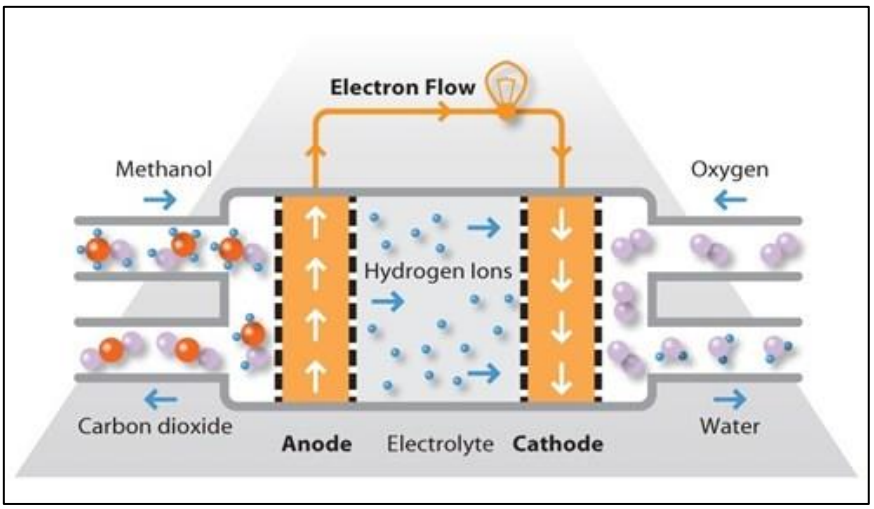


**Figure 3-1** Schematic presentation of a Direct Methanol Fuel Cell (DMFC)[21].

Diamond has attracted interest recently for fuel cell applications on account of its resistance to electrocorrosion[10,22,23]. Platinum is a highly active electrocatalyst anode for the aforementioned fuel cell. However, Pt electrocatalysts tend to be poisoned by the intermediates of methanol oxidation (e.g. CO) and are also expensive[24]. Consequently, much effort has been made to reduce both Pt poisoning and the amount of Pt used. The development of Pt-based core-shell structures[25–30] and the incorporation of non-noble metals[7,31] such as Cu promises to improve its stability in DMFC, as well as lower its cost. The chapter presents the first study of the formation of Cu-Pt core-shell structures on diamond and an investigation into the properties

of this modified electrode. In particular, the activity towards the oxidation of methanol with Pt-modified BDD was compared to the Pt-Cu/BDD. The motivation for the work was ultimately to understand how such core-shell structures on diamond compare to similar structures on other forms of carbon. The second objective of this study was to develop a simple Cu-modified BDD electrode that could be used as a sensitive non-enzymatic amperometric glucose sensor. A simple Cu electrodeposition approach was used to modify the diamond electrode. A significant number of the population worldwide has diabetes, and this number is expected to increase over the coming decade[32]. Glucose sensors (Figure 3-2) are not only relevant for the blood sugar monitoring but also in many other fields such as the food industry[33] and fuel cells[9,34–39]. Although an early preliminary study at relatively high glucose concentrations suggested the potential of Cu/BDD and especially Ni/BDD electrode systems in this area[40], subsequent work has tended to focus on instrumentally more complex Cu ion implantation approaches[41,42] and the use of microelectrodes or patterned electrodes[43,44]. Here, simple large area Cu/BDD electrodes prepared by electrodeposition without additional complications demonstrate of very sensitive detection of glucose.

In both these cases, the electrochemical modifications introduced by the deposition of the nanoparticles reflect in part the particular properties of the metal, and in part their interaction with the underlying diamond. In this context the present work was carried out on oxidised electrode surface so the interaction involved is that with oxidised diamond interfaces.

**Figure 3-2** Schematic representation of a glucose meter[45].

# 3.2 Aims of the project and principal outcomes

The overall aim of the project is the electrochemical synthesis of boron-doped diamond (BDD) electrodes decorated with Pt-Cu for the electrooxidation of methanol and with pure Cu particles for glucose sensing. A two-step electrochemical method that involved the electrodeposition of Cu, followed by the Pt was used to synthesise the bimetallic Pt-Cu particles and a potentiostatic method was used to deposit the pure Cu onto BDD. The electrochemical evaluation of the Pt-Cu/BDD electrode towards methanol oxidation and its comparison with the catalytic activity of the Pt/BDD electrode itself is demonstrated. Higher current densities and less fouling at Pt-Cu/BDD catalysts during methanol oxidation were seen compared to the Pt alone. Also, a simple and cost-effective method of BDD electrode modification using Cu nanoparticles was explored. The main target of the second approach was the development of a simple Cu modified BDD electrode that can be used as a sensitive non-enzymatic amperometric glucose sensor. High sensitivity and current response to glucose oxidation in KOH was observed as well as good reproducibility and stability. Selectivity of the Cu/BDD towards glucose in KOH was observed in the presence of low concentrations of interfering species.

# 3.3 Experimental section

## 3.3.1 Chemical reagents

Copper (II) sulphate pentahydrate ($CuSO_4 \cdot 5H_2O$); D-(+)-Glucose ($C_6H_{12}O_6$) and potassium hydroxide (KOH were purchased from Sigma-Aldrich and were used as-received without any further purification. Potassium hexachloroplatinate (IV) ($K_2PtCl_6$) was purchased from Alfa Aesar. All aqueous solutions were freshly prepared, using milli-Q water (18 MΩ cm at 23 °C). All the solutions were deoxygenated using nitrogen gas for at least 15 minutes when the experiments required oxygen-free solutions.

## 3.3.2 Equipment and experimental set-up

BDD wafers ([B]>$10^{20}$ $cm^{-3}$) of 10 x 10 x 0.6 mm were obtained from Element Six Co (UK) and mounted in a home-built PTFE holder with a circular area of 0.38 $cm^2$ exposed to the electrolyte. The electrochemical measurements were performed with an Autolab PGSTAT 128N potentiostat/galvanostat. The electrochemical depositions were conducted at room temperature (24 ± 1.0°C), using a standard three electrode cell comprised of a Pt counter electrode and a Ag/AgCl reference electrode. The analysis was done with OriginPro 8.5 software (OriginLab Ltd.). The morphology of the deposits was characterised by a Hitachi S530 and Zeiss SEM with a 20kV and 5kV acceleration voltage, respectively and the composition of the deposits was measured by XPS using an Al Kα (1486.6 eV) X-ray source. XPS data was curve fitted with a Shirley background[47] and CasaXPS software[46]. The C 1s peak was calibrated to 285 eV with the following relative sensitivity factors (R.S.F.): C 1s (1.0), O 1s (2.93), Pt 4f (15.5), and Cu 2p (16.7).

## 3.3.3 Fabrication and working electrodes

Prior to each use, all working electrodes were polished on a polishing machine with alumina micropolish II (Buehler, UK) of decreasing particle size (1 μm to 0.05 μm) on soft lapping pads (Buehler, Chemonet I for 8'' wheel) to aid removal of previous metallic deposits and ensure fresh, active surfaces, free of deactivating layers and contamination, which consequently leads to better signal to noise in the electrochemical data[48]. After the electrodes had been polished with the 1 μm alumina, the electrodes were rinsed gently with distilled water and were sonicated for 5 minutes in water and acetone (1:1 ratio). This was followed by polishing with 0.05 μm alumina, a rinse in water, and sonication for 30 minutes in acetone. The electrodes then were cycled in 0.1M nitric acid between the potential range of -1.7V and 2.5V for 10 sweeps, which yielded a high concentration of oxygen functionalities at the electrode surface[4].

Pt-Cu bimetallic catalysts were fabricated on BDD by potentiostatic electrodeposition of Cu particles followed by Pt, Cu was deposited first; this was done onto BDD from a deaerated 1M $H_2SO_4$ solution containing 5mM $CuSO_4 \cdot 5H_2O$. The deposition potential was held at -0.8V (vs Ag/AgCl) until 157.9 mC/cm$^2$ (19.76 μg/cm$^2$) charge was passed through the surface. This potential was chosen as it produces well dispersed copper nanoparticles on the electrode surface[49]. The Cu/BDD electrode was then removed, rinsed gently with ultrapure water, and dried with $N_2$. Pt electrocatalytic particles were electrodeposited onto Cu/BDD from a deaerated 1M $H_2SO_4$ solution containing 5mM $K_2PtCl_6$. Again, a potentiostatic method was used in which the potential was held at -0.3V (vs Ag/AgCl) until 78.9 mC/cm$^2$ (30.3 μg/cm$^2$) was passed through the electrode surface[31].

The glucose sensor consisted of Cu/BDD, with Cu being electrodeposited onto BDD from a deaerated 5mM $CuSO_4 \cdot 5H_2O$ in 1M $H_2SO_4$ solution by chronoamperometry at a

potential of -0.8V (vs Ag/AgCl) until 157.9 mC/cm$^2$ (19.76 μg/cm$^2$) charge had passed through the electrode surface.

# 3.4 Results and discussion

## 3.4.1 Oxidation of methanol using Pt-Cu modified diamond

### 3.4.1.1 Morphology and XPS characterization of the deposits on BDD

SEM images of Cu, Pt (157.9 mC/cm$^2$ and 78.9 mC/cm$^2$ apiece) and Pt-Cu particles on BDD are shown in figure 3-3 (a-c), respectively. Cu deposits in a non-uniform manner on grain boundaries are displayed. The particles are approximately 475 nm (± 92 nm) in size at this metal loading. Pt also deposits in a non-uniform manner with visible agglomeration along some grain boundaries. These particles are similar in size to Cu, approximately 480 nm (± 104 nm) in size. In contrast the sequential deposition of Pt/Cu produced smaller particles around 215 nm (± 47 nm). The non-uniform nature of the deposition sensitively reflects the variations in the lateral conductivity of the diamond, as a result of the non-uniform distribution of the B dopant[50].

The element composition and chemical and electronic states of Cu, Pt, and Pt-Cu at the diamond interface were investigated by XPS. Figure 3-4 (a) shows the survey scans of the modified electrodes, with the relevant elemental Cu, Pt, and Pt-Cu modified BDDs, respectively with the appropriate elemental ratios given in Table 3-1.

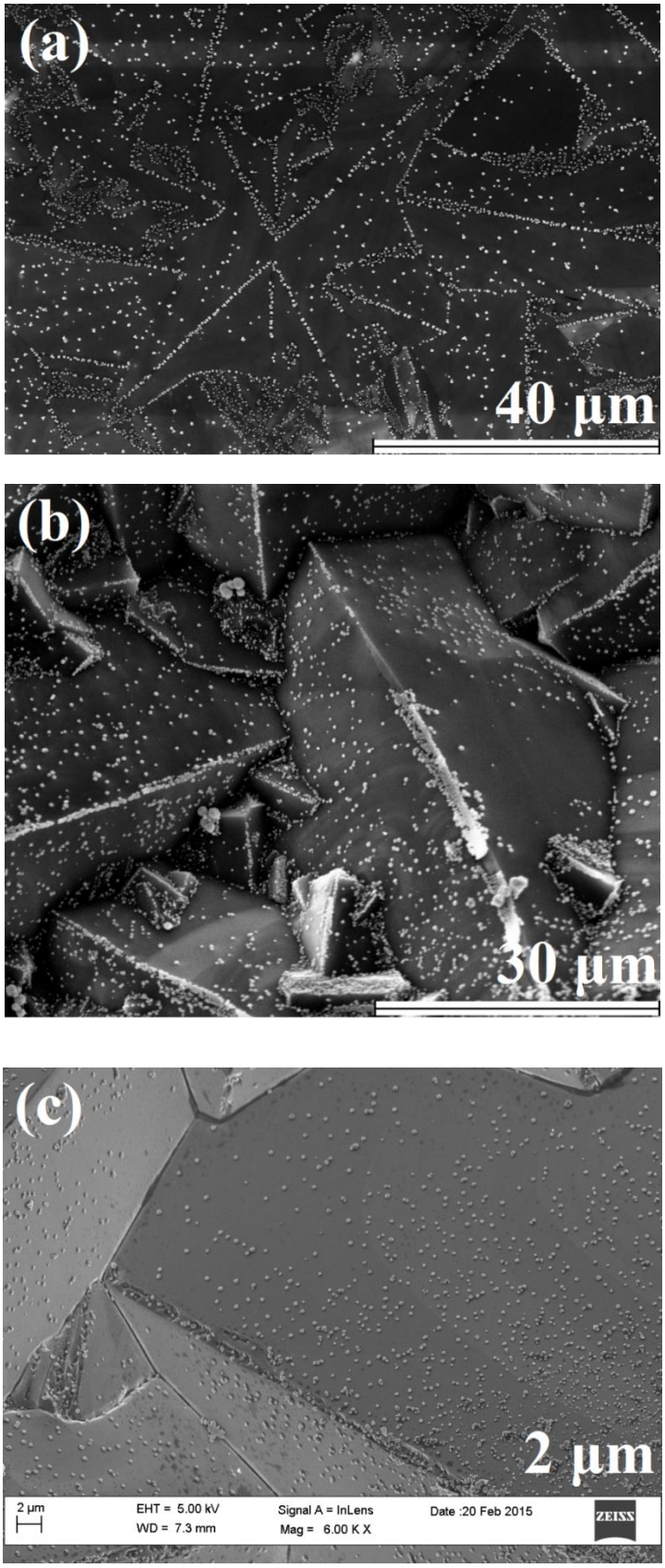


**Figure 3-3** (a) SEM image of Cu deposited on BDD electrodes, (b) Pt on BDD and (c) Pt-Cu deposited on BDD, respectively through chronoamperometry at -0.8V for the Cu and -0.3V for the Pt, respectively.

The elemental ratios were derived from the Cu 2p, Pt 4f and C 1s peak areas after correction for the XPS sensitivity factors. The survey scans indicate that these electrodes contain O, C, and metal photoelectron peaks, consistent with the modification of the BDD with either Cu, Pt, or Pt-Cu nanoparticles. BDD modified with Pt nanoparticles has Pt $4f_{7/2}$ and Pt $4f_{5/2}$ peaks at 74 eV and 77.4 eV, respectively[51]. Modification with Pt-Cu nanoparticles leads to the Pt 4f peaks shifting to 73.6 eV and 77 eV, respectively. This observation is consistent with metallic bonding between Pt and Cu, which occurs when they are in contact with each other within the same nanoparticle[52]. The modification of BDD with Cu leads to typical Cu $2p_{3/2}$ and $2p_{1/2}$ peaks at 934 eV and 954 eV, respectively[51]. This signal largely disappeared in the case of Pt/Cu-modified diamond surfaces, as shown in figure 3-4 (b). Either the Cu had been removed or its photoelectron signal had been attenuated by an overlayer of Pt.

**Table 3-1** XPS % elemental ratio of different electrodes.

| Sample | (Cu)/C | (Pt)/C |
|---|---|---|
| Cu/BDD | 0.52 | - |
| Pt/BDD | - | 2.02 |
| Pt-Cu/BDD | 0.03 | 0.70 |

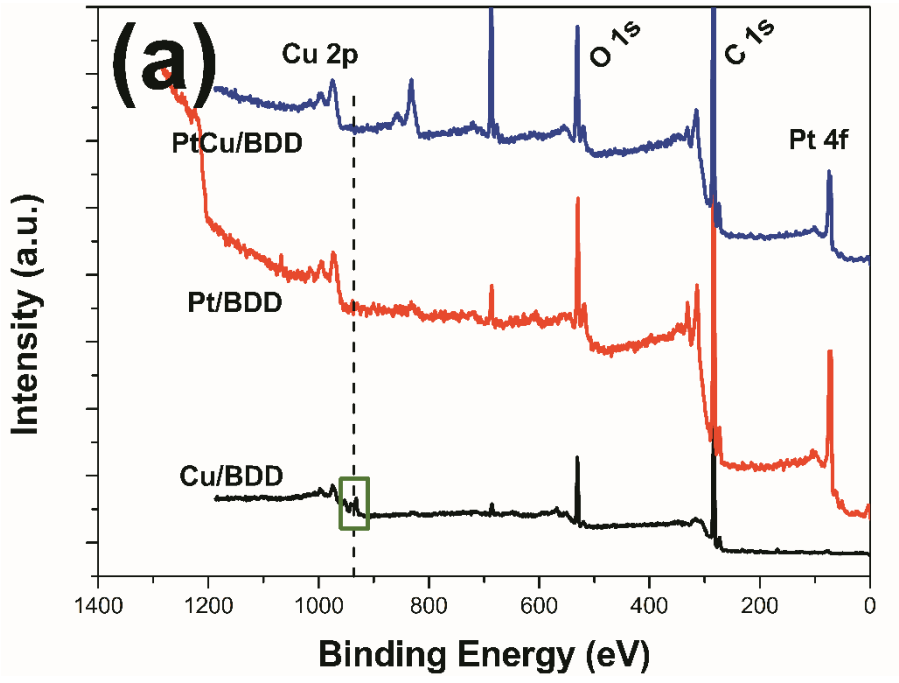

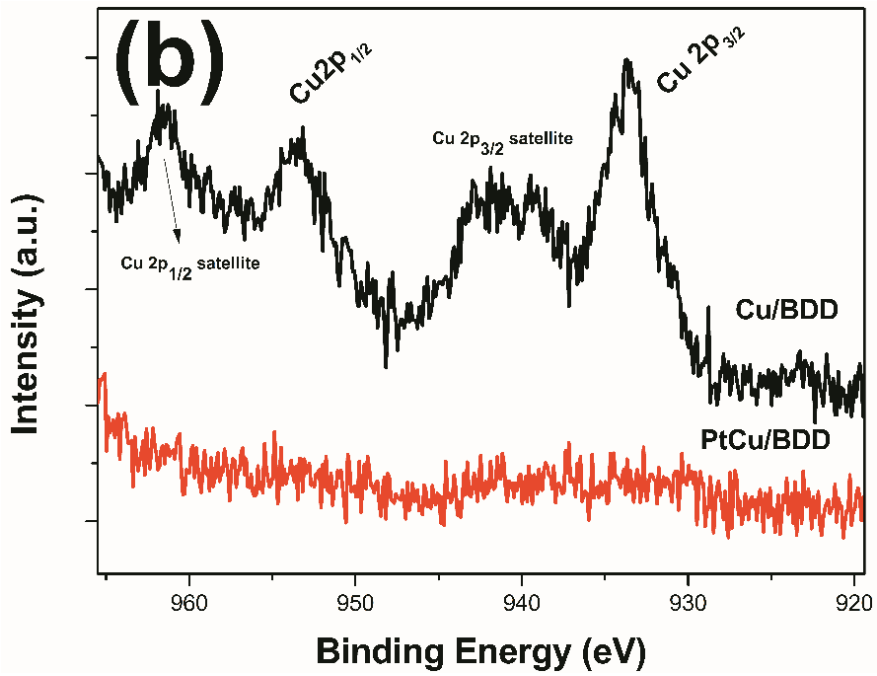


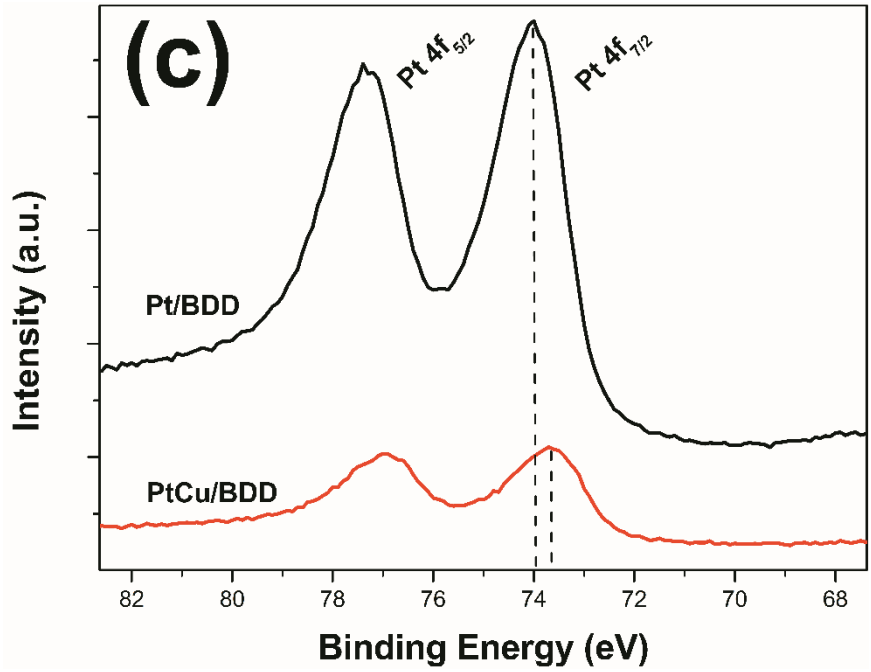


**Figure 3-4** (a) XPS spectra of wide scans of the Cu/BDD, Pt/BDD and Pt-Cu/BDD, respectively. (b) Typical Cu 2p peaks of Cu and Pt-Cu modified BDD catalysts, respectively. (c) Typical Pt 4f peaks of Pt and Pt-Cu modified BDD catalysts, respectively.

## 3.4.1.2 Voltammetric characterisation

### 3.4.1.2.1 Electrodeposition of the electrocatalysts

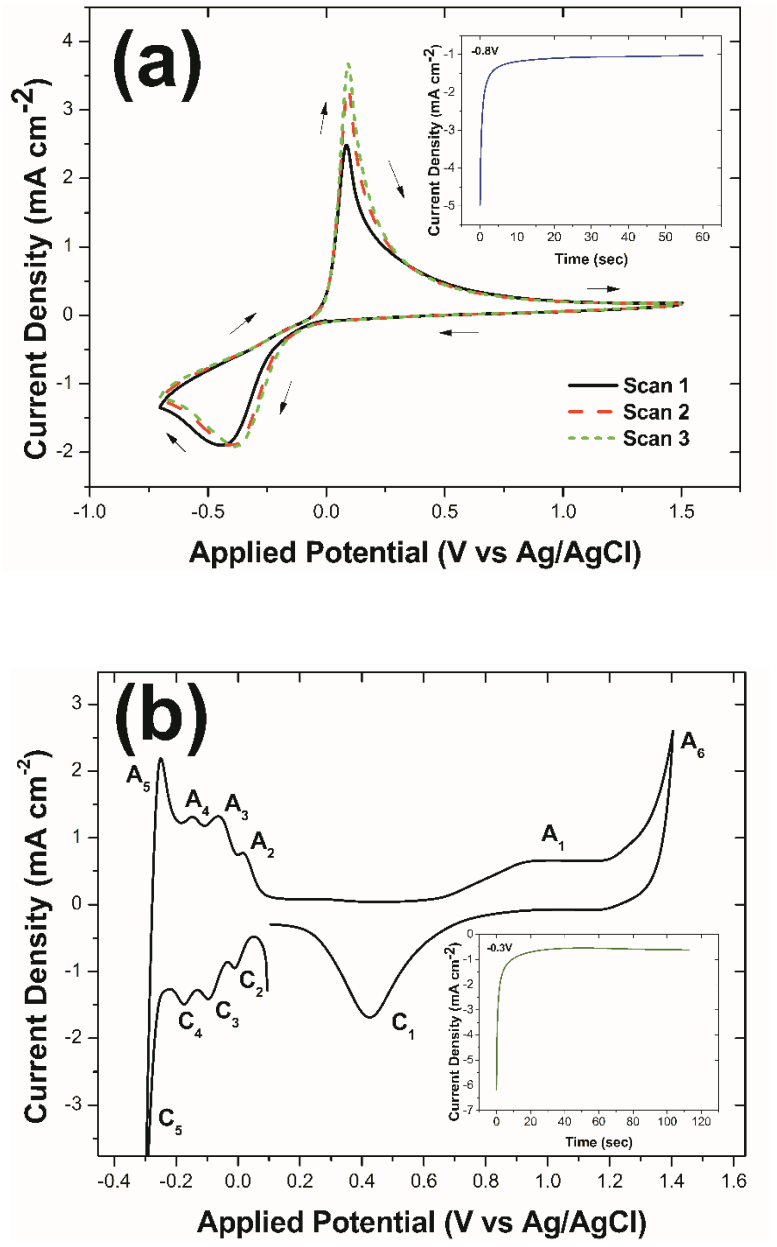


**Figure 3-5** (a) Cyclic voltammogram of bare BDD in a solution containing 5mM $CuSO_4 \cdot 5H_2O$ in 1M $H_2SO_4$ at scan rate of 0.1 V/s (inset: chronoamperogram of Cu deposition in 5mM $CuSO_4 \cdot 5H_2O$ in 1M $H_2SO_4$ on bare BDD at constant potential of -0.8V). (b) Cyclic voltammogram of bare BDD in a solution containing 1M $H_2SO_4$ and 5mM $K_2PtCl_6$ respectively at scan rate of 0.1 V/s (inset: chronoamperogram of Pt deposition in 5mM $K_2PtCl_6$/1M $H_2SO_4$ on bare BDD at constant potential of -0.3V).

A typical cyclic voltammogram of bare BDD in a solution containing 5mM copper sulfate in 1M sulfuric acid is shown in figure 3-5 (a). Figure 3-5 (a) shows the signal recorded

when the BDD electrode was cycled from 0V to -0.7V to +1.5V and back to 0V continuously for three scans in 1M sulfuric acid. The copper deposition started at around -0.07V and a small peak first appeared at -0.437V. When continuous scans were carried out, the potential is changed to -0.403V on the second scan and reached a steady state at -0.376V in subsequent scans. The Cu is stripped in the anodic scan with a sharp peak at potential +0.08V. The integration of the area between -0.437V and -0.7V gave the charge of the Cu deposition while the area between -0.04V and +0.78V represents the charge of the Cu which is stripped. The overpotential for the deposition of copper was reduced in subsequent voltammograms, which indicates that the deposition process became kinetically more favourable, until the overpotential became stable at the steady value of -0.37V. Also, the fact that the deposition peak decreased whereas the stripping peak increased on subsequent scans is consistent with incomplete stripping of the copper[53]. In the first scan, a larger amount of metal was deposited than removed, but for subsequent scans a much higher proportion, of the metal was stripped[53]. That suggests that during the first scan the BDD surface was clean but on subsequent scans there were metal nuclei present which created a larger initial surface area that resulted in greater charge transfer and a higher metal deposition rate.

The lowering of the overpotential required to deposit metal can be explained by considering the substrate onto which the metal is deposited. In the first scan, the only available surface is BDD so a set overpotential is required to initiate the nucleation of the metal. In subsequent scans, a metal surface is available that has a higher affinity for depositing. Hence, the process of deposition becomes more energetically favourable and the overpotential is lowered. A constant overpotential is reached when the surface of the BDD no longer changes from one scan to the next.

In figure 3-5 (b) a typical voltammogram in a solution containing 5mM $K_2PtCl_6$/1M $H_2SO_4$ is illustrated. The Pt is deposited in the forward scan in the potential range +0.63V and -0.28V. A cathodic current has initially observed at +0.42V (peak $C_1$) this current stayed steady until an overpotential of -0.01V (peak $C_2$) was reached at which point it gradually increased to -0.09V (peak $C_3$) and -0.17V (peak $C_4$), respectively near to the diffusion-limited reduction of Pt ions. An increase in the current due to bulk $H_2$ evolution (peak $C_5$) followed. The potential region of +0.42V and -0.01V represents the Pt metal deposition without hydrogen underpotential deposition ($H_{UPD}$) and after this potential, in the cathodic range between -0.01V and -0.27V deposition occurs simultaneously with $H_{UPD}$ onto the freshly deposited Pt in which $A_2$-$A_5$ peaks are due to the H desorption process. The $A_1$/$C_1$ peaks represent the Pt stripping from the electrode surface having a maximum peak at +0.97V and the reduction of it at +0.42V in the anodic and cathodic scan, respectively. The $A_6$ peak represent the oxygen evolution at 1.4V.

### 3.4.1.2.2 Electrochemical activity of the electrocatalysts

The electrochemical activity of the Pt-Cu electrocatalysts supported on diamond was characterized by cyclic voltammetry in 1M $H_2SO_4$ and compared to pure Cu and Pt. In figure 3-6 (a) shows various features: Cu stripping is seen at a potential of +0.1V. Hydrogen adsorption and desorption due to Pt occured between 0V and -0.3V; Pt oxidation and reduction waves occured at +1.0V and +0.4V, respectively[4,54,55]. The weak features at +0.45V which only occured in the Pt-Cu-modified BDD and which were not seen at its Pt or Cu modified counterparts[26,56–58]. The weak features at +0.45V were consistent with the Cu particles serving as reactive centres for the subsequent deposition of Pt, such that the resultant Pt-Cu nanoparticles have core-shell structure.

The Pt coverage was estimated from the charge obtained from the area under the voltammogram as shown in equation 3-1[59] (see also Table 3-2):

$$Metal\ Loading = \frac{Charge \times Molar\ weight\ of\ Pt}{F \times n} \qquad (3\text{-}1)$$

where $F$ is the Faraday constant (96485 C mol$^{-1}$) and $n$ is the number of the electrons involved in the redox process.

The electroactive surface area (EAS) of the pure Pt electrocatalyst can be determined from the charge required to oxidise a monolayer of hydrogen on the Pt (111) surface[5,54]:

$$EAS = \frac{Q_H}{0.21} \qquad (3\text{-}2)$$

where the $Q_H$ (mC cm$^{-2}$) is the coulombic charge of the hydrogen desorption.

In addition, the specific surface area (SSA) is defined as the electroactive surface area divided by the metal loading (Equation 3-3):

$$SSA = \frac{EAS}{Metal\ Loading} \qquad (3\text{-}3)$$

For spherical nanoparticles the diameter is determined by the following expression:

$$d = \frac{6}{\rho \times S} \qquad (3\text{-}4)$$

where $\rho$ is the density of Pt and $S$ corresponds to the specific surface area (SSA). The particle size calculated using equation 3-4 is significantly smaller than the SEM images suggest as has been previously noted[60]. High resolution SEM images actually show the surface of the particles to be extremely rough and textured, which probably explains the differences. If the same approximations is made for the Pt-Cu particles, then the data in the second column of Table 3-2 indicates roughly similar SSA are obtained for the two electrodes.

XPS suggested that some Cu remained at the Pt-Cu-modified interface but the reduction in Cu XPS signal indicated that Pt is covering Cu. The weak features of the CV at +0.45V are consistent with a core-shell Pt-Cu nanostructure since these peaks are not seen for the pure Pt or pure Cu. Further evidence for this core-shell structure was obtained by linear sweep voltammetry (LSV). These experiments were conducted for each of the three types of modified BDD and the results are shown in figure 3-6 (b). There were two oxidation maxima associated with Pt-Cu deposition. The one at the higher overpotential is consistent with Pt deposition onto BDD, whilst the peak at +0.45V was specified the same feature seen in the CV in figure 3-6 (a); the evidence in figure 3-6 (b) further confirms that this latter peak was unique to the Pt-Cu-modification, which feasibly arose from the oxidative stripping of Cu. There was no Cu stripping peak at +0.1V associated with Pt-Cu, which is consistent with the fact that Pt is electrodeposited onto the Cu. This layering prevents the inhibition of the re-oxidation at +0.1V.

Further evidence for the formation of the core-shell structures was acquired from the cyclic voltammogram in 1M $H_2SO_4$ in figure 3-6 (c). In addition to the features previously discussed the hydrogen adsorption and desorption areas and the Pt oxidation and reduction peaks increased with the amount of Pt. Furthermore, the LSV data in figure 3-5 (d) were fully consistent with the cyclic voltammograms. While the Pt loading increase, the Pt features at higher overpotential at +1.0V also increased.

Although electrodeposition as imposed by the external potential contributes dominantly to the deposition of Pt, this was not the only reaction channel. In particular, some Pt was deposited on the Cu coated diamond electrode if the electrode was simply immersed in the solution containing the Pt salt. This indicates that galvanic replacement of the Cu by the Pt is occurring, as depicted in figure 3-6[58,61–64] so that two channels are responsible for controlling the Pt loading in this type of structure. The Pt loading is therefore likely to be bigger than that

given in Table 3-2 corresponding to 78.9 mC/cm$^2$ of charge but given that the galvanic replacement was a minor channel will still be significantly less than that in the first column of Table 3-2 which corresponds to 157.9 mC/cm$^2$ of charge.

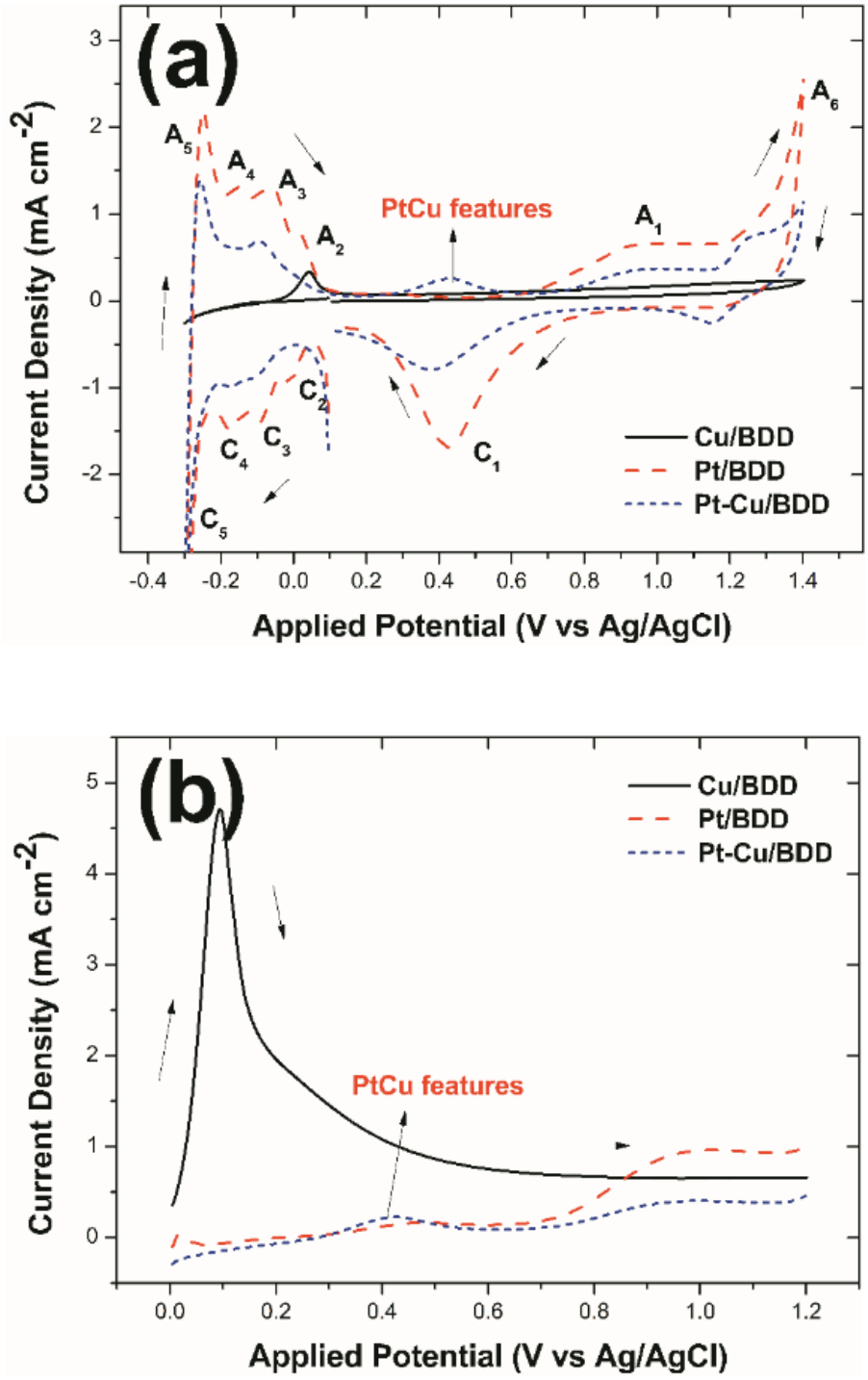


**Figure 3-6** (a) Cyclic voltammogram and (b) linear sweep voltammogram of the Cu, Pt and Pt-Cu deposited on BDD, respectively in 1M $H_2SO_4$ solution at scan rate of 0.1 V/s.

**Table 3-2** Pt features after electrodeposition through chronoamperometry.

| Pt features | Pt/BDD | Pt-Cu/BDD |
|---|---|---|
| **Pt loading (µg/cm$^2$)** | 30.3 | 15.16 |
| **H desorption charge (mC/cm$^2$)** | 2.1 | 1.3 |
| **Electroactive Surface Area, EAS (cm$^2$/ cm$^2$)** | 10 | 6.19 |
| **Specific Surface Area, SSA (m$^2$/g)** | 33 | 40.83 |
| **Particle Size (nm) - Diameter** | 20 | 10 |

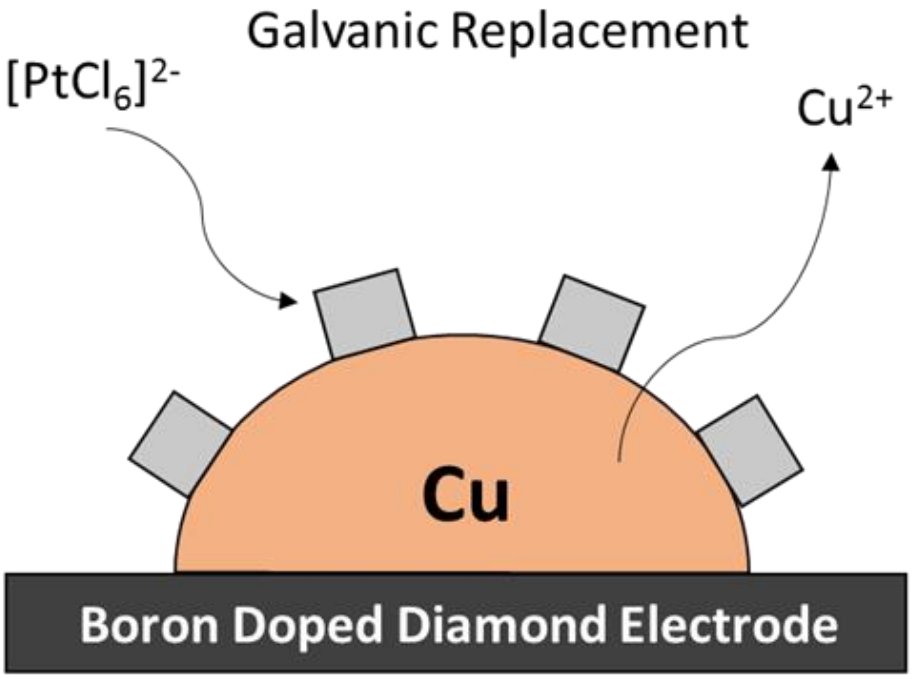


**Figure 3-7** Galvanic replacement or transmetallation.

## 3.4.1.3 Evaluation of Pt-Cu electrocatalysts preparation conditions on methanol oxidation characteristics

The BDD-supported Pt-Cu nanoparticles were evaluated for their catalytic activity towards the oxidation of methanol. The modified electrodes were placed in solutions containing 0.5M $H_2SO_4$ and 1M $CH_3OH$ and cyclic votammograms were obtained. The results are shown in figure 3-8 (a). There is no current response before +0.2V, which implies that the electrode was inactive until this overpotential was reached.

The electrode was activated at +0.65V (the "forward' peak), which represented the oxidation of the fresh methanol species. The electrode was deactivated at +1.0V and reactivated again at around +0.45V, giving a second oxidation wave the ("backward" peak) in the reverse scan as reported in literature[65,66] for incompletely oxidized carbonaceous species that accumulate on the surface. Experiments in which the concentration of the deposited nanoparticles were changed showed that the recorded current densities increased approximately monotonically with the particle concentration, showing under these experimental conditions the methanol oxidation process therefore seemed to be controlled by the concentration active sites at the electrode interface rather than being under diffusion control.

Compared to Pt-modified BDD, the Pt-Cu-modified BDD exhibited somewhat higher current densities for methanol oxidation in the "forward" peak as can be seen from figure 3-8 (a). However, the Pt loading for the pure Pt particles was up to twice as great than for the Pt-Cu structure. Therefore the Pt appears to be much more efficiently used in the Pt-Cu system, as well as more resistant to poisoning. The overall electrode activity that measured the resistance of the electrode to poisoning by the adsorbed incompletely carbonaceous species of the methanol was correlated to the ratio of the forward oxidation current peak ($I_f$) and the backward current peak ($I_b$)[67,68]. The larger $I_f/I_b$ ratio is, the larger the tolerance to poisoning the electrodes. From figure 3-8 (a) the Pt-Cu is clearly the more tolerant electrode. These properties may be due to the core-shell nanostructure offering better Pt dispersion and more favourable electronic properties than in its elemental state.

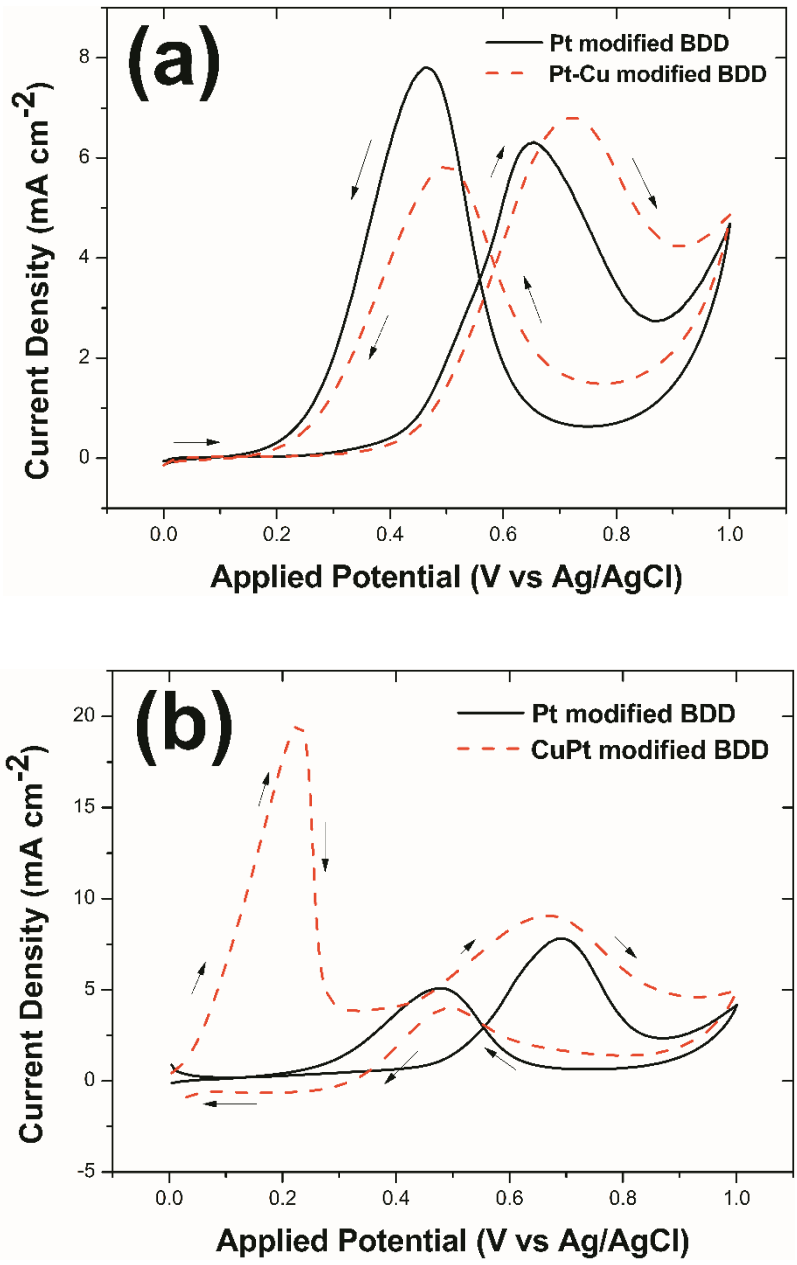


**Figure 3-8** (a) Cyclic voltammograms of Pt and Pt-Cu modified BDD in 0.5M $H_2SO_4$ and 1M $CH_3OH$ at scan rate of 0.1 V/s. (b) Cyclic voltammogram of Pt and CuPt modified BDD in 0.5M $H_2SO_4$ and 1M $CH_3OH$ at scan rate of 0.1 V/s.

A limited number of experiments were carried out to compare the effects of changing the order in which the metals were deposited. Data in figure 3-8 (b) was obtained from a Cu-Pt modified BDD, results are similar to those in figure 3-8 (a). This particular electrode is prepared by changing the order of the two metals deposition; namely, the Pt was deposited first, followed by Cu. As expected, the CV of the "inverted" electrode shows Cu stripping first

at +0.1V, followed by the two oxidation waves seen in figure 3-8 (a) and 3-8 (b). Clearly this structure is unstable under methanol oxidation conditions and the encapsulation of the Cu by the Pt is a crucial requirement to prevent the significant oxidative loss of Cu form the alloy particle.

## 3.4.2 Cu/BDD electrodes for glucose sensing

The second objective of this study was the fabrication of a non-enzymatic amperometric sensor based on a Cu-modified BDD electrode. Figure 3-9 (a) shows the cyclic voltammogram of Cu/BDD electrode in 0.1M KOH. For clarification reasons the amount of copper in this figure is larger than the similar one in figure 3-9 (b) in the absence of glucose and therefore it leads to higher current density and a slightly different pattern compared to its counterpart in figure 3-9 (b). Based on previous reports[69,70] the oxidation peaks correspond to Cu(I)/Cu(II) [$A_1$] and the reduction of Cu(II)/Cu(I) [$C_1$], respectively within superficial oxide/hydroxide layers that form on the Cu particles despite the deoxygenation of the electrolyte. Therefore, possible reaction mechanisms include[69,70]:

$$A_1:\ Cu_2O + 2OH^- \rightarrow 2CuO + H_2O + 2e^- \qquad (3\text{-}4)$$

$$CuO + H_2O \rightleftharpoons Cu(OH)_2 \qquad (3\text{-}5)$$

$$C_1:\ 2Cu(OH)_2 + 2e^- \rightarrow Cu_2O + 2OH^- + H_2O \qquad (3\text{-}6)$$

Based on this understanding of the behaviour of copper-modified BDD in alkaline media, figure 3-9 (b), which presents CVs of unmodified and Cu-modified BDD in the presence and absence of glucose within an aqueous solution of 0.1M KOH can be evaluated. For the unmodified electrode, no catalytic current response was observed. The result for Cu/BDD showed that the oxidation of glucose in alkaline media was possible.

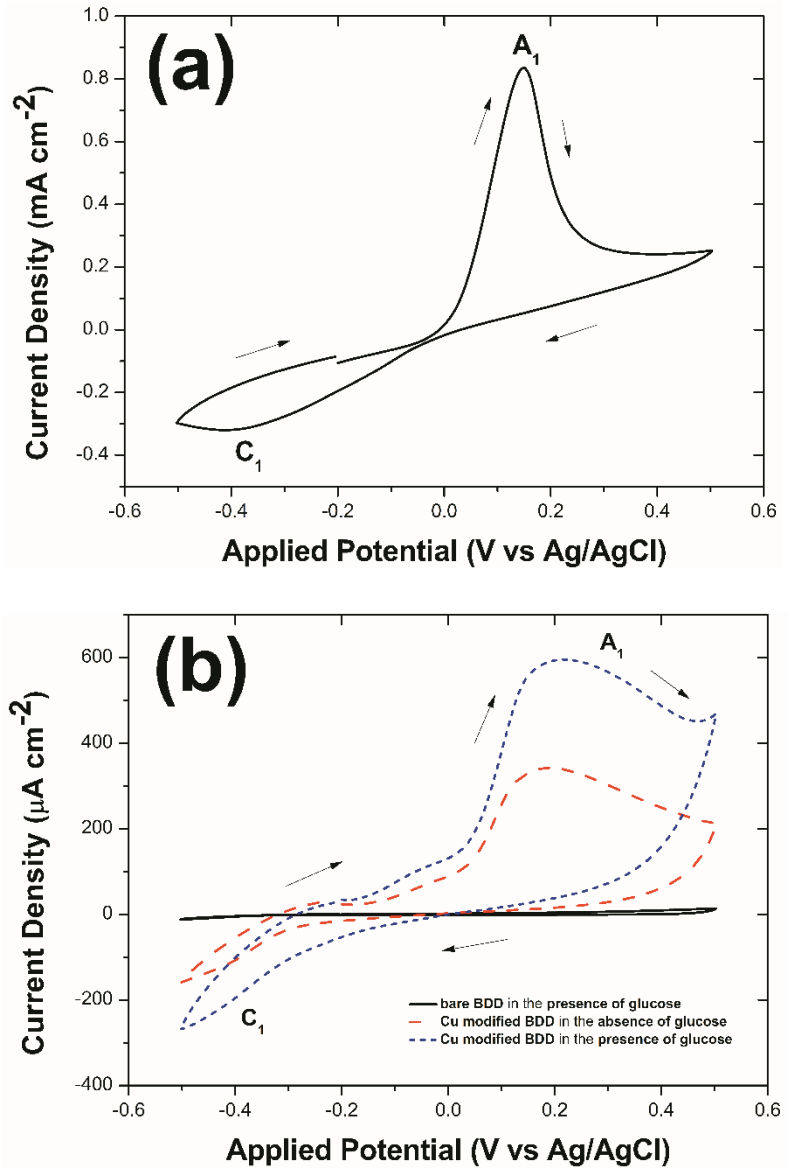


**Figure 3-9** (a) Cyclic voltammogram of Cu modified BDD in 0.1M KOH at scan rate 0.1 V/s. (b) Cyclic voltammograms of bare BDD in the absence and presence of 10mM glucose, Cu/BDD in the absence and presence of 10mM glucose in 0.1M KOH at scan rate of 0.1 V/s.

The electrochemical properties of the copper modified BDD was further evaluated by cyclic voltammetry (CV) in a pH 7 phosphate buffered solution. Figure 3-10 shows the responses of the Cu modified BDD electrode in the latter solution at sweeping scan rate between 0.025 V/s and 0.25 V/s. The cathodic and anodic peak currents were ascribed to electrochemical reactions including the Cu(I)/Cu(II) redox couple. Figure 3-10 (a) shows the cyclic voltammograms of Cu/BDD in PBS (pH 7) in the absence and presence of glucose at

various concentrations at scan rate of 0.025 V/s. The oxidation of glucose was observed only at the concentrations of 1 and 2.5 mM. The current responses at 5 and 10 mM of glucose were much lower than in the blank solution at this specific scan rate and therefore no glucose oxidation occured. In contrast, figure 3-10 (b) shows the cyclic voltammograms of Cu modified BDD in PBS (pH 7) at scan rate of 0.05 V/s. The current densities are higher than the one in the absence of glucose; however, the oxidation of glucose was not linear with the increase of glucose concentration. Rather a random behaviour was observed to take place. Figure 3-10 (c) illustrates the same electrode under the same conditions at scan rate of 0.1 V/s. On the one hand all the current densities were greater than the Cu/BDD in PBS in the absence of glucose but on the other hand the current responses were not high enough in order for a glucose oxidation to be considered. On the contrary, a superficial oxide/hydroxide layer might have formed concurrently on the Cu particles with glucose oxidation. Figure 3-10 (d) illustrates the Cu/BDD under exactly the same conditions at scan rate of 0.15 V/s. The current was higher in the presence of glucose but without a linear correlation of the oxidation current with the glucose concentration. Figures 3-10 (e) and (f) show the Cu modified BDD in pH 7 PBS solution at scan rates of 0.2 V/s and 0.25 V/s respectively. For the former scan rate only 10mM of glucose oxidation gave a considerable current response, whereas at a scan rate of 0.25 V/s, 5mM of glucose showed higher current density in comparison with lower concentrations.

Overall, two reactions appeared to have occurred simultaneously. The first reaction was the formation of superficial oxide/hydroxide layers onto the freshly prepared Cu particles and the second reaction was the oxidation of glucose. The formation of oxide layers prevented the oxidation current of glucose from associating linearly with the glucose concentration. All the aforementioned may suggest a surface passivation phenomenon in the presence of glucose on Cu modified BDD. As a result of this, the study focused on glucose sensing in a KOH supporting electrolyte.

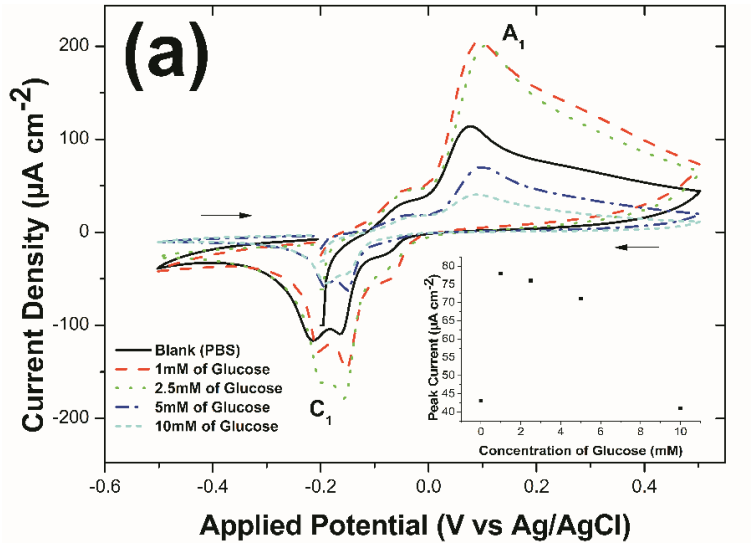
(a)
A1
C1
Blank (PBS)
1mM of Glucose
2.5mM of Glucose
5mM of Glucose
10mM of Glucose
Current Density (μA cm-2)
Applied Potential (V vs Ag/AgCl)
Peak Current (μA cm-2)
Concentration of Glucose (mM)

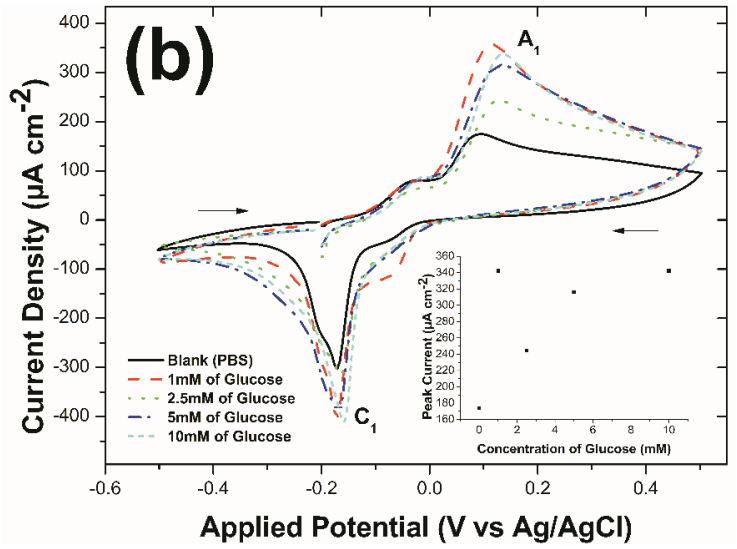
(b)
A1
C1
Blank (PBS)
1mM of Glucose
2.5mM of Glucose
5mM of Glucose
10mM of Glucose
Current Density (μA cm-2)
Applied Potential (V vs Ag/AgCl)
Peak Current (μA cm-2)
Concentration of Glucose (mM)

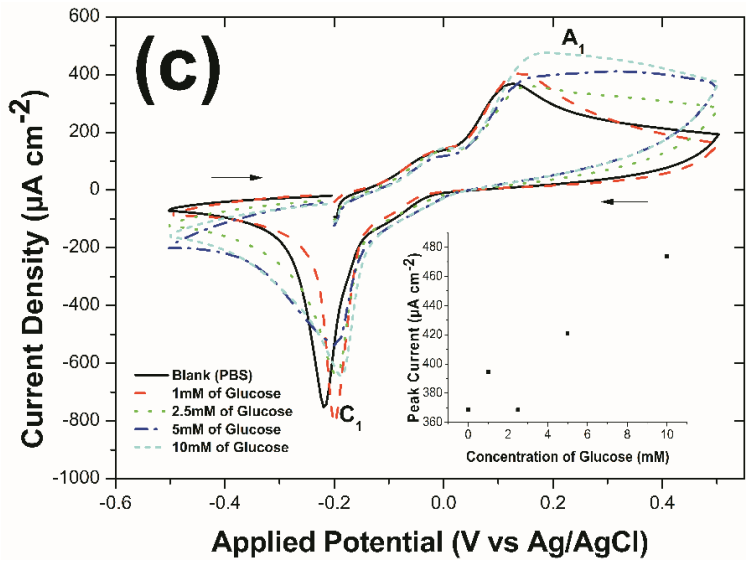
(c)
A1
C1
Blank (PBS)
1mM of Glucose
2.5mM of Glucose
5mM of Glucose
10mM of Glucose
Current Density (μA cm-2)
Applied Potential (V vs Ag/AgCl)
Peak Current (μA cm-2)
Concentration of Glucose (mM)

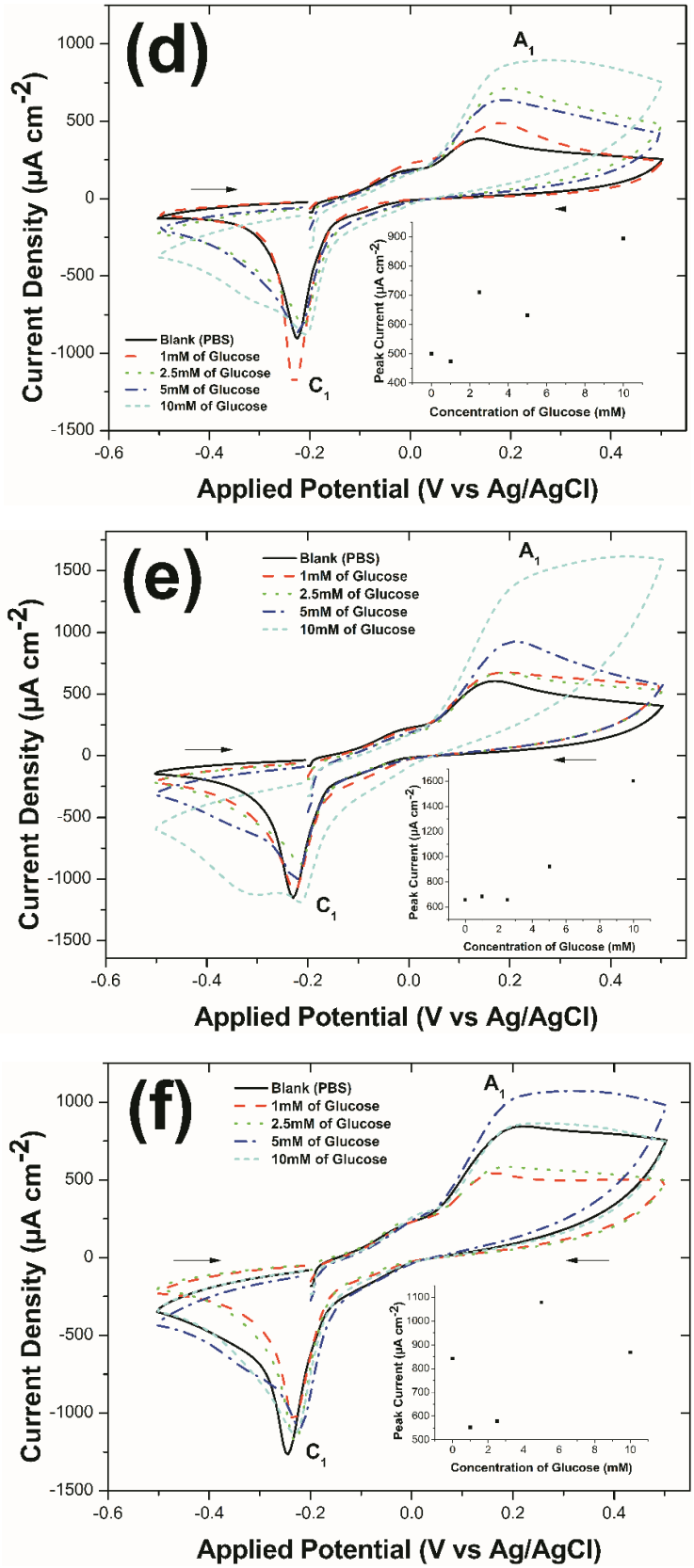


**Figure 3-10** Cyclic voltammograms of Cu modified BDD in PBS at (a) scan rate 0.025 V/s, (b) 0.05 V/s, (c) 0.1 V/s, (d) 0.15 V/s, (e) 0.2 V/s and (f) 0.25 V/s in the absence and presence of 1, 2.5, 5 and 10mM glucose respectively.

### 3.4.2.1 Amperometric detection of glucose with Cu/BDD electrodes

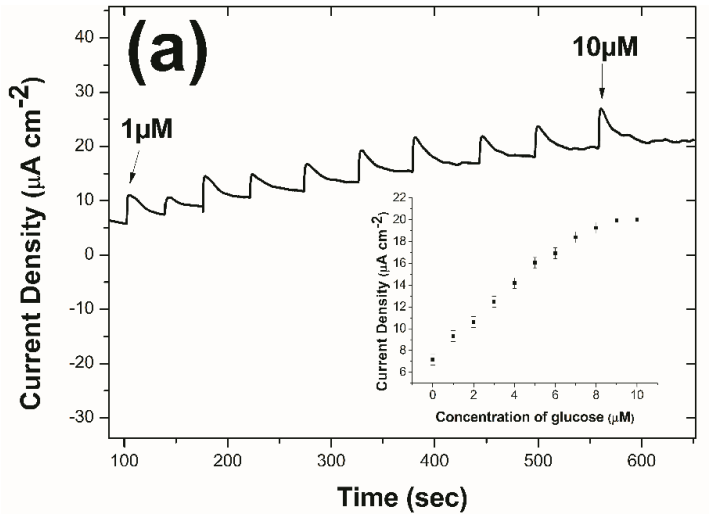


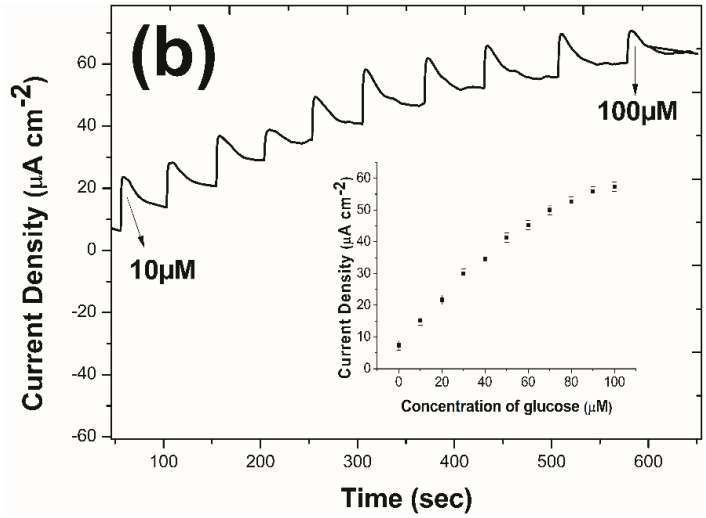


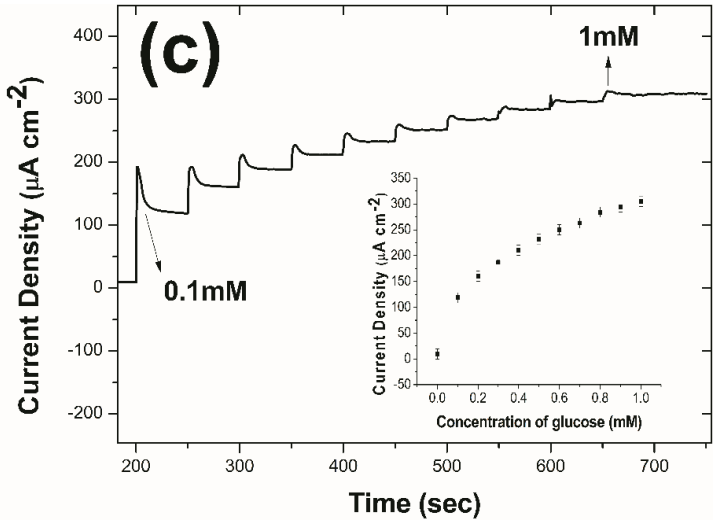

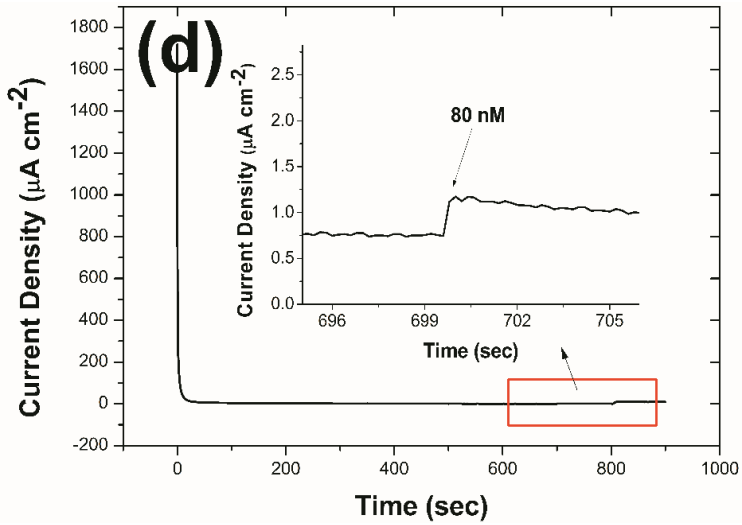


**Figure 3-11** (a) Amperometric responses of Cu/BDD in 0.1M KOH between the concentrations range of 1μM and 10μM, (b) 10μM and 100μM, (c) 0.1mM and 1mM and (d) 80nM. Inset shows the current vs concentration plot.

Chronoamperometry was performed to quantify the ability of Cu-modified BDD to oxidise glucose. A solution of 0.1M KOH was stirred, and glucose was added every 50 seconds varying (glucose) from 1μM to 10mM at a constant potential of +0.4V. The result is shown in figure 3-11. The amperometric response indicated that Cu/BDD was capable of detecting glucose at concentrations around 1μM; optimisation studies at low concentration to minimise electrode contamination indicated that concentrations less than 80nM were detectable (see figure 3-11 (d)). This is a very low limit of detection in comparison with other advanced electrodes[9], promising competitive performance from this electrode structure. The copper-supported BDD electrode had a linear response within defined concentration regions as well as good stability and reproducibility at these concentrations. However, loss of sensitivity gradually occured as the glucose concentration rose, which showed that the Cu nanoparticles were fouled by the glucose and its oxidation products were likely to be problematic at high concentration.

## 3.4.2.2 Stability and anti-interference test

The ability of the Cu/BDD to operate over a long period was demonstrated by the results in figure 3-12 (a). As the electrode was held at +0.4V, chronoamperometry was performed for 1800 seconds. The current density remained stable for this period. The results within figure 3-12 (a) also show that the Cu/BDD electrode had a fast response time (< 0.5 sec).

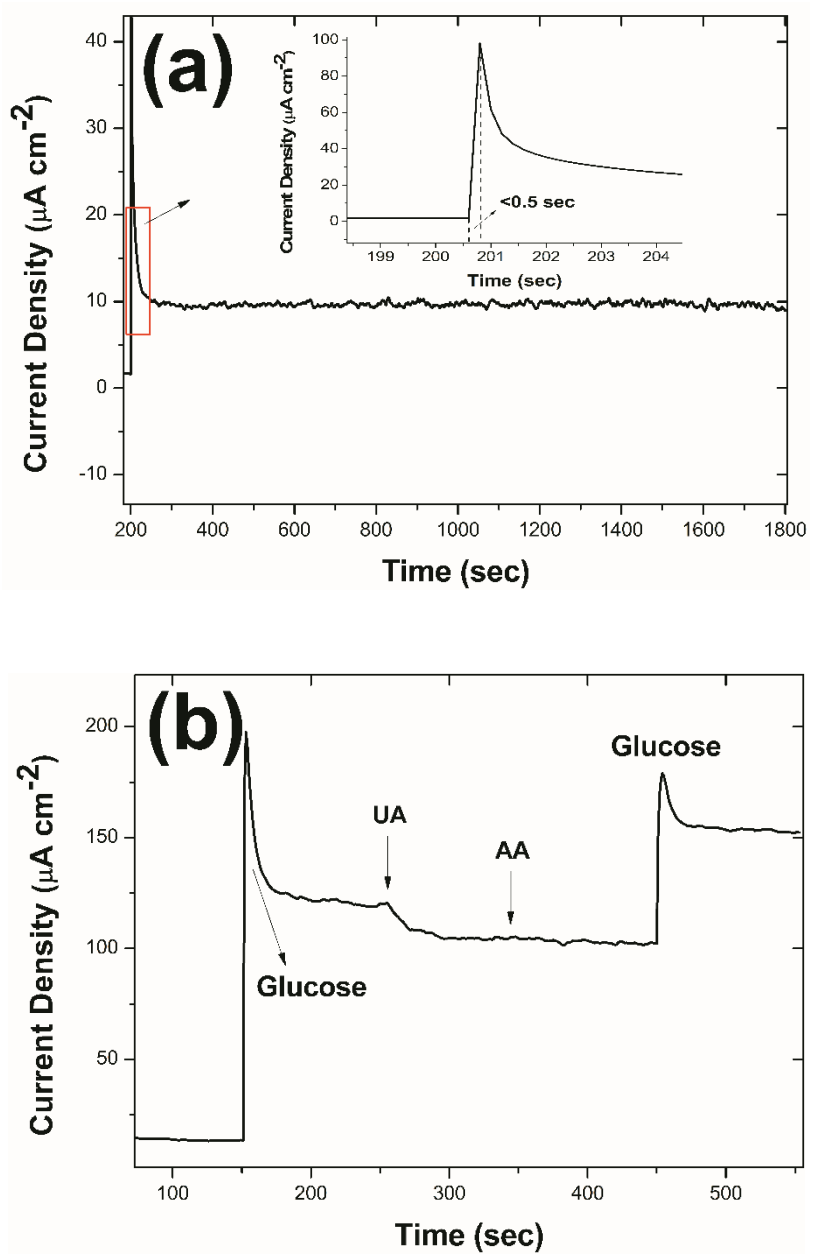


**Figure 3-12** (a) Stability test of the Cu/BDD in 0.1M KOH in the presence of 10μM glucose at +0.4V for 1800 sec and (b) anti-interference property of the Cu/BDD in the presence of 0.1mM glucose, 20μM UA and AA, respectively at +0.4V.

The ability of Cu/BDD to detect glucose in the presence of interferents was important to evaluate, as medical glucose tests are conducted in physiological media, in which easily oxidised species such as dopamine, ascorbic acid, uric acid and carbohydrate compounds usually co-exist. The electrochemical response of Cu/BDD in the presence of two species known to have high physiological concentration, ascorbic acid (AA) and uric acid (UA), was checked by fixing their concentrations at 20μM and attempting to detect glucose. The current density responses from the interferents within such a mixed solution was found to be negligible (see Figure 3-12 (b)). The concentration of glucose is normally greater by thirty times greater compared to the concentration of other interfering species in body fluids; therefore good selectivity should be displayed by this Cu/BDD sensor[71]. Figure 3-12 (b) shows that the injection of UA actually decreases the measured current, which may be due to some partial fouling of the Cu nanoparticles on the electrode surface by UA.

# 3.5 Conclusions

The fabrication of diamond electrodes modified with Pt-Cu and Cu nanoparticles by use of electrodeposition techniques was explored. A two-step, potentiostatic deposition process in which Cu was deposited first, followed by Pt was used to make the bimetallic electrode. XPS and electrochemical evidence suggests that Pt was preferentially deposited onto the Cu particles at the diamond surface to form Pt-Cu core-shell structures. This has been shown this to occur as a joint result of potentiostatic deposition and spontaneous galvanic replacement of Cu by Pt. Methanol oxidation by Pt-Cu/BDD electrodes occured with higher current densities and with less electrode fouling than the Pt only BDD electrode. This is likely to arise from a better dispersion of Pt due to surface coating the deposited Cu nanoparticles and due to electronic modifications of the Pt through the interaction with the underlying Cu. The pure Cu/BDD electrode was tested for glucose sensing and may be a simple, robust, and

cost-effective route towards an advanced glucose sensor. The Cu/BDD showed high sensitivity and current density response to glucose oxidation in KOH. The electrode presented good reproducibility and stability. Finally, amperometric glucose sensors must be able to separate any interfering species from the target analyte; Cu/BDD electrode showed a good selectivity towards glucose in KOH even imn mixed solutions. These two modified electrodes have electrochemical advantages that may be of benefit for their future use in fuel cell or biosensing applications.

# 3.6 Bibliography

1. Bouilov LL, Spitsyn BV, Krotova MD. Photoelecfrochemical properties of semiconductor diamond. *J. Electroanal. Chem.* 1987;228:19–27.

2. Rao TN, Fujishima A. Recent advances in electrochemistry of diamond. *Diam. Relat. Mater*. 2000;9(3-6):384–389. doi:10.1016/S0925-9635(99)00234-4.

3. Swain GM. *Thin-Film Diamond II*. Elsevier, San Diego, 2004:121-148. doi:10.1016/S0080-8784(04)80016-4.

4. Shpilevaya I, Smirnov W, Hirsz S, Yang N, Nebel CE, Foord JS. Nanostructured diamond decorated with Pt particles: preparation and electrochemistry. *RSC Adv*. 2014;4(2):531. doi:10.1039/c3ra43763a.

5. Chen L, Hu J, Foord JS. Electrodeposition of a Pt-$PrO_{2-x}$ electrocatalyst on diamond electrodes for the oxidation of methanol. *Phys. Status Solidi*. 2012;209(9):1792–1796. doi:10.1002/pssa.201200049.

6. Kraft A, Doped Diamond : A Compact Review on a New, Versatile Electrode Material. *J. Electrochem. Sci.* 2007;2:355–385.

7. Lu X, Hu J, Foord JS, Wang Q. Electrochemical deposition of Pt–Ru on diamond electrodes for the electrooxidation of methanol. *J. Electroanal. Chem*. 2011;654(1-2):38–43. doi:10.1016/j.jelechem.2011.01.034.

8. McCreery RL. Advanced carbon electrode materials for molecular electrochemistry. *Chem. Rev*. 2008;108(7):2646–87. doi:10.1021/cr068076m.

9. Toghill KE, Compton RG. Electrochemical Non-enzymatic Glucose Sensors : A Perspective and an Evaluation. *Int. J. Electrochem. Sci.* 2010;5:1246–1301.

10. Compton RG, Foord JS, Marken F. Electroanalysis at Diamond-Like and Doped-Diamond Electrodes. *Electroanalysis*. 2003;15(17):1349–1363. doi:10.1002/elan.200302830.

11. Ivandini TA, Sato R, Makide Y, Fujishima A, Einaga Y. Electrochemical Detection of Arsenic (III) Using Electrodes. *Anal. Chem.* 2011;78(18):6291–6298.

12. Toghill KE, Compton RG. Metal Nanoparticle Modified Boron Doped Diamond Electrodes for Use in Electroanalysis. *Electroanalysis*. 2010;22(17-18):1947–1956. doi:10.1002/elan.201000072.

13. Panizza M, Cerisola G. Application of diamond electrodes to electrochemical processes. *Electrochim Acta*. 2005;51(2):191–199. doi:10.1016/j.electacta.2005.04.023.

14. Swain GM, Anderson AB, Angus JC. Applications of Diamond Thin Films in Electrochemistry. *MRS Bulletin* 1998;(September):56-60.

15. Wei M, Terashima C, Lv M, Fujishima A, Gu ZZ. Boron-doped diamond nanograss array for electrochemical sensors. *Chem. Commun*. 2009;(24):3624–6. doi:10.1039/b903284c.

16. Lv M, Wei M, Rong F, Terashima C, Fujishima A, Gu ZZ. Electrochemical Detection of Catechol Based on As-Grown and Nanograss Array Boron-Doped Diamond Electrodes. *Electroanalysis*. 2010;22(2):199–203. doi:10.1002/elan.200900296.

17. Szunerits S, Coffinier Y, Galopin E, Brenner J, Boukherroub R. Preparation of boron-doped diamond nanowires and their application for sensitive electrochemical detection of tryptophan. *Electrochem. commun*. 2010;12(3):438–441. doi:10.1016/j.elecom.2010.01.014.

18. Daibing L, Liangzhuan W, Jinfang Z. Fabrication of Boron-Doped Diamond Nanorod Forest Electrodes and Their Application in Nonenzymatic Amperometric Glucose Biosensing. *ACS Nano.* 2009;3(8):2121–2128.

19. Antonio M, Alfaro Q, Ferro S, Martínez-huitle CA, Vong YM. Boron Doped Diamond Electrode for the Wastewater Treatment. *Chem. Soc.* 2006;17(2):227–236.

20. Hamnett A. Mechanism and electrocatalysis in the direct methanol fuel cell. *Catal. Today*. 1997;38(4):445–457. doi:10.1016/S0920-5861(97)00054-0.

21. http://www.fuelcelltoday.com/technologies/dmfc.

22. Oliveira CA, Stein MF, Saito E, Zanin H, Vieira LS, Raniero L, Trava-Airoldi VJ, Lobo AO, Marciano FR. Effect of gold oxide incorporation on electrochemical corrosion resistance of diamond-like carbon. *Diam. Relat. Mater*. 2015;53:40–44. doi:10.1016/j.diamond.2015.01.009.

23. Ramos BC, Saito E, Trava-Airoldi VJ, Lobo AO, Marciano FR. Diamond-like carbon electrochemical corrosion resistance by addition of nanocrystalline diamond particles for biomedical applications. *Surf. Coatings Technol*. 2014;259:732–736. doi:10.1016/j.surfcoat.2014.09.066.

24. Nart FC, Iwasita T. On the adsorption of sulfate species on polycrystalline platinum An FTIR study in fluoride base electrolyte. *J. Electroanal. Chem.* 1991;308:277–293.

25. Zhong CJ, Luo J, Fang B, Nanostructured catalysts in fuel cells. *Nanotechnology*. 2010;21(6):062001. doi:10.1088/0957-4484/21/6/062001.

26. Wei ZD, Feng YC, Li L, Wanzala N, Njoki PN, Loukrakpam R, Yin G, Electrochemically synthesized Cu/Pt core-shell catalysts on a porous carbon electrode for polymer electrolyte membrane fuel cells. *J. Power Sources*. 2008;180(1):84–91. doi:10.1016/j.jpowsour.2008.01.086.

27. Hsu C, Huang C, Hao Y, Liu F. Synthesis of highly active and stable Au-PtCu core-shell nanoparticles for oxygen reduction reaction. *Phys Chem Chem Phys*. 2012;14(42):14696–701. doi:10.1039/c2cp42716h.

28. Kristian N, Yu Y, Lee JM, Liu X, Wang X. Synthesis and characterization of Cocore–Ptshell electrocatalyst prepared by spontaneous replacement reaction for oxygen reduction reaction. *Electrochim. Acta*. 2010;56(2):1000–1007. doi:10.1016/j.electacta.2010.09.073.

29. Ge X, Chen L, Kang J, Fujita T, Hirata A, Jiang J, Chen M. A Core-Shell Nanoporous Pt-Cu Catalyst with Tunable Composition and High Catalytic Activity. *Adv. Funct. Mater*. 2013;23(33):4156–4162. doi:10.1002/adfm.201300114.

30. Strasser P, Koh S, Anniyev T, Greely J, More K, Yu C, Liu Z, Kaya S, Nordlund D, Ogasawara H, Toney M, Nilsson A. Lattice-strain control of the activity in dealloyed core-shell fuel cell catalysts. *Nat. Chem*. 2010;2(6):454–60. doi:10.1038/nchem.623.

31. Hu J, Lu X, Foord JS. Nanodiamond pretreatment for the modification of diamond electrodes by platinum nanoparticles. *Electrochem. commun*. 2010;12(5):676–679.

doi:10.1016/j.elecom.2010.03.004.

32. Wild S, Roglic G, Green A, Sicree R, King H. Estimates for the year 2000 and projections for 2030. *World Health*. 2004;27(5):1047–1053.

33. Cheng X, Zhang S, Zhang H, Wang Q, He P, Fang Y. Determination of carbohydrates by capillary zone electrophoresis with amperometric detection at a nano-nickel oxide modified carbon paste electrode. *Food Chem.* 2008;106(2):830–835. doi:10.1016/j.foodchem.2007.06.063.

34. Prilutsky S, Schechner P, Bubis E, Makarov V, Zussman E, Cohen Y. Anodes for glucose fuel cells based on carbonized nanofibers with embedded carbon nanotubes. *Electrochim. Acta*. 2010;55(11):3694–3702. doi:10.1016/j.electacta.2010.02.005.

35. Davis F, Higson SPJ. Biofuel cells-recent advances and applications. *Biosens. Bioelectron*. 2007;22(7):1224–35. doi:10.1016/j.bios.2006.04.029.

36. Kerzenmacher S, Ducrée J, Zengerle R, von Stetten F. Energy harvesting by implantable abiotically catalyzed glucose fuel cells. *J. Power Sources*. 2008;182(1):1–17. doi:10.1016/j.jpowsour.2008.03.031.

37. Jin C, Taniguchi I. Electrocatalytic activity of silver modified gold film for glucose oxidation and its potential application to fuel cells. *Mater. Lett*. 2007;61(11-12):2365–2367. doi:10.1016/j.matlet.2006.09.013.

38. Schechner P, Kroll E, Bubis E, Chervinsky S, Zussman E. Silver-Plated Electrospun Fibrous Anode for Glucose Alkaline Fuel Cells. *J. Electrochem. Soc*. 2007;154(9):B942. doi:10.1149/1.2752975.

39. Appleby AJ, Van Drunen C. Anodic Oxidation of Carbohydrates and Related Compounds in Neutral Saline Solution. *J. Electrochem. Soc*. 1971;118(1):95. doi:10.1149/1.2407962.

40. Uchikado R, Rao TN, Tryk DA, Fujishima A. Metal-Modified Diamond Electrode as an Electrochemical Detector for Glucose. *Chem. Lett*. 2001;30(2):144–145. doi:10.1246/cl.2001.144.

41. Zhao J, Tian R, Zhi J. Electroless deposition of copper and fabrication of copper micropatterns on CVD diamond film surfaces. *Appl. Surf. Sci*. 2008;254(11):3282–3287. doi:10.1016/j.apsusc.2007.11.008.

42. Chiku M, Watanabe T, Einaga Y. Fabrication of Cu-modified boron-doped diamond

microband electrodes and their application for selective detection of glucose. *Diam. Relat. Mater*. 2010;19(7-9):673–679. doi:10.1016/j.diamond.2010.01.048.

43. Ivandini TA, Sato R, Makide Y, Fujishima A, Einaga Y. Electroanalytical application of modified diamond electrodes. *Diam. Relat. Mater*. 2004;13(11-12):2003–2008. doi:10.1016/j.diamond.2004.07.004.

44. Watanabe T, Ivandini TA, Makide Y, Fujishima A, Einaga Y. Selective detection method derived from a controlled diffusion process at metal-modified diamond electrodes. *Anal. Chem*. 2006;78(22):7857–7860. doi:10.1021/ac060860j.

45. https://leadwayservice.wordpress.com/2013/01/01/non-invasive-gluco-meter/blood-glucose-meter/.

46. http://www.casaxps.com/.

47. Taylor RI. X-Ray Photoemission Spectra of Crystalline and Amorphous Si and Ge Valence Bands. *Phys. Rev. Lett*. 1972;29(16):1088–1092.

48. Cardwell TJ, Mocaka J, Santosa JH, Bondb AM. Preparation of Microelectrodes : Comparison of Polishing Procedures by Statistical Analysis of Voltammetric Data. *Analyst*. 1996;121:357-362.

49. Welch CM, Simm AO, Compton RG. Oxidation of Electrodeposited Copper on Boron Doped Diamond in Acidic Solution: Manipulating the Size of Copper Nanoparticles Using Voltammetry. *Electroanalysis*. 2006;18(10):965–970. doi:10.1002/elan.200603493.

50. Yagi I, Ishida T, Uosaki K. Electrocatalytic reduction of oxygen to water at Au nanoclusters vacuum-evaporated on boron-doped diamond in acidic solution. *Electrochem. commun*. 2004;6(8):773–779. doi:10.1016/j.elecom.2004.05.025.

51. Wagner CD, Riggs WM, Davis LE, Moulder JF, and Muilenburg GE, Handbook of X-ray Photoelectron Spectroscopy (Perkin-Elmer Co., Minnesota, 1979).

52. http://srdata.nist.gov/xps/Default.aspx.

53. Hyde ME, Banks CE, Compton RG. Anodic stripping voltammetry: An AFM study of some problems and limitations. *Electroanalysis*. 2004;16(5):345–354. doi:10.1002/elan.200302863.

54. Pozio A, Francesco M De, Cemmi A, Cardellini F, Giorgi L. Comparison of high surface Pt/C catalysts by cyclic voltammetry. *J. Power Sources*. 2002;105:13–19.

55. Feltham AM, Spiro M. Platinized Platinum Electrodes. *Chemical Reviews*, 1970;71(2):177-193.

56. Kulp C, Gillmeister K, Widdra W, Bron M. Synthesis of Cu(core) Pt(shell) nanoparticles as model structures for core-shell electrocatalysts by direct platinum electrodeposition on copper. *Chemphyschem*. 2013;14(6):1205–10. doi:10.1002/cphc.201200891.

57. Kloke A, Köhler C, Gerwig R, Zengerle R, Kerzenmacher S. Cyclic electrodeposition of PtCu alloy: facile fabrication of highly porous platinum electrodes. *Adv. Mater*. 2012;24(21):2916–21. doi:10.1002/adma.201200806.

58. Georgieva J, Valova E, Mintsouli I, Sotiropoulos S, Armyanov S, Kakaroglou A, Hubin A, Steenhaut O, Dille J. Carbon-supported Pt(Cu) electrocatalysts for methanol oxidation prepared by Cu electroless deposition and its galvanic replacement by Pt. *J. Appl. Electrochem*. 2013;44(2):215–224. doi:10.1007/s10800-013-0618-2.

59. Bagotsky VS. *Fundamentals of electrochemistry*. Russian Academy of Sciences, Moscow, Russia, 2005. doi:10.1385/1-59259-877-3:003.

60. Wang JX, Inada H, Wu L, Zhu Y, Choi Y, Liu P, Zhou W, Adzic R. Oxygen reduction on well-defined core-shell nanocatalysts: Particle size, facet, and Pt shell thickness effects. *J. Am. Chem. Soc*. 2009;131(18):17299–17302. doi:10.1021/ja9067645.

61. Adzic RR, Zhang J, Sasaki K, Vukmirovic MB, Shao M, Wang JX, Nilekar AU, Mavrikakis M, Valerio JA, F. Uribe. Platinum Monolayer Fuel Cell Electrocatalysts. *Top Catal*. 2007;46(3-4):249–262. doi:10.1007/s11244-007-9003-x.

62. Geboes B, Mintsouli I, Wouters B, Vukmirovic MB, Shao M, Wang JX, Nilekar AU, Mavrikakis M, Valerio JA, Uribe F. Surface and electrochemical characterisation of a Pt-Cu/C nano-structured electrocatalyst, prepared by galvanic displacement. *Appl. Catal. B Environ*. 2014;150-151:249–256. doi:10.1016/j.apcatb.2013.12.020.

63. Papadimitriou S, Armyanov S, Valova E, Hubin A, Steetnhaut O, Pavlidou E, Kokkinidis G, Sotiropoulos S. Methanol Oxidation at Pt-Cu , Pt-Ni , and Pt-Co Electrode Coatings Prepared by a Galvanic Replacement Process. *J. Phys. Chem. C* 2010:114 (11):5217–5223.

64. Sarkar A, Manthiram A. Synthesis of Pt@Cu Core-Shell Nanoparticles by Galvanic Displacement of Cu by $Pt^{4+}$ Ions and Their Application as Electrocatalysts for Oxygen

Reduction Reaction in Fuel Cells. *J. Phys. Chem.* 2010:4725–4732.

65. Li F, Guo Y, Chen M, Qiu H, Sun X, Wang W, Liu Y, Gao J. Comparison study of electrocatalytic activity of reduced graphene oxide supported Pt–Cu bimetallic or Pt nanoparticles for the electrooxidation of methanol and ethanol. *Int. J. Hydrogen Energy*. 2013;38(33):14242–14249. doi:10.1016/j.ijhydene.2013.08.093.

66. Qi Y, Bian T, Choi SI, Jiang Y, Jin C, Fu M, Zhang H, Yang D. Kinetically controlled synthesis of Pt-Cu alloy concave nanocubes with high-index facets for methanol electro-oxidation. *Chem. Commun*. 2014;50(5):560–2. doi:10.1039/c3cc48061e.

67. Chen M, Wang ZB, Ding Y, Yin GP. Investigation of the Pt–Ni–Pb/C ternary alloy catalysts for methanol electrooxidation. *Electrochem. commun*. 2008;10(3):443–446. doi:10.1016/j.elecom.2008.01.012.

68. Knudsen J, Nilekar AU, Vang RT, Schnadt J, Kunkes EL, Dumesic JA, Mavrikakis M, Besenbacher F. A Cu/Pt Near-Surface Alloy for Water-Gas Shift Catalysis. *J. Am. Chem. Soc.* 2007;(3):3838–3842.

69. Le WZ, Liu YQ. Preparation of nano-copper oxide modified glassy carbon electrode by a novel film plating/potential cycling method and its characterization. *Sensors Actuators B Chem*. 2009;141(1):147–153. doi:10.1016/j.snb.2009.05.037.

70. Priya S, Berchmans S. CuO Microspheres Modified Glassy Carbon Electrodes as Sensor Materials and Fuel Cell Catalysts. *J. Electrochem. Soc*. 2012;159(4):F73. doi:10.1149/2.087204jes.

71. Zhuang Z, Su X, Yuan H, Sun Q, Xiao D, Choi MF. An improved sensitivity non-enzymatic glucose sensor based on a CuO nanowire modified Cu electrode. *Analyst*. 2008;133(1):126–32. doi:10.1039/b712970j.

# Chapter 4

# Electrochemical modification of Au (111) and Diamond electrodes with Pd nanoparticles for Ethanol Electrooxidation

## 4.1 Introduction

Noble metal nanoparticles (NPs) usually smaller than 10 nm exhibit better electrocatalytic and electronic properties than their bulk counterparts due to their special shape, size and surface morphology[1–4]. Palladium (Pd) NPs have received considerable interest in recent years due to their application in various electrocatalytic processes such as in organic synthesis[5,6], pharmaceuticals[7], hydrogenation of unsaturated hydrocarbons[8,9], hydrogen storage[10–12], bio-electrochemical sensors[13,14], cancer treatment[15], fuel cells[16–19] and co-catalysts in photocatalysis[20–22]. Controlling the shape and/or surface of metal NPs is crucial to their exploitation in specific applications from catalysis to chemical sensing and drug manufacturing[1,3,4,23]. To date, various synthetic approaches such as the reduction of metal salts or the decomposition of organometallic compounds have been investigated as feasible routes to the synthesis of noble metal NPs[24–30]. Organic functional reagents such as polymers, surfactants and ionic liquids are generally used in these wet chemical syntheses to control the morphology, dispersibility and stabilisation of NPs in the homogeneous solution phase. The actual size of synthetic NPs varies with the to method since the final formation is not controlled

by a single parameter, but instead by the complex and combined effects of the surfactant, reducing agent, solvent, species concentrations, temperature and reaction time.

Another popular approach is the seed-mediated growth method, in which target NPs are grown from a solution of seeding NPs of a given crystallite or shape, metal precursor salt and a mild reducing agent[31,32]. Recently, ad-atoms were reported to not remain on the same crystal planes upon deposition, but move to other crystallite planes due to self-surface diffusion processes[33]. This phenomenon often disrupts the growth mode and therefore, the final shape or morphology of the NPs. Although homogeneous dispersion of Pd NPs has been achieved in the seeding strategies or in some of the wet chemical synthetic methods referred to above, the capability to synthesise well-defined shape and highly dispersed Pd NPs of less than 10 nm dimensions has yet to be achieved. Additionally, advanced electrocatalysis/electroanalysis based on Pd requires the Pd NPs to be conductive thin film format to miniaturise the overall electrode and device dimension, particularly for handheld and portable devices. In particular, there is an increasing interest in the complementary metal–oxide–semiconductor (CMOS) compatible electrodeposition method that meets the underlined demand of synthetic Pd NPs with high dispersibility, large surface-to-volume ratio and enhanced atomic surface distribution. Among these, a direct electrodeposition method based on a sacrificial anode has been demonstrated to synthesise size-selective Pd NPs in an organic electrolyte[34,35]. Under an applied current or potential, the bulk metallic Pd at the anode is dissolved as $Pd^{2+}$ ions, which then migrate/diffuse to the cathode where they are reduced as ad-atoms. The size of the NPs can be controlled via a number of parameters such as solvent polarity, current density, charge flow, distance between electrodes, etc[34]. This method is further improved by the direct electroreduction of metal precursor salts in aqueous electrolytes i.e., metallic ions are directly provided by electrolyte rather than the sacrificial anode[36–39]. Despite the improvement, an inherent drawback to the method consists of the two competing processes that occur at the

cathode; one is the reduction of metal ions to NPs and the other is the reduction of the ions to form a metallic film[40]. To shift the balance in favour of NPs growth, a surfactant is typically used to enhance the rate of NPs formation rather than the metallic thin film deposition.The choice of surfactant is crucial to stabilising the metal ions as nanoclusters in the solution phase, which prevents precipitation as solid metal before the ions reach the cathode. The molecular nature of the surfactant, however, strongly affects the size and dispersibility of the synthesised metallic NPs. Moreover, to find a suitable surfactant for the specific size-selective synthesis of metal NPs is not always possible.

Here, an overpotential dependent growth of Pd metallic NPs on Au (111) and diamond substrates by electrodeposition from a surfactant-free "green" electrolyte is reported. The growth modes of Pd NPs were analysed in details and correlated with their electrocatalytic performance. The electrolyte consisted of $PdCl_2$ as the precursor ion source in an aqueous and mildly acidic environment at room temperature allowing sufficient time to form a ligand-stabilised coordinated complex $[PdCl_4]^{2-}$, in which $Pd^{2+}$ ions were stabilised by the ligand effects of $Cl^-$ ions, or $H_2O$ or both depending on the electrolyte pH. For the case of Au (111) substrates, the effects of the applied overpotential and deposition duration were systematically investigated for their influence on the nucleation, growth, size and morphology of the Pd NPs, while other parameters, such as precursor concentration and pH of the electrolyte were kept constant. For the diamond electrodes, the chemical surface terminations affect on the size and the distribution of the particles and eventually the overall conductivity and electrocatalytic activity were examined. To separate the hydrogen adsorption/absorption and evolution effects from the electrodeposition process, the overpotential for Pd deposition was maintained positive relative to the potential of the underpotential hydrogen deposition ($H_{UPD}$).

# 4.2 Aims of the project and principal outcomes

Comprehension of the electrochemical nucleation and growth mechanism of nanoparticles is extremely important, especially given the strong influence on nanoparticle size distribution, crystal structure and surface morphology this mechanism exerts. These parameters in turn determine the electrocatalytic properties of the NPs. In this study, the early stage electrochemical nucleation and growth of palladium nanoparticles (Pd NPs) under potentiostatic control has been investigated on a single crystalline Au (111) substrate. The size distribution and surface structure of the ex-situ as-deposited Pd NPs were investigated by means of high resolution Scanning Electron Microscopy. Together with the electrochemical measurements, the clusters of nuclei were revealed grew either by the fresh reduction of ions or by the aggregative growth mechanism. This finding contradicts the classical theories for electrochemical nucleation and growth that proceed only by the fresh reduction of ions. The electrochemical nucleation and growth at the early stages was demonstrated to be overpotential dependent and in fact proceed either by the fresh reduction of ions when deposited at lower overpotential or by the aggregation of small clusters through surface diffusion when deposited at relatively higher overpotential. The electrodeposited Pd NPs were very pure as confirmed by X-ray Photoelectron Spectroscopy due to the surfactant-free green electrodeposition process and highly dispersed with an average particle size below 5 nm. The density of small size particles increases with the overpotential except where particles grow by aggregation as the dominant mechanism. The synthesised Pd NPs demonstrated a large specific surface area (4 times larger than commercial Pd-C) and electrocatalytic activity in ferrocyanide/ferricyanide redox and ethanol electrooxidation processes (35 times larger signal than commercial Pd-C). This work represents an important step in achieving and redefining a fundamental

understanding of the nucleation and growth mechanism of nanoparticles, a mechanism that is correlated to the electrocatalytic performances.

Diamond electrodes possess stable chemical terminations and the second objective of this work was to understand of the deposition of Pd NPs on oxygen (BDD) and hydrogen (HBDD) terminated boron-doped diamond electrodes. The hydrogen-terminated surface was determined to be more conductive than the oxygen-terminated surface which led to better distribution of nanoparticles. The surface termination also affects the size of the particles which leads to higher electrocatalytic activity and less poisoning effect towards ethanol oxidation. The morphology, the elemental composition and electrochemical characterisation were measured with SEM, XPS and cyclic voltammetry respectively.

# 4.3 Experimental section

## 4.3.1 Chemical reagents

Chemical reagents were purchased from Sigma-Aldrich and used as received without any further purification. These were: palladium (II) chloride ($PdCl_2$); and hydrochloric acid (HCl). All aqueous solutions were freshly prepared, using milli-Q water (18 MΩ cm). All the solutions were deoxygenated using nitrogen gas for a minimum of 20 minutes when the experiments required oxygen-free solutions.

## 4.3.2 Equipment and experimental set-up

Au (111) single crystal of 10 nm thickness was deposited by a sputtering process on a $Ti/SiO_2/Si$ wafer. The underlying layers of Ti (10 nm) and $SiO_2$ (500 nm) were deposited by a similar physical method on Si wafer to improve the adhesion of Au and to create an electrical conductivity barrier with the semiconducting Si, respectively. For discussion purposes, the

electrode is referred to as a Au (111) substrate only. The wafer was diced into 15 mm x 5 mm pieces and a diced coupon with the area of 0.6 $cm^2$ (12 mm x 5 mm) was immersed in the electrolyte for deposition. The remaining 3 mm at the top of the coupon was left for electrical connection to the potentiostat. The diced Au electrodes were cleaned by sonication in isopropyl alcohol for 1 hour and dried under $N_2$ gun prior to each of the Pd deposition experiments.

BDD wafers ([B]>$10^{20}$ $cm^{-3}$) of 10 x 10 x 0.6 mm were obtained from Element Six Co (UK) and mounted in a home-built PTFE holder with a circular area of 0.38 $cm^2$ exposed to the electrolyte. The electrochemical measurements were performed with an Autolab PGSTAT 128N potentiostat/galvanostat. The electrochemical depositions were conducted at room temperature (24 ± 1.0°C), with a standard three electrode cell made of a Pt counter electrode, a Ag/AgCl and Hg/HgO reference electrodes. The analysis was done with OriginPro 8.5 software (OriginLab Ltd.). Scanning Electron Microscopy images were obtained using a high resolution Field Emission Gun–Scanning Electron Microscope (FEGSEM), LEO Gemini 1525. The images were taken at 400K magnification with an extraction voltage of 15 kV, a working distance (WD) of 5 mm and were captured with the resolution of about 2.5 pixels per nm. The morphology of the deposits on diamond electrodes was characterised by a Hitachi S530 and Zeiss SEM with a 20kV and 5kV acceleration voltage, respectively. The size of the Pd NPs was analyzed with ImageJ[41]. X-ray diffraction (XRD) analysis was carried out with a Philips X'pert PW3710-MPD diffractometer using filtered Cu-Kα (λ = 1.54 Å) radiation operated at 40 kV and 40 mA. The composition of the deposits was measured by X-ray Photoelectron Spectroscopy (XPS) using an Al Kα (1486.6 eV) X-ray source. XPS data were curve fitted using CasaXPS software and a Shirley background[42]. The C 1s peak was calibrated to 285 eV with the following relative sensitivity factors (R.S.F.): C 1s (1.0), O 1s (2.93) and Pd 3d (16.0).

## 4.3.3 Fabrication and working electrodes

### 4.3.3.1 Modification of Au (111) electrodes

Cyclic voltammetry (CV) at 0.005 V/s was employed to study the reduction kinetics of $[PdCl_4]^{2-}$ from an aqueous electrolyte consisting of 0.1M $PdCl_2$ and 0.1M HCl. Pt wire and Ag/AgCl saturated KCl were used as the counter and reference electrode, respectively. The potential measured against the Ag/AgCl saturated KCl were converted to the reversible hydrogen electrode (RHE) scale using the equation $E_{RHE} = E_{Ag/AgCl} + 0.059 \times pH + 0.197V$. A potentiostatic method was applied to grow Pd NPs from the same electrolyte at pH 1.3. The electrode potential was conditioned and equilibrated at an open-circuit potential (OCP) of ca. $+0.79V_{RHE}$ vs. $V_{RHE}$ for 10 seconds for each step and then held at the potentials $+0.54V_{RHE}$, $+0.16V_{RHE}$, $+0.06V_{RHE}$ and $-0.002V_{RHE}$ for a chosen period (0.2-3600s). All solutions were prepared in milli-Q water (18 MΩ cm) and deaerated by nitrogen gas flow for at least 30 minutes in a closed pyrex electrochemical cell. After the electrodeposition, the deposits were promptly rinsed with deionised (DI) water and dried in flowing $N_2$. The adsorbed $[PdCl_4]^{2-}$ ions on the Pd NPs surface were removed during CV scans, recorded in a 0.1M $H_2SO_4$ by cycling the potentials negatively from OCP to $0V_{RHE}$ with a scan rate of 0.02 V/s until a steady-state voltammogram was obtained. The mass of the Pd NPs deposited on the Au (111) electrode surface was estimated from the cathodic charges passed during the electrodeposition assuming 100% Faradaic efficiency. The electrocatalytic performance of the Pd NPs for ethanol oxidation was determined in a mixture of 0.5M KOH and 1M EtOH solution by CV scanning negatively from OCP (of ca. $+0.4V_{RHE}$) with a scan rate of 0.025 V/s. In this case, Pt wire and a Hg/HgO were used as the counter and reference electrodes, respectively, and the measured potential was converted to RHE using the following equation $E_{RHE} = E_{Hg/HgO} + 0.059 \times pH + 0.115V$.

### 4.3.3.2 Modification of diamond electrodes

Pd catalyst was electrodeposited onto BDD from a deaerated 0.1M HCl solution containing 1mM $PdCl_2$ by a potentiostatic method. The deposition potential was held at -0.15V (vs Ag/AgCl) until 10.52 and/or 21.05 $mC/cm^2$ charge passed through the surface. The corresponding metal loading of the aforementioned charges was 5.8 and/or 11.6 $\mu g/cm^2$ respectively. The electrodepositions potential was chosen after cyclic voltammetry on bare diamond wafer in the $PdCl_2$ solution over a potential range (-0.1V to -0.4V) in which Pd reduction occurs[43].

Prior to deposition, all BDD electrodes were put in MW-CVD at 600 °C, 45 Torr pressure, 1.5 kW microwave power and $H_2$ gas flow at 200 sccm for a duration of 45 minutes. After the plasma and heating elements had both been turned off, the samples were left to cool down in the MW-CVD in the presence of hydrogen gas so as to avoid surface re-oxidation.

The electrodes were taken out from MW-CVD and examined for hydrogen termination by XPS.

Pd catalyst was then electrodeposited onto HBDD from a deaerated 0.1M HCl solution containing 1mM $PdCl_2$ by a potentiostatic method. The deposition potential was held at -0.15V (vs Ag/AgCl) until 10.52 and/or 21.05 $mC/cm^2$ charge passed through the surface. The corresponding metal loading of the aforementioned charges was 5.8 and/or 11.6 $\mu g/cm^2$ respectively. The electrodepositions potential was chosen after cyclic voltammetry on bare diamond wafer in the aforementioned solution, a potential range (-0.1V to -0.4V) in which Pd reduction occurs[43].

# 4.4 Results and discussion

## 4.4.1 Overpotential dependent electrochemical growth of Pd for ethanol electrooxidation

### 4.4.1.1 Electrochemical deposition of Pd

The CV in figure 4-1 (a) shows a wide onset potential region 0.27-0.7$V_{RHE}$ for Pd deposition that is well positive of the underpotential deposited hydrogen ($H_{UPD}$) region below +0.27$V_{RHE}$. A cathodic current due to the reduction reaction 4-1 (below) started to flow around +0.7$V_{RHE}$, followed by a substantial current rise to a maximum at +0.02$V_{RHE}$ near the diffusion-limited reduction of $[PdCl_4]^{2-}$. No cathodic peaks for underpotential deposition of Pd were observed. The current decreases sharply beyond the peak at +0.02$V_{RHE}$ as the mass transfer diffusion dominates and reaches a minimum at -0.002$V_{RHE}$ that is followed by an increase in current density due to hydrogen evolution. The potential region of 0.27-0.7$V_{REH}$ is where the Pd metal deposition occurs without $H_{UPD}$ and deposition occurs simultaneously with $H_{UPD}$ on the freshly deposited Pd after this point. As the cathodic potential limit gradually increases into the $H_{UPD}$ region, an anodic current due to Pd stripping at +0.98$V_{RHE}$ increases i.e., the stripping current is linearly proportional to the overpotential, which indicates the deposition of Pd within the selected potential window. A pair of peaks ($C_1$, $A_1$) appears (Figure 4-1 (b)) as a result of the H adsorption ($H_{ads}$) and desorption ($H_{des}$), respectively, when voltammogram (D) was scanned negatively to +0.12$V_{RHE}$. As the cathodic potential was scanned into and beyond the $H_{UPD}$ region, a sharp anodic peak appears at +0.11$V_{RHE}$ (voltammetry B and C) due to H absorption ($H_{abs}$) into the Pd lattice and its re-oxidation. The higher cathodic current in the reverse scan for the potential region of 0.27-0.48$V_{RHE}$ shown in

figure 4-1 (b) supports the fact that the deposition of Pd on Pd surface is faster than the nucleation on the Au electrode surface.

$$[PdCl_4]^{2-} + 2e^- \rightarrow Pd(0) + 4Cl^- \qquad (4\text{-}1)$$

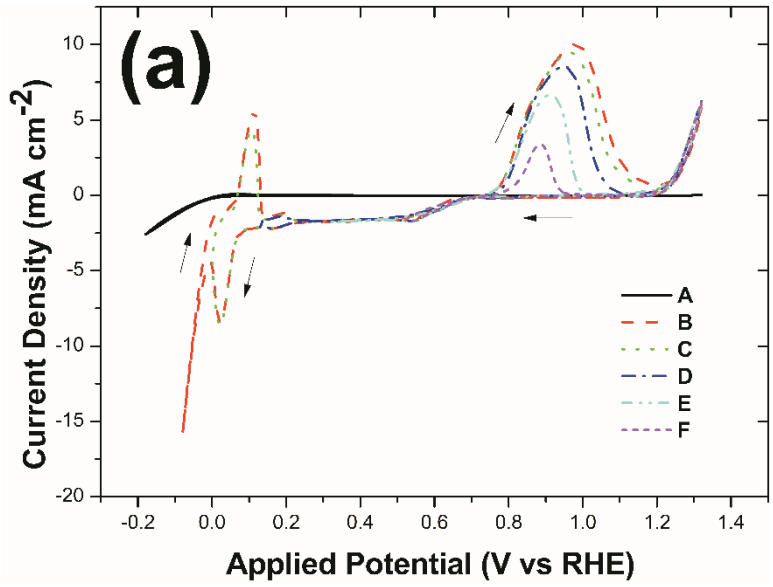


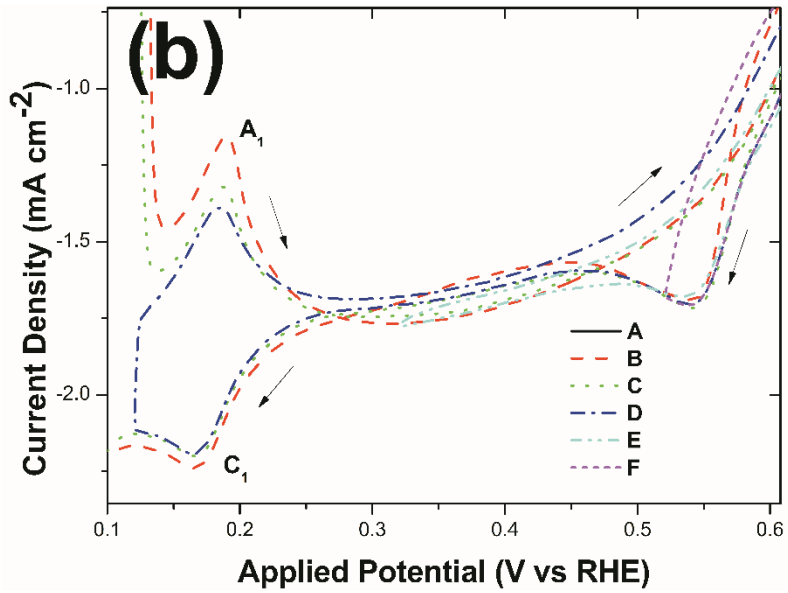


**Figure 4-1** (a) Cyclic voltammetry of the Au (111) substrate recorded in deaerated 0.1M HCl solution containing 10 mM $PdCl_2$ scanned negatively from OCP with a scan rate of 0.005 V/s (initial/conditioning: $+0.79V_{RHE}$, 10s), the upper potential limit was selected at $1.3V_{RHE}$ and reverse potential at $+0.52V_{RHE}$ (F), $+0.32V_{RHE}$ (E), $+0.12V_{RHE}$ (D), $-0.002V_{RHE}$ (C) and $-0.08V_{RHE}$ (B), where A represents the voltammogram of the substrate in 0.1M HCl electrolyte. (b) Expanded current densities within the selected potential region +0.1 to $+0.6V_{RHE}$.

Figure 4-2 (a) shows the linear sweep voltammetry (LSV) of the Au (111) substrate measured in the same electrolyte used for the CV analysis. The marked circles on the LSV curve are four potentials selected for the Pd deposition in the small (+0.54$V_{RHE}$), medium (+0.16$V_{RHE}$), large (+0.06$V_{RHE}$) and overlarge (-0.002$V_{RHE}$) potential regions. Figure 4-2 (b) shows typical time dependencies of the electrode potential-current density curves during the potentiostatic electrodeposition of Pd at the selected potentials. When a small overpotential (+0.54$V_{RHE}$) was applied, the cathodic current dropped initially but increased gradually to reach a maximum of ca. -3.0 mA $cm^{-2}$ at 2s. After that the current decreased again and became constant at ca. 1.5 mA $cm^{-2}$ for longer deposition times to 600 s. The behaviour indicated that deposition proceeded in a well-established nucleation and growth mode[44]. At all other electrode potentials, the cathodic current started to flow at a high value and dropped sharply to a constant maximum current of ca. -2.1 mA $cm^{-2}$ for +0.16$V_{RHE}$, -2.5 mA $cm^{-2}$ for +0.06$V_{RHE}$, and -3.75 mA $cm^{-2}$ for -0.002$V_{RHE}$ for 600 s deposition time.

The nucleation and growth of Pd at these selected overpotentials was investigated by potentiostatic transient measurement, in which Pd was deposited by a short pulse width of 5s and stripped at +1.0$V_{RHE}$, a potential sufficiently positive to ensure that no Pd remain on the surface. The current-time transients in figure 4-3 (a) shows an initial drop in cathodic current due to the adsorption and/or double layer charging effects and pass through a minimum before reaching a steady state at longer deposition times[45]. Since there is an important contribution of the charging current at the beginning of the deposition, the last part of the current-transient is shown in figure 4-3 (b). The resulting current-time transients recorded for the small, medium, large and overlarge deposition potentials, all show the characteristic shape for an electrochemically driven, mass-transfer diffusion controlled, nucleation and growth process[44,46,47]. The cathodic current is consistent with the Cottrelian decay, which indicates planar diffusion-controlled growth. Thus, the selected overpotential region (i.e., small,

medium, large and overlarge overpotential) is large enough to overcome the potential barrier to nucleate the stable Pd nuclei for further growth.

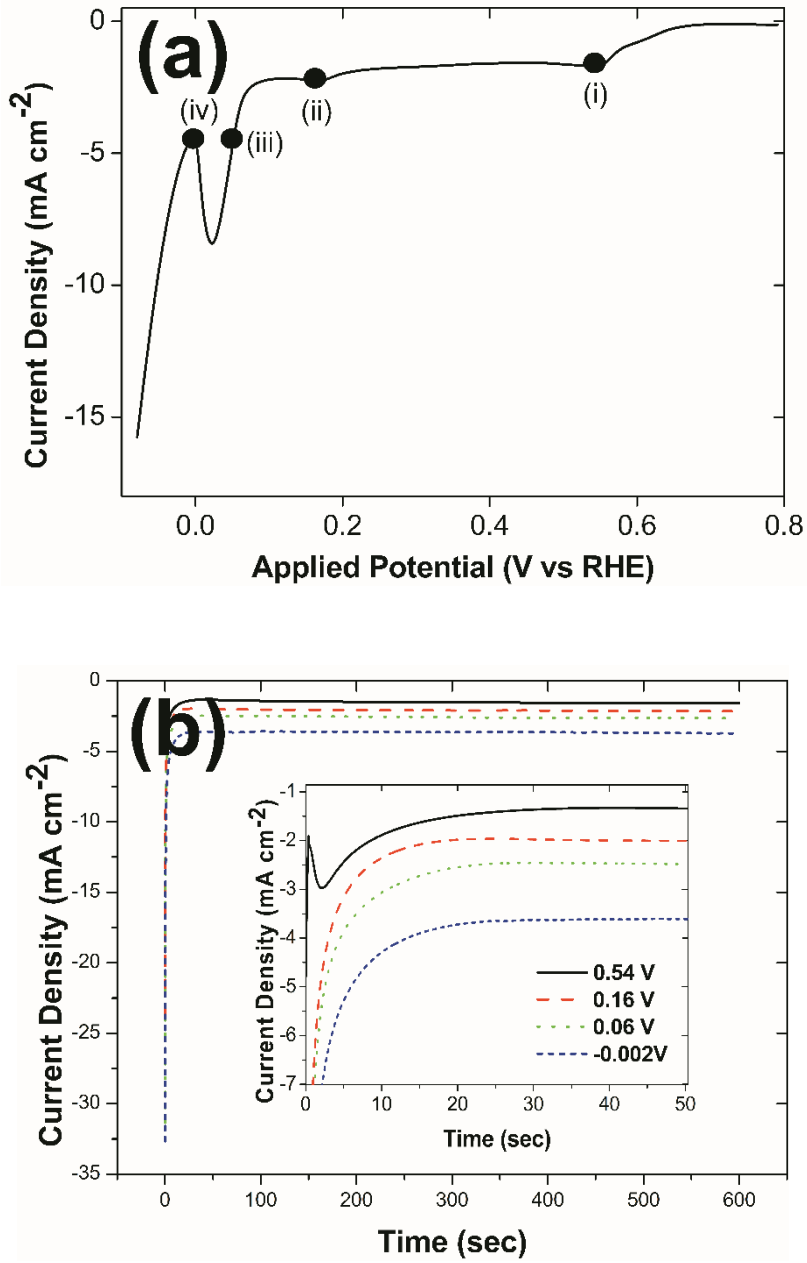


**Figure 4-2** (a) Pd electrodeposition on a Au (111) substrate in deaerated 0.1M HCl solution containing 10 mM $PdCl_2$ (a) by liner sweep voltammetry (LSV) with a scan rate of 0.005 V/s (initial/conditioning: $0.79V_{RHE}$, 10s); (b) by constant potential (potentiostatic) at four different potentials as marked by closed circles on LSV curve at (i) $+0.54V_{RHE}$ (small), (ii) $+0.16V_{RHE}$ (medium), (iii) $+0.06V_{RHE}$ (large) and (iv) $-0.002V_{RHE}$ (overlarge) (initial/conditioning: $+0.79V_{RHE}$, 10 s). The inset shows the time dependent current density in the shorter time scales. The legend shows the corresponding Pd deposition overpotential at $+0.54V_{RHE}$, $+0.16V_{RHE}$, $+0.06V_{RHE}$ and $-0.002V_{RHE}$.

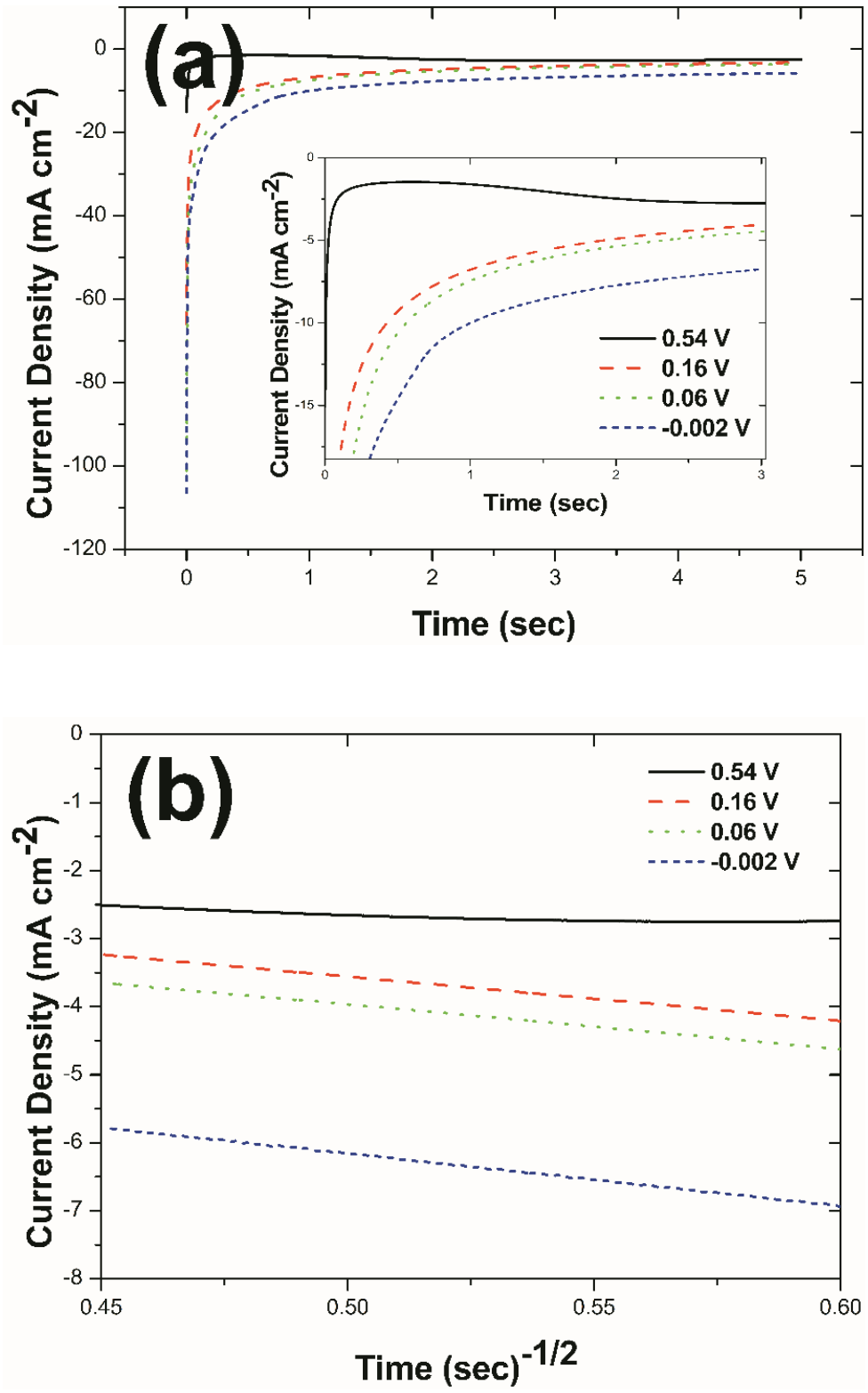


**Figure 4-3** (a) Current-time transient recorded at various overpotentials vs. RHE on a Au (111) substrate in deaerated 0.1M HCl solution containing 10 mM $PdCl_2$ (initial/conditioning: $+0.79V_{RHE}$, 10s); (b) plot of current vs. time$^{-1/2}$ showing linear characteristic consistent with the Cottrell equation. The legend shows the corresponding Pd deposition potential at $+0.54V_{RHE}$, $+0.16V_{RHE}$, $+0.06V_{RHE}$ and $-0.002V_{RHE}$.

### 4.4.1.2 Characterisation of Pd nanoparticle deposits by cyclic voltammetry in aqueous acidic electrolyte

Figure 4-4 shows CVs of the Au (111) electrode recorded in 0.1M $H_2SO_4$ electrolyte at 0.02 V/s after Pd was deposited potentiostatically at (a) +0.54$V_{RHE}$ (small overpotential), (b) +0.16$V_{RHE}$ (medium overpotential), (c) +0.06$V_{RHE}$ (large overpotential) and (d) -0.002$V_{RHE}$ (overlarge overpotential) for different deposition times. The CVs for all Pd electrodes show the characteristic peaks ($C_4$, $A_4$) for Pd oxide reduction ($PdO_{red}$)/formation ($Pd_{oxi}$) at around 0.64/0.92$V_{RHE}$ and peaks ($C_1$, $C_2$ and $A_1$, $A_2$) for $H_{UPD}$ i.e., adsorption ($H_{ads}$), absorption ($H_{abs}$) and desorption ($H_{des}$), respectively, in the potential range 0.2-0.06$V_{RHE}$. A pair of peaks ($C_3$, $A_3$) represents the bulk process of hydrogen absorption/evolution and re-oxidation from the surface of the Pd at potential +0.01$V_{RHE}$ or more. A pair of broader peaks ($C_5$, $A_5$) at around +1.16$V_{RHE}$ and +1.4$V_{RHE}$ that corresponds to the Au oxide ($Au_2O_3$) reduction and formation, is suppressed when the deposition time was more than 0.2s. The peak corresponding to the reduction of $Au_2O_3$ was no longer detected as the deposition time increased suggesting that the Au surface was fully covered by the Pd deposits and no Au surface remained exposed to the solution. The shape of the CVs in the $H_{UPD}$ region is similar to those obtained at Pd layers deposited on Au (111) and Au (100) substrates[48–50], which indicates that Pd was deposited epitaxially. The peak current due to $PdO_{red}$/$Pd_{oxi}$ ($C_4$, $A_4$), $H_{ads}$/$H_{abs}$ and $H_{des}$ ($C_1$, $C_2$ and $A_1$, $A_2$), bulk hydrogen absorption/re-oxidation ($C_3$, $A_3$) and oxygen evolution (at larger than +1.5$V_{RHE}$) from Pd surfaces increases with the deposition time (see figure 4-4).

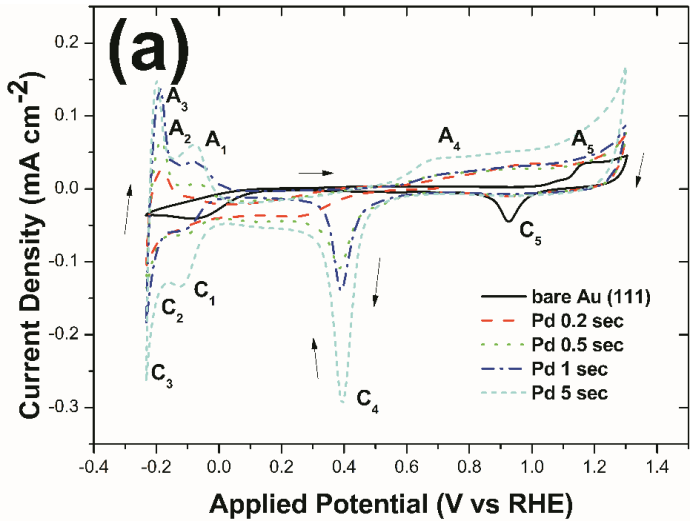
(a)
Current Density (mA cm-2)
Applied Potential (V vs RHE)
A1
A2
A3
A4
A5
C1
C2
C3
C4
C5
bare Au (111)
Pd 0.2 sec
Pd 0.5 sec
Pd 1 sec
Pd 5 sec

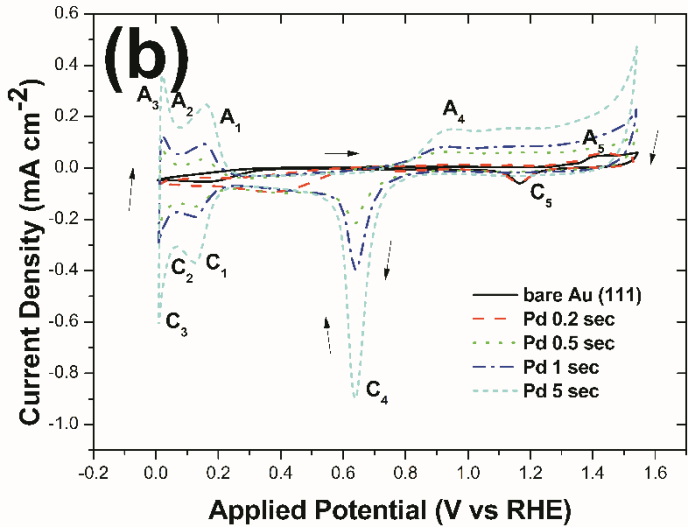
(b)
Current Density (mA cm-2)
Applied Potential (V vs RHE)
A1
A2
A3
A4
A5
C1
C2
C3
C4
C5
bare Au (111)
Pd 0.2 sec
Pd 0.5 sec
Pd 1 sec
Pd 5 sec

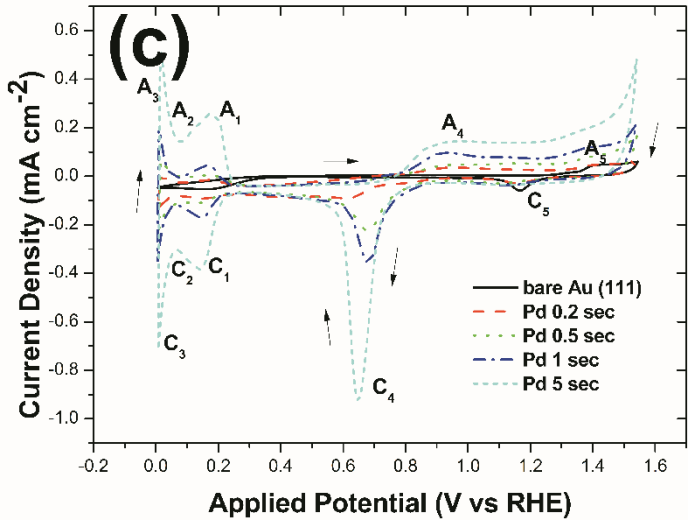
(c)
Current Density (mA cm-2)
Applied Potential (V vs RHE)
A1
A2
A3
A4
A5
C1
C2
C3
C4
C5
bare Au (111)
Pd 0.2 sec
Pd 0.5 sec
Pd 1 sec
Pd 5 sec

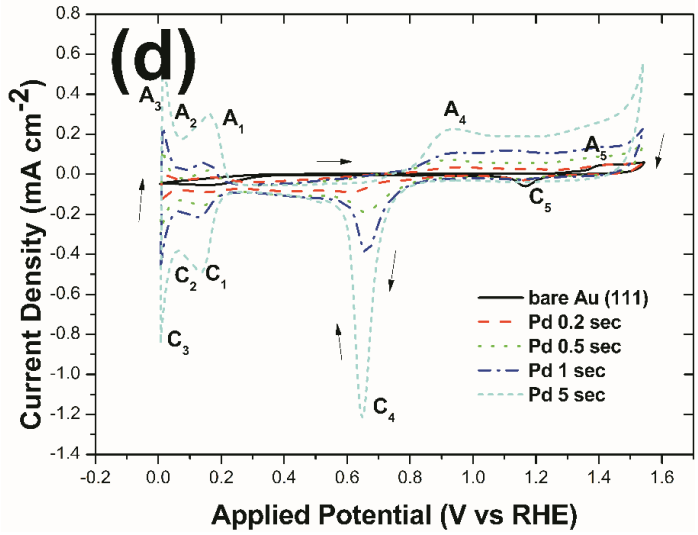


**Figure 4-4** Cyclic voltammetry of the Pd deposited on a Au (111) substrate at (a) +0.54$V_{RHE}$, (b) +0.16$V_{RHE}$, (c) +0.06$V_{RHE}$ and (d) -0.002$V_{RHE}$ in deaerated 0.1M $H_2SO_4$ solution shows $H_{ads}$/ $H_{abs}$/$H_{des}$ as well as Pd oxide formation/reduction peaks. CVs were recorded in static conditions with a scan rate of 0.02 V/s (initial/conditioning: +0.9$V_{RHE}$, 10s). The legend indicates the corresponding Pd deposition time.

### 4.4.1.3 Growth mode and structural characterisation of Pd nanoparticle deposits

Cyclic voltammetry of the deaerated 0.1M HCl solution containing 0.001M $PdCl_2$ shows similar characteristics with a wide overpotential range 0.7-0.27$V_{RHE}$ for Pd deposition and a simultaneous deposition with $H_{UPD}$ at overpotentials lower than +0.27$V_{RHE}$. Following the deposition of Pd from this solution by the potentiostatic pulse at various overpotentials, Pd nanoparticles (Pd NPs) were observed in an ex-situ examination of the electrode surface using a high resolution FEGSEM. Figure 4-5 shows ex-situ FEGSEM of the different sizes of Pd NPs grown on Au (111) surface where the deposition charge was controlled to 433 μC $cm^{-2}$ (corresponding to almost a full Pd monolayer on Au (111), 1ML = 440 μC $cm^{-2}$)[51] for each potential. The nanoparticles are grown by direct electrochemical reduction of $[PdCl_4]^{2-}$ ions from the electrolyte on the Au surface according to equation 4-1. The nanoparticles are

randomly dispersed and spherical in shape except for Pd deposited at large overpotential (+0.06$V_{RHE}$), in which nanoparticles are agglomerated and a large fraction of the substrate is unoccupied. The results clearly imply that the growth mode of the electrochemically deposited Pd was overpotential dependent. The unoccupied space accounts for the planar, diffusion-controlled growth of the nuclei as the deposition progresses, which complies with the current transient of Pd deposition shown in figure 4-3. The mean particle diameter and distribution were determined by measuring the sizes of at least 1500 particles, as shown in the insets of the corresponding SEM images in figure 4-5. The mean diameter of particles deposited at small, medium and overlarge overpotential are 3.8 nm ($\sigma$ = 1.8), 2.8 nm ($\sigma$ = 1.2), and 3.2 nm ($\sigma$ = 1.7), respectively. However, it was not possible to measure the particle size when deposition took place at large overpotential (0.06$V_{RHE}$) due to agglomerate formation. The three histograms in the inset of figure 4-5 show that particle sizes vary slightly at each overpotential. The obtained results imply that the critical radius of clusters of nuclei before particle formation at the electrode/solution interface is inversely proportional to the overpotential i.e., the critical radius of the clusters of nuclei decreases as the overpotential increases. A close inspection suggests that the electrochemical nucleation and growth of Pd NPs occurred primarily at the step edges on the Au surface, then on adjacent terraces. When the deposition potential was 0.06$V_{RHE}$ (i.e., large overpotential), clusters of nuclei aggregate with each other and form larger agglomerates as observed in the ex-situ FEGSEM image in figure 4-5 (c). At larger overpotentials, very small nuclei (as for example particle 1 in figure 4-5 (c)) or clusters of nuclei (particles such as 2 in figure 4-5 (c)) are formed randomly dispersed on the Au surface, and some neighbouring clusters may have already coalesced into medium sized nanoparticles (particles such 3 in figure 4-5 (c)) at the beginning of nucleation. As the nucleation proceeds, more clusters are formed and travel around the surface. Because of the weak forces between the NPs and the Au surface they aggregated with each other to form

larger agglomerates (particles such as 4 in figure 4-5 (c))[52]. New clusters may also grow independently, without travelling to join aggregates, by the direct reduction of fresh $[PdCl_4]^{2-}$ ions on them, as for example, particles in figure 4-5 (c). A similar result about the electrochemical aggregative growth mechanism of silver nanoparticles on carbon surface has been described by using a carbon coated TEM grids as electrode substrate[53].

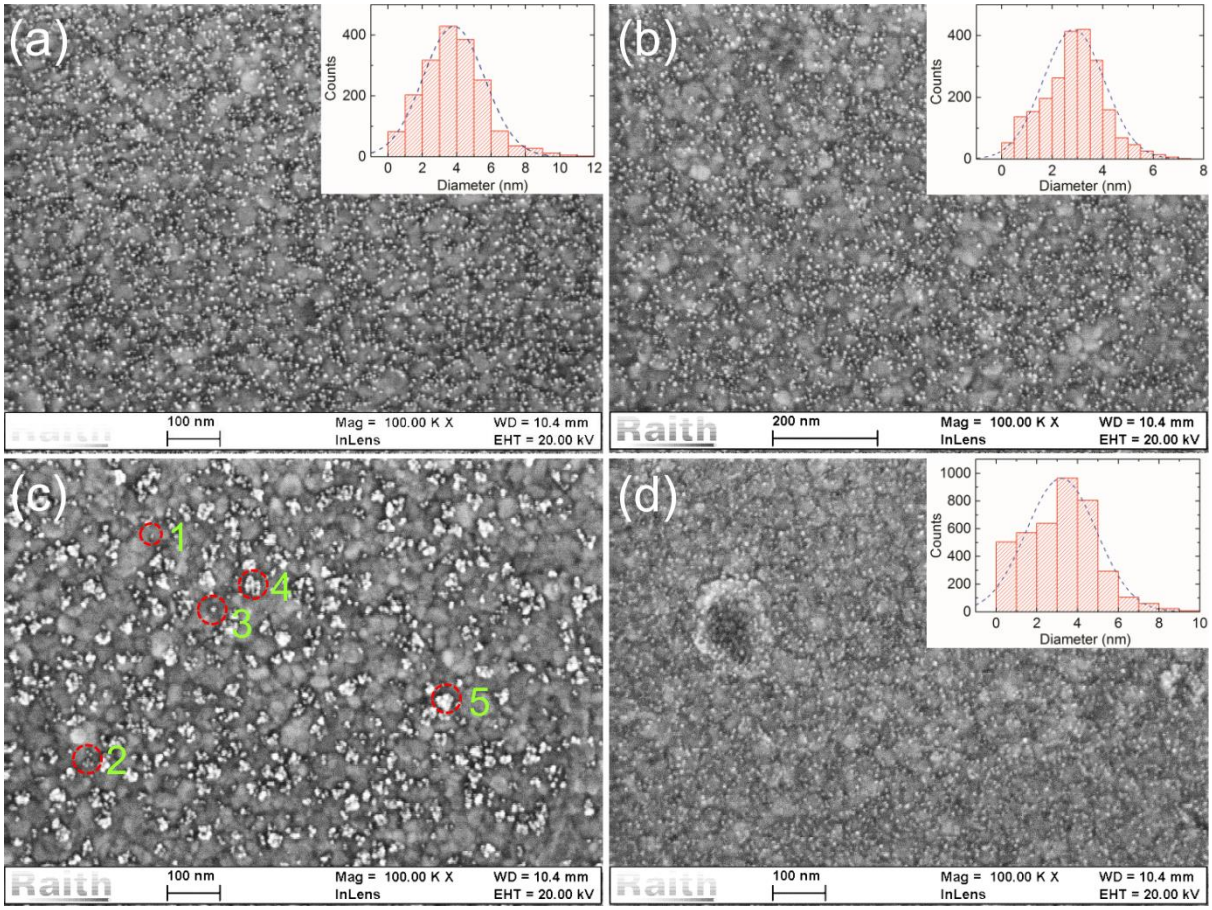


**Figure 4-5** Ex-situ FEGSEM images for Pd nucleation and growth on a Au (111) substrate electrodeposited potentiostatically at (a) $+0.54V_{RHE}$, (b) $+0.16V_{RHE}$, (c) $+0.06V_{RHE}$ and (d) $-0.002V_{RHE}$ for a 433 μC $cm^{-2}$ deposition charge (0.98 monolayer equivalent). The electrolyte was made up with deaerated 0.1M HCl solution containing 0.001M $PdCl_2$.

The overpotential-dependent growth mode of Pd NPs was further examined by increasing the amount of Pd deposition charge. A Pd deposition charge of 3183 μC $cm^{-2}$, which is 7.3 times larger than that of figure 4-5, was controlled potentiostatically on each electrode and representative FEGSEM images are shown in figure 4-6. Pd NPs gradually cover the whole Au surface with a high degree of monodispersity as the deposition progressed. When the Pd deposition charge increased from 433 μC $cm^{-2}$ to 3183 μC $cm^{-2}$, agglomeration of the particles disappeared completely. The mean diameter of the particles are also increased as the deposition progressed from 3.8 nm to 6.6 nm (σ = 3.1), 2.8 nm to 4.0 nm (σ = 2.4) medium, 5.1 nm (σ = 3.2) and 3.2 nm to 5.0 nm (σ = 2.9) for small, medium, large and overlarge overpotential, respectively. The size distribution pattern of Pd NPs also becomes wider with the increase in Pd deposition charge. The major particle size ranges are 5-8 nm, 1-6 nm, 1-8 nm and 1-8 nm for small, medium, large and overlarge overpotential, respectively. Hence, the particles size is relatively large at small overpotentials compared to that of the large overpotential deposition. According to the particle number density, 3.5 nm and 5 nm are the most common particle sizes for deposition charge of 433 μC $cm^{-2}$ and 3183 μC $cm^{-2}$, respectively, irrespective of the overpotential applied. However, the density of small particles is higher for medium ($+0.16V_{RHE}$) and overlarge ($-0.002V_{RHE}$) overpotential by comparison with the small ($+0.54V_{RHE}$) and large ($+0.06V_{RHE}$) overpotential.

This result indicates that a few mechanisms may be occurring in parallel depending on the overpotential applied: (1) formation of randomly dispersed nuclei and clusters of nuclei throughout the surface; (2) growth of small clusters by direct reduction of $[PdCl_4]^{2-}$ ions; (3) coalescence of the nearest small clusters to form medium size nanoparticles; (4) surface movement of small clusters to form agglomerates (only in the case of large overpotential); (5) recrystallisation into mono-dispersed larger nanoparticles (also only for large overpotential). The aggregation of small clusters of nuclei occurs due to the thermodynamic driving force to

attain the lowest energy configuration[52] and as such the particle size in this case is mostly controlled by surface thermodynamic processes. The $H_{UPD}$ might also interfere in the formation/growth of individual nuclei or clusters of nuclei depending on the hydrogen adsorption/absorption magnitude. Thus, at overlarge overpotential, in which $H_{UPD}$ was much pronounced, clusters were static after their formation but grew by the fresh reduction of $[PdCl_4]^{2-}$ ions on them. A schematic model for the electrochemical nucleation and growth mechanism of Pd deposition at small, medium, large and overlarge overpotential based on the results discussed above is shown in figure 4-7.

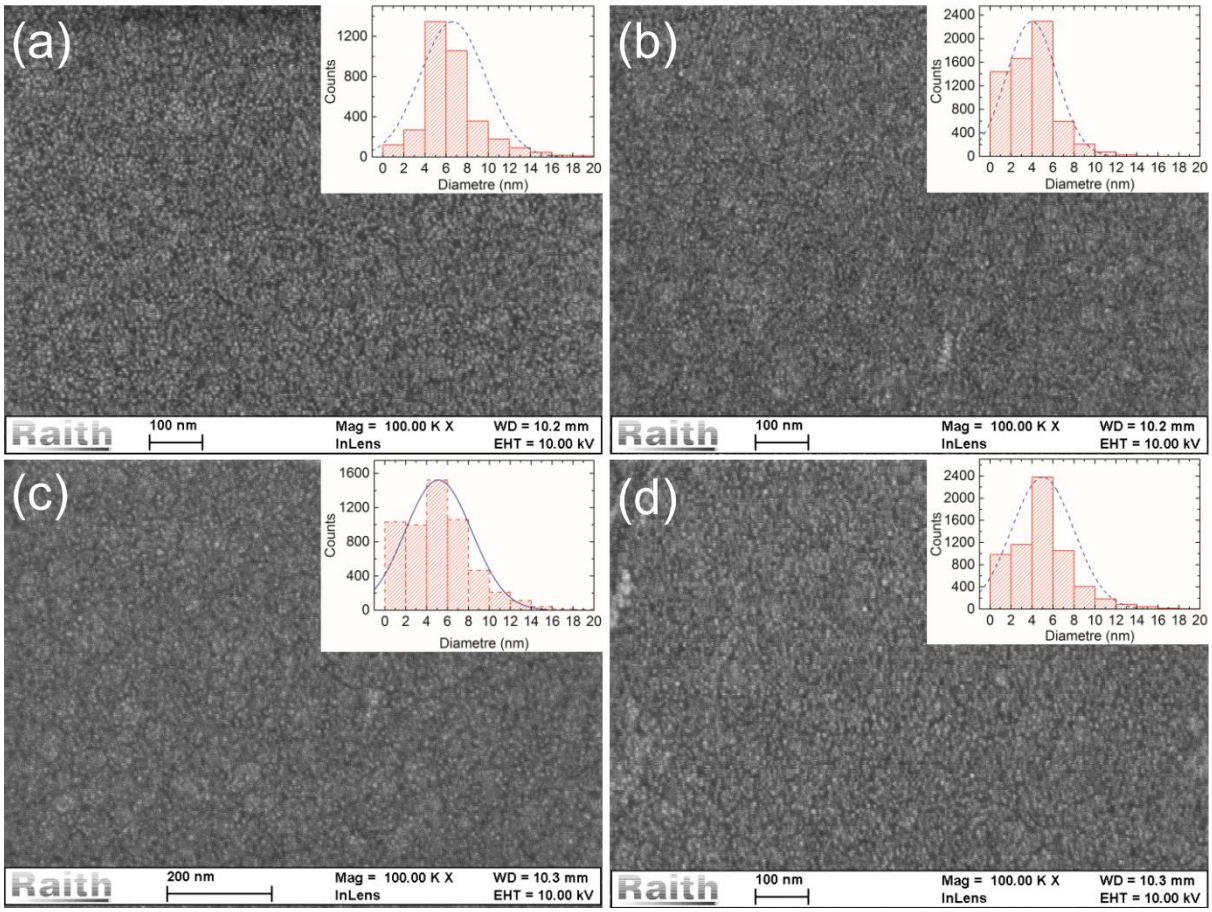


**Figure 4-6** Ex-situ FEGSEM images of the Pd NPs on a Au(111) substrate as electrodeposited potentiostatically at (a) +0.54$V_{RHE}$, (b) +0.16$V_{RHE}$, (c) 0.06$V_{RHE}$ and (d) -0.002$V_{RHE}$ for a 3183 μC $cm^{-2}$ deposition charge (7.2 monolayer equivalent). The electrolyte was made up with deaerated 0.1 M HCl solution containing 0.001 M $PdCl_2$.

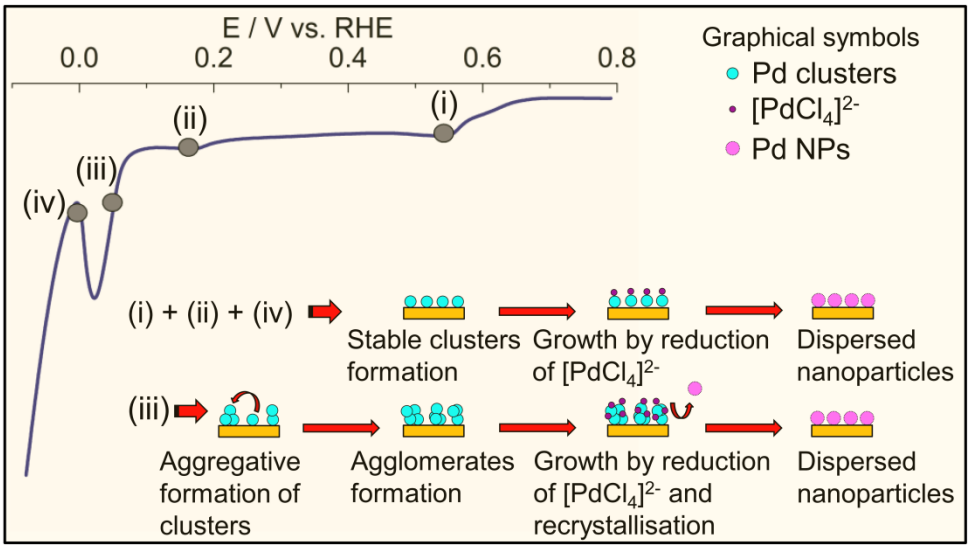


**Figure 4-7** Schematic illustration of the electrochemical growth mechanism of the Pd deposition on a Au (111) substrate when the overpotential is (i) small, (ii) medium, (iii) large and (iv) overlarge.

The elemental composition and the chemical and electronic states of Pd NPs at the Au (111) interface were investigated by XPS as shown in figure 4-8 (a) for a deposition charge of 3183 μC $cm^{-2}$, similar to the deposition charge for which FEGSEM is shown in figure 4-6. Survey scans were carried out initially on a contaminant free Au (111) surface. The survey showed that all the samples contain O, C and Pd photoelectron peak consistent with the modification of the Au (111) surface with Pd NPs. Pd NPs on the gold surface were prepared by applying various potentials while the same deposition charge was maintained. Hence, Au (111) modified with Pd nanoparticles has spin orbit doublets with Pd $3d_{5/2}$ and Pd $3d_{3/2}$ peaks at 335.8 eV and 341.3 eV, respectively. The latter observation seems to be the same for all the electrodes regardless of the applied potential during palladium deposition, which means that there was not any binding energy shift. The absence of a binding energy shift indicates that the deposited metallic Pd NPs are pure or contaminant-free. To investigate the crystal structure of Pd NPs, XRD measurements were performed as shown in figure 4-8 (b). A strong diffraction peak was observed, which was assigned to the (111) face-centered cubic (fcc) structure of metallic Pd along with a tiny peak for the (200) facet.

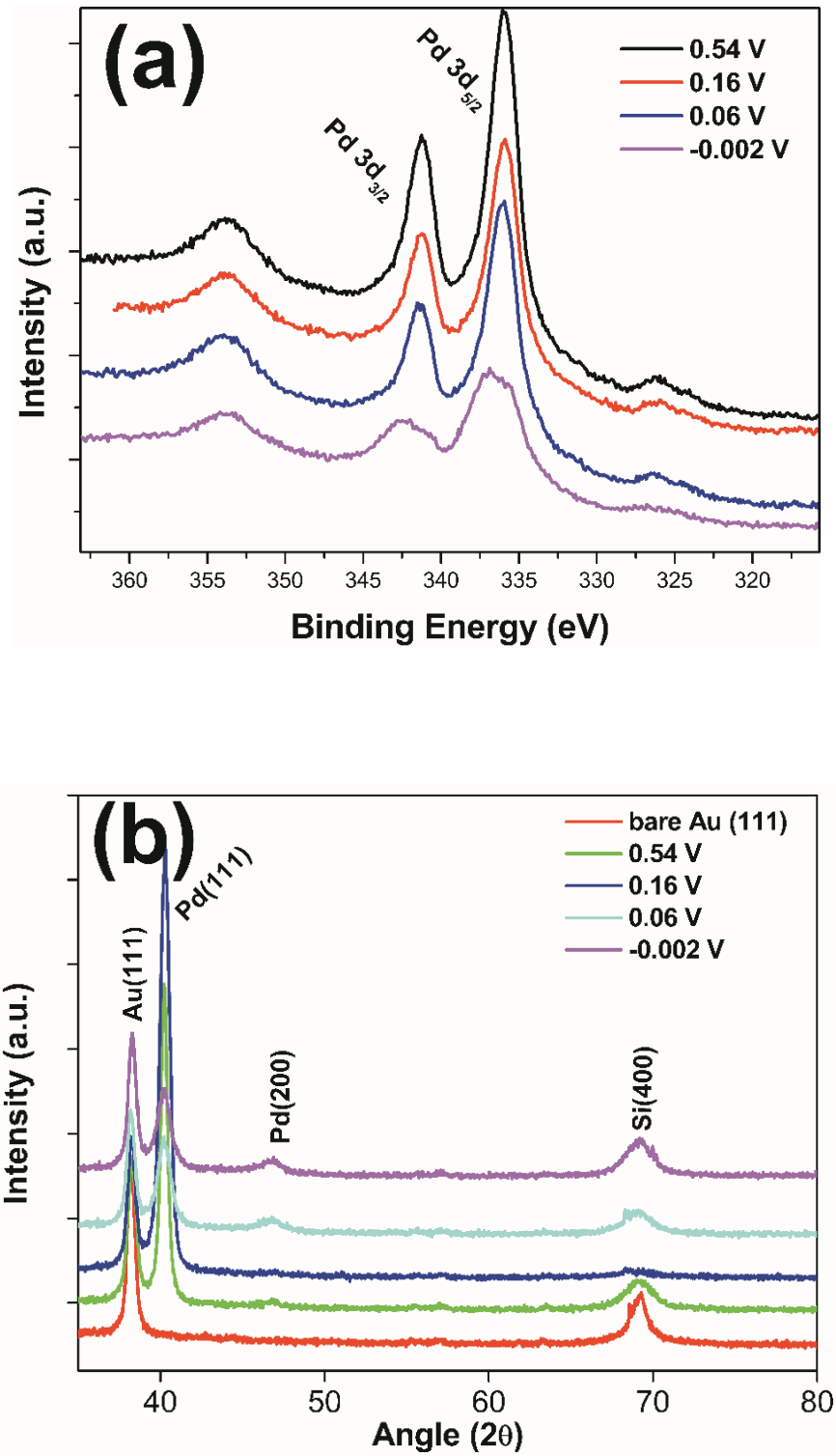


**Figure 4-8** (a) XPS and (b) XRD of Pd NPs on a Au (111) substrate for a total deposition charge of 3183 μC $cm^{-2}$.

## 4.4.1.4 Electrocatalytic performance of Pd nanoparticles

CVs of the Pd NPs based electrode (for which ex-situ FEGSEM images were shown in figure 4-6) were recorded for the ferrocyanide ($[Fe(CN)_6]^{4-}$)/ferricyanide [$(Fe(CN)_6]^{3-}$ system, which demonstrate a quasi-reversible one-electron redox behaviour at the Pd NPs as shown in figure 4-9. Before the ferro/ferricyanide redox behaviour was examined, the deposited Pd NPs were electrochemically cleaned by CV in 0.5M KOH. As can be seen from the figure 4-9, the redox peak potentials of the ferrocyanide/ferricyanide system are similar for all Pd NPs electrodes irrespective of the overpotential applied for their deposition. The anodic ($E_{pa}$) and cathodic ($E_{pc}$) peak potential for all Pd NPs are observed at $+0.96V_{RHE}$ and $+0.87V_{RHE}$, respectively, and the corresponding anodic-cathodic peak potential separation ($\Delta E_p = E_{pa} - E_{pc}$) is 0.09V. The obtained $\Delta E_p$ value for Pd NPs is comparable to the value of the Au substrate ($\Delta E_p = 0.085V$), but the Au particles were deposited under vacuum by a sputtering technique, which affords high-purity, blanket deposits but is more expensive compared to the electrodeposition method. A small $\Delta E_p$ value obtained for Pd NPs indicates that a good reversibility and electrochemical activity are maintained on the Pd nanoparticles surface[44]. The redox current of Pd NPs varies slightly with each overpotential applied for their deposition, which are $I_{pa} = 0.80$ mA $cm^{-2}$ and $I_{pc} = -0.86$ mA $cm^{-2}$ (small overpotential), $I_{pa} = 0.75$ mA $cm^{-2}$ and $I_{pc} = -0.80$ mA $cm^{-2}$ (medium overpotential), $I_{pa} = 0.78$ mA $cm^{-2}$ and $I_{pc} = -0.87$ mA $cm^{-2}$ (large overpotential), $I_{pa} = 0.77$ mA $cm^{-2}$ and $I_{pc} = -0.85$ mA $cm^{-2}$ (overlarge overpotential). The ratio of the cathodic to anodic current is close to 1, suggesting that the reaction undergoes a quasi-reversible redox process. The redox currents for Pd NPs are higher than for the Au substrates due to a larger electrochemically active surface area of the electrodeposited Pd NPs by comparison with the sputtered Au.

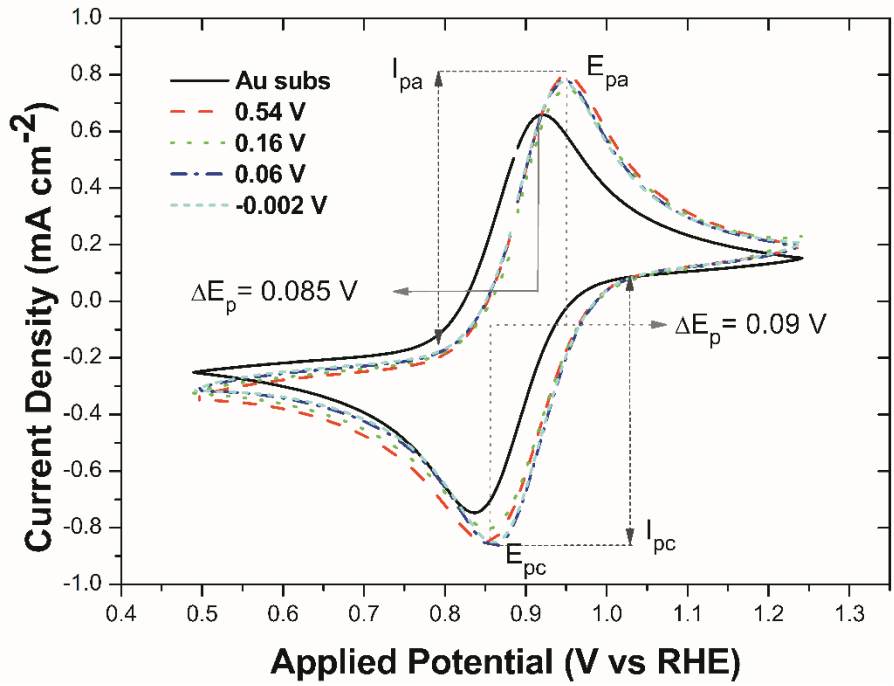


**Figure 4-9** Cyclic voltammetry of Pd NPs deposited on a Au (111) substrate recorded in deaerated 5mM $K_3[FeCN]_6$ and 1M KCl electrolyte. CVs were recorded in static conditions with a scan rate of 0.05 V/s (initial/conditioning: +0.9$V_{RHE}$, 10s). Each electrode contains total Pd deposition charge of 3183 μC cm$^{-2}$ (i.e., 1.75 x 10$^{-6}$ g cm$^{-2}$).

Pd NPs were characterised by CV in deaerated 0.5M KOH aqueous electrolyte, as shown in figure 4-10. A typical CV of various electrodes electrodeposited at different overpotentials as previously described shows characteristic features to those reported in the literature for hydrogen adsorption ($C_2$, $C_3$) and desorption ($A_2$, $A_3$), oxide formation ($A_1$) and reduction ($C_1$)[54]. The pre-peak ($A'_1$) is associated with the oxidation of the Pd NPs surface before the main oxidation process. The real electroactive surface area (EASA) was calculated from Pd oxide reduction ($PdO_{red}$) peak at +0.658$V_{RHE}$ after subtraction of the double layer charging capacitance charge. 424 μC cm$^{-2}$ was used corresponding to the removal of a full monolayer of Pd oxide. The amount of Pd deposit was calculated from the coulombic charge of Pd deposition by applying Faraday's Law assuming 100% efficiency. In addition, the specific surface area (SSA) of the Pd NPs in m$^2$/g was defined as the EASA of the Pd NPs (cm$^2$/cm$^2$ Au substrate) divided by the amount Pd loading. These data are summarised in Table

4-1 along with the electrocatalytic activity for ethanol electrooxidation in aqueous alkaline electrolytes.

**Table 4-1** Overpotential dependent electroactive surface area (EAS), specific surface area (SSA), ethanol electrooxidation and mass activity of Pd NPs.

| $V_{RHE}$ for Pd NPs deposition | Pd loading $gcm^{-2} \times 10^{-6}$ | EAS $cm^2$ (Pd) $cm^{-2}$ (subs) | SSA $m^2g^1$ (Pd) | Ethanol electrooxidation current $mAcm^{-2}$ (subs) | Ethanol electrooxidation specific activity $mAcm^{-2}$ (Pd) | Mass activity $mAg^{-1}$ (Pd) $\times 10^6$ | $I_f/I_b$ |
|---|---|---|---|---|---|---|---|
| **0.54** | 1.75 | 1.58 | 90.28 | 17.23 | 6.54 | 9.85 | 0.92 |
| **0.16** | 1.75 | 1.62 | 92.57 | 16.41 | 6.07 | 9.38 | 0.88 |
| **0.06** | 1.75 | 1.60 | 91.43 | 19.75 | 7.40 | 11.28 | 1.1 |
| **-0.002** | 1.75 | 1.64 | 93.71 | 18.90 | 6.91 | 10.80 | 1.01 |

*The specific activity was normalised to the EASA of Pd. The activities were measured at the forward peak potential and geometrical surface area of the Au (111) substrate was 0.6 $cm^2$.

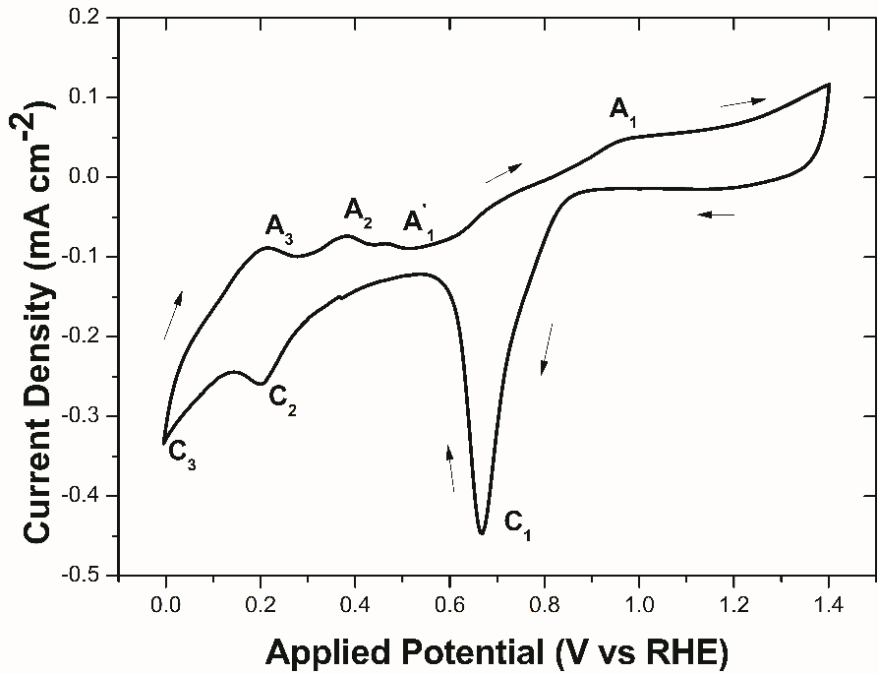


**Figure 4-10** Cyclic voltammetry of Pd NPs deposited on a Au (111) substrate recorded in deaerated 0.5M KOH aqueous electrolyte. CVs were recorded in static conditions with a scan rate of 0.02 V/s (initial/conditioning: +1.0$V_{RHE}$, 10s). Electrode contains a total Pd deposition charge of 3183 μC $cm^{-2}$ (i.e., 1.75 x $10^{-6}$ g $cm^{-2}$).

The specific surface area (SSA) of Pd NPs deposited at all overpotentials at a similar mass loading varies only slightly for each deposit. However, this difference can be attributed to the particle size and distribution variation as seen in the FEGSEM images (Figure 4-6). The

lowest SSA value (90.28 $m^2$ $g^{-1}$) for Pd NPs deposited at +0.54$V_{RHE}$ is due to comparatively large particle sizes (5-8 nm) while the highest value (93.71 $m^2$ $g^{-1}$) for the Pd NPs deposited at -0.002$V_{RHE}$ is due the combined effects of smaller particles sizes (1-8 nm) and narrower size distribution with the maximum counts for only 5 nm Pd NPs. Comparatively, a small particle size and narrow distribution for Pd NPs deposited at +0.16$V_{RHE}$ (see figure 4-6) led to a higher SSA value (92.57 $m^2$ $g^{-1}$) compared to that of the Pd NPs deposited at 0.06$V_{RHE}$ (91.43 $m^2$ $g^{-1}$). The SSA values of the electrochemically deposited Pd NPs are remarkably higher than the values for electrodeposited nonporous Pd (60 $m^2$ $g^{-1}$)[55], Pd coated carbon nanotubes (25.8 $m^2$ $g^{-1}$)[56], Pd nanowires synthesised by electron beam irradiation of a precursor mixture (12 $m^2$ $g^{-1}$)[57] and Pd black (17-23 $m^2$ $g^{-1}$)[58].

The electrocatalytic performance of Pd NPs as anode catalysts for alkaline direct alcohol fuel cells (ADAFCs) was evaluated by electrooxidation of ethanol. Typical CVs for electrooxidation of ethanol on Pd NPs and the Au substrate electrode in alkaline electrolyte are shown in figure 4-11 (a). Ethanol electrooxidation exhibited two well-defined current peaks, the first at +0.8$V_{RHE}$ on the forward scan under anodic conditions and the second at +0.68$V_{RHE}$ on the reverse scan under cathodic conditions. The forward and reverse peaks for all Pd NPs electrode are sharper with a higher electrooxidation current by comparison with the substrate Au electrode. The peak on the forward scan is attributed to the electrooxidation of the freshly chemisorbed ethanol species on the Pd NPs and the peak on the reverse scan is caused by the oxidation of the incompletely oxidised carbonaceous species e.g., $(CH_3CO)_{ads}$, formed during the dissociative adsorption of ethanol on the Pd during the forward scan[59,60]. The formation of the oxide layer can block the adsorption of the new reactive species on the Pd surface and eventually lead to the decrease in the electrocatalytic activity.

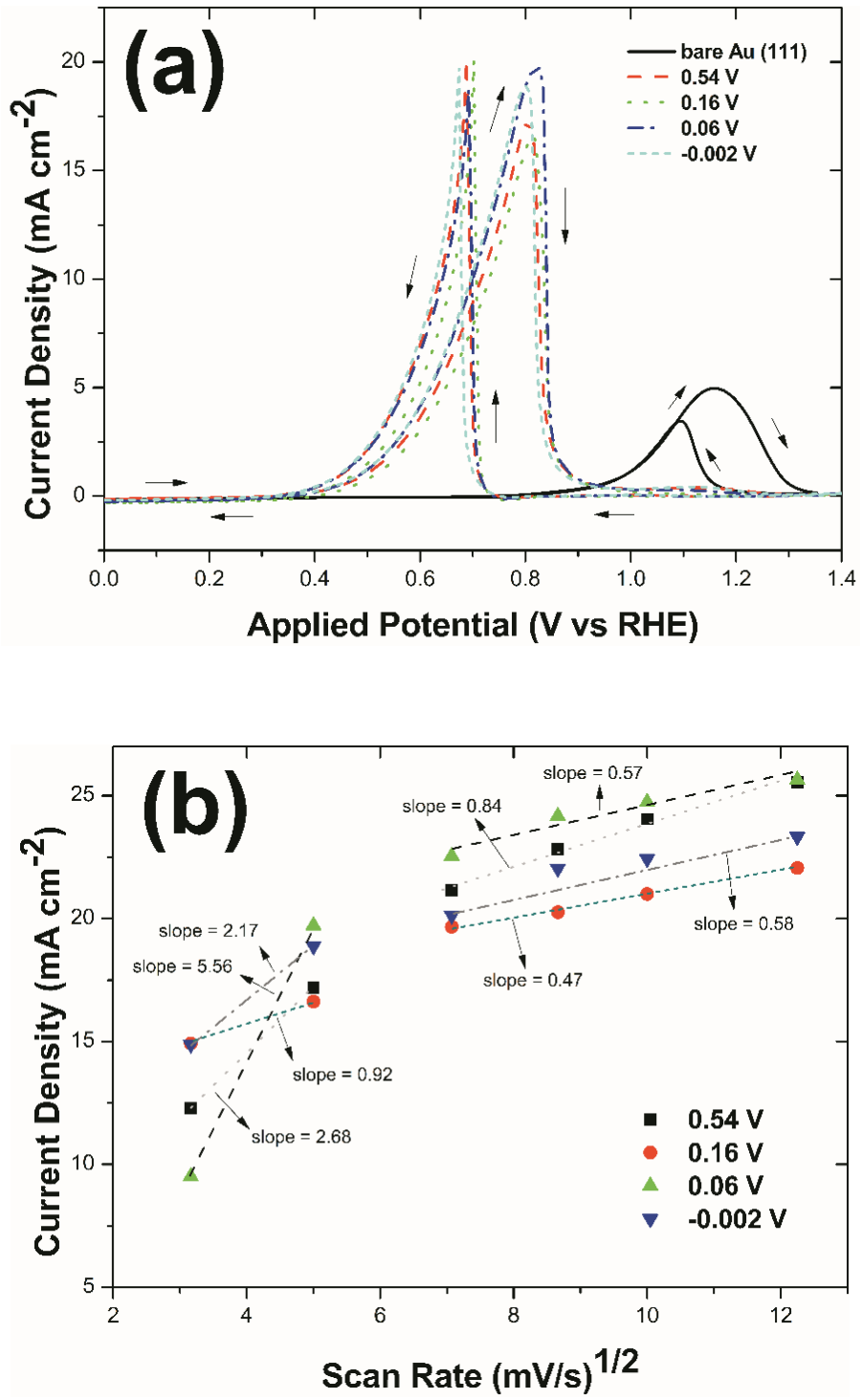


**Figure 4-11** Cyclic voltammetry of Pd NPs deposited on a Au (111) substrate for the electrooxidation of ethanol in deaerated 1M EtOH and 0.5M KOH electrolyte. CVs were recorded in static conditions with a scan rate of 0.025 V/s (initial/conditioning: +0.4$V_{RHE}$, 10s). Each electrode contains total Pd deposition charge of 3183 µC $cm^{-2}$ (i.e., 1.75 x $10^{-6}$ g $cm^{-2}$).

As the anodic scan continues, more Pd oxide covers the surface of the Pd NPs and therefore the current for the electrooxidation of ethanol decreases at $+0.9V_{RHE}$ and thereafter no current flows. The electrode reactivates again in the reverse scan once the oxide is removed from the Pd NPs surface, thus a second oxidation peak at $+0.68V_{RHE}$ is observed[61,62]. The forward scan onset potential refers to the overpotential required for the electrooxidation of ethanol and the current is observed to start to flow for all Pd NPs electrodes at an overpotential ca. $+0.38V_{RHE}$, approximately 0.35V more negative than at the Au substrate ($+0.73V_{RHE}$). This fact indicates that the stripping reaction of the dissociative adsorbed intermediates $(H_3CO)_{ads}$ of ethanol on the Pd NPs commences at a more negative potential than that of Au. The stripping reaction is known to be the rate determining step for the electrooxidation of ethanol on Pd electrocatalyst in alkaline electrolytes as previously reported[61]. Therefore, electrooxidation of ethanol in alkaline electrolyte is kinetically more favourable on Pd NPs than on Au.

The forward peak potential and corresponding peak current density for electrooxidation of ethanol do not vary significantly between the four Pd NPs electrodes. Although, the EASA value for the four Pd NPs electrodes does not differ much, a higher EASA is generally accepted have more active sites for the electrooxidation of ethanol. However, the highest electrooxidation current obtained for Pd NPs deposited at $+0.06V_{RHE}$ corresponded to a specific activity of 7.4 mA $cm^{-2}$(Pd) followed by 6.91 mA $cm^{-2}$(Pd) for Pd NPs deposited at $-0.002V_{RHE}$ although the former electrode has a lower EASA value than the latter. This phenomenon is related to the presence of defect sites on Pd NPs surface as described by Ustarroz *et al*[53]. Hence, a higher number of defect sites would have been created on the Pd NPs surface when the clusters growth mode is through the recrystallisation process rather than the direct attachment of ions. The specific activity for electrooxidation of ethanol is comparatively higher on Pd NPs for those deposited at large and overlarge overpotential i.e., a region where Pd deposition occurred simultaneously with the hydrogen adsorption ($H_{ads}$)/absorption ($H_{abs}$) reactions. The

adsorbed/absorbed hydrogen on Pd NPs surface may further enhance the formation of defect sites favourable for the electrooxidation of ethanol.

The electrocatalytic properties of the Pd NPs are known to be influenced by their crystalline structure, size, distribution and surface morphology. The enhanced electrocatalytic performance of ethanol electrooxidation mass activity (≈ 10,000 mA $mg^{-1}$) of the electrochemically deposited Pd NPs is about 13, 10.5, 10.8 and 35 times higher than the corresponding activity reported for Pd nanoflowers/Ni nanowires electrode (765 mA $mg^{-1}$)[61], $Pd_{45}Pt_{55}$ nanowires on glassy carbon electrode (950 mA $mg^{-1}$)[63], Pd/rGO/carbon fibre paper (925 mA $mg^{-1}$)[64] and commercial Pd-C/CFP(286 mA $mg^{-1}$)[64], respectively. The normalised specific activities corresponding to the amount of Pd loading is also remarkably high as presented in Table 4-1. As the ethanol electrooxidation on the forward scan occurs under diffusion control, the mass transport behaviour on Pd NPs catalysts has been investigated. Figure 4-11 (b) shows the correlation between the peak current density (in the forward scan) and the square root of the scan rate during the electrooxidation process of ethanol at different scan rates. The electrooxidation current of ethanol has a linear relationship with different scan rates with two slope values: the first at lower scan rate with a larger value and the second at higher scan rate with a smaller value. This observation indicates that the electrooxidation process of ethanol on Pd NPs was controlled by concentration polarisation or diffusion processes at higher scan rates of above 0.025 V/s. At lower than 0.025 V/s scan rate, the electrooxidation was dominated by the activation polarisation of the Pd NPs over the diffusion electrochemistry. The ratio of the forward anodic peak current density ($I_f$) to the backward anodic peak current density ($I_b$) is an important index to measure the tolerance to carbonaceous oxidative intermediates accumulated on the catalyst surface during the electrooxidation of ethanol. A high $I_f/I_b$ ratio implies the effective oxidation of ethanol to the end products and low accumulation and/or effective elimination of carbonaceous oxidative intermediates on/from the

electrocatalyst surface[60]. The $I_f/I_b$ ratio of Pd NPs in this work is between 0.9 to 1.1, comparable with the commercial Pd-C catalyst and other reported values[64]. However, the method developed in this work for electrochemical deposition of highly dispersed Pd NPs could be transferred to alternative substrates, which provide faster electron transfer and mass transport by comparison with the Au substrate of this work enabling catalysts that are more tolerant to oxidative intermediates. After 50 potential cycles, the electrooxidation current for ethanol on the anodic scan had decreased by only ≈ 3.5%, which means that the electrochemically deposited Pd NPs are active and stable catalysts.

## 4.4.2 Oxidation of ethanol using Pd modified diamond

### 4.4.2.1 Morphology and XPS characterization of the deposits on boron-doped diamond electrodes

Figure 4-12 illustrates Pd particles on oxygen and hydrogen-terminated boron-doped diamond electrodes after 10.52 mC/cm$^2$ passage of charge at the potentials described in the previous sections. Figure 4-12 (a) shows Pd particles on BDD. The theoretical value of the size of the nanoparticles is 38.89 nm at this metal loading. Clearly, Pd deposits have been electrodeposited mainly on the edge of the diamond, in areas with high energy. The non-uniform nature and poor distribution of the deposits on the surface sensitively reflects the variation in the lateral conductivity of the diamond as a result of the non-uniform distribution of B dopant. Figure 4-12 (b) shows Pd nanoparticles on HBDD after 10.52 mC/cm$^2$ passage of charge, same metal loading with the BDD surface. The size of the particles at this surface is 17.73 nm. In contrast to BDD, Pd deposits have been distributed in a more uniform manner and cover more surface on diamond. The latter likely arises from the fact that the hydrogen-terminated surface is more conductive[65,66]. Additionally, we will try to prove the

aforementioned through XPS analysis and subsequently through the electrochemical characterisation as well as electrochemical oxidation of ethanol. Furthermore, the hydrogen terminated surface significantly affected the size of the particles fact which plays an important role to the overall electrocatalytic activity of the electrode.

XPS spectra in figure 4-13 exhibit the elemental composition of Pd/BDD and Pd/HBDD, respectively. Survey scans of the modified diamond electrodes are shown in figure 4-13 (a). The survey scans indicate that these electrodes contain O, C and metal photoelectron peaks of Pd. It is worth noting that due to the hydrogen termination the O peak is smaller for the Pd/HBDD as well as the photoelectron peak of Pd is greater than its counterpart on the oxidised surface. The latter observation could be better proved by IR spectroscopy but due to difficulty to access the IR spectroscopic facilities, this work was limited to XPS characterisation regarding the hydrogen termination of the BDD surface. This result is in agreement with the SEM images that show more Pd particles on the HBDD while poorly distributed Pd particles on the BDD surface. Figure 4-13 (b) exhibits the main palladium peaks of the two electrodes. BDD and HBDD modified with Pd nanoparticles have Pd $3d_{5/2}$ and Pd $3d_{3/2}$ peaks at 336 and 342.5 eV respectively. There is a very tiny shift in binding energy for the HBDD due to the different termination, 336.5 and 343 eV respectively. Also, the signal of the Pd/HBDD seems to be six times larger than the Pd/BDD. The latter is also consistent with the SEM image in figure 4-12 (b).

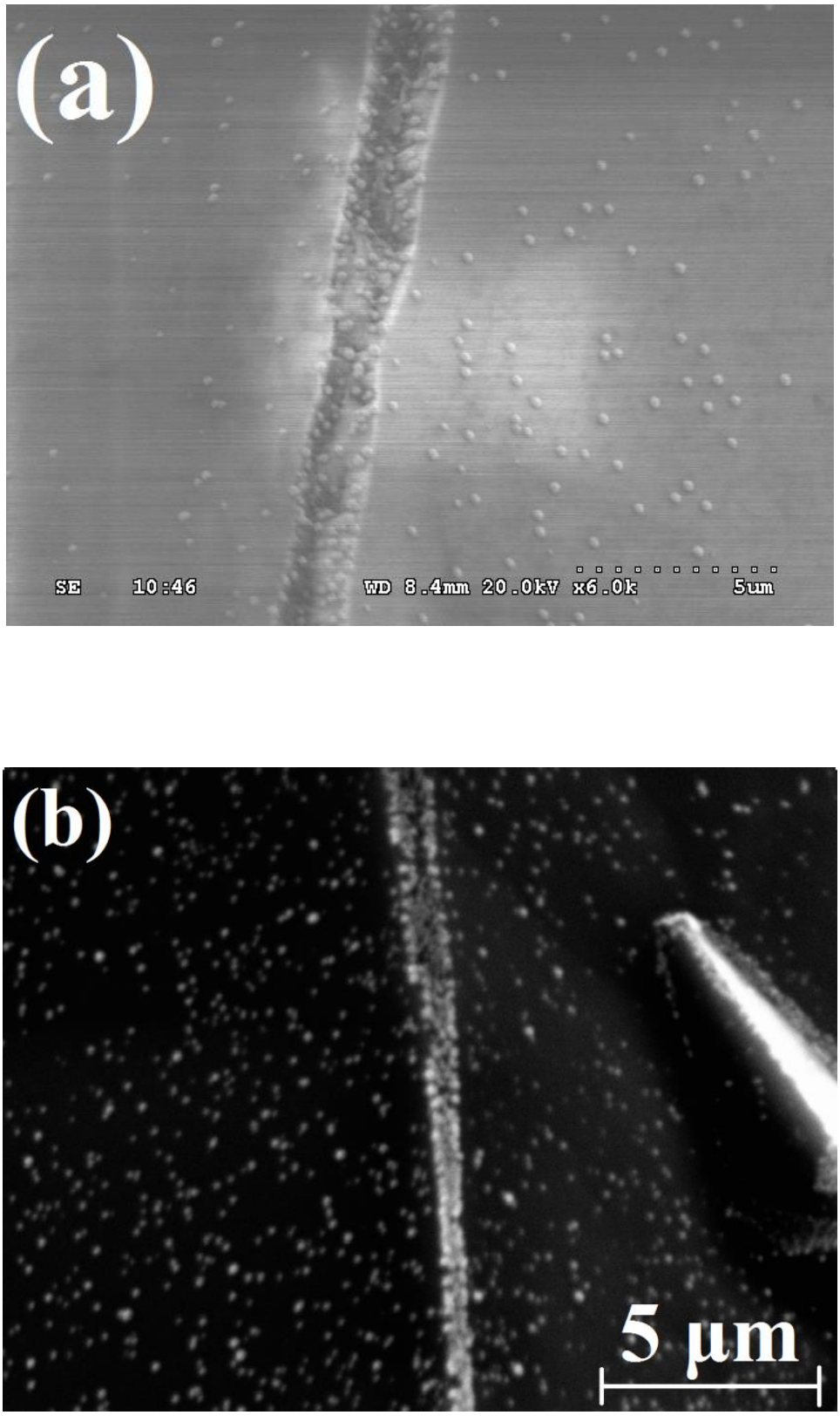


**Figure 4-12** SEM images of (a) Pd deposited on BDD electrode and (b) Pd deposited on HBDD electrode, respectively through chronoamperometry at -0.15V.

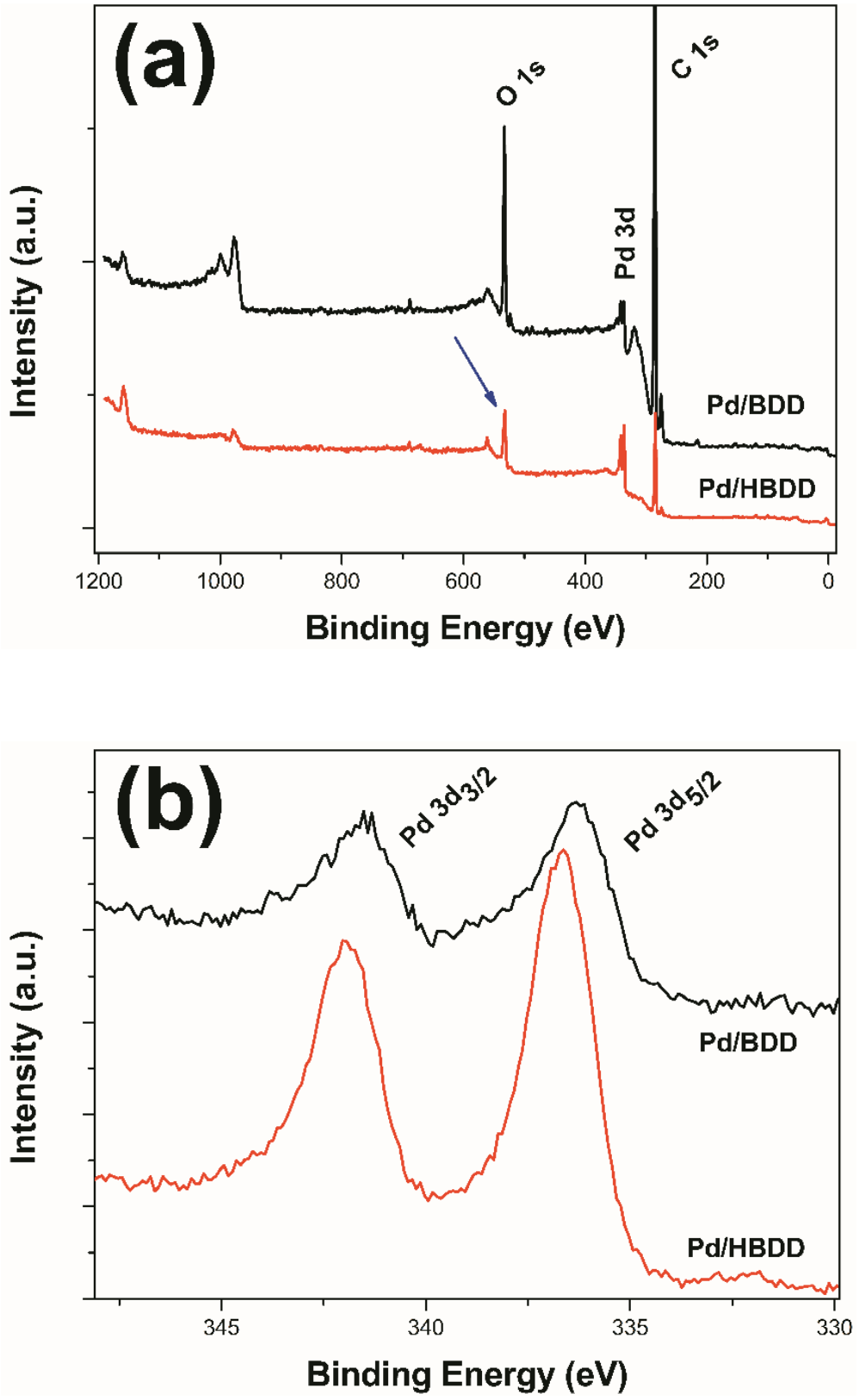


**Figure 4-13** (a) XPS spectra of wide scans of the Pd/BDD and Pd/HBDD, respectively. (b) Typical Pd 3d peaks of Pd modified BDD and HBDD catalysts, respectively.

## 4.4.2.2 Voltammetric characterisation

### 4.4.2.2.1 Electrodeposition of the electrocatalysts

Typical chronoamperograms of bare BDD and HBDD respectively in a solution containing 1mM $PdCl_2$ and 0.1M HCl are shown in figure 4-14. The Pd is electrodeposited through chronoamperometry at a constant potential of -0.15V. The solid line represents the electrodeposition of Pd onto the bare BDD surface. A nucleation peak is appeared immediately at 0 sec and then a growth pattern is followed until 10.52 $mC/cm^2$ of charge passed through the surface as described in the previous sections. The same procedure was followed for the electrodeposition of Pd onto the HBDD surface. The chronoamperogram of this deposition is shown with the short dash line. In contrast to the Pd deposition on BDD, there is only a growth pattern and the same amount of Pd to be deposited on the surface faster than on BDD. This can be ascribed to the fact that HBDD electrode is more conductive due to hydrogen termination and the electrodeposition of Pd species is more energetically favourable on this surface.

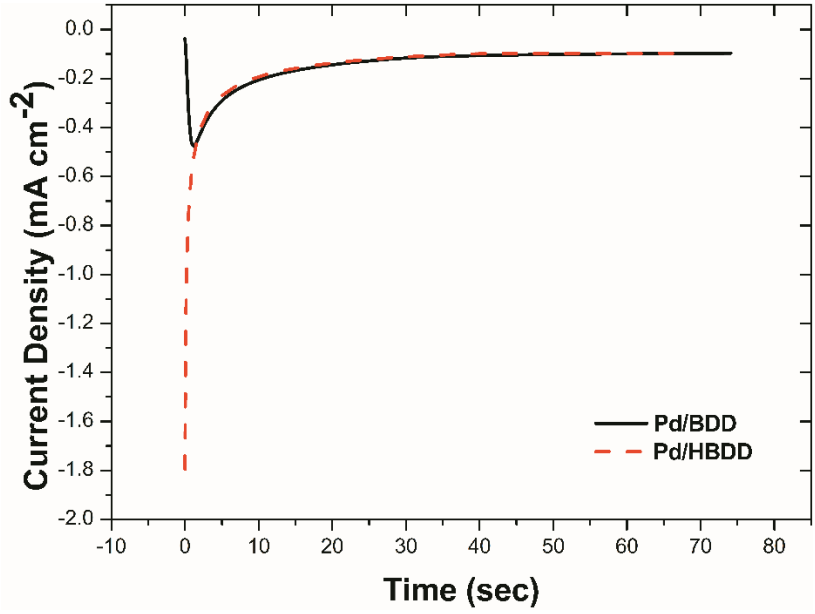


**Figure 4-14** Chronoamperogram of Pd deposition in 1mM $PdCl_2$/0.1M HCl on bare BDD and HBDD electrodes, respectively at constant potential of -0.15V.

#### 4.4.2.2.2 Electrochemical activity of the electrocatalysts

The electrochemical activity of Pd electrocatalysts supported on BDD and HBDD, respectively was characterised by cyclic voltammetry and linear sweep voltammetry, respectively in 0.5M KOH. Figure 4-15 (a) illustrates the cyclic voltammograms of the bare and Pd deposited diamond electrodes. No current response was detected for the unmodified/bare surfaces of BDD and HBDD electrodes. On the contrary, the modified surface with Pd nanoparticles gives various features as shown in figure 4-15 (a). Regarding the Pd/BDD electrode, Pd oxidation and reduction waves occur at +0.05V and -0.21V respectively ($A_1/C_1$); hydrogen adsorption and desorption peaks due to Pd occurs between -0.5V and -0.9V ($A_2/C_2$, $A_3/C_3$). A shoulder is also observed at around -0.27V in the anodic scan which corresponds to the oxidation at favourable sites on the palladium surface[54]. The same features are observed for the Pd/HBDD electrode. Pd oxidation and reduction waves occur at +0.05V and -0.25V respectively ($A_1/C_1$) and hydrogen adsorption and desorption peaks due to Pd which occurs between -0.5V and -0.9V ($A_2/C_2$, $A_3/C_3$). A small binding energy shift of the PdO reduction peak may arise from the amount of Pd coupled with some electronic effects between the Pd particles and hydrogen functionalities. Two small pre-peaks are seen at -0.3V and -0.2V respectively before the main oxidation peak of Pd. The overall current density is higher for the Pd modified HBDD than this of the BDD electrode. The Table 4-2 provides information for various Pd features after electrodeposition through chronoamperometry and shows the electroactive and specific surface areas are higher and the particle size is smaller for the Pd/HBDD electrode than for Pd/BDD.

**Table 4-2** Pd features after electrodeposition through chronoamperometry.

| Pd features | Pd/BDD | Pd/HBDD |
|---|---|---|
| **Pd loading (µg/cm$^2$)** | 5.80 | 5.80 |
| **O desorption charge (mC/cm$^2$)** | 0.32 | 0.69 |
| **Electroactive Surface Area, EAS (cm$^2$/cm$^2$)** | 0.75 | 1.64 |
| **Specific Surface Area, SSA (m$^2$/g)** | 12.83 | 28.14 |
| **Particle Size (nm) – Diameter** | 38.89 | 17.73 |

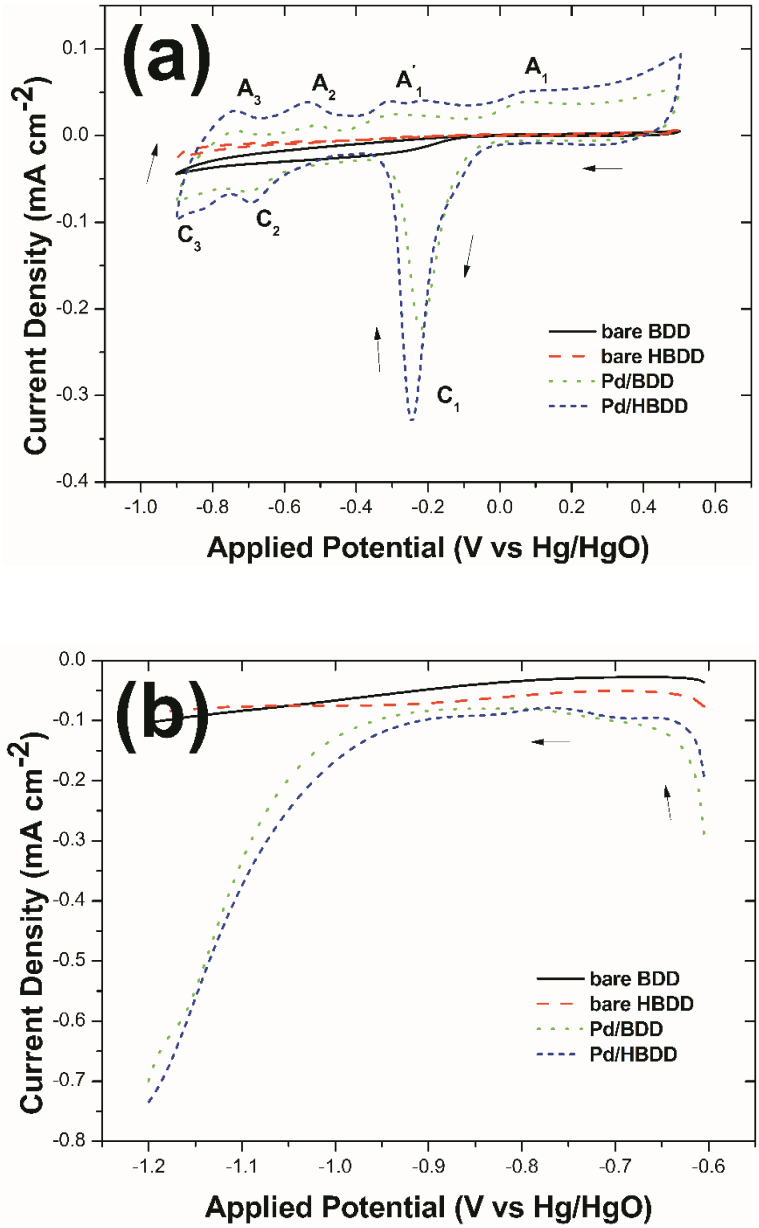


**Figure 4-15** (a) Cyclic voltammogram of Pd/BDD and Pd/HBDD (5.80 µg/cm$^2$) and (b) Linear sweep voltammograms of the Pd modified BDD and HBDD (5.80 µg/cm$^2$), respectively in 0.5M KOH solution at scan rate of 0.02 V/s (all CVs were started from open circuit potential).

The modification of BDD and HBDD electrodes with noble metal Pd nanoparticles led to hydrogen adsorption as evinced from adsorption and desorption peaks in figure 4-15 (a). However, more evidence in regards to hydrogen evolution is provided from the linear sweep voltammograms in figure 4-15 (b). As seen in both the cyclic and the linear sweep voltammograms, there is no hydrogen evolution for the unmodified surface of diamond electrodes. The hydrogen evolution on Pd/BDD surface occurs in the cathodic scan at the potential of -0.8V; the onset potential is much lower when Pd is deposited onto the oxidised surface compared to Pd/HBDD electrode in which hydrogen evolution occurs at -0.85V. The final current response of the hydrogen evolution is 0.03V higher than on the oxidised surface.

### 4.4.2.3 Evaluation of Pd electrocatalysts preparation conditions on ethanol oxidation characteristics

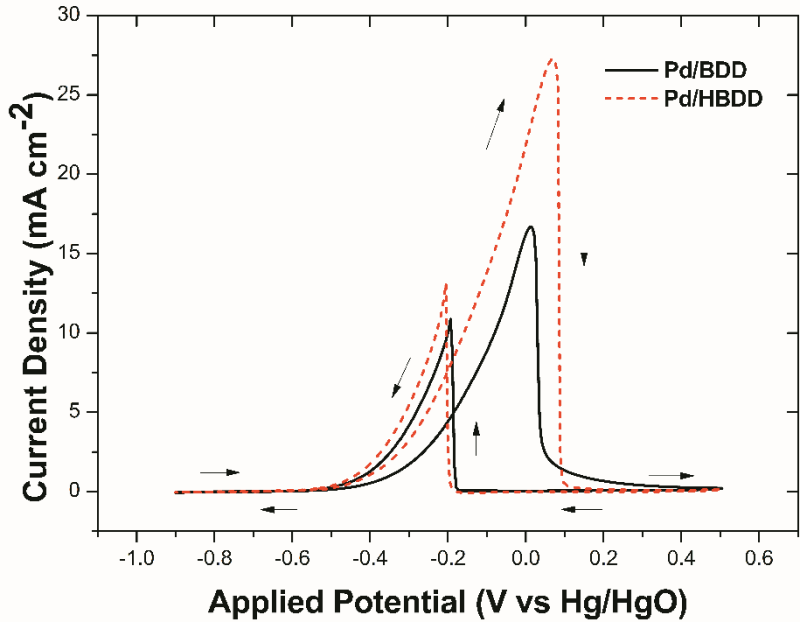


**Figure 4-16** Cyclic voltammograms of Pd modified BDD and HBDD with 5.80 μgr/cm$^2$ (i.e., 10.52 mC/cm$^2$ charge) Pd loading, respectively in 0.5M KOH and 1M EtOH at scan rate of 0.02 V/s. Cyclic voltammograms shown here are taken after 10 cycles.

The Pd/BDD and Pd/HBDD electrocatalysts were evaluated for their electrocatalytic activity towards ethanol oxidation through cyclic voltammetry in a solution containing 0.5M KOH and 1M EtOH at scan rate of 0.02 V/s and the results are shown in figure 4-16. As shown in figure 4-16, there is no current response before -0.5V for the HBDD and -0.4V for the BDD, which implies that the electrode is inactive until the overpotentials are reached. The Pd/HBDD electrode is activated at -0.4V while the Pd/BDD is activated at -0.3V which corresponds to the oxidation of the fresh ethanol species. Both electrodes are then deactivated at around +0.1V. The electrodes are reactivated again, which gives a second oxidation wave at around -0.2V for the Pd/HBDD and Pd/BDD respectively (backward peaks). This process shows the oxidation of the partially oxidised carbonaceous species that accumulate on the surface. The Pd-modified HBDD exhibits higher current response than the oxidised BDD surface. The resistance of the electrode to poisoning by the absorbed ethanol species is correlated to the ratio of the forward and backward current peaks. Thus, the Pd/HBDD (2.08) is more tolerant to poisoning than the Pd/BDD (1.54). Table 4-3 shows a summary of various Pd loadings as well as their anodic current peak of ethanol electrooxidation along with the ratio of their anodic and cathodic current peaks, which gives information regarding the tolerance of the electrocatalysts towards the electrooxidation of ethanol.

**Table 4-3** Pd features after electrodeposition through chronoamperometry.

| Electrodes | Charge (mC/cm$^2$) | Pd metal loading (μg/cm$^2$) | Forward current peak ($I_f$) of Ethanol electrooxidation (mA/cm$^2$) | $I_f$/ $I_b$ |
|---|---|---|---|---|
| **Pd/BDD** | | | 0.89 | 0.58 |
| **Pd/HBDD** | 5.2 | 2.9 | **3.97** | **0.86** |
| **Pd/BDD** | 10.4 | | 10.15 | 1.33 |
| **Pd/HBDD** | | 5.8 | **20.10** | **1.40** |
| **Pd/BDD** | | | 16.68 | 1.54 |
| **Pd/HBDD** | 21 | 11.6 | **27.27** | **2.10** |
| **Pd/BDD** | | | 21.81 | 1.47 |
| **Pd/HBDD** | 39.4 | 21.7 | **33.39** | **2.15** |

## 4.4.2.4 Amperometric response of the catalysts in ethanol

Chronoamperometry was performed in 0.5M KOH and 1M EtOH in order to examine the stability of the electrocatalysts towards the ethanol oxidation and the results are demonstrated in figure 4-17. Pd-modified BDD and HBDD electrodes were held at a fixed potential of -0.15V for 2 hours. The current density decayed initially for both electrocatalysts. Current densities remain stable for this extended operational time of 7200 seconds and the results are in agreement with the performance of the cyclic voltammetry as described in the previous section (section 4.2.2.2). More specifically, the Pd-modified HBDD electrode showed the highest current density of the two electrodes. The current decrease with time, which can be ascribed to the combined effects of electrocatalyst poisoning by the chemisorbed carbonaceous oxidative intermediate species of ethanol and the concentration polarisation with time.

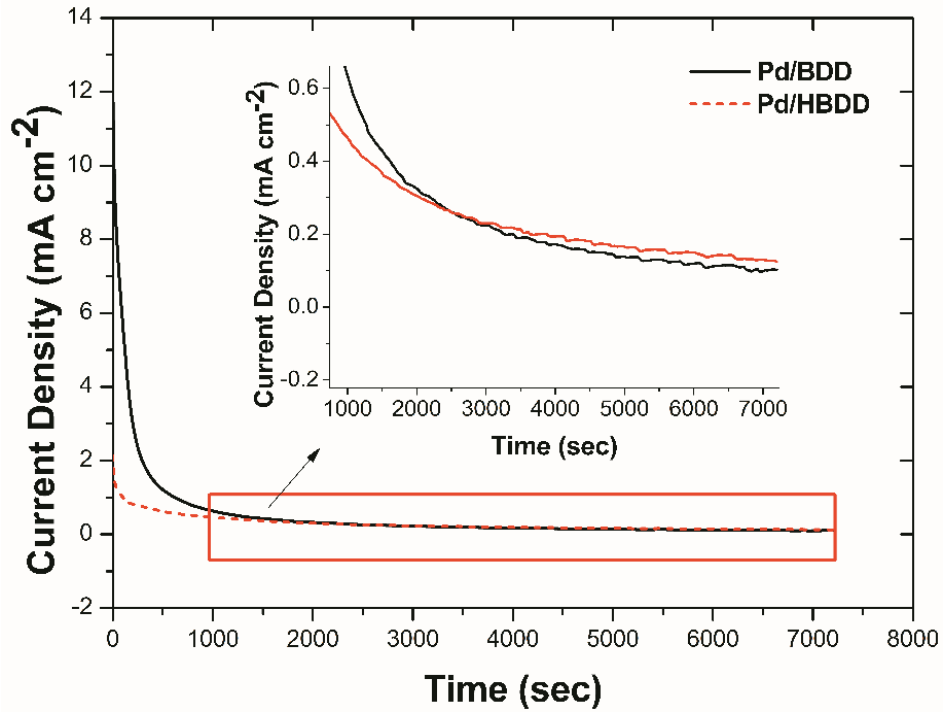


**Figure 4-17** Chronoamperometric response of Pd modified BDD and HBDD respectively after 5.2 mC/cm$^2$ passage of charge in 0.5M KOH and 1M EtOH at potential -0.15V.

# 4.5 Conclusions

This work investigated the electrochemical deposition of Pd metallic NPs on a Au (111) substrate in a deaerated 0.1M HCl solution containing 1mM $PdCl_2$ at small, medium, large and overlarge overpotential. The effects of the applied overpotential and deposition duration on nucleation, growth, size and morphology of Pd NPs were systematically investigated while other parameters such as precursor concentration and electrolyte pH were kept constant. The overpotential for Pd deposition was maintained positive of the potential of underpotential deposition of hydrogen ($H_{UPD}$) by pH dependent ligand coordination effects of $Cl^-$ and $H_2O$ with $Pd^{2+}$ ions. Therefore, the nucleation and growth of Pd NPs at a specific pH were controlled only by the applied overpotential. The structural characterisation by high resolution FEGSEM revealed that the electrochemical nucleation occurred randomly at the step edges and adjacent terraces on Au (111) substrates when the applied overpotential was small ($0.54V_{RHE}$), medium ($0.16V_{RHE}$) and overlarge ($-0.002V_{RHE}$). At these overpotentials, the randomly nucleated and highly dispersed small nuclei or clusters throughout the surface grew independently by the direct reduction of $[PdCl_4]^{2-}$ ions towards the complete coverage of the substrate. When a large overpotential was applied ($0.06V_{RHE}$), clusters were also formed randomly but diffused on the surface because of thermodynamic driving forces and aggregated to form larger agglomerates to attain the lowest overall energy configuration. Afterwards, the larger agglomerates recrystallised into mono-dispersed Pd NPs with a full coverage of the electrode surface as the deposition proceeded. $H_{UPD}$ was more pronounced at overlarge overpotential ($-0.002V_{RHE}$), which prevented the cluster movement due to an increase in van der Waals forces and thus the clusters grew by the fresh reduction of $[PdCl_4]^{2-}$ ions as also seen for the small and medium overpotential deposition.

The results obtained in this study reveal that classical theories for electrochemical nucleation and growth do not fully describe the route for nanoparticles electrodeposition. The nucleation and growth mode of the electrochemically deposited Pd NPs is overpotential dependent i.e. clusters of nuclei grow either by the fresh reduction of ions at lower overpotentials or by the aggregative growth mechanism at higher overpotentials. The most common particle size is 3.5 nm and 5 nm for a single and a few monolayer equivalent deposition, respectively. The density of small size particles increases as the overpotential increase except in the case where particles grew by an aggregative route as the predominant mechanism. The synthesis of nanoparticles by overpotential control and a thorough understanding of the nucleation and growth mechanisms are extremely important since these influence nanoparticle size distribution, crystal structure and surface morphology, which in turn determines the electrocatalytic properties of the nanoparticles. The synthesised Pd NPs were mono-dispersed with a hemispherical shape and highly pure as examined by XPS, thanks to the surfactant-free electrochemical deposition process. The high dispersibility, to lack of organic contaminants and to small particle size (< 8 nm) of the resulting Pd NPs resulted in the largest specific surface area (4 times greater than commercial Pd-C) and demonstrated high electrocatalytic activity towards ethanol electrooxidation processes. The mass activity ($\approx$ 10,000 mA $mg^{-1}$) for ethanol electrooxidation on these electrochemically deposited Pd NPs is about 35 times higher than the corresponding activity on commercial Pd-C (286 mA $mg^{-1}$) reported to date[64].

This work also investigated the electrochemical deposition of Pd metallic NPs on oxygen and hydrogen terminated diamond substrates in a deaerated 0.1M HCl solution containing only 1mM $PdCl_2$. The structural characterisation revealed that the Pd nanoparticles are better distributed on the hydrogen terminated surface. This is because the hydrogenated surface is more conductive and thus allows higher passage of charge through the surface and

consequently more Pd is deposited. More evidence was provided from XPS spectra that revealed that the Pd photoelectron peak of the HBDD is much higher and almost six times bigger than the Pd peak of the BDD surface. At the same time, the intensity of the O peak is much lower compared to the corresponding of the Pd/BDD, which confirms the presence of hydrogen functionalities on the surface. Cyclic and linear sweep voltammograms showed higher current response and hydrogen evolution on the Pd/HBDD surface in comparison with the Pd/BDD. The evaluation of the electrodeposits towards ethanol oxidation showed much higher densities on the hydrogen terminated surface as well as a greater tolerance of the electrocatalysts towards the intermediate carbonaceous species of ethanol oxidation. This result is due to the high surface area coupled with the hydrogenated surface. Likewise, Pd/HBDD exhibits better performance over a period of 2 hours. As a final overview, boron-doped diamond possesses stable chemical terminations. Hydrogen terminated boron-doped diamond is more conductive than the oxygen terminated surface. The improved conductivity of HBDD probably arises due to the increase in the valence band energy which is achieved through the changes of diamond surface termination from oxygen to hydrogen[67].

# 4.6 Bibliography

1. McGilvray KL, Fasciani C, Bueno-Alejo CJ, Schwartz-Narbonne R, Scaiano JC. Photochemical strategies for the seed-mediated growth of gold and gold-silver nanoparticles. *Langmuir*. 2012;28(46):16148–16155. doi:10.1021/la302814v.

2. Henglein A. Physichochemical Properties of Small Metal Particles in Solution: "Microelectrode" Reactions, Chemisorption, Composite Metal Particles, and the Atom-to-Metal Transition. *J. Phys. Chem.* 1993;97(21):5457–5471. doi:10.1021/j100123a004.

3. Fan FR, Liu DY, Wu YF, Duan S, Xie ZX, Jiang ZY, Tian ZQ. Epitaxial growth of heterogeneous metal nanocrystals: From gold nano-octahedra to palladium and silver nanocubes. *J. Am. Chem. Soc*. 2008;130(22):6949–6951. doi:10.1021/ja801566d.

4. Burda C, Chen X, Narayanan R, El-Sayed MA. *Chemistry and properties of nanocrystals of different shapes*.; 2005. doi:10.1021/cr030063a.

5. Wu XF, Neumann H, Beller M. Palladium-catalyzed oxidative carbonylation reactions. *ChemSusChem*. 2013;6(2):229–241. doi:10.1002/cssc.201200683.

6. Lu J, Zhang H, Chen X, Liu H, Jiang Y, Fu H. Palladium-catalyzed synthesis of aromatic ketones and isoindolobenzimidazoles via selective aromatic C-H bond acylation. *Adv. Synth. Catal*. 2013;355(2-3):529–536. doi:10.1002/adsc.201200743.

7. Ravi Krishna E, Muralidhar Reddy P, Sarangapani M, Hanmanthu G, Geeta B, Shoba Rani K, Ravinder V. Synthesis of $N_4$ donor macrocyclic Schiff base ligands and their Ru (II), Pd (II), Pt (II) metal complexes for biological studies and catalytic oxidation of didanosine in pharmaceuticals. *Spectrochim. Acta - Part A Mol. Biomol. Spectrosc*. 2012;97:189–196. doi:10.1016/j.saa.2012.05.073.

8. Bridier B, Karhánek D, Pérez-Ramírez J, López N. Molecular Understanding of Enyne Hydrogenation over Palladium and Copper Catalysts. *ChemCatChem*. 2012;4(9):1420–1427. doi:10.1002/cctc.201200021.

9. Berhault G, Bisson L, Thomazeau C, Verdon C, Uzio D. Preparation of nanostructured Pd particles using a seeding synthesis approach-Application to the selective hydrogenation of buta-1,3-diene. *Appl. Catal. A Gen.* 2007;327(1):32–43. doi:10.1016/j.apcata.2007.04.028.

10. Ksar F, Sharma GK, Audonnet F, Beaunier P, Remita H. Palladium urchin-like nanostructures and their $H_2$ sorption properties. *Nanotechnology*. 2011;22(30):305609. doi:10.1088/0957-4484/22/30/305609.

11. Kalidindi SB, Oh H, Hirscher M, Esken D, Wiktor C, Turner S, Van Tendeloo G, Fischer RA. Metal@COFs: Covalent organic frameworks as templates for pd nanoparticles and hydrogen storage properties of Pd@COF-102 hybrid material. *Chem. - A Eur. J*. 2012;18(35):10848–10856. doi:10.1002/chem.201201340.

12. Vermisoglu EC, Labropoulos A, Romanos GE, Kouvelos E, Papageorgiou S, Karanikolos G, Katsaros F, Kanellopoulos NK. Hydrogen storage in polymer-functionalized Pd-decorated single wall carbon nanotubes. *J. Nanosci. Nanotechnol.* 2010;10;5971-5980. doi:10.1166/jnn.2010.2610.

13. Chang CM, Hon MH, Leu IC. Outstanding $H_2$ sensing performance of Pd nanoparticle-decorated ZnO nanorod arrays and the temperature-dependent sensing mechanisms. *ACS Appl. Mater. Interfaces*. 2013;5:135–143. doi:10.1021/am302294v.

14. You JM, Han MH, Jeon S. Synthesis of electrochemically reduced graphene oxide bonded to thiodiazole-Pd and applications to biosensor. *J. Nanosci. Nanotechnol.* 2015;15;5961-5698. doi:10.1166/jnn.2015.10294.

15. Fang W, Tang S, Liu P, Fang X, Gong J, Zheng N. Pd nanosheet-covered hollow mesoporous silica nanoparticles as a platform for the chemo-photothermal treatment of cancer cells. *Small*. 2012;8(24):3816–3822. doi:10.1002/smll.201200962.

16. Na H, Zhang L, Qiu H, Wu T, Chen M, Yang N, Li L, Xing F, Gao J. A two step method to synthesize palladium-copper nanoparticles on reduced graphene oxide and their extremely high electrocatalytic activity for the electrooxidation of methanol and Ethanol. *J. Power Sources*. 2015;288:160–167. doi:10.1016/j.jpowsour.2015.04.116.

17. Prodromidis MI, Zahran EM, Tzakos AG, Bachas LG. Preorganized composite material of polyaniline-palladium nanoparticles with high electrocatalytic activity to mEthanol and Ethanol oxidation. *Int. J. Hydrogen Energy*. 2015;40(21):6745–6753. doi:10.1016/j.ijhydene.2015.03.102.

18. Antolini E. Palladium in fuel cell catalysis. *Energy Environ. Sci*. 2009;2(9):915. doi:10.1039/b820837a.

19. Shao M. Palladium-based electrocatalysts for hydrogen oxidation and oxygen reduction reactions. *J. Power Sources*. 2011;196(5):2433–2444. doi:10.1016/j.jpowsour.2010.10.093.

20. Verho O, Akermark T, Johnston EV, Gustafson KPJ, Tai CW, Svengren H, Karkas MD, Backvall JE, Akermark B. Well-defined palladium nanoparticles supported on siliceous mesocellular foam as heterogeneous catalysts for the oxidation of water. *Chem. - A Eur. J*. 2015;21(15):5909–5915. doi:10.1002/chem.201406279.

21. Su R, Tiruvalam R, Logsdail AJ, He Q, Downing CA, Jensen MT, Dimitratos N, Kesavan L, Wells PP, Bechstein R, Jensen H, Wendt S, Catlow CRA, Kiely CJ, Hutchings GJ, Besenbacher F. Designer titania-supported Au-Pd nanoparticles for efficient photocatalytic hydrogen production. *ACS Nano*. 2014;8(4):3490–3497. doi:10.1021/nn500963m.

22. Yang J, Wang D, Han H, Li C. Roles of Cocatalysts in Photocatalysis and Photoelectrocatalysis. *Acc. Chem. Res*. 2012;46(8):1900-1909.

23. Zhang A, Liu M, Liu M, Xiao Y, Li Z, Chen J, Sun Y, Zhao J, Fang S, Jia D, li F. Homogeneous Pd nanoparticles produced in direct reactions: green synthesis, formation mechanism and catalysis properties. *J. Mater. Chem. A.* 2014;2(5):1369–1374. doi:10.1039/C3TA14299J.

24. Ganesan M, Freemantle RG, Obare SO. Monodisperse Thioether-Stabilized Palladium Nanoparticles. *Chem. Mater.* 2007;19:3464–3471.

25. Pandey PC, Singh R. Controlled synthesis of Pd and Pd–Au nanoparticles: effect of organic amine and silanol groups on morphology and polycrystallinity of nanomaterials. *RSC Adv*. 2015;5(15):10964–10973. doi:10.1039/C4RA16201C.

26. Reetz MT, Maase M. Redox-Controlled Size-Selective Fabrication of Nanostructured Transition Metal Colloids. *Adv. Mater*. 1999;11:773–777. doi:10.1002/(SICI)1521-4095(199906)11:9<773::AID-ADMA773>3.0.CO;2-1.

27. Zhang Q, Xie J, Yang J, Lee JY. Monodisperse icosahedral Ag, Au and Pd nanoparticles: size control strategy and Superlattice Formation. *Society*. 2009;3(1):139–48. doi:10.1021/nn800531q.

28. Ananikov VP, Orlov N V., Beletskaya IP, Khrustalev VN, Antipin MY, Timofeeva T V. New approach for size- and shape-controlled preparation of Pd nanoparticles with organic ligands. Synthesis and application in catalysis. *J. Am. Chem. Soc*. 2007;129(23):7252–7253. doi:10.1021/ja071727r.

29. Sato R, Kanehara M, Teranishi T. Homoepitaxial size control and large-scale synthesis of highly monodisperse amine-protected palladium nanoparticles. *Small*. 2011;7(4):469–473. doi:10.1002/smll.201001685.

30. Mazumder V, Sun S. Oleylamine-mediated synthesis of Pd nanoparticles for catalytic formic acid oxidation. *J. Am. Chem. Soc*. 2009;131(13):4588–4589. doi:10.1021/ja9004915.

31. Chen H, Wei G, Ispas A, Hickey SG, Eychmuller A. Synthesis of palladium nanoparticles and their applications for surface-enhanced Raman scattering and electrocatalysis. *J. Phys. Chem. C*. 2010;114(50):21976–21981.

doi:10.1021/jp106623y.

32. Brown KR, Walter DG, Natan MJ. Seeding of colloidal Au nanoparticle solutions. 2. Improved control of particle size and shape. *Chem. Mater*. 2000;12(2):306–313. doi:10.1021/cm980065p.

33. Xia X, Xie S, Liu M, Peng HC, Lu N, Wang J, Kim MJ, Xia Y. On the role of surface diffusion in determining the shape or morphology of noble-metal nanocrystals. *Proc. Natl. Acad. Sci. USA*. 2013;110(17):6669–73. doi:10.1073/pnas.1222109110.

34. Reetz MT, Winter M, Breinbauer R, Thurn-Albrecht T, Vogel W. Size-selective electrochemical preparation of surfactant-stabilized Pd-, Ni- and Pt/Pd colloids. *Chem. - A Eur. J*. 2001;7(5):1084–1094. doi:10.1002/1521-3765(20010302)7:5<1084::AID-CHEM1084>3.0.CO;2-J.

35. Reetz M, Helbig W. Size-selective synthesis of nanostructured transition metal clusters. *J. Am. Chem. Soc*. 1994;116(1 1):7401–7402. doi:10.1021/ja00095a051.

36. Huang S, Ma H, Zhang X, Yong F, Feng X, Pan W, Wang X, Wang Y, Chen S. Electrochemical synthesis of gold nanocrystals and their 1D and 2D organization. *J. Phys. Chem. B*. 2005;109(42):19823–19830. doi:10.1021/jp052863q.

37. Yin B, Ma H, Wang S, Chen S. Electrochemical Synthesis of Silver Nanoparticles under Protection of Poly(N-vinylpyrrolidone). *J. Phys. Chem. B*. 2003;107(34):8898–8904. doi:10.1021/jp0349031.

38. Ma H, Yin B, Wang S, Jiao Y, Pan W, Huang S, Chen S, Meng F. Synthesis of Silver and Gold Nanoparticles by a Novel Electrochemical Method. *ChemPhysChem*. 2004;5(1):68–75. doi:10.1002/cphc.200300900.

39. Pan W, Zhang X, Ma H, Zhang J. Electrochemical synthesis, voltammetric behavior, and electrocatalytic activity of Pd nanoparticles. *J. Phys. Chem. C*. 2008;112(7):2456–2461. doi:10.1021/jp710092z.

40. Rodrguez-Snchez ML, Rodrguez MJ, Blanco MC, Rivas J, Lpez-Quintela M a. Kinetics and Mechanism of the Formation of Ag \rNanoparticles by Electrochemical Techniques: A \rPlasmon and Cluster Time-Resolved Spectroscopic Study. *J. Phys. Chem. B*. 2005;109:1183–1191.

41. Schneider CA, Rasband WS, Eliceiri KW. NIH Image to ImageJ: 25 years of image analysis. *Nat. Methods*. 2012;9(7):671–675. doi:10.1038/nmeth.2089.

42. Taylor RI. X-Ray Photoemission Spectra of Crystalline and Amorphous Si and Ge Valence Bands. *Phys. Rev. Lett*. 1972;29(16):1088–1092.

43. Ding LX, Wang AL, Ou YN, Li Q, Zhao WX, Tong YX, Li GR. Hierarchical Pd-Sn alloy nanosheet dendrites: an economical and highly active catalyst for Ethanol electrooxidation. *Sci. Rep*. 2013;3:1181. doi:10.1038/srep01181.

44. Bard A. J. and Faulkner L. R. Electrochemical Methods: fundamentals and applications. *John Wiley Sons*. 2001.

45. Rezaei M, Tabaian SH, Haghshenas DF. Nucleation and growth of Pd nanoparticles during electrocrystallization on pencil graphite. *Electrochim. Acta*. 2012;59:360–366. doi:10.1016/j.electacta.2011.10.081.

46. Al Abass NA, Denuault G, Pletcher D. The unexpected activity of Pd nanoparticles prepared using a non-ionic surfactant template. *Phys. Chem. Chem. Phys*. 2014;16(10):4892. doi:10.1039/c3cp54531h.

47. Rezaei M, Tabaian SH, Haghshenas DF. Electrochemical nucleation of palladium on graphene: A kinetic study with an emphasis on hydrogen co-reduction. *Electrochim. Acta*. 2013;87:381–387. doi:10.1016/j.electacta.2012.09.092.

48. Naohara H, Ye S, Uosaki K. Thickness dependent electrochemical reactivity of epitaxially electrodeposited palladium thin layers on Au(111) and Au(100) surfaces. *J. Electroanal. Chem*. 2001;500(1-2):435–445. doi:10.1016/S0022-0728(00)00390-9.

49. Naohara H, Ye S, Uosaki K. Electrochemical layer-by-layer growth of palladium on an Au(111) electrode surface: Evidence for important role of adsorbed Pd complex. *J. Phys. Chem. B*. 1998;102(22):4366–4373. doi:Doi 10.1021/Jp980624f.

50. Naohara H, Ye S, Uosaki K. Epitaxial growth of a palladium layer on an Au(100) electrode. *J. Electroanal.Chem*. 1999;473(1):2–9. doi:10.1016/S0022-0728(99)00083-2.

51. Baldauf M, Kolb DM. Formic acid oxidation on ultrathin Pd films on Au(hkl) and

Pt(hkl) electrodes. *J. Phys. Chem.* 1996;100(27):11375–11381. doi:Doi 10.1021/Jp952859m.

52. Zhang Z, Lagally MG. Atomistic Processes in the Early Stages of Thin-Film Growth. *Science (80- ).* 1997;276(5311):377–383. doi:10.1126/science.276.5311.377.

53. Ustarroz J, Ke X, Hubin A, Bals S, Terryn H. New insights into the early stages of nanoparticle electrodeposition. *J. Phys. Chem. C.* 2012;116(3):2322–2329. doi:10.1021/jp210276z.

54. Denuault G, Milhano C, Pletcher D. Mesoporous palladium-the surface electrochemistry of palladium in aqueous sodium hydroxide and the cathodic reduction of nitrite. *Phys. Chem. Chem. Phys.* 2005;7(20):3545–3551. doi:10.1039/b508835f.

55. Cherevko S, Kulyk N, Chung C-H. Nanoporous palladium with sub-10 nm dendrites by electrodeposition for Ethanol and ethylene glycol oxidation. *Nanoscale.* 2012;4(c):103. doi:10.1039/c1nr11316j.

56. Hsieh C Te, Liu YY, Cheng YS, Chen WY. Microwave-assisted synthesis and pulse electrodeposition of palladium nanocatalysts on carbon nanotube-based electrodes. *Electrochim. Acta*. 2011;56(18):6336–6344. doi:10.1016/j.electacta.2011.05.025.

57. Ksar F, Surendran G, Ramos L, Keita B, Nadjo L, Prouzet E, Beaunier P, Hagege A, Audonnet F, Remita H. Palladium nanowires synthesized in hexagonal mesophases: Application in Ethanol electrooxidation. *Chem. Mater*. 2009;21(8):1612–1617. doi:10.1021/cm803492j.

58. Surendran G, Ksar F, Ramos L, Keita B, Nadjo L, Prouzet E, Beaunier P, Dieudonne P, Audonnet F, Remita H. Palladium nanoballs synthesized in hexagonal mesophases. *J. Phys. Chem. C*. 2008;112(29):10740–10744. doi:10.1021/jp801703z.

59. Hasan M, Newcomb SB, Rohan JF, Razeeb KM. Ni nanowire supported 3D flower-like Pd nanostructures as an efficient electrocatalyst for electrooxidation of Ethanol in alkaline media. *J. Power. Sources*. 2012;218:148–156. doi:10.1016/j.jpowsour.2012.06.017.

60. Manoharan R, Goodenough JB. Methanol Oxidation in Acids on Ordered NiTi. *ChemInform*. 1992;23(50):62–62. doi:10.1002/chin.199250062.

61. Hasan M, Newcomb SB, Rohan JF, Razeeb KM. Ni nanowire supported 3D flower-like Pd nanostructures as an efficient electrocatalyst for electrooxidation of Ethanol in alkaline media. *J. Power. Sources*. 2012;218(0):148–156. doi:10.1016/j.jpowsour.2012.06.017.

62. Liang ZX, Zhao TS, Xu JB, Zhu LD. Mechanism study of the Ethanol oxidation reaction on palladium in alkaline media. *Electrochim. Acta*. 2009;54(8):2203–2208. doi:10.1016/j.electacta.2008.10.034.

63. Zhu C, Guo S, Dong S. PdM (M = Pt, Au) bimetallic alloy nanowires with enhanced electrocatalytic activity for electro-oxidation of small molecules. *Adv. Mater*. 2012;24(17):2326–2331. doi:10.1002/adma.201104951.

64. Sawangphruk M, Krittayavathananon A, Chinwipas N, Ultraporous palladium supported on graphene-coated carbon fiber paper as a highly active catalyst electrode for the oxidation of mEthanol. *Fuel Cells*. 2013;13(5):881–888. doi:10.1002/fuce.201200159.

65. Shpilevaya I, Smirnov W, Hirsz S, Yang N, Nebel CE, Foord JS. Nanostructured diamond decorated with Pt particles: preparation and electrochemistry. *RSC Adv*. 2014;4(2):531. doi:10.1039/c3ra43763a.

66. Nebel CE, Rezek B, Shin D, Watanabe H. Surface electronic properties of H-terminated diamond in contact with adsorbates and electrolytes. *Phys. Status Solidi Appl.Mater. Sci*. 2006;203(13):3273–3298. doi:10.1002/pssa.200671401.

67. Nebel CE. Surface-Conducting Diamond. *Science*. 2007;318(5855):1391–1392.

# Chapter 5

# Electrochemical modification and Surface Pre-treatment of Diamond electrodes with Pd-Sn and Pd-Ni nanoparticles for Ethanol Electrooxidation

## 5.1 Introduction

Fuel cells have received increasing attention in recent years due to their ability to increase overall energy efficiency compared to conventional power sources, such as internal combustion engines or batteries. Particularly, the direct alcohol fuel cells (DAFCs) have attracted current research effort because of their ability to convert chemical energy into electricity and therefore act as power sources in portable electronics, transportation and other emerging applications[1–4].

Hybrid materials, consisting of graphitic nanostructures (e.g. carbon nanotubes or graphene) and various metal particles have been widely studied as functional components in catalysis and fuel cell applications[4–6]. Metal nanoparticle surface modification of carbon substrates constitute common catalysts and have a plethora of benefits to the fuel cell performance[7–11]. Examples of the benefits include: the increase of the oxidation efficiency of alkaline electrolytes compared to the non-functionalised catalyst, the oxidative removal of some poisons and consequently the improved tolerance as well as the durability of electrocatalyst. Boron-doped diamond is a good alternative to other carbon materials due to the special features that have been described in previous reports[12–19] and discussed in chapters 3

and 4. Diamond electrodes can be modified by metal nanoparticles that enhance its sensitivity towards various analytes compared to the unmodified electrode area[12,20]. However, the resistance of diamond to electrocorrosion is that makes BDD so attractive, especially in the field of fuel cells[21–23].

Another interesting feature is the stable chemical surface termination that diamond electrodes exhibit. The surface can be altered from oxygenated to hydrogenated termination by subjecting the electrodes to microwave plasma of hydrogen [24–27]. Shpilevaya *et al.* have shown that metal nanoparticles on a hydrogen-terminated diamond electrode can differ from those on an oxygen terminated electrode in microstructure[16]. As a result, the hydrogen terminated surface provides stronger electrochemical response and improved physical stability[28]. Nebel *et al*. also have proved that a high concentration of hydrogen functionalities on the surface can increase conductivity[29]. According to the literature, Pt is one of the most effective, widely used catalysts; nevertheless, the high cost as well as its tendency to be poisoned by the intermediates of ethanol species during the ethanol oxidation can be prohibitive for future use[30,31]. Because of the drawbacks of the Pt catalyst, core-shell structures[13,32–37] and the embodiment of non-noble metals[13,34,38] promise to enhance the stability of the electrocatalysts in DAFCs as well as to reduce their cost. One of the challenges in this field is the development of efficient catalysts capable to produce $CO_2$ after the ethanol oxidation and in other words break the C-C bonds[39]. Pd has recently shown that it can be more active, stable and poison tolerant towards the intermediates of ethanol species[40–43]. Furthermore, Pd is fifty times more earth abundant than Pt and is a promising candidate to replace the latter in the field of alkaline fuel cells[44]. Pd can also be used in numerous other electrochemical applications including pharmaceutical applications[45], organic synthesis[46,47], sensing[48] and hydrogen storage[49,50].

In this work, Pd-Sn and Pd-Ni modified hydrogen (HBDD) and oxygen-terminated (BDD) boron-doped diamond electrodes are proposed for ethanol oxidation of relevance to the direct alkaline fuel cells (DAFC). The motivation for this work is ultimately the continuation of our understanding of how such core-shell structures behave on diamond compared to similar structures on other forms of carbon[13]. The second objective of this study is to gain further understanding of how different core metals behave on diamond and how they can affect the stability, electrochemical activity and finally the tolerance ratio towards the oxidation of ethanol. In both these cases, the electrochemical modifications introduced by the electrodeposition of the metal nanoparticles reflect the particular properties of the metal, the interface interaction between the two metals and their interaction with the underlying diamond.

## 5.2 Aims of the project and principal outcomes

The aim of this work is the modification of hydrogen (HBDD) and oxygen (BDD) terminated diamond electrodes with pure Pd, Pd-Sn and Pd-Ni nanoparticles respectively. For the synthesis of the HBDD and BDD electrodes, a potentiostatic and a two-step electrochemical method involving the electrodeposition of Sn or Ni followed by Pd were used. The modification of the HBDD and BDD electrodes with Sn or Ni as well as Pd by forming shell-core nanoparticles leads to higher electrochemical activity. The electrochemical evaluation of the catalysts involved the oxidation of the ethanol. Higher electrochemical response towards the electrooxidation of ethanol is observed for the bimetallic catalysts due to electronic effects between the interfaces of the two metals. Chronopotentiometric measurements revealed that Pd is more stable when anchored to the Ni nanoparticles towards the ethanol electrooxidation in alkaline media. All the aforementioned catalysts of this research possessing good stability and efficiency towards ethanol electrooxidation in alkaline media over a long operational time.

# 5.3 Experimental section

## 5.3.1 Chemical reagents

Chemical reagents were purchased from Sigma-Aldrich and used as received without any further purification. These were: palladium (II) chloride ($PdCl_2$); and hydrochloric acid (HCl) aqueous. Tin (II) methanesulfonate 50% aqueous solution ($C_2H_6O_6S_2Sn$), methanesulfonic acid 70% aqueous solution ($CH_3SO_3H$), nickel (II) nitrate hexahydrate ($Ni(NO_3)_2 \cdot 6H_2O$), acetic acid (AcOH) and sodium acetate (NaOAc) were obtained from Alfa Aesar. All aqueous solutions were freshly prepared, using milli-Q water (18 MΩ cm). All the solutions were deoxygenated using oxygen-free nitrogen gas for a minimum of 20 minutes when the experiments required oxygen-free solutions.

## 5.3.2 Equipment and experimental set-up

BDD wafers ([B]>$10^{20}$ $cm^{-3}$) of 10 x 10 x 0.6 mm were obtained from Element Six Co (UK) and mounted in a home-built PTFE holder with a circular area of 0.38 $cm^2$ exposed to the electrolyte. The electrochemical measurements were performed with an Autolab PGSTAT 128N potentiostat/galvanostat. The electrochemical depositions were conducted at room temperature (24 ± 1.0°C), using a standard three electrode cell comprised of a Pt counter electrode, a Ag/AgCl or Hg/HgO reference electrodes. The analysis was done with OriginPro 8.5 software (OriginLab Ltd.). The morphology of the Pd-Sn deposits was characterised by a Hitachi S530 SEM with a 20 kV acceleration voltage. The morphology of the Pd-Ni deposits was characterised by a high resolution Field Emission Gun-Scanning Electron Microscope (FEGSEM), LEO Gemini 1525. All the images were taken at 400K magnification with an acceleration voltage of 20 kV and a working distance (WD) of around 3.5 mm. The

composition of the deposits was measured by XPS using an Al Kα (1486.6 eV) X-ray source. XPS data were curve fitted with a Shirley background[52] and CasaXPS software[51]. The C 1s peak was calibrated to 285 eV with the following relative sensitivity factors (R.S.F.): C 1s (1.0), O 1s (2.93), Pd 3d (16.0), Sn 3d (25.1) and Ni 2p (22.2).

## 5.3.3 Fabrication and working electrodes

### 5.3.3.1 Modification of HBDD electrodes

Prior to deposition, all BDD electrodes were put in MW-CVD at 600 °C, 45 Torr pressure, 1.5 kW microwave power and $H_2$ gas flow at 200 sccm for a duration of 45 minutes. At the end of 45 minutes, hydrogen plasma etching was achieved, the microwave power reduced to zero and the samples cooled down naturally to room temperature in the presence of hydrogen gas. The electrodes were taken out from MW-CVD and examined for hydrogen termination by XPS.

Pd catalyst was then electrodeposited onto HBDD from a deaerated 0.1M HCl solution containing 1mM $PdCl_2$ by a potentiostatic method. The deposition potential was held at -0.15V (vs Ag/AgCl) until 2.6, 5.2 and 10.4 $mC/cm^2$ charge passed through the surface. The corresponding metal loading of these charges was 1.45, 2.90 and 5.80 $\mu g/cm^2$ respectively. The electrodeposition potential was chosen from the Pd reduction peak found by cyclic voltammetry on bare diamond wafer in the $PdCl_2$ solution. The CVs were done over a potential range (-0.1V to -0.4V) in which Pd reduction occurs[53].

The second electrode comprised Pd-Sn/HBDD, with Sn being electrodeposited onto HBDD from a deaerated 0.26M $C_2H_6O_6S_2Sn$ in 1M $CH_3SO_3H$ solution through cyclic voltammetry at a potential between -0.6V and +0.5V (vs Ag/AgCl) at 0.01 V/s for one cycle. The Sn/HBDD electrode was then removed, rinsed with ultrapure water and dried with $N_2$. Pd

electrocatalytic particles were electrodeposited onto Sn/HBDD (158 mC/cm$^2$: 97 μg/cm$^2$) from a deaerated 0.1M HCl solution containing 1mM $PdCl_2$. Again, a potentiostatic method was used in which the potential was held at -0.15V (vs Ag/AgCl) until 2.6, 5.2 and 10.4 mC/cm$^2$ passed through the electrode surface giving 1.45, 2.90 and 5.80 μg/cm$^2$ palladium loading as referred to in the previous paragraph.

### 5.3.3.2 Modification of BDD electrodes

To ensure fresh, active surfaces, free of deactivating layers and contamination, which consequently leads to better signal to noise in the electrochemical data[54] all working electrodes were polished on a polishing machine with alumina micropolish II (Buehler, UK) of decreasing particle size (1 μm to 0.05 μm) on soft lapping pads (Buehler, Chemonet I for 8'' wheel). When the polishing had been finished with the 1 μm alumina, the electrodes were rinsed gently with distilled water and were sonicated for 5 minutes in water and acetone (1:1 ratio). This was followed by polishing with 0.05 μm alumina, a rinse in water, and sonication for 30 minutes in acetone. The electrodes were then cycled in 0.1M nitric acid between -1.7V and 2.5V for 10 sweeps, which yields a high concentration of oxygen functionalities at the electrode surface[16].

The Pd catalyst was then electrodeposited onto BDD from a deaerated 0.1M HCl solution containing 1mM $PdCl_2$ by a potentiostatic method. The deposition potential was held at -0.15V (vs Ag/AgCl) until 5.2 and 21 mC/cm$^2$ charge passed through the surface, which correspond to a metal loading 2.9 and 11.6 μg/cm$^2$ respectively.

The second electrode, which consisted of Pd-Ni/BDD, was fabricated by electrodeposition of Ni NPs onto BDD from a deaerated 10mM [$Ni(NO_3)_2 \cdot 6H_2O$] in acetate buffer solution by a potentiostatic method. The deposition potential was held at -1.2V (vs Ag/AgCl) until 658 mC/cm$^2$ charge was passed through the surface. The Ni/BDD electrode was then removed from the solution, rinsed with ultrapure water and dried with $N_2$. Pd

electrocatalytic particles were electrodeposited onto Ni/BDD (5.2 mC/cm$^2$: 2.9 μg/cm$^2$) from a deaerated 0.1M HCl solution containing 1mM $PdCl_2$. Again, a potentiostatic method was used in which the potential was held at -0.15V (vs Ag/AgCl) until 5.2 and 21 mC/cm$^2$ passed through the electrode surface giving 2.9 and 11.6 μg/cm$^2$ palladium loading.

# 5.4 Results and discussion

## 5.4.1 Oxidation of ethanol using Pd-Sn nanoparticles on hydrogen-terminated diamond electrodes

### 5.4.1.1 Morphology and XPS characterization of the deposits on HBDD

SEM images of Pd and Pd-Sn after 10.4 mC/cm$^2$ passage of charge at the potential described in the previous section are shown in figure 5-1 (a-b), respectively. Pd particles in a non-uniform manner are displayed in figure 5-1 (a-b). The size of the particles is approximately 10 nm and seems to be similar throughout the electrode surface at this metal loading. The non-uniform nature comes from the lateral conductivity of the diamond as well as of the non-uniform distribution of the B dopant as described in a previous report[55]. Elemental mapping provides information about the elemental composition of the electrodes and shows Pd-Sn alloys (Figure 5-1 (c)). Pd nanoparticles partially cover the Sn nanoparticles and allow the two metals to exchange metallic properties and facilitate their electronic interaction. The elemental mapping investigation also found that the Sn particles were preferentially deposited on the electroactive areas of diamond, whereas the Pd nanoparticles cover these areas. In other words, the conductive site of the underlying diamond and the active sites of Sn nanoparticles act as reactive centres for the deposition of Pd nanoparticles. The elemental mapping suggests that

Pd nanoparticles are able to be deposited on areas with a lower B concentration whilst Sn is less likely to be deposited on such areas.

XPS was performed in order to investigate the elemental composition of Sn, Pd and Pd-Sn at the diamond interface for the samples in figure 5-2. Figure 5-2 (a) shows the survey scans of the Sn, Pd and Pd-Sn modified HBDDs, respectively. The wide scans indicate that these electrodes contain C, O, Pd and Pd-Sn. The Sn modified HBDD has Sn $3d_{5/2}$ and Sn $3d_{3/2}$ peaks at 488 and 497.5 eV respectively[56] (Figure 5-2 (b)). After the modification with Pd, the Sn $3d_{5/2}$ and Sn $3d_{3/2}$ peaks are shifted slightly at 487.5 and 497 eV respectively (Figure 5-2 (b)). Clearly the Sn signal was significantly reduced in the case of the Pd-Sn modified HBDD, which indicates that the Sn particles were covered by Pd. The latter can also be derived by the fact that the intensity of the Sn peak of the Sn/HBDD electrode was initially quite strong and after the modification with Pd this peak was attenuated five times. Furthermore, Pd peak has a Pd $3d_{5/2}$ and Pd $3d_{3/2}$ peaks at 338 and 343 eV respectively. The Pd-Sn modified HBDD showed also a tiny shift as seen in figure 5-2 (c). The Pd $3d_{5/2}$ and Pd $3d_{3/2}$ peaks were shifted at 337 and 342 eV respectively, which implies some electronic interaction between the two metals.

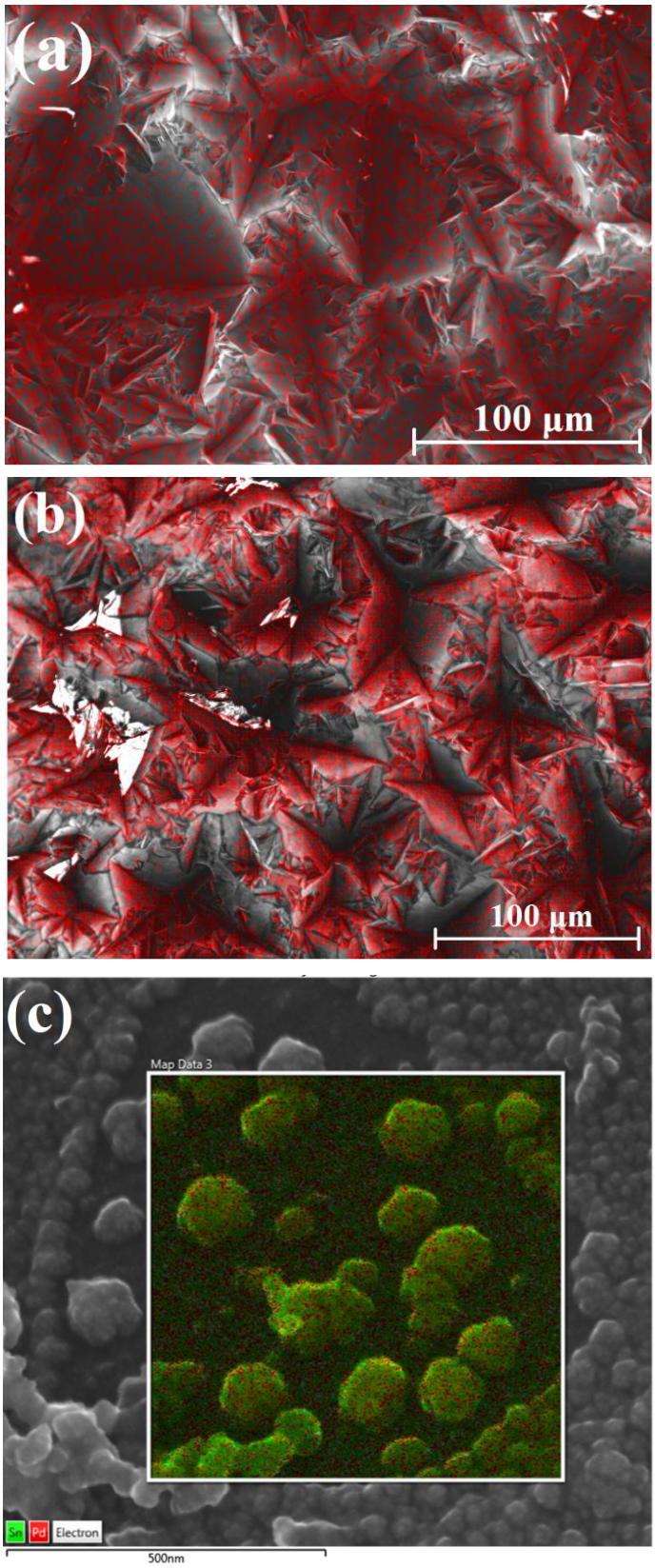


**Figure 5-1** SEM images of (a) Pd deposited on HBDD electrodes and (b) Pd-Sn on HBDD through chronoamperometry at -0.15V for the Pd and cyclic voltammetry between -0.6V and +0.5V at scan rate of 0.01 V/s for the Sn. (c) Elemental mapping of Pd-Sn modified HBDD.

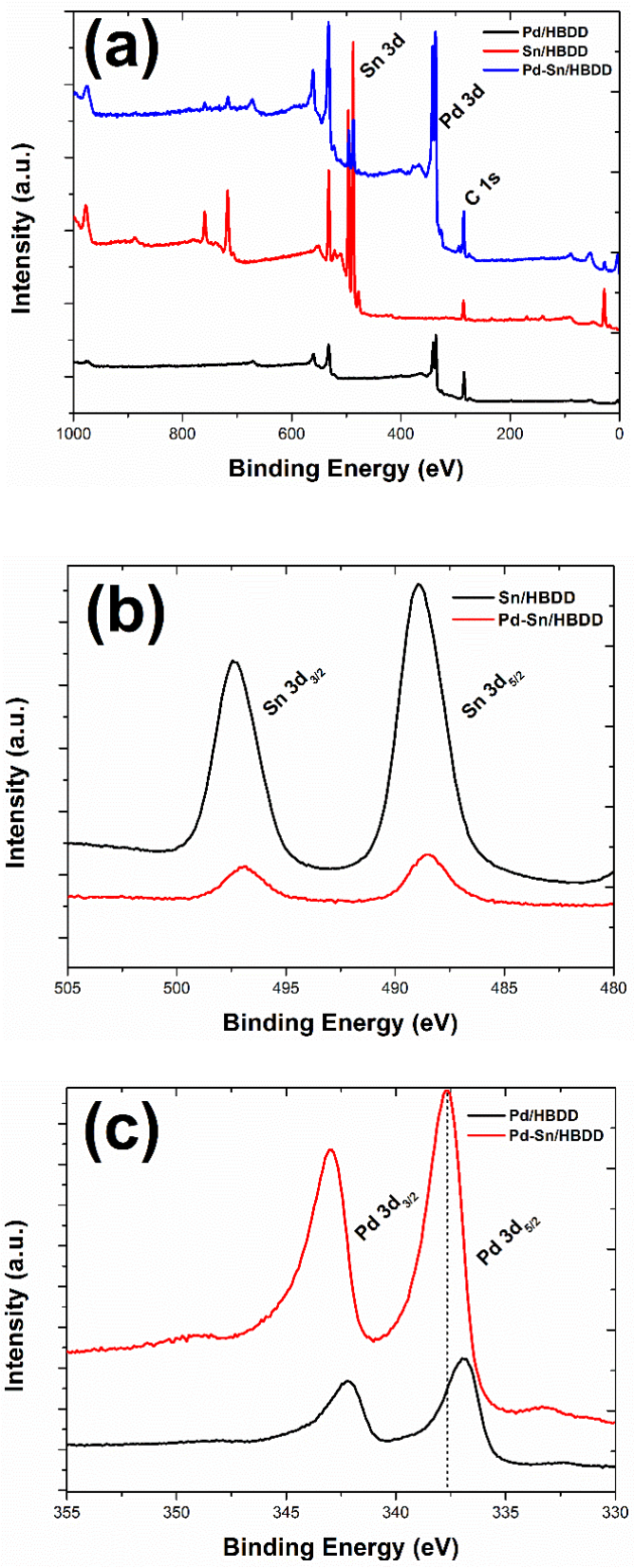


**Figure 5-2** (a) XPS spectra of wide scans of the Sn/HBDD, Pd/HBDD and Pd-Sn/HBDD, respectively. (b) Typical Sn 3d peaks of Sn and Pd-Sn modified HBDD catalysts, respectively. (c) Typical Pd 3d peaks of the Pd and Pd-Sn modified HBDD catalysts, respectively.

## 5.4.1.2 Voltammetric characterisation

### 5.4.1.2.1 Electrodeposition of the electrocatalysts

A typical cyclic voltammogram of bare HBDD in a solution containing 0.26M $C_2H_6O_6S_2Sn$ in 1M $CH_3SO_3H$ is shown in figure 5-3 (a). The Sn is deposited in the cathodic scan in the potential range of -0.49V and - 0.6V and stripped out in the anodic scan with a sharp peak at potential -0.35V. A pronounced nucleation loop at -0.58V in the cathodic scan indicates that Sn deposition on HBDD surface occurred through the formation of small nuclei followed by further growth. A typical voltammogram of bare HBDD in a solution containing 1mM $PdCl_2$/0.1M HCl is also illustrated in figure 5-3 (b). The Pd is deposited in the forward can scan in the potential range of +0.22V and -0.37V. The cathodic current peaked initially at 0.15V (peak $C_1$) and stayed steady until reached the sufficient overpotential value at -0.25V and then increased sharply to a maximum at -0.33V (peak $C_3$) near the diffusion-limited reduction of Pd ions. Beyond this peak the cathodic current decreased as the mass transfer became diffusion limited, reached a minimum at -0.34V (peak $C_4$) followed by an increase due to bulk $H_2$ evolution (peak $C_5$). The potential region of 0.22-0.15V completely represents the Pd metal deposition without hydrogen underpotential deposition ($H_{UPD}$), and after this point i.e, in the cathodic range between -0.15V and -0.37V deposition occurs simultaneously with $H_{UPD}$ onto the freshly deposited Pd , in which peaks $A_2$, $A_4$, $A_5$) are due to the H desorption process. The $A_1/C_1$ peaks show the Pd stripping from the electrode surface having a maximum peak at +0.58V and the reduction of it with a peak at +0.14V in the anodic and cathodic scan respectively.

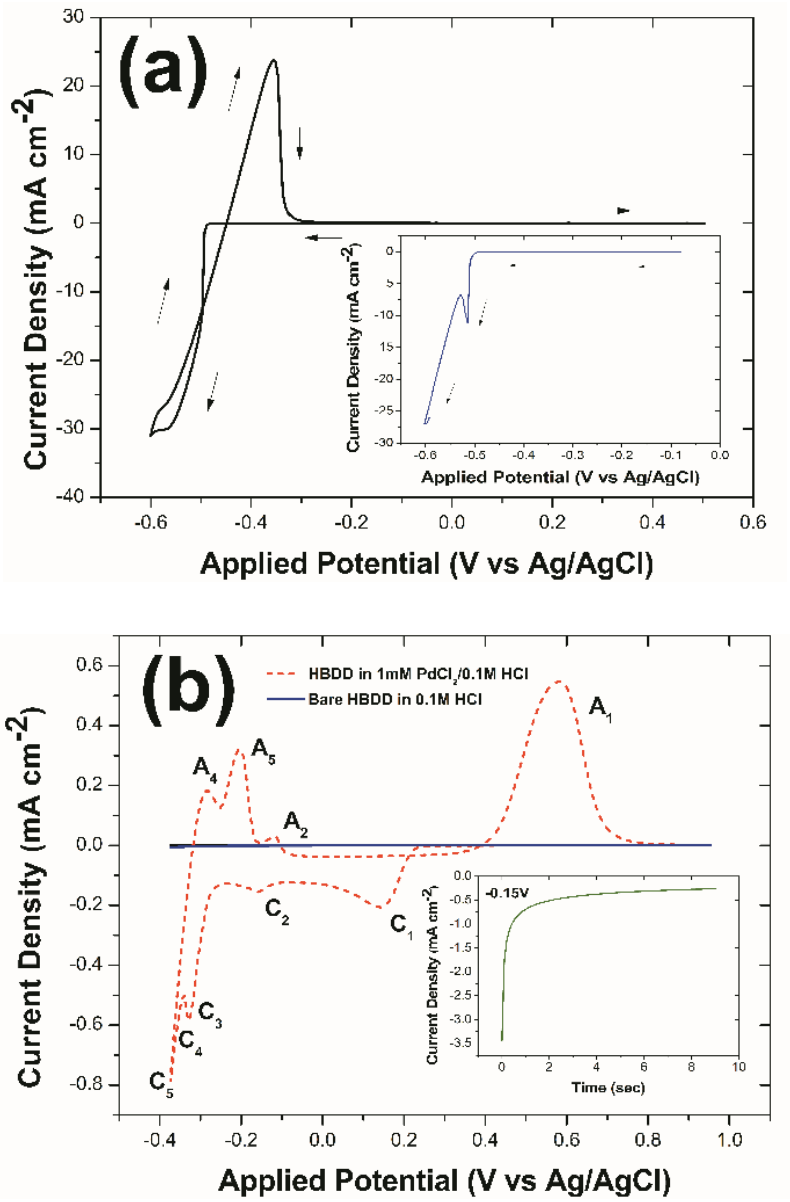


**Figure 5-3** (a) Cyclic voltammogram of bare HBDD in a solution containing 0.26M $C_2H_6O_6S_2Sn$ in 1M $CH_3SO_3H$ at scan rate of 0.01 V/s (inset: linear sweep voltammogram of bare HBDD in 0.26M $C_2H_6O_6S_2Sn$ in 1M $CH_3SO_3H$). (b) Cyclic voltammogram of bare HBDD in a solution containing 0.1M HCl and 1mM $PdCl_2$/0.1M HCl respectively at scan rate of 0.01 V/s (inset: chronoamperogram of Pd deposition in 1mM $PdCl_2$/0.1M HCl on bare HBDD at constant potential of -0.15V).

### 5.4.1.2.2 Electrochemical activity of the electrocatalysts

The electrochemical activity of the electrocatalysts was characterised by cyclic voltammetry in 0.5M KOH. The behaviour of Pd nanoparticles on fairly oxidised surface and on hydrogen terminated surface was initially compared (Figure 5-4 (a)). In figure 5-4 (a)

various features are observed, (i) Pd oxidation and reduction peaks ($A_1/C_1$) at +0.05V and -0.23V can be attributed to the formation of a palladium oxide layer on the surface of the catalyst. The exact mechanism of the Pd oxidation remains unclear[57], and $OH^-$ ions are generally accepted to be first chemisorbed in the initial stage of the oxide formation and they transform into higher valence oxides at higher potentials, as reported in literature[58–60], (ii) Hydrogen adsorb and desorb at the Pd surface at -0.65V and -0.9V ($C_2$, $C_3$ and $A_3$); (iii) a prepeak ($A'_1$) appears at -0.2 V in the anodic scan before the main Pd surface oxidation process start, which corresponds to oxidation at favourable sites on the palladium surface[61]. The corresponding oxide reduction peak for $A_1$ may appear towards incomplete oxidation and reduction (peak $A_1/C_1$) of the Pd surface as described in elsewhere[61]. However, the hydrogen-terminated Pd/HBBD electrode showed higher current densities and ability to adsorb hydrogen ions than the oxygen terminated Pd/BDD electrode. This is likely to arise from the fact that there is a high concentration of hydrogen functionalities on the surface and the overall conductivity is increased according to a previous report[29]. Hence, this study was focused on the hydrogen-terminated BDD surfaces as the working electrode and modification of the electrode by electrochemically deposited shell-core Pd-Sn nanoparticles towards electrooxidation of ethanol. According to the SEM images both the Sn and Pd nanoparticles appear to be spherical. The cyclic voltammogram of Sn/HBDD (Figure 5-4 (b)) does not show electrochemical activity in potential range of -0.9V to +0.1V and thus, Sn is inactive within the electrochemical window where Pd is electrocatalytically active. However, a cathodic peak at potential more negative than -1.1V and an anodic peak at -1.02V in the reverse scan are seen, which is due to deposition and dissolution of unknown electroactive species onto the Sn surface. The cyclic voltammogram of 5.2 $mC/cm^2$ passage of charge (2.90 $\mu gr/cm^2$) of the Pd onto HBBD and Sn/HBDD electrode are illustrated in figure 5-4 (c). Various features, as the ones observed for the Pd/OBDD and Pd/HBDD catalysts, are distinguished at the same

potential range. However, the feature at -0.22V in the reverse (anodic) scan which only occur in the Pd-Sn modified HBDD and are not seen at its Pd, bare HBDD or Sn modified counterparts[62–64] (see also figure 5-4 (b)). The aforementioned features are consistent with the Sn particles serving as reactive centres for the subsequent deposition of Pd, such that the resultant Pd-Sn nanoparticles seem to have core-shell structures. The modification of the HBBD electrode with transition metal Sn and noble metal Pd by forming shell-core nanoparticles leads to higher currents and more hydrogen adsorption. Regarding the hydrogen evolution, more evidence is provided from the linear sweep voltammogram in figure 5-4 (d). The hydrogen evolution on Pd-Sn/HBDD surface occurs in cathodic scan at the potential of -1.0V, the onset potential is much lower when Pd interacts with the underlying Sn compare to Pd/HBDD electrode alone in which hydrogen evolution occurs at -1.07V. This result is evidenced that a thin layer of Pd has been formed on top of the Sn helping the electronic interaction between the two metals.

The metal coverage of Pd can be estimated from the charge obtained from the area under the voltammogram applying Faraday's Law. Determining the ratio of the charge required for desorption of an oxygen monolayer on the Pd (111) surface[65] (0.424 mC $cm^{-2}$) to that of $Q_o$ which is the coulombic charge of the oxygen desorption on the Pd surface, the electroactive surface area (EAS) of the pure Pd electrocatalyst can be also estimated. In addition, the specific surface area (SSA) can be defined as the electroactive surface area divided by the metal loading. Both EAS and SSA are included in the Table 5-1 (see section 5.4.1.3).

The EAS and the SSA are almost the same for the two catalysts. The particles size is also approximately the same, which is verified by the SEM images. The difference between the Pd/HBDD and the bimetallic catalyst is roughly 1.5 nm which cannot be observed from the SEM images.

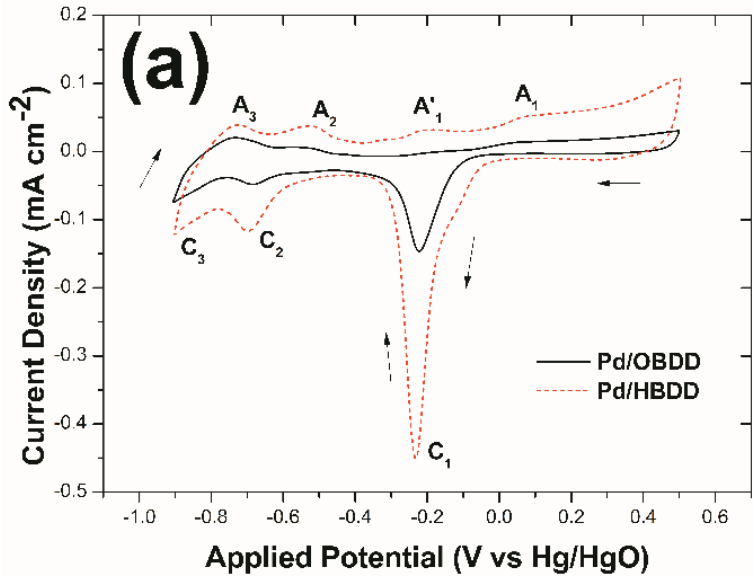
(a)
A3
A2
A'1
A1
C3
C2
C1
Pd/OBDD
Pd/HBDD
Current Density (mA cm-2)
Applied Potential (V vs Hg/HgO)

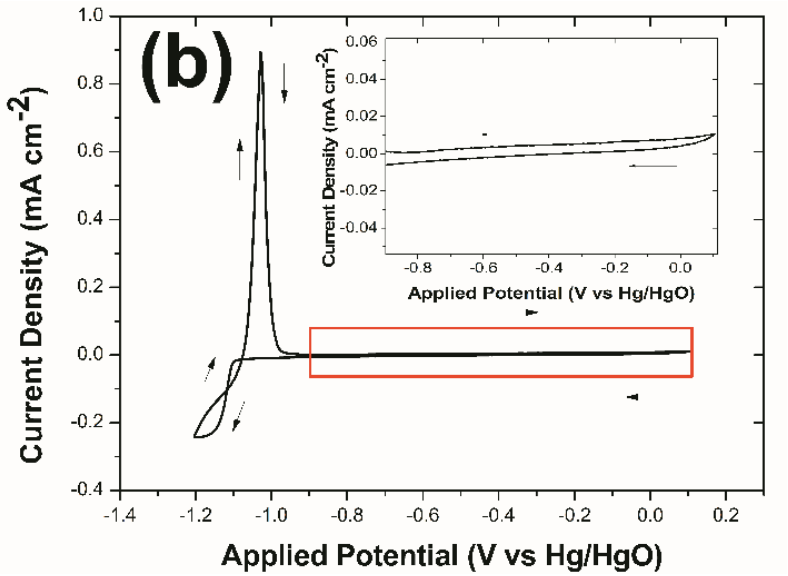
(b)
Current Density (mA cm-2)
Applied Potential (V vs Hg/HgO)

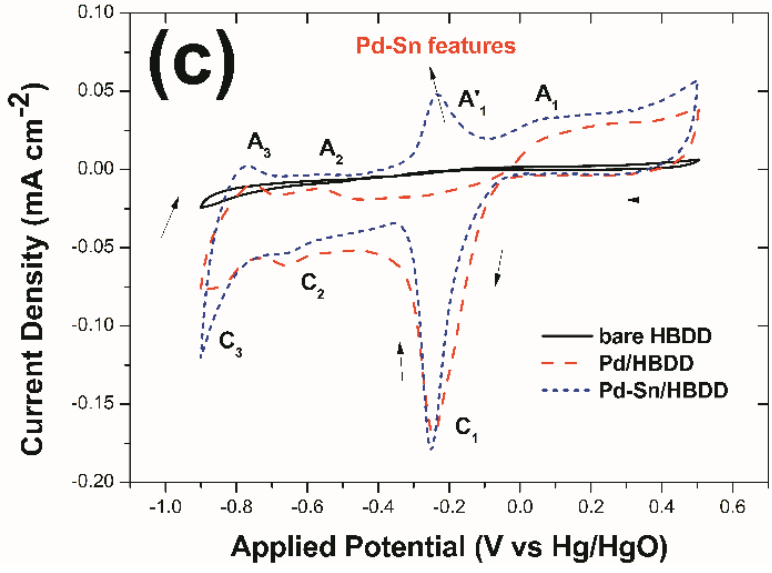
(c)
Pd-Sn features
A'1
A1
A3
A2
C2
C3
C1
bare HBDD
Pd/HBDD
Pd-Sn/HBDD
Current Density (mA cm-2)
Applied Potential (V vs Hg/HgO)

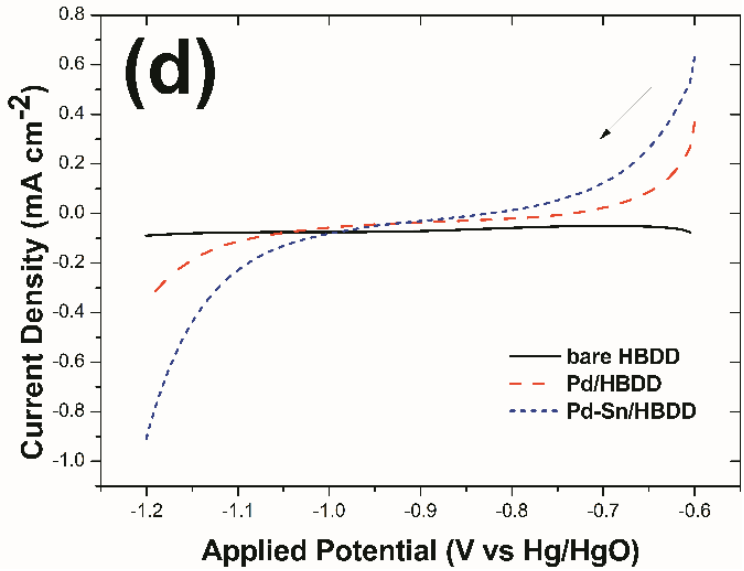


**Figure 5-4** Cyclic voltammogram of (a) Pd/OBDD and Pd/HBDD (5.80 μg/cm$^2$), (b) Sn/HBDD (97 μgr/cm$^2$), (c) Pd and Pd-Sn modified HBDD (2.90 μg/cm$^2$), and (d) Linear sweep voltammograms of the Pd and Pd-Sn modified HBDD (2.90 μg/cm$^2$), respectively in 0.5M KOH solution at scan rate of 0.02 V/s (all CVs were started from open circuit potential).

### 5.4.1.3 Evaluation of Pd-Sn electrocatalysts preparation conditions on ethanol oxidation characteristics

The electrocatalytic activity of the Pd/HBDD and Pd-Sn/HBDD towards the oxidation of ethanol was evaluated through cyclic voltammetry. The modified electrodes were placed in solutions containing 0.5M KOH+1M EtOH and cyclic voltammograms were obtained. The results are shown in figure 5-5 (a) and 5-5 (b). The onset potential for electrooxidation of ethanol on the clean electrode is observed at -0.5V, with no current response before -0.5V, which implies that the electrode is inactive before this overpotential. A considerable amount of current passed through the electrode as the potential scanned positively (anodic scan) higher than the respective onset electrooxidation potential and the peak current at around -0.1V, -0.12V and -0.02V were due to the ethanol oxidation onto electrodes Pd/HBDD (1.45μg/cm$^2$), Pd-Sn/HBDD (2.90 μg/cm$^2$), and Pd-Sn/HBBD (5.80 μg/cm$^2$), respectively as shown in

figure 5-5. However, the peak position is slightly shifted as the Pd loading increased, which is due to the electronic interaction of the Pd in outer shell of the nanoparticles with the Sn core. The peak in the forward scan refers to the oxidation of the fresh ethanol species accumulated on the surface. All electrodes are deactivated at the same potential around +0.1V and reactivated again in the reverse scan (cathodic) at -0.18V giving a second oxidation wave at around -0.24V [62,64]. The second peak implies the oxidation of the incomplete carbonaceous species of the ethanol. Previous studies suggested that the reduced current at more positive potentials was related to the formation of a Pd oxide layer on the surface of the electrode at higher potentials[58,66–68]. The formation of the oxide layer can block the adsorption of the reactive species onto the Pd surface and lead to a decrease in the electrocatalytic activity. As long as positive sweep proceeds more Pd oxide covers the surface of the electrode and therefore the current of the ethanol oxidation is further decreased[57]. The overall electrode resistance to poisoning by the incomplete oxidation of the adsorbed carbonaceous species ($CH_3CO_{ads}$) of the ethanol is correlated to the ratio of the forward oxidation current peak ($I_f$) and the backward oxidation current peak ($I_b$)[69,70]. In figure 5-6 (a), Pd-Sn modified HBDD with the lowest amount of Pd (2.6 mC/cm$^2$ charge i.e., 1.45 μg/cm$^2$,) gives higher current responses compared to the Pd/HBBD electrode but the resistance to poisoning is relatively low (see also Table 5-1). The tolerance ratio towards the ethanol is getting larger when the amount of Pd is increased as it is shown in figure 5-5 (b) and 5-5 (c). Conversely, the Pd-Sn/HBDD with the higher Pd loading in figure 5-5 (b) (2.90 μg/cm$^2$) not only showed higher current densities in comparison with Pd/HBDD itself but also the resistance of the electrode to poisoning by the absorbed ethanol species was higher than the Pd/HBDD. To be more precise, the tolerance ratio of the Pd-Sn/HBDD with 2.90 μg/cm$^2$ loading seems to have its highest value ($I_f/I_b$=1.63) not only compared to the Pd/HBDD of the same metal loading ($I_f/I_b$=0.89) but also of the one that

has twice the amount of palladium ($I_f/I_b$=1.35). Furthermore, there was a slight shift in the potential from -0.1V to -0.12V for the Pd modified HBDD and the Pd-Sn/HBDD, respectively.

On the other hand, when the loading of the catalyst increased, the current responses of both Pd/HBDD and Pd-Sn/HBDD were almost the same (Figure 5-5 (c)). That means that the electronic interaction between the two metals started to disappear because thicker overlayers of Pd onto the inner Sn metal nanoparticles began to form. Consequently, the threshold of Pd loading and therefore the higher ratio of resistance to poisoning by the adsorbed ethanol species was 2.90 μg/cm$^2$ (5.2 mC/cm$^2$ passage of charge).

Stability tests of up to 1 hour and 40 minutes voltammetry in the ethanol solution showed good stability. Despite a small initial current drop during the first 2-3 scans, Pd and Pd-Sn nanoparticles are bonded in a stable fashion on the hydrogen-terminated surface.

Experiments were also conducted on Sn electrodes with fifteen times more Pd on the surface and the result showed that there is no interaction between the two metals. Clearly, a huge overlayer of Pd was created onto the surface of Sn nanoparticles and therefore, the current increased without exceeding that of pure Pd. In addition the tolerance towards the ethanol oxidation was reduced due to the big Pd overlayer, which hid the electronic properties of the two metals as well as the properties and extra conductivity from the hydrogen-termination. An overall picture of the mechanism of ethanol oxidation reaction and at the same time the role of various Pd loading towards the latter oxidation reaction is illustrated in Figure 5-6.

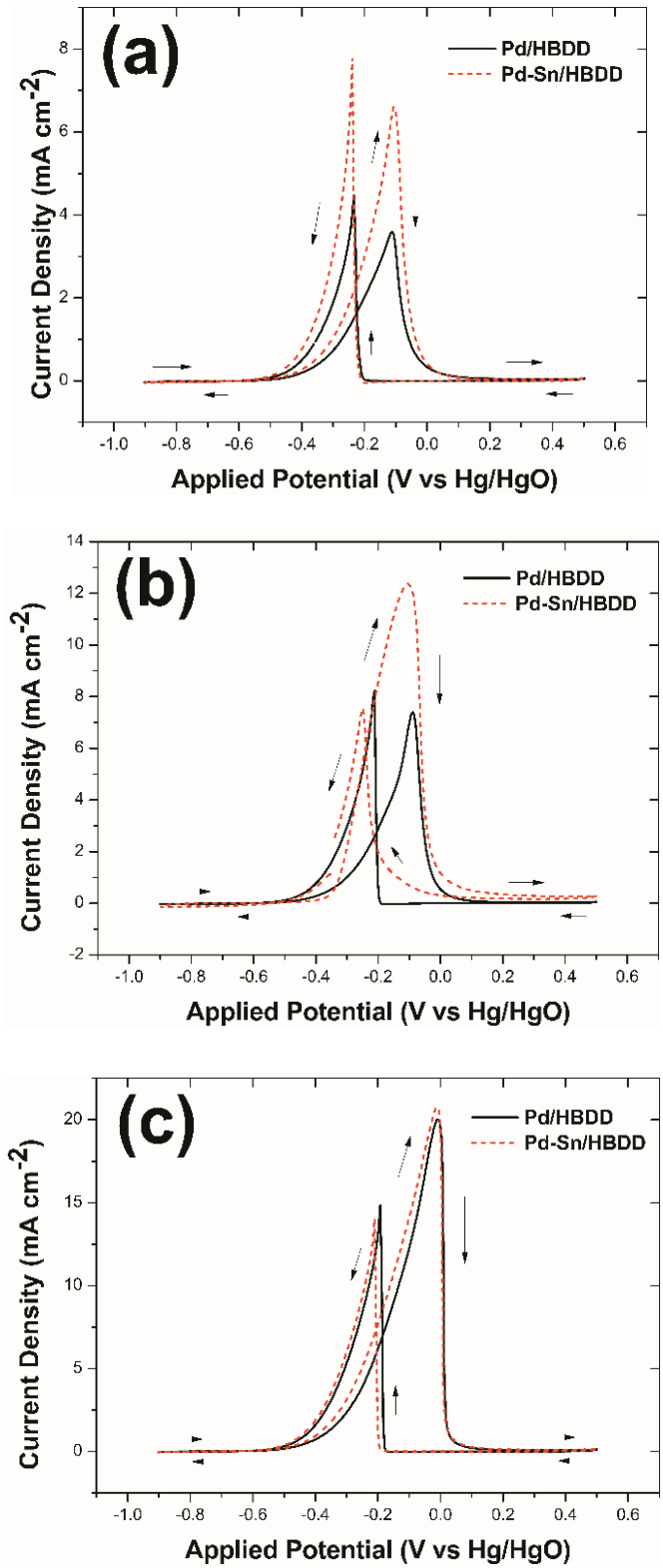


**Figure 5-5** (a, b) Cyclic voltammograms of Pd and Pd-Sn modified HBDD with 1.45 μg/cm$^2$ (i.e., 2.6 mC/cm$^2$ charge) and 2.90 μg/cm$^2$ (i.e., 5.2 mC/cm$^2$ charge) Pd loading, respectively in 0.5M KOH and 1M EtOH at scan rate of 0.02 V/s. (c) Cyclic voltammograms of Pd and Pd-Sn modified HBDD (with 5.80 μg/cm$^2$ Pd loading) in 0.5M KOH and 1M EtOH at scan rate of 0.02 V/s. (all CVs were started from open circuit potential). Cyclic voltammograms shown here are steady state CVs taken after 10 cycles.

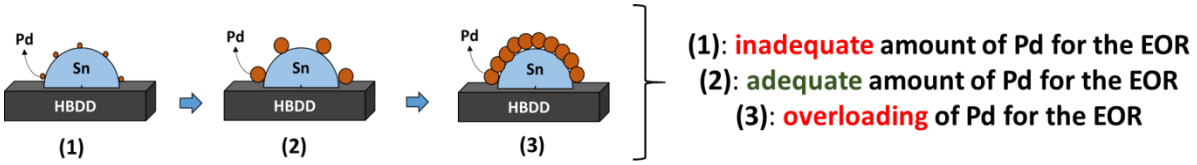


**Figure 5-6** Representation of mechanism of Ethanol Oxidation Reaction (EOR) on various Pd loadings of shell-core Pd-Sn nanostructures.

**Table 5-1** Pd features after electrodeposition through chronoamperometry.

| Electrodes | Charge ($mC/cm^2$) | Pd loading ($\mu g/cm^2$) | O des. charge ($mC/cm^2$) | Electroactive surface area, EAS ($cm^2/cm^2$) | Specific surface area, SSA ($m^2/g$) | Mass activity (mA/g) x $10^6$ | Particles size (nm) | Forward current peak ($I_f$) of ethanol electrooxidation ($mA/cm^2$) | $I_f/I_b$ |
|---|---|---|---|---|---|---|---|---|---|
| **Pd/HBDD** | 2.6 | 1.45 | 0.71 | 1.67 | 115.17 | 2.48 | 4.33 | 3.60 | 0.81 |
| **Pd-Sn/HBDD** | | | 0.81 | 1.92 | 132.41 | 4.56 | 3.77 | 6.61 | 0.86 |
| **Pd/HBDD** | 5.2 | 2.90 | 0.71 | 1.67 | 57.59 | 2.55 | 8.66 | **7.39** | **0.89** |
| **Pd-Sn/HBDD** | | | 0.74 | 1.74 | 60.00 | 4.26 | 8.32 | **12.37** | **1.63** |
| **Pd/HBDD** | 10.5 | 5.8 | 1.81 | 4.28 | 73.79 | 3.45 | 6.76 | 20.02 | 1.35 |
| **Pd-Sn/HBDD** | | | 1.66 | 3.91 | 67.41 | 3.58 | 7.40 | 20.78 | 1.49 |

## 5.4.1.4 Tafel analysis of Pd-Sn electrocatalysts

The electrochemical activity of Pd and Pd-Sn modified HBDD electrodes was investigated further by measuring the anodic polarisation curve and calculating kinetic parameters from Tafel plots as shown in figure 5-7. The Tafel plots are calculated from the cyclic voltammograms shown in figure 5-5. Figure 5-7 (a) shows slopes in the lower onset potential region, namely the charge transfer control region, which are approximately the same for the both electrodes: 135.1 and 133.5 mV $dec^{-1}$ for Pd/HBDD and Pd-Sn/HBDD respectively with a Pd loading of 1.45 $\mu g/cm^2$. The Tafel slope indicates that the kinetics of ethanol oxidation reaction in the lower potential region of -0.6V to -0.25V is dominated by the adsorption of hydroxyl ions on the Pd surface[57]. Nevertheless, the small deviation in the Tafel slope between the Pd/HBDD and Pd-Sn/HBDD shows that the kinetics of the ethanol oxidation reaction is not only controlled by the adsorption of hydroxyl ions but the kinetics are also altered by other surface reactions e.g. oxide layer formation on the surface of the Pd as reported in section 5.4.1.2. The same description can be attributed for the figure 5-7 (b) with 2.90 $\mu g/cm^2$

Pd loading catalysts. Each plot has been fitted to one linear region. The Tafel slope for Pd/HBDD (202 mV $dec^{-1}$) is higher than that of Pd-Sn/HBDD (75.2 mV $dec^{-1}$) in the potential region -0.35V to 0.25V (above the charge transfer control region) indicating the adsorption of higher hydroxyl ($OH_{ads}$) ions on the surface of the shell-core Pd-Sn nanoparticles. The lowest value indicates the higher charge transfer during the ethanol electrooxidation on the Pd-Sn/HBDD electrode compared to its counterpart Pd/HBDD. This is probably due to the Sn core structure, which suppresses the formation of the inactive oxide layer at potentials higher than -0.35V. In figure 5-7 (c), the Tafel plot of the Pd/HBDD and Pd-Sn/HBDD with a Pd loading of 5.80 μg/$cm^2$ is illustrated. The slopes slightly differ from each other in the charge-transfer control region, which are 145.7 mV $dec^{-1}$ and 134.9 mV $dec^{-1}$ for the former and the latter, respectively. The Tafel slopes are similar for all electrodes and good agreement with the Temkin-type adsorption for hydroxyl ($OH_{ads}$) and acyl ($CH_3CO_{ads}$) ions at lower potential regions (-0.6V to -0.4V), which indicates the similarity of the reaction mechanism for ethanol electrooxidation[57].

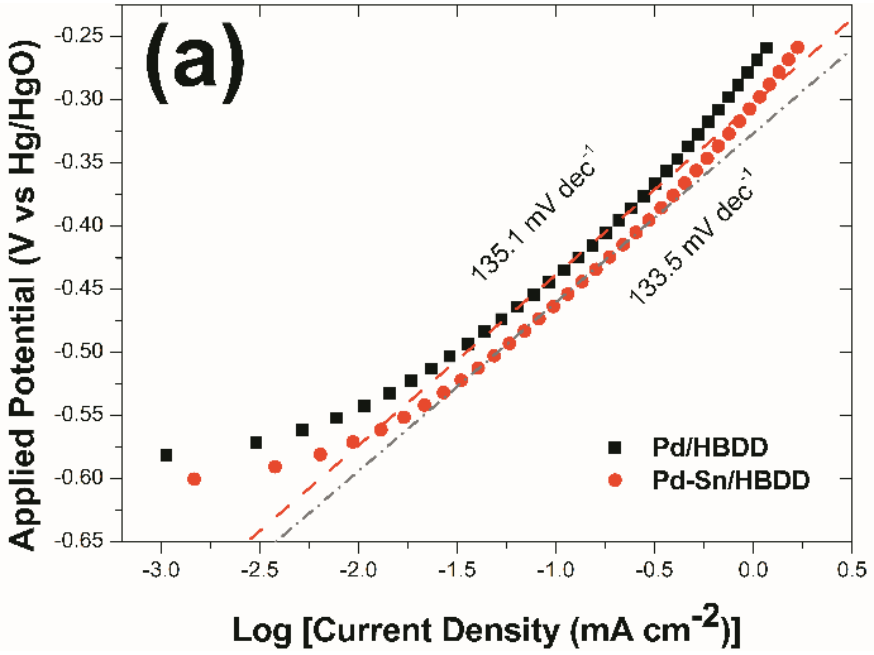

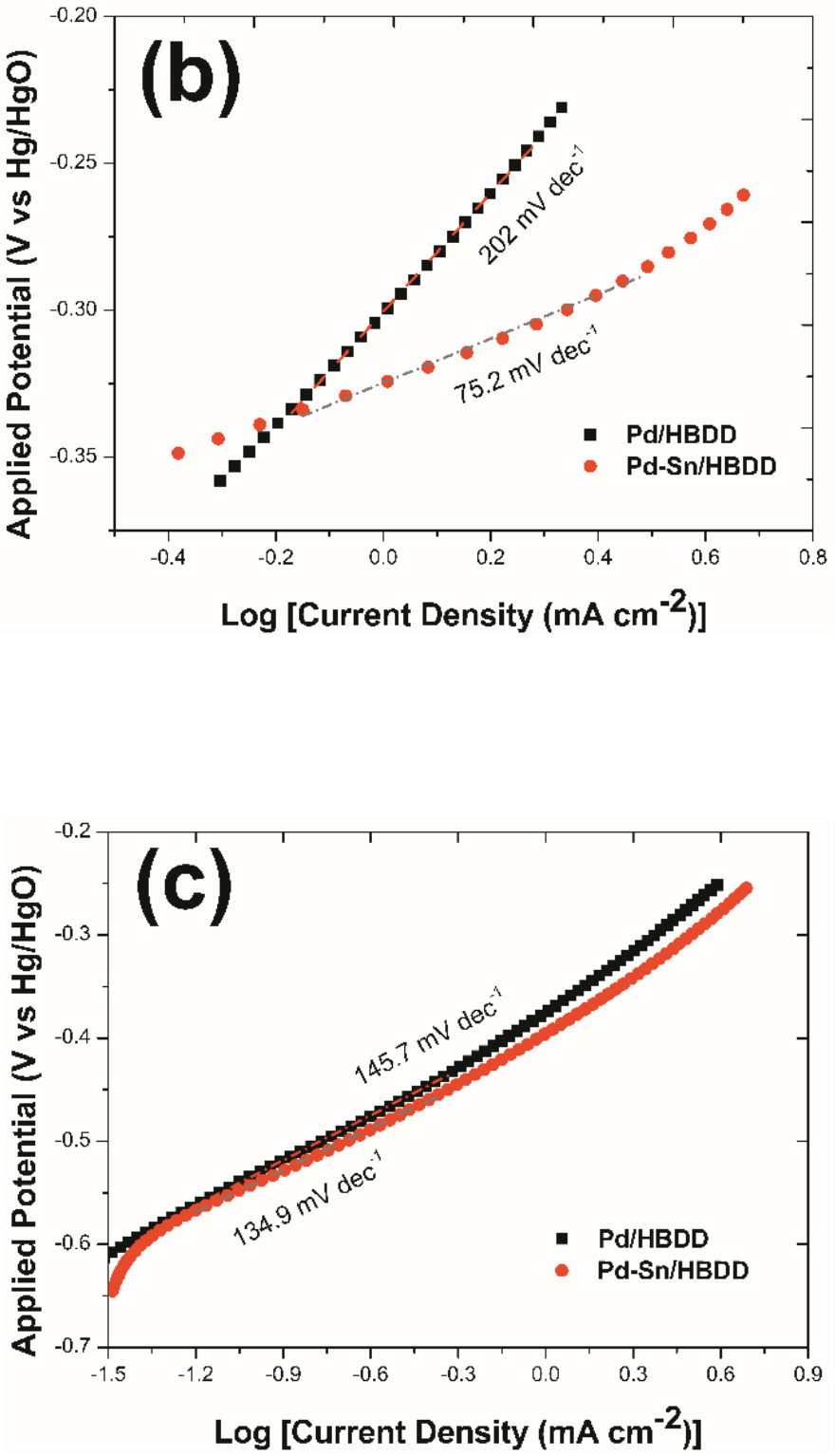


**Figure 5-7** Tafel plots of anodic polarisation curve for ethanol oxidation in 0.5M KOH and 1M EtOH: (a, b) of Pd and Pd-Sn modified HBDD with 1.45 μg/cm$^2$ (i.e., 2.6 mC/cm$^2$) and 2.90 μg/cm$^2$ (i.e., 5.2 mC/cm$^2$) Pd loading, respectively. (c) of Pd and Pd-Sn modified HBDD (with 5.80 μg/cm$^2$ Pd loading).

## 5.4.1.5 Amperometric response of the catalysts in ethanol

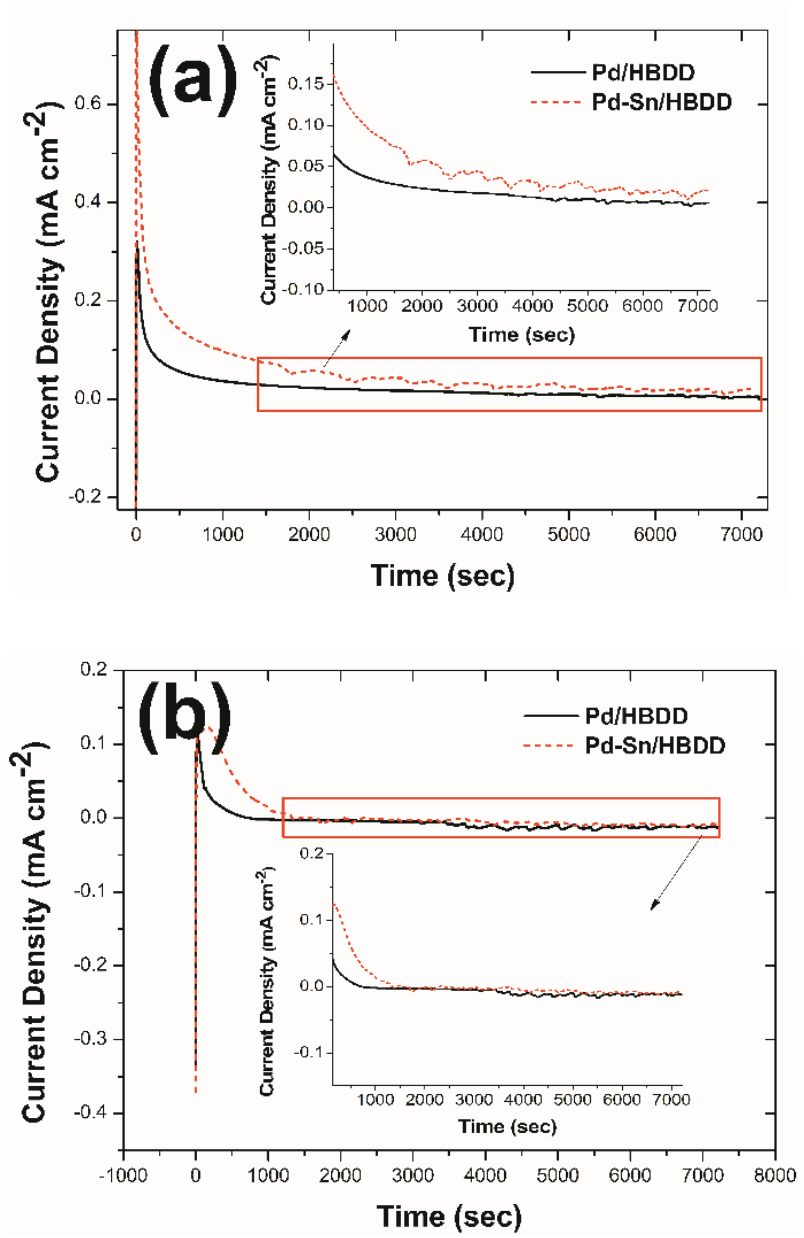


**Figure 5-8** (a, b) Chronoamperometric response of Pd and Pd-Sn modified HBDD after 2.6 mC/cm$^2$ and 5.2 mC/cm$^2$ passage of charge respectively in 0.5M KOH and 1M EtOH at potential -0.15V.

Chronoamperometry was performed to investigate the stability of Pd-Sn/HBDD electrocatalysts towards ethanol oxidation and the obtained result is compared with that of Pd/HBDD, as shown in figure 5-8. The electrodes were held at fixed potential of -0.15V for 7200 seconds. The current density decayed sharply for the Pd/HBDD but gradually for the Pd-

Sn/HBDD electrocatalyst. Current densities remained stable for much of this period and finally the results were consistent with the performance of the cyclic voltammetry as described in section 5.4.1.3. Specifically, the Pd-Sn/HBDD showed the highest current response compared to the pure Pd. The decrease of current with the increase in time is attributed to the combined effects of electrocatalyst poisoning by the chemisorbed carbonaceous oxidative intermediates and the concentration polarisation with time (i.e., limited mass transport with increasing reaction time).

## 5.4.2 Oxidation of ethanol using Pd-Ni nanoparticles on oxygen-terminated diamond electrodes

### 5.4.2.1 Morphology, EDX and XPS characterization of the deposits on BDD

The morphology of the deposits was characterised by a SEM and the images are shown in figure 5-9 (a-c). Ni nanoparticles after a passage of 658 mC/cm$^2$ charge at -1.2V are displayed in figure 5-9 (a), which shows that Ni particles have been deposited in a non-uniform manner along the diamond edges with visible agglomeration probably due to the high metal loading. The agglomeration makes the Ni NPs size difficult to estimate. Figure 5-9 (b) illustrates the Pd nanoparticles deposited onto diamond in an equally non-uniform manner to the Ni ones. However, Pd shows no agglomeration effects, probably due to the small metal loading (2.9 mC/cm$^2$). The size of the Pd particles is approximately 26 nm. Pd-Ni nanoparticles are shown in figure 5-9 (c). The sequential deposition of Pd/Ni produced smaller particles around 13 nm. The lateral conductivity of diamond as well as the non-uniform distribution of the B dopant led to the non-uniform distribution of the deposits as reported in previous work[13]. The elemental composition of the electrodes is displayed in figure 5-10. EDX spectra shows a

stronger Ni peaks than the Pd peaks as than expected from the metal loading (see Figure 5-10 (a), (b) and (c), respectively).

The elemental composition as well as the chemical and electronic states were explored by XPS and spectra are shown in figure 5-11. Figure 5-11 (a) shows the wide scan survey of the oxygen-terminated BDD electrodes with the relevant elements of Ni, Pd and Pd-Ni. The wide scan survey illustrates the presence of C, O and the relevant the main metals. Figure 5-11 (b) illustrates the Ni 2p peaks of the Ni/BDD and Pd-Ni/BDD electrodes. The Ni modified BDD has Ni $2p_{3/2}$ and Ni $2p_{1/2}$ peaks at 856.6 eV and 874.5 eV, respectively[56]. The Ni photoelectron peak of the Pd-Ni/BDD electrode is significantly attenuated. As reported in previous works[13], the Pd has in all likelihood covered the underlying Ni. The Pd-modified BDD shows both, the Pd $3d_{5/2}$ peak at 336.4 eV and the Pd $3d_{3/2}$ at 341.7 eV. The Pd photoelectron peak of the bimetallic electrode has the same peaks. There is a binding energy shift of 0.2 eV that implies also some electronic interaction between the two metals.

At this point, it is worth reminding the dissimilarity of chemical terminations compared to the preparation conditions in the previous section. From the SEM images we can see that the hydrophilic oxygen-terminated surface is manifestly less conductive, which leads to a non-uniform distribution of particles. Further evidence of this is provided by the EDX spectra as well as the XPS data where the intensity of the EDX and photoelectron peaks is weak in comparison with their counterparts in the previous section. Furthermore, both EDX and XPS data show a strong carbon peak which is not the case in the hydrophobic hydrogen-terminated diamond and due to this reason the intensity of the carbon peak is lower.

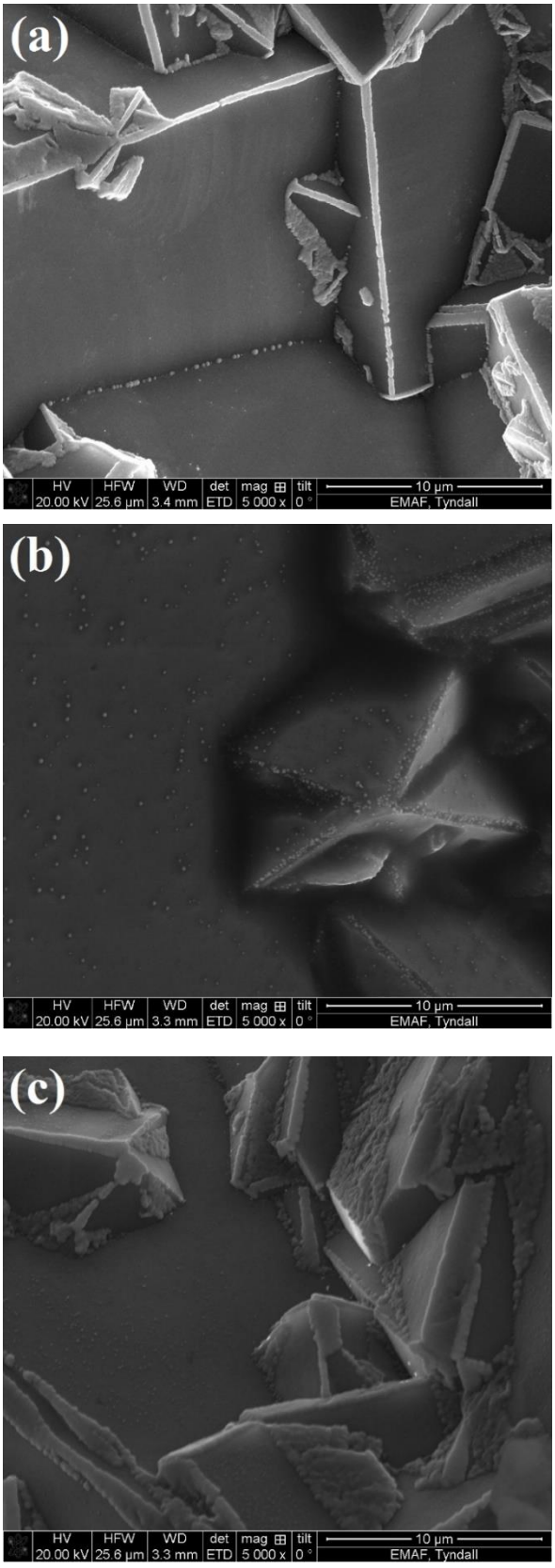


**Figure 5-9** SEM images of (a) Ni deposited on BDD electrodes, (b) Pd on BDD and (c) Pd-Ni deposited on BDD, through chronoamperometry at -1.2V for the Ni and -0.15V for the Pd.

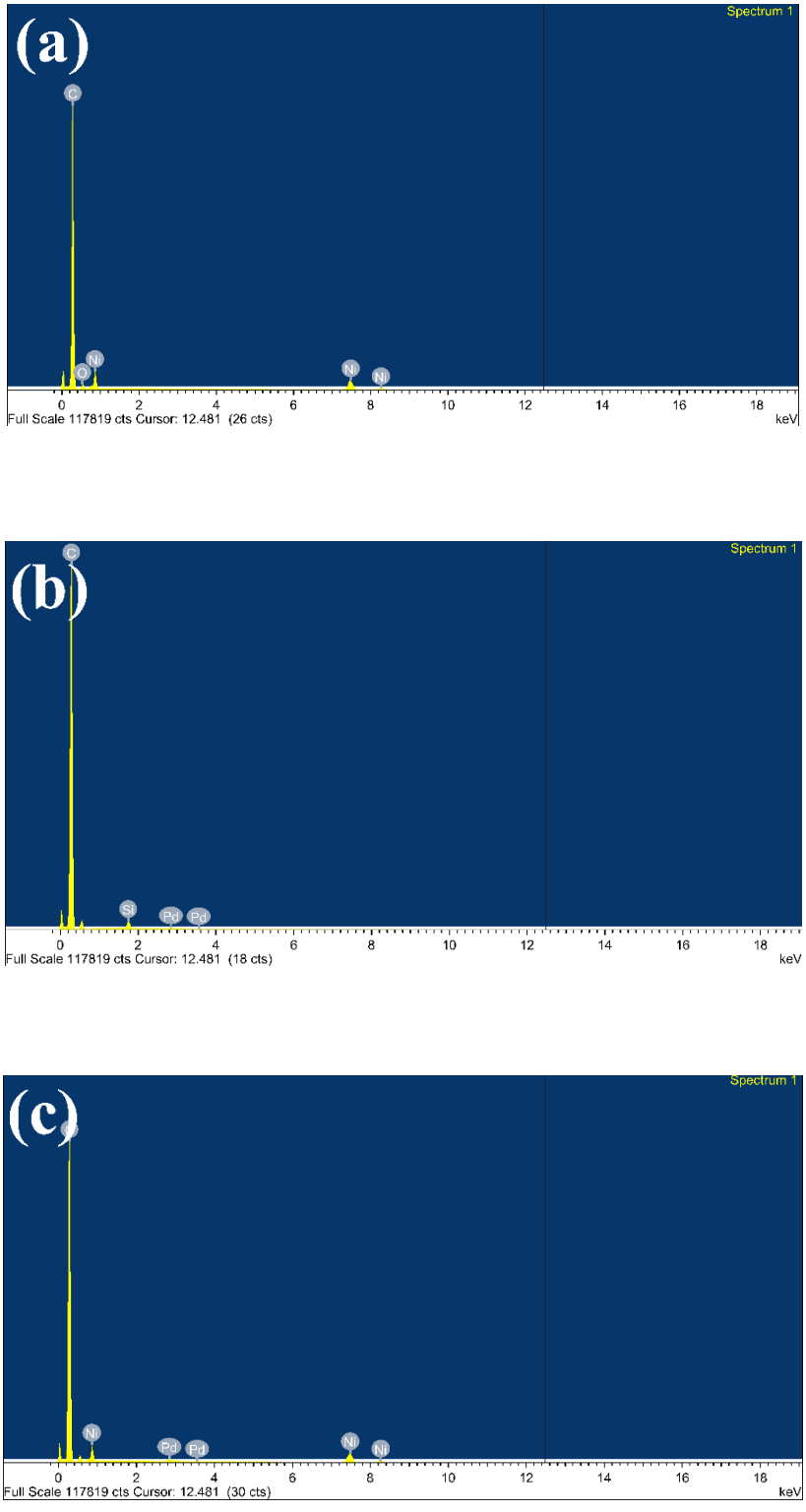


**Figure 5-10** EDX spectra of (a) Ni deposited on BDD electrodes, (b) Pd on BDD and (c) Pd-Ni on BDD, respectively.

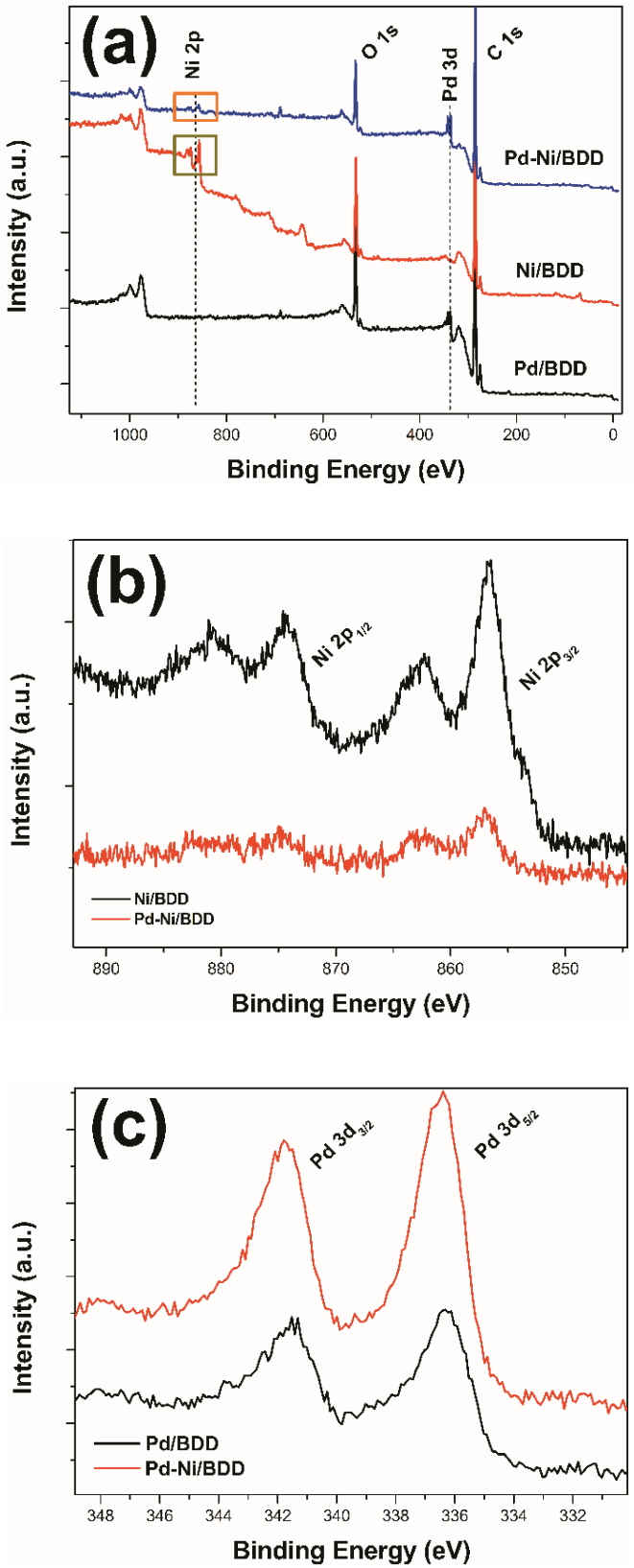


**Figure 5-11** XPS spectra of wide scans of the Ni/BDD, Pd/BDD and Pd-Ni/BDD, respectively. (b) Ni 2p peaks of Ni and Pd-Ni modified BDD catalysts, respectively. (c) Pd 3d peaks of the Pd and Pd-Ni modified BDD catalysts, respectively.

## 5.4.2.2 Voltammetric characterisation

### 5.4.2.2.1 Electrodeposition of the electrocatalysts

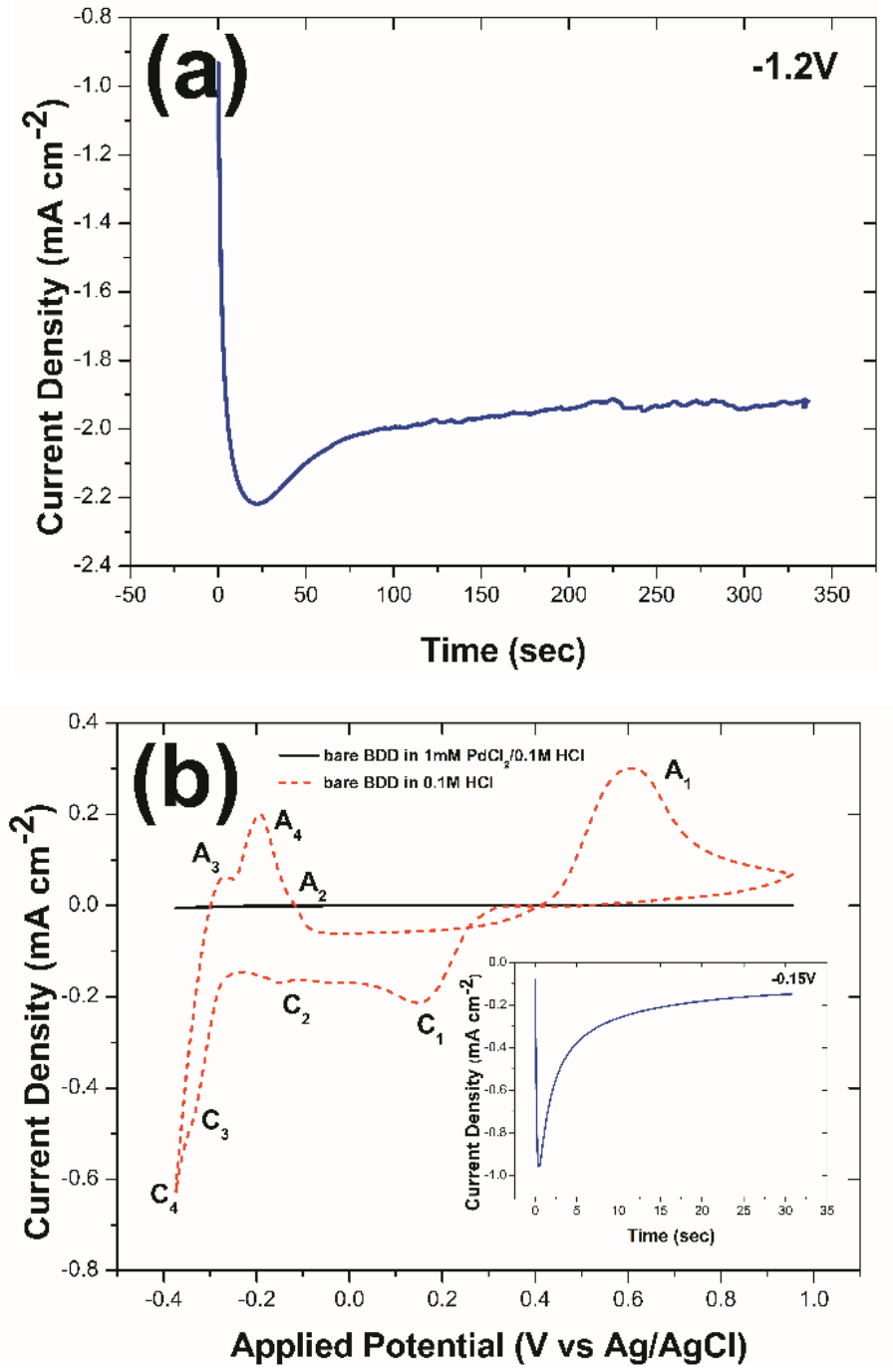


**Figure 5-12** (a) Chronoamperogram of bare BDD in a solution containing 10mM $[Ni(NO_3)_2 \cdot 6H_2O]$ in acetate buffer at constant potential of -1.2V. (b) Cyclic voltammogram of bare BDD in a solution containing 0.1M HCl and 1mM $PdCl_2$/0.1M HCl respectively at scan rate of 0.01 V/s (inset: chronoamperogram of Pd deposition in 1mM $PdCl_2$/0.1M HCl on bare BDD at constant potential of -0.15V).

A typical chronoamperogram of bare BDD in a solution containing 10mM [$Ni(NO_3)_2 \cdot 6H_2O$] in acetate buffer is shown in figure 5-12 (a). The Ni has deposited under a constant potential of -1.2V until 658 mC/cm$^2$ passed through the surface. The increase in current for the first 25 seconds indicate the formation of small Ni nuclei followed by further growth until the full charge passage as described in the previous sections. A typical cyclic voltammogram of bare BDD in a solution containing 1mM $PdCl_2$/0.1M HCl is also illustrated in figure 5-12 (b). The deposition of Pd occurred between the potential range of +0.23V and -0.35V. In this region, there is a cathodic current peak maximum at +0.15V (peak $C_1$). This current stayed stable until the overpotential value of -0.26V was reached and then increased again sharply until a maximum at -0.35V (peak $C_3$). The area around -0.35V can be described as the area near the diffusion-limited reduction of Pd ions. In this area, there is no hydrogen evolution or hydrogen underpotetnial deposition ($H_{UPD}$). After this point, there is a cathodic current at -0.37V (peak $C_4$) which represents the area of the simultaneous underpotential deposition of hydrogen onto the freshly deposited Pd particles. Due to the latter process, peaks $A_2$, $A_3$ and $A_4$ correspond to the H desorption process. The Pd is stripped from the electrode surface at +0.60V ($A_1$) and reduced back onto the surface at +0.15V ($C_1$).

### 5.4.2.2.2 Electrochemical activity of the electrocatalysts

All the catalysts were electrochemically characterised by cyclic voltammetry and linear sweep voltammetry in 0.5M KOH as shown in figure 5-13. Figure 5-13 (a) shows the voltammograms of the bare BDD, Ni, Pd and Pd-Ni modified BDD with 2.9 μg/cm$^2$ Pd loading. There is no electrochemical activity on the unmodified electrode and the current response is close to zero. The Ni/BDD is not electrochemically active in the area that the Pd is active. Peaks $A_2$/$C_2$ represent the oxidation and reduction of freshly deposited Ni particles on the

diamond surface at +0.49V and +0.43 respectively. Regarding the Pd/BDD electrode, various features are observed.

(i) Pd oxidation and reduction peaks ($A_1/C_1$) occur in the cathodic forward scan at +0.15V and -0.24V respectively; these peaks can be attributed to the formation of a palladium oxide layer on the surface of the BDD catalyst. However, the exact mechanism of the Pd oxidation formation remains unclear as reported in a previous study[57]. (ii) Hydrogen adsorption and desorption peaks at the Pd surface are at -0.53V and -0.9V ($C_3$ and $A_3$). The Pd-Ni/BDD has the same features as the Pd/BDD. However, there is a binding energy shift due to the bimetallic nature of the catalyst. (i) Pd oxidation and reduction waves occur at +0.05V and $2_2$-0.24V respectively. (ii) H $_a$dsorption and desorption due to Pd between -0.66V and -0.9V. (iii) Ni oxidation and reduction waves at +0.5V and +0.44V respectively. (iv) a shoulder ($A'_1$) appeared at -0.27V in the anodic backward scan corresponds to oxidation at favourable sites on the palladium surface[61] and is not seen at the Ni and Pd counterparts. The feature (iv) may be consistent with the Ni particles serving as reactive centres for the subsequent deposition of Pd as a result the Pd-Ni core-shell structure. This formation has already been discussed in a previous work with Pt and Cu nanoparticles on oxidised diamond electrodes[13]. Figure 5-13 (b) shows the cyclic voltammograms of the same electrodes but with four times more Pd loading (11.6 μg/cm$^2$). The same features and a higher current response due to the bigger metal loading on the surface is observed. However, in the case of the Pd-Ni/BDD catalyst there is no shoulder as in the first case. This is likely due to the fact that the four times larger Pd loading has created a thick layer on top of the Ni particles, which disabled the electronic interaction between the two metals and the core-shell structure. Figures 5-13 (c and d) illustrate the linear sweep voltammograms of the above catalysts with 2.9 μg/cm$^2$ and 11.6 μg/cm$^2$ Pd loading respectively. All the catalysts were scanned in the H evolution region starting from -0.6V and ending to -1.2V. In both cases, there is no electrochemical response for the unmodified BDD.

The Pd/BDD electrodes showed lower current response and therefore lower H evolution than the Ni/BDD. The maximum current densities were provided by the bimetallic core-shell catalysts giving the highest hydrogen evolution on their surfaces.

The metal coverage of Pd can be estimated from using the charge obtained from the area under the voltammogram in Faraday's Law. Determining the ratio of the charge required for desorption of an oxygen monolayer on the Pd (111) surface[65] (0.424 mC $cm^{-2}$) to that of $Q_o$ which is the coulombic charge of the oxygen desorption on the Pd surface, the electroactive surface area (EAS) of the pure Pd electrocatalyst can be also estimated. In addition, the specific surface area (SSA) can be defined as the electroactive surface area divided by the metal loading. All the above information is included in Table 5-2 (see section 5.4.2.3).

The electroactive and the specific surface areas are double for the Pd-Ni/BDD catalysts. The particle size is also half the size in the case of the bimetallic catalysts. However, the mass activity of the Pd-Ni catalysts with four times less Pd loading is bigger than the pure Pd/BDD with eight times more metal loading. All these results are shown in Table 5-2 (see section 5.4.2.3).

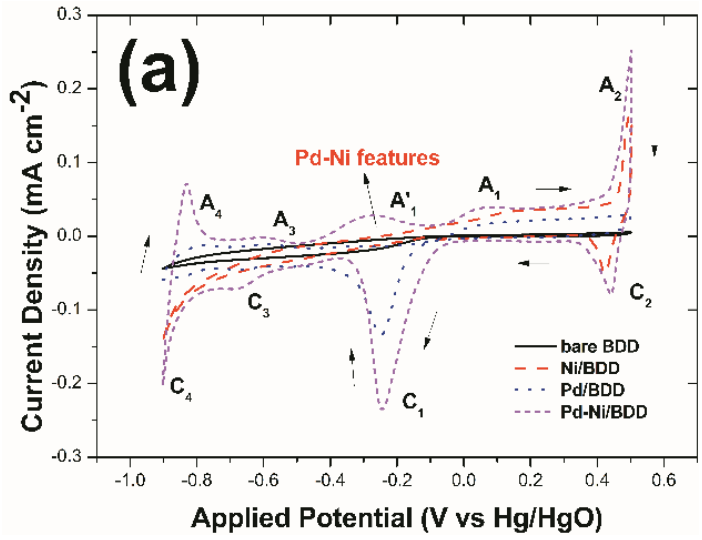

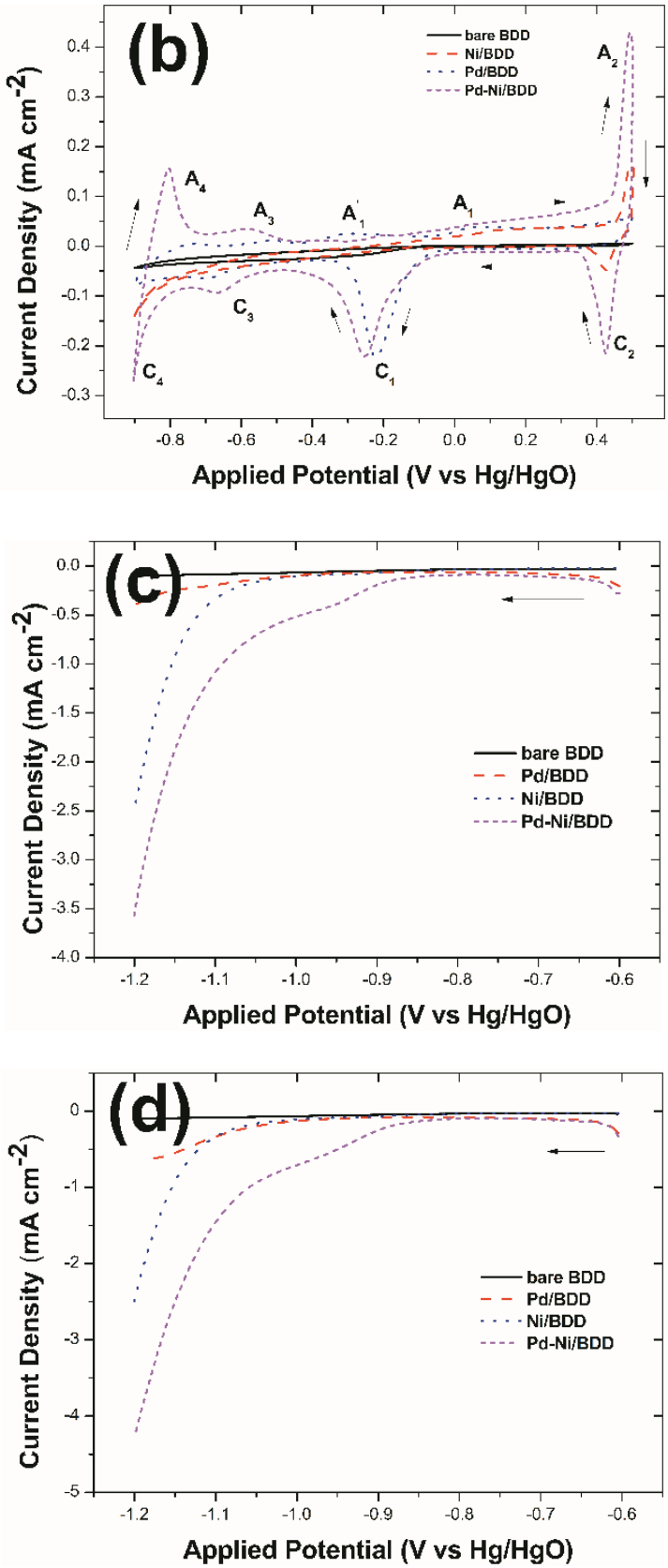


**Figure 5-13** Cyclic voltammograms (a and b) and linear sweep voltammogras (c and d) of the Ni/BDD (658 mC/cm$^2$), Pd/BDD (Pd loading: 2.9 (a) and 11.6 (b) µg/cm$^2$) and Pd-Ni modified BDD (Pd loading: 2.9 (a) and 11.6 (b) µg/cm$^2$, respectively), respectively in 0.5M KOH solution at scan rate of 0.02 V/s (all CVs and LSVs were started from open circuit potential).

### 5.4.2.3 Evaluation of Pd-Ni electrocatalysts preparation conditions on ethanol oxidation characteristics

The Pd-Ni/BDD electrocatalysts were evaluated through cyclic voltammetry and compared to Pd/BDD for ethanol oxidation. Cyclic voltammograms of the modified electrodes were obtained after scan in a solution containing 0.5M KOH+1M EtOH. The results are shown in figure 5-14 (a) and (b). The onset overpotential is observed at -0.55V and all the electrodes are inactive before this overpotential. When the applied potential was scanned positively in the anodic scan, current passed through the electrode and caused an electrooxidation current at around -0.1V, -0.08V, -0.01V and +0.03V for the Pd/BDD (2.9 μg/cm$^2$), Pd-Ni/BDD (2.9 μg/cm$^2$), Pd/BDD (11.6 μg/cm$^2$), and Pd-Ni/BDD (11.6 μg/cm$^2$), respectively as shown in figure 5-14 (a) and (b). The peak position is slightly shifted as the Pd loading increased, which implies some electronic interaction between the interfaces of the two metals. The ethanol oxidation wave in the anodic scan addresses to the oxidation of the fresh carbonaceous species of ethanol accumulated on the surface of the electrode. After this oxidation wave, all the electrodes deactivated at around -0.07V (Pd/BDD) and -0.04V (Pd-Ni/BDD) for the electrodes in figure 5-14 (a) and at around 0V (Pd/BDD) and +0.05V (Pd-Ni/BDD) for the electrodes in figure 5-14 (b). The electrodes with 2.9 μg/cm$^2$ palladium loading are activated again at -0.23V and the electrodes with 11.6 μg/cm$^2$ palladium loading at -0.19V giving a second oxidation wave that addressed the oxidation of the incompletely oxidised carbonaceous species of ethanol that were still present on the surface of the electrode. The backward oxidation gives a second peak at around -0.26V and -0.25V for the Pd/BDD and Pd-Ni/BDD respectively (Pd loading: 2.9 μg/cm$^2$). The corresponding peaks for the electrodes with the higher loading (11.6 μg/cm$^2$) were at -0.21V and -0.22V for the Pd/BDD and Pd-Ni/BDD respectively. In the context of the

poisoning tolerance the Pd-Ni is not tolerant enough towards the ethanol oxidation. The values of the tolerance ratios are presented in Table 5-2.

Figure 5-14 (c) illustrates various electrodes with a certain amount of Pd on them but with a different Ni loadings. The purpose of that investigation was to find the optimum amount of Ni needed to interact electronically with the Pd coating. A very small amount of Ni was found to behave the same as the pure Pd/BDD catalysts, which suggests a negligible electron interaction. Conversely, an electrode with up to twenty-five times more Ni was needed to serve as reactive centres for the subsequent deposition of Pd in order to form a core-shell catalyst. Clearly, the shell-core metal ratio is important not only for the particular properties of the metals but also of the electronic effects between them. Furthermore, an adequate shell-core metal ratio can increase the poisoning tolerance towards alcohol analytes and works as protection for the noble metal to be poisoned by the carbonaceous intermediates of the alcohol electrolytes.

Stability tests were conducted up to 1 hour and 40 minutes in alkaline solution. There was only 12% decrease of the current density on the Pd-Ni/BDD catalysts instead of 35% current drop as on the Pd/BDD catalyst itself.

**Table 5-2** Pd features after electrodeposition through chronoamperometry.

| **Electrodes** | **Charge ($mC/cm^2$)** | **Pd loading ($\mu g/cm^2$)** | **O des. charge ($mC/cm^2$)** | **Electroactive surface area, EAS ($cm^2/cm^2$)** | **Specific surface area, SSA ($m^2/g$)** | **Mass activity (mA/g) x $10^6$** | **Particles size (nm)** | **Forward current peak ($I_f$) of ethanol electrooxidation ($mA/cm^2$)** | **$I_f/I_b$** |
|---|---|---|---|---|---|---|---|---|---|
| Pd/BDD | 5.2 | 2.9 | 0.24 | 0.56 | 19.31 | **2.25** | 25.84 | **6.52** | 1.23 |
| Pd-Ni/BDD | | | 0.46 | 1.08 | 37.24 | **3.63** | 13.40 | **10.53** | 0.94 |
| Pd/BDD | 21 | 11.6 | 0.27 | 0.63 | 5.43 | 1.60 | 91.91 | 18.56 | 1.75 |
| Pd-Ni/BDD | | | 0.48 | 1.13 | 9.74 | 2.02 | 51.24 | 23.47 | 1.50 |

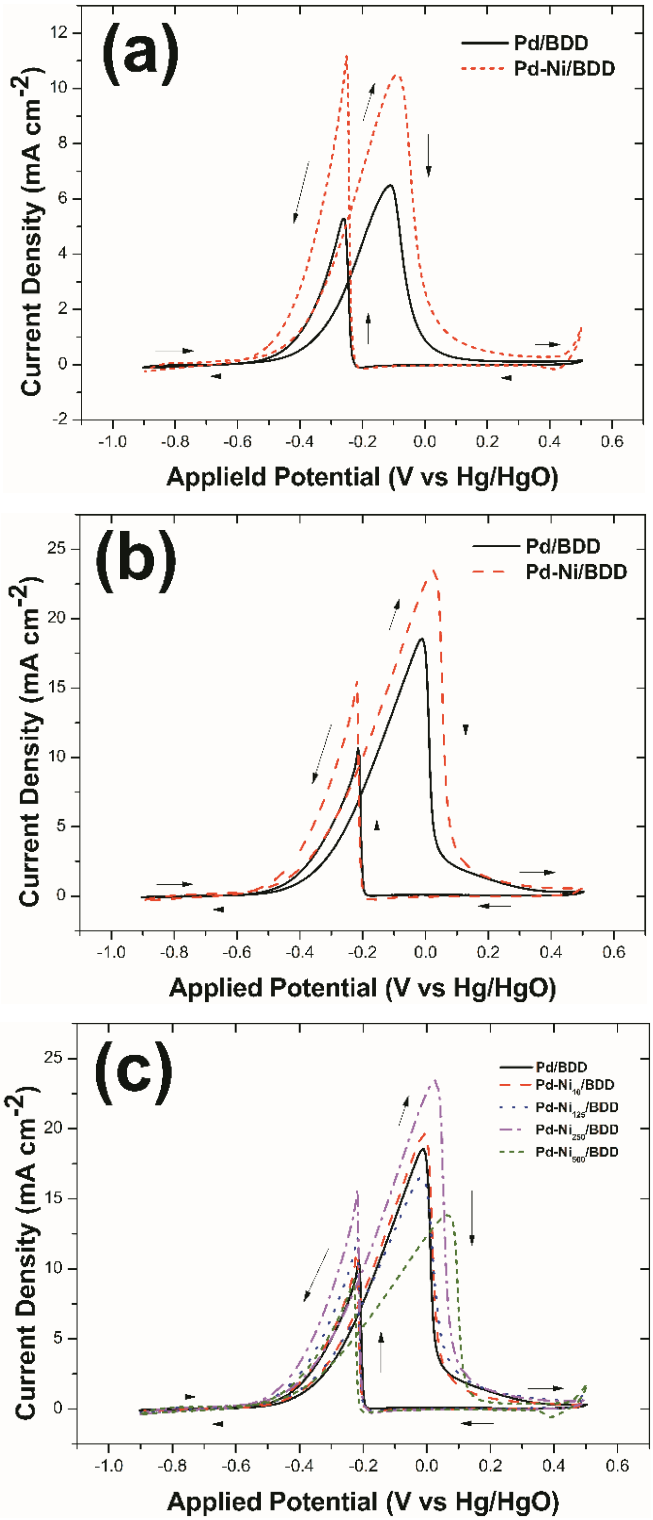


**Figure 5-14** (a, b) Cyclic voltammograms of Pd and Pd-Ni modified BDD with 2.9 μg/cm$^2$ (i.e., 5.2 mC/cm$^2$ charge) and 11.6 μg/cm$^2$ (i.e., 21 mC/cm$^2$ charge) Pd loading, respectively in 0.5M KOH and 1M EtOH at scan rate of 0.1 V/s. (c) Cyclic voltammograms of Pd and Pd-Ni modified BDD (with 2.9 μgr/cm$^2$: Pd loading and various Ni loadings) in 0.5M KOH and 1M EtOH at scan rate of 0.1 V/s. (all CVs were started from open circuit potential). The subscript values in the legend in Fig. (c) show the Ni charge per 1 cm$^2$ of electrode. Cyclic voltammograms shown here are taken after 10 cycles.

## 5.4.2.4 Tafel analysis of Pd-Ni electrocatalysts

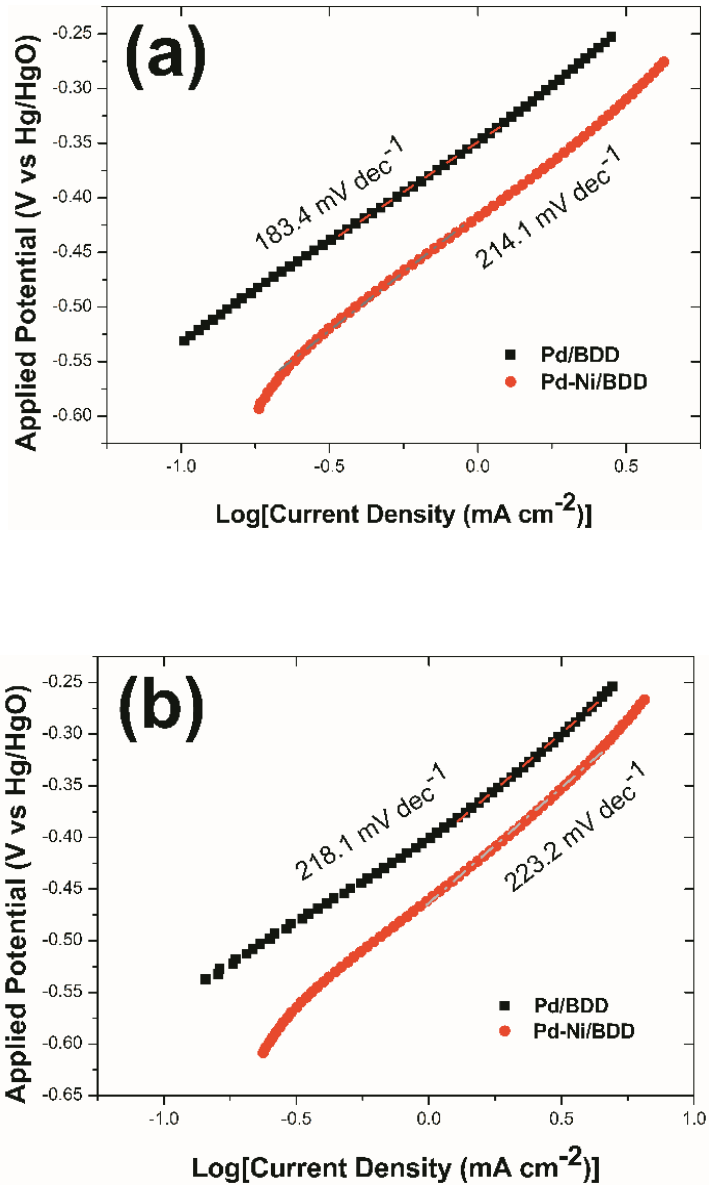


**Figure 5-15** Tafel plots of anodic polarisation curve for ethanol oxidation in 0.5M KOH and 1M EtOH (a, b) of Pd and Pd-Ni modified BDD with 2.9 μg/cm$^2$ (i.e., 5.2 mC/cm$^2$) and 11.6 μg/cm$^2$ (i.e., 21 mC/cm$^2$) Pd loading, respectively.

The electrocatalytic activity of the electrocatalysts was further investigated by tafel analysis. The measurements includes the anodic polarisation curve during the oxidation of ethanol and calculation of the kinetic parameters. The results are demonstrated in figure 5-15. Steady-state cyclic voltammograms were used in the lower potential region of -0.6V to -0.25V, which is dominated by the adsorption hydroxyl ions on the Pd surface as reported in a previous

study[57]. In figure 5-15 (a) the slope of the Pd/BDD is 183.4 mV $dec^{-1}$ lower than that of Pd-Ni/BDD (214.1 mV $dec^{-1}$) with 2.9 μg/$cm^2$ palladium loading. The Tafel slope indicate the kinetics of ethanol oxidation in the above potential region. Furthermore, the relatively small deviation of the Tafel slope between the Pd/BDD and Pd-Ni/BDD indicates that the kinetics of the oxidation of ethanol was controlled by multiple surface reactions such as the formation of oxide layers as reported in section 5.4.1.4. In figure 5-15 (b) the slope of the Pd/BDD is 218.1 mV $dec^{-1}$, which is lower than that of Pd-Ni/BDD (223.2 mV $dec^{-1}$) with up to four times greater palladium loading. All the plots have been fitted to a linear region. The lowest value of the slopes obtained from the monometallic catalysts of pure Pd indicate the higher charge transfer during the ethanol oxidation reaction. The latter may explain the fact that the monometallic catalysts showed better tolerance ratio towards the ethanol oxidation.

## 5.4.2.5 Amperometric response of the catalysts in ethanol

In order to compare the stability of Pd-Ni electrocatalysts with that of pure Pd/BDD, chronoamperometric experiments were carried out towards the oxidation of ethanol and the results are seen in figure 5-16. All the electrodes were held at a fixed potential of -0.15V for 2 hours. Current densities of all the electrodes remained stable for the duration of the experiment. However, the core-shell catalysts showed the highest current response compared to the pure Pd. The Pd-Ni/BDD with only 2.9 μg/$cm^2$ palladium loading gave the highest amperometric response than the pure Pd/BDD with 11.6 μg/$cm^2$ palladium loading (Figure 5-16 (b)). The latter can be attributed to the easier electrocatalyst poisoning by some of the carbonaceous intermediates of the ethanol oxidation reaction. In contrast, the electronic effects of the Pd-Ni/BDD catalysts along with metal properties of Pd supported on Ni particles protected the electrocatalyst for longer time.

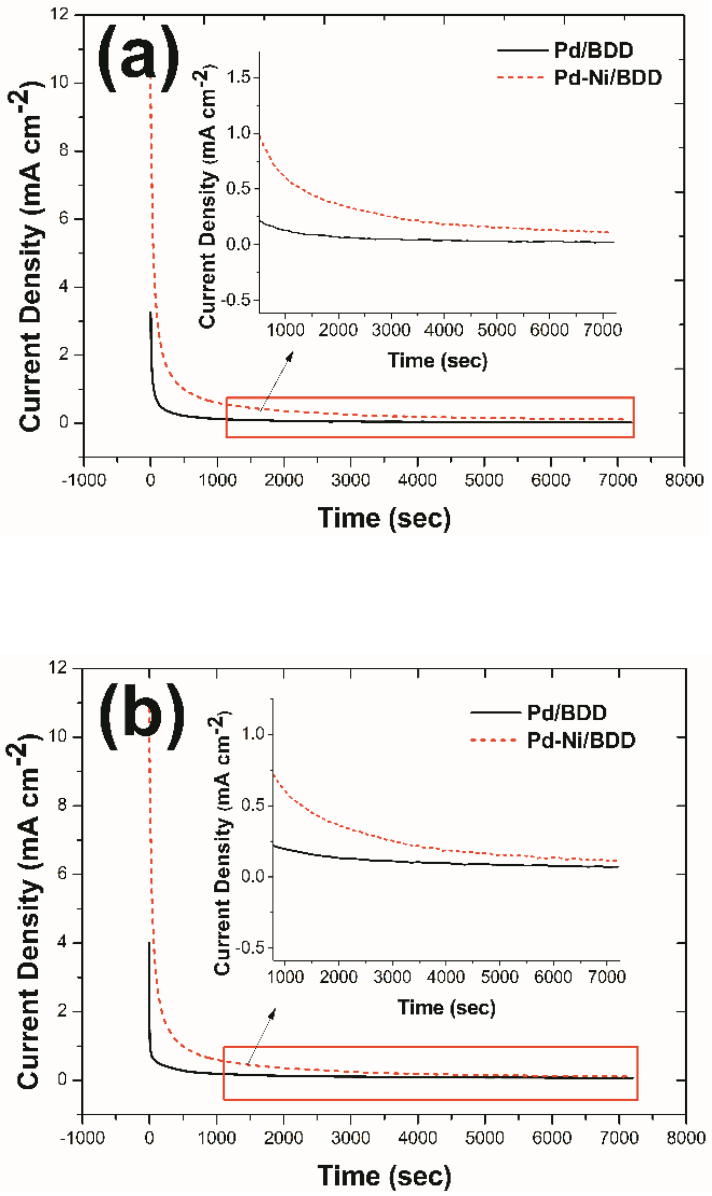


**Figure 5-16** (a) Chronoamperometric response of Pd and Pd-Ni modified BDD after 5.2 mC/cm$^2$ passage of charge and (b) after 21 mC/cm$^2$ and 2.9 mC/cm$^2$ passage of charge respectively in 0.5M KOH and 1M EtOH at potential -0.15V.

# 5.5 Conclusions

The hydrogen (HBDD) and oxygen (BDD) terminated boron doped diamond electrodes were modified with Pd, Pd-Sn and Pd-Ni nanoparticles by electrochemical techniques. A potentiostatic electrochemical deposition method was used to deposit noble-metal Pd and transition-metals Sn and Ni as nanoparticles onto HBDD and BDD for the investigation of their

electrocatalytic properties. XPS and electrochemical experiments suggested that Pd was deposited onto the Sn and Ni in order to form shell-core nanoparticles where the size of the particles in the case of Pd and Pd-Sn on HBDD was almost the same regardless of the catalyst's composition (monometallic or bimetallic). In contrast, the particle size differed between the two systems on the oxygen-terminated surface. The modification of the HBDD electrode with Sn and Pd by shell-core nanoparticles formation led to higher electrochemical activity. Ethanol oxidation on shell-core Pd-Sn/HBDD electrodes occurred at higher current densities and with less electrode poisoning than the pure Pd/HBDD. This phenomenon was attributed to better dispersion of the Sn nanoparticles on the hydrogen-terminated electrode surface and consequently electronic properties were altered in the bimetallic interface as well as in the reaction interface owing to the thin shell-core nanoarchitecture. Likewise, the electrochemical modification with Pd-Ni particles led to higher current densities than the pure Pd/BDD. Comparison between the Pd-Sn/HBDD and Pd-Ni/BDD electrocatalysts with the same amount of Pd loading towards the ethanol oxidation showed greater electrocatalytic activity for the former. This was likely due to the hydrogen-termination, which improved in conductivity according to previous reports and as mentioned in section 5.1. Nevertheless, the Pd-Ni nanoparticles on BDD were far more stable than all the electrocatalysts examined. The Ni particles seemed to serve better conditions for the deposition of Pd, which was proved by the stability tests. The observed current drop was only 12% instead of 35% was for the Pd-Sn particles. The tolerance ratio towards the poisoning of the catalyst by ethanol oxidation by-products remained lower for the bimetallic catalysts than the pure Pd. However, the Pd-Ni/BDD catalysts showed high mass activity when operated in alkaline media. Additionally, the Pd loading was found to be important. Low amounts of palladium formed a thin overlayer on top of the Sn and Ni nanoparticles, which allowed an electronic interaction between them. Higher amounts of Pd loading did not facilitate such interface interaction between the two

metals. Finally, the shell-core Pd-Sn/HBDD and Pd-Ni/BDD catalysts showed higher stability towards ethanol oxidation over a long period of time in comparison with the Pd/HBDD and Pd/BDD alone. After chronoamperotric experiments, the bimetallic shell-core Pd-Ni/BDD catalysts showed higher stability during the ethanol oxidation of 2 hours duration compared to the Pd/BDD alone. The proper tuning of the Pd shell thickness on a second transition metal along with the surface termination effects of the boron-doped diamond electrode played a crucial role in achieving the high mass and specific electrocatlytic activity of Pd towards ethanol electrooxidation.

# 5.6 Bibliography

1. Antolini E. Catalysts for direct ethanol fuel cells. *J. Power Sources*. 2007;170(1):1–12. doi:10.1016/j.jpowsour.2007.04.009.

2. Bianchini C, Shen PK. Palladium-Based Electrocatalysts for Alcohol Oxidation in Direct Alcohol Fuel Cells. *Chem. Rev.* 2009;109:4183-4206. doi:10.1007/978-1-4419-5580-7.

3. Lamy C, Lima A, LeRhun V, Delime F, Coutanceau C, Léger JM. Recent advances in the development of direct alcohol fuel cells (DAFC). *J. Power Sources*. 2002;105(2):283–296. doi:10.1016/S0378-7753(01)00954-5.

4. Verma A, Basu S. Direct use of alcohols and sodium borohydride as fuel in an alkaline fuel cell. *J. Power Sources*. 2005;145(2):282–285. doi:10.1016/j.jpowsour.2004.11.071.

5. Pang G, Sun M, Liu P, Hou L, Gao F. Facile synthesis of Pd nanostructures with enhanced electrocatalytic performance for ethanol oxidation by a bio-based method. *RSC Adv*. 2016;6(24):19734–19741. doi:10.1039/C6RA00560H.

6. Li Y, Han L, An B, Wang Y, Wang L. Preparation of platinum catalysts supported on functionalized graphene and the electrocatalytic properties for ethanol oxidation in direct ethanol fuel cell. *J. Mater. Sci. Mater. Electron*. 2016. doi:10.1007/s10854-016-4551-0.

7. Cunha EM, Ribeiro J, Kokoh KB, De Andrade AR. Preparation, characterization and application of Pt-Ru-Sn/C trimetallic electrocatalysts for ethanol oxidation in direct fuel cell. *Int. J. Hydrogen Energy*. 2011;36(17):11034–11042. doi:10.1016/j.ijhydene.2011.06.011.

8. Hsu RS, Higgins D, Chen Z. Tin-oxide-coated single-walled carbon nanotube bundles supporting platinum electrocatalysts for direct ethanol fuel cells. *Nanotechnology*. 2010;21:165705. doi:10.1088/0957-4484/21/16/165705.

9. Loukrakpam R, Brankovic SR, Strasser P. A Study of Au/C Nanoparticles with Pt Monolayer and Sub-Monolayer Electrocatalysts for Ethanol Oxidation Reaction. *ECS Trans*. 2013;58(1):1733–1736. doi:10.1149/05801.1733ecst.

10. Gacutan EM, Climaco MI, Telan GJ, Malijan F, Hsu HY, Garcia J, Fulo H, Tongol BJ. Nanostructured carbon-supported Pd electrocatalysts for ethanol oxidation: synthesis and characterization. *Adv. Nat. Sci. Nanosci. Nanotechnol*. 2012;3:045016. doi:10.1088/2043-6262/3/4/045016.

11. Kepeniene V, Tama auskaite-Tama i naite L, Jablonskiene J, Vaiciuniene J, Kondrotas R, Juskenas R, Norkus E. Investigation of Graphene Supported Platinum-Cobalt Nanocomposites as Electrocatalysts for Ethanol Oxidation. *J. Electrochem. Soc*. 2014;161(14):F1354–F1359. doi:10.1149/2.0511414jes.

12. Kraft A, Doped Diamond : A Compact Review on a New, Versatile Electrode Material. *J. Electrochem. Sci.* 2007;2:355–385.

13. Mavrokefalos CK, Nelson GW, Poll CG, Compton RG, Foord JS. Electrochemical aspects of Pt–Cu and Cu modified boron-doped diamond. *Phys Status Solidi (a)* 2015;2567(11):1–9. doi:10.1002/pssa.201532163.

14. McCreery RL. Advanced carbon electrode materials for molecular electrochemistry. *Chem. Rev*. 2008;108(7):2646–87. doi:10.1021/cr068076m.

15. Rao TN, Fujishima A. Recent advances in electrochemistry of diamond. *Diam. Relat. Mater*. 2000;9(3-6):384–389. doi:10.1016/S0925-9635(99)00234-4.

16. Shpilevaya I, Smirnov W, Hirsz S, Yang N, Nebel CE, Foord JS. Nanostructured diamond decorated with Pt particles: preparation and electrochemistry. *RSC Adv*. 2014;4(2):531. doi:10.1039/c3ra43763a.

17. Swain GM, Anderson AB, Angus JC. Applications of Diamond Thin Films in Electrochemistry. 1998;(September).

18. Toghill KE, Xiao L, Phillips MA, Compton RG. The non-enzymatic determination of glucose using an electrolytically fabricated nickel microparticle modified boron-doped diamond electrode or nickel foil electrode. *Sensors Actuators, B Chem*. 2010;147(2):642–652. doi:10.1016/j.snb.2010.03.091.

19. Toghill KE, Xiao L, Stradiotto NR, Compton RG. The determination of methanol using an electrolytically fabricated nickel microparticle modified boron doped diamond electrode. *Electroanalysis*. 2010;22(5):491–500. doi:10.1002/elan.200900523.

20. Ivandini TA, Sato R, Makide Y, Fujishima A, Einaga Y. Electrochemical Detection of Arsenic ( III ) Using Iridium-Implanted Boron-Doped Diamond Electrodes. *Anal. Chem*. 2006;78(18):6291–6298.

21. Ramos BC, Saito E, Trava-Airoldi VJ, Lobo AO, Marciano FR. Diamond-like carbon electrochemical corrosion resistance by addition of nanocrystalline diamond particles for biomedical applications. *Surf. Coatings Technol*. 2014;259:732–736. doi:10.1016/j.surfcoat.2014.09.066.

22. Oliveira CAGS, Stein MF, Saito E, Zanin H, Vieira LS, Raniero L, Trava-Airoldi VJ, Lobo AO, Marciano FR. Effect of gold oxide incorporation on electrochemical corrosion resistance of diamond-like carbon. *Diam. Relat. Mater*. 2015;53:40–44. doi:10.1016/j.diamond.2015.01.009.

23. Compton RG, Foord JS, Marken F. Electroanalysis at Diamond-Like and Doped-Diamond Electrodes. *Electroanalysis*. 2003;15(17):1349–1363. doi:10.1002/elan.200302830.

24. Nebel CE, Yang N, Uetsuka H, Osawa E, Tokuda N, Williams O. Diamond nano-wires, a new approach towards next generation electrochemical gene sensor platforms. *Diam Rela.t Mater*. 2009;18(5-8):910–917. doi:10.1016/j.diamond.2008.11.024.

25. Mehedi H, Hebert C, Ruffinatto S, Eon D, Omnes F, Gheeraert E. Formation of oriented nanostructures in diamond using metallic nanoparticles. *Nanotechnology*. 2012;23:455302. doi:10.1088/0957-4484/23/45/455302.

26. Kriele A, Williams OA, Wolfer M, Hees JJ, Smirnov W, Nebel CE. Formation of nano-

pores in nano-crystalline diamond films. *Chem. Phys. Lett*. 2011;507(4-6):253–259. doi:10.1016/j.cplett.2011.03.089.

27. Smirnov W, Hees JJ, Brink D, Muller-Sebert W, Kriele A, Williams OA, Nebel CE. Anisotropic etching of diamond by molten Ni particles. *Appl. Phys. Lett*. 2010;97(2010):17–20. doi:10.1063/1.3480602.

28. Shpilevaya I, Foord JS. Electrochemistry of Methyl Viologen and Anthraquinonedisulfonate at Diamond and Diamond Powder Electrodes: The Influence of Surface Chemistry. *Electroanalysis*. 2014;26(10):2088–2099. doi:10.1002/elan.201400310.

29. Nebel CE, Rezek B, Shin D, Watanabe H. Surface electronic properties of H-terminated diamond in contact with adsorbates and electrolytes. *Phys. Status Solidi (a).* 2006;203(13):3273–3298. doi:10.1002/pssa.200671401.

30. Nart FC, Iwasita T. On the adsorption of sulfate species on polycrystalline platinum An FTIR study in fluoride base electrolyte. *J. Electroanal. Chem*. 1991;308:277–293.

31. Qiu C, Shang R, Xie Y, Bu Y, Li C, Ma H. Electrocatalytic activity of bimetallic Pd-Ni thin films towards the oxidation of methanol and ethanol. *Mater. Chem. Phys*. 2010;120(2-3):323–330. doi:10.1016/j.matchemphys.2009.11.014.

32. Ge X, Chen L, Kang J, Fujita T, Hirata A, Jiang J, Chen M. A Core-Shell Nanoporous Pt-Cu Catalyst with Tunable Composition and High Catalytic Activity. *Adv. Funct. Mater*. 2013;23(33):4156–4162. doi:10.1002/adfm.201300114.

33. Hsu C, Huang C, Hao Y, Liu F. Synthesis of highly active and stable Au-PtCu core-shell nanoparticles for oxygen reduction reaction. *Phys. Chem. Chem. Phys*. 2012;14(42):14696–701. doi:10.1039/c2cp42716h.

34. Hu J, Lu X, Foord JS. Nanodiamond pretreatment for the modification of diamond electrodes by platinum nanoparticles. *Electrochem. commun*. 2010;12(5):676–679. doi:10.1016/j.elecom.2010.03.004.

35. Kristian N, Yu Y, Lee JM, Liu X, Wang X. Synthesis and characterization of Cocore–Ptshell electrocatalyst prepared by spontaneous replacement reaction for oxygen reduction reaction. *Electrochim. Acta*. 2010;56(2):1000–1007. doi:10.1016/j.electacta.2010.09.073.

36. Wei ZD, Feng YC, Li L, Wanzala N, Njoki PN, Loukrakpam R, Yin G, Electrochemically synthesized Cu/Pt core-shell catalysts on a porous carbon electrode for polymer electrolyte membrane fuel cells. *J. Power Sources*. 2008;180(1):84–91. doi:10.1016/j.jpowsour.2008.01.086.

37. Zhong CJ, Luo J, Fang B, Nanostructured catalysts in fuel cells. *Nanotechnology*. 2010;21(6):062001. doi:10.1088/0957-4484/21/6/062001.

38. Hasan M, Newcomb SB, Rohan JF, Razeeb KM. Ni nanowire supported 3D flower-like Pd nanostructures as an efficient electrocatalyst for electrooxidation of ethanol in alkaline media. *J. Power Sources*. 2012;218(0):148–156. doi:10.1016/j.jpowsour.2012.06.017.

39. Yu EH, Krewer U, Scott K. Principles and materials aspects of direct alkaline alcohol fuel cells. *Energies*. 2010;3(8):1499–1528. doi:10.3390/en3081499.

40. Xu C, Wang H, Shen PK, Jiang SP. Highly ordered Pd nanowire arrays as effective electrocatalysts for ethanol oxidation in direct alcohol fuel cells. *Adv. Mater*. 2007;19(23):4256–4259. doi:10.1002/adma.200602911.

41. Hu F, Chen C, Wang Z, Wei G, Shen PK. Mechanistic study of ethanol oxidation on Pd-NiO/C electrocatalyst. *Electrochim. Acta*. 2006;52(3):1087–1091. doi:10.1016/j.electacta.2006.07.008.

42. Zheng HT, Li Y, Chen S, Shen PK. Effect of support on the activity of Pd electrocatalyst for ethanol oxidation. *J. Power Sources*. 2006;163(1 SPEC. ISS.):371–375. doi:10.1016/j.jpowsour.2006.09.062.

43. Xu C, Shen P kang, Liu Y. Ethanol electrooxidation on Pt/C and Pd/C catalysts promoted with oxide. *J. Power Sources*. 2007;164(2):527–531. doi:10.1016/j.jpowsour.2006.10.071.

44. Antolini E, Gonzalez ER. Alkaline direct alcohol fuel cells. *J. Power Sources*. 2010;195(11):3431–3450. doi:10.1016/j.jpowsour.2009.11.145.

45. Ravi Krishna E, Muralidhar Reddy P, Sarangapani M, Hanmanthu G, Geeta B, Shoba Rani K, Ravinder V. Synthesis of $N_4$ donor macrocyclic Schiff base ligands and their Ru (II), Pd (II), Pt (II) metal complexes for biological studies and catalytic oxidation of didanosine in pharmaceuticals. *Spectrochim. Acta - Part A Mol. Biomol. Spectrosc*. 2012;97:189–196. doi:10.1016/j.saa.2012.05.073.

46. Lu J, Zhang H, Chen X, Liu H, Jiang Y, Fu H. Palladium-catalyzed synthesis of aromatic ketones and isoindolobenzimidazoles via selective aromatic C-H bond acylation. *Adv Synth Catal*. 2013;355:529–536. doi:10.1002/adsc.201200743.

47. Wu XF, Neumann H, Beller M. Palladium-catalyzed oxidative carbonylation reactions. *ChemSusChem*. 2013;6:229–241. doi:10.1002/cssc.201200683.

48. Chang CM, Hon MH, Leu IC. Outstanding $H_2$ sensing performance of Pd nanoparticle-decorated ZnO nanorod arrays and the temperature-dependent sensing mechanisms. *ACS Appl Mater Interfaces*. 2013;5:135–143. doi:10.1021/am302294v.

49. Kalidindi SB, Oh H, Hirscher M, Esken D, Wiktor C, Turner S, Van Tendeloo G, Fischer RA. Metal@COFs: Covalent organic frameworks as templates for Pd nanoparticles and hydrogen storage properties of Pd@COF-102 hybrid material. *Chem. - A Eur. J.* 2012;18:10848–10856. doi:10.1002/chem.201201340.

50. Ksar F, Sharma GK, Audonnet F, Beaunier P, Remita H. Palladium urchin-like nanostructures and their H2 sorption properties. *Nanotechnology*. 2011;22:305609. doi:10.1088/0957-4484/22/30/305609.

51. http://www.casaxps.com/.

52. Taylor RI. X-Ray Photoemission Spectra of Crystalline and Amorphous Si and Ge Valence Bands. *Phys. Rev. Lett*. 1972;29(16):1088–1092.

53. Ding LX, Wang AL, Ou YN, Li Q, Guo R, Zhao WX, Tong YX, Li GR. Hierarchical Pd-Sn alloy nanosheet dendrites: an economical and highly active catalyst for ethanol electrooxidation. *Sci. Rep*. 2013;3:1181. doi:10.1038/srep01181.

54. Cardwell TJ, Mocaka J, Santosa JH, Bond AM. Preparation of Microelectrodes : Comparison of Polishing Procedures by Statistical Analysis of Voltammetric Data. *Analyst*. 1996;121:357-362.

55. Mavrokefalos CK, Nelson GW, Poll CG, Compton RG, Foord JS. Electrochemical aspects of Pt–Cu and Cu modified boron-doped diamond. *Phys Status Solidi (a)* 2015;2567(11):1–9. doi:10.1002/pssa.201532163.

56. Wagner CD, Riggs WM, Davis LE, Moulder JF, and Muilenburg GE, Handbook of X-ray Photoelectron Spectroscopy (Perkin-Elmer Co., Minnesota, 1979).

57. Liang ZX, Zhao TS, Xu JB, Zhu LD. Mechanism study of the ethanol oxidation reaction on palladium in alkaline media. *Electrochim. Acta*. 2009;54(8):2203–2208. doi:10.1016/j.electacta.2008.10.034.

58. Grdeń M, Czerwiński A. EQCM studies on Pd-Ni alloy oxidation in basic solution. *J Solid State Electrochem*. 2008;12(4):375–385. doi:10.1007/s10008-007-0452-8.

59. Vračar L, Burojević S, Krstajić N. The surface processes at Pd–Ni alloy in acid and alkaline solutions. *Int. J. Hydrogen Energy*. 1998;23(12):1157–1164. doi:10.1016/S0360-3199(97)00176-6.

60. Jeong MC. Voltammetric Studies on the Palladium Oxides in Alkaline Media. *J. Electrochem. Soc*. 1993;140(7):1986. doi:10.1149/1.2220750.

61. Denuault G, Milhano C, Pletcher D. Mesoporous palladium-the surface electrochemistry of palladium in aqueous sodium hydroxide and the cathodic reduction of nitrite. *Phys Chem. Chem. Phys*. 2005;7(20):3545–3551. doi:10.1039/b508835f.

62. Cai J, Zeng Y, Guo Y. Copper@palladium–copper core–shell nanospheres as a highly effective electrocatalyst for ethanol electro-oxidation in alkaline media. *J. Power Sources*. 2014;270:257–261. doi:10.1016/j.jpowsour.2014.07.131.

63. Hu GZ, Nitze F, Jia X, Sharifi T, Barzegar HR, Gracia-Espino E, Wagberg T. Reduction free room temperature synthesis of a durable and efficient Pd/ordered mesoporous carbon composite electrocatalyst for alkaline direct alcohols fuel cell. *RSC Adv*. 2014;4(2):676–682. doi:10.1039/C3RA42652A.

64. Peng C, Hu Y, Liu M, Zheng Y. Hollow raspberry-like PdAg alloy nanospheres: High electrocatalytic activity for ethanol oxidation in alkaline media. *J. Power Sources*. 2015;278:69–75. doi:10.1016/j.jpowsour.2014.12.056.

65. Ahmed MS, Jeon S. Synthesis and Electrocatalytic Activity Evaluation of Nanoflower Shaped Ni-Pd on Alcohol Oxidation Reaction. *J. Electrochem Soc*. 2014;161(12):F1300–F1306. doi:10.1149/2.1041412jes.

66. Bagchi J, Bhattacharya SK. Electrocatalytic activity of binary Palladium Ruthenium anode catalyst on Ni-support for ethanol alkaline fuel cells. *Transit. Met. Chem*. 2007;32(1):47–55. doi:10.1007/s11243-006-0127-9.

67. Grden M, Kotowski J, Czerwinski A. The study of electrochemical palladium behavior using the quartz crystal microbalance. *J. Solid State Electrochem*. 2000;4(5):273–278.

68. Prabhuram J, Manoharan R. Effects of incorporation of Cu and Ag in Pd on electrochemical oxidation of methanol in alkaline solution. *J. Appl. Electrochem*. 1998;28:935–941.

69. Chen M, Wang ZB, Ding Y, Yin GP. Investigation of the Pt–Ni–Pb/C ternary alloy catalysts for methanol electrooxidation. *Electrochem. commun*. 2008;10(3):443–446. doi:10.1016/j.elecom.2008.01.012.

70. Knudsen J, Nilekar AU, Vang RT, Schnadt J, Kunkes EL, Dumesic JA, Mavrikakis M, Besenbacher F. A Cu/Pt Near-Surface Alloy for Water-Gas Shift Catalysis. *J. Am. Chem. soc*. 2007;129(3):3838–3842.

# Chapter 6

# Electrochemical modification of Diamond electrodes with $Cu_2O$ for Water Splitting and $CO_2$ Reduction

## 6.1 Introduction

A major challenge – some would argue *the* major challenge – currently facing our planet today relates to the problem of anthropogenically driven climate change and its inextricable link to our global society's present and future energy needs. The exploitation of solar energy is undoubtedly one of the most promising ways to deal with issues such as climate change, energy shortage and environmental pollution. Solar water splitting into hydrogen and oxygen is a propitious means of converting solar energy into a "solar fuel" given that both water and sunlight are abundant[1–5]. Hydrogen is widely regarded as a key energy solution for the 21st century due to its high-mass energy density and environmental friendliness[6]. Collection, conversion and storage of solar energy can all be integrated in a single photoelectrochemical (PEC) cell; the solar energy collecting the PEC is converted into chemical energy that is stored within the H-H chemical bond, as hydrogen gas[7–9]. Hence, water splitting in a PEC cell has attracted a lot of attention in both academia and industry[5,10–12]. In theory, a PEC cell consists of a photoanode and a photocathode. Solar energy is captured at the photocathode and electrons are extracted *via* the water oxidation reaction (Equation 6-1); at the

photocathode the electrons are used for hydrogen generation *via* proton reduction (Equation 6-2).

$$2H_2O \rightarrow O_2 + 4H^+ + 4e^- \quad (6\text{-}1)$$

$$2H^+ + 2e^- \rightarrow H_2 \quad (6\text{-}2)$$

Another major scientific, technological and economic challenge facing our planet nowadays is the diminishing fossil fuel supply and the day-to-day growth in $CO_2$ emission. Consequently, considerable efforts are being undertaken worldwide to develop effective $CO_2$ capture and storage technology[13–15]. The utilization of $CO_2$ as carbon source for the production of fuels and chemicals is also being investigated to reduce human contribution to climate change[16,17]. Photocatalysis and photoelectrocatalysis using solar energy are two highly attractive methods for the reduction of $CO_2$ with $H_2O$ to fuels and chemicals. In most cases, the strategies typically adopted for $H_2O$ splitting have also been exploited for $CO_2$ reduction. However, the activation of $CO_2$ is more difficult than that of $H_2O$. The reduction of $CO_2$ by photogenerated electrons may compete with the reduction of $H_2O$, which makes the catalyst requirement for the two processes quite different.

Generally, light-harvesting, photogenerated electron-hole separation or photo-carrier transfer as well as surface reactions are the three key steps that should be mainly considered for the design of an efficient, semiconductor-based photocatalyst or photoelectrocatalyst. The latter are common to both $H_2O$ splitting and $CO_2$ reduction, the two biggest, most challenging reactions using solar energy currently being investigated. Prof. Ye Wang *et al.* reported that some of the most acute issues to $CO_2$ reduction are (a) the adsorption ability and reactivity of the catalyst surfaces towards $CO_2$ reduction, (b) the catalysts selectivity toward $CO_2$ reduction, given that the reduction of $H_2O$ to $H_2$ may occur faster on photocatalyst or photoelectrode surfaces due to the lower reactivity of $CO_2$, (c) the selectivity of products from $CO_2$ reduction

and (d) the semiconductor structure which can affect either the separation of photogenerated electron-hole pairs of the reactivity of catalyst surfaces or both[18].

In principle, photocatalysts consist of semiconductor materials that absorb visible light as the redox mediators for hydrogen and oxygen evolution reactions. The basic requirements of the semiconductor materials are: a direct band gap in order to absorb a large and adequate portion of the solar spectrum, good electrical conductivity for the photogeneration of charge carriers and stability in an aqueous environment[19]. Copper (I) oxide ($Cu_2O$), a naturally abundant element, is a p-type semiconductor that has a direct band gap (2.17 eV) and seems to be suitable for solar energy harvesting which makes it an attractive photocathode material. Its direct band gap allows efficient absorption of visible light[20–25] and it has a conduction band at 0.7V negative of the hydrogen evolution potential[22,25]. However, $Cu_2O$ tends to self-photo-corrosion in electrolyte solutions which makes this material unstable[26]. Various synthesis methods such as thermal relaxation[27], holographic lithography[28], sputtering[29], thermal evaporation[30] and electrochemical synthesis[31–34] of photoactive $Cu_2O$ have been previously reported. The obstacle of self-photo-corrosion of $Cu_2O$ can be overcome if $Cu_2O$ is combined with an n-type semiconductor. In this way, the n-type semiconductor acts as protective layer for the underlying $Cu_2O$ and the combination of n-type semiconductor and $Cu_2O$ allows the adequate transfer of photogenerated electron from the p-type semiconductor (i.e. $Cu_2O$) to the n-type semiconductor (e.g. ZnO). As a result of this, the stability of $Cu_2O$ can be improved in aqueous solutions[24,35–37]. In previous works, nickel hydroxide[38–40] and nickel oxide[41–43] were found to be of use in solar hydrogen generation[38,43] as effective co-catalysts in order to trap photoelectrons and thus delay the charge recombination.

Carbon materials can be used to support to all the above catalysts due to their characteristics such as chemical stability and high specific surface area. One very promising

candidate as a catalytic substrate for sustainable technologies is boron-doped diamond (BDD). Boron-doped diamond[44] possesses a wide potential window, low background current, resistance to fouling, resistance to electrocorrosion and as reported in previous work is available at a low economic cost when grown by chemical vapour deposition (CVD). BDD also possesses very stable chemical surface terminations as also reported previously[45,46]. Hence, BDD can separate charge within the semiconductor, acting as a good electron acceptor and in general facilitating photocatalytic activities.

This work reports the electrochemical modification of BDD electrodes decorated with $Cu_2O$-NiO particles. The method involves the electrodeposition of $Cu_2O$ cubical particles on BDD from a surfactant-free "green" electrolyte followed by deposition of NiO nanoparticles by dip-coating with an alcoholic solution of nickel acetate. The electrochemical results showed that using NiO NPs co-catalyst led to higher photocurrent densities by comparison with $Cu_2O$ photocatalyst only. In order to understand the morphology, dispersion and size of the particles, the electrodes were characterised by high-resolution SEM and XPS.

# 6.2 Aims of the project and principal outcomes

Herein, a novel photocathode for the water splitting reaction by artificial photosynthesis is reports and the electrochemical deposition of $Cu_2O$ particles on boron doped diamond (BDD) electrode is described. NiO deposited onto $Cu_2O$ particles by a dip-coating method to act as a co-catalyst for the hydrogen evolution reaction. The morphology analysis by SEM revealed that $Cu_2O$ particles are cubical and decorated sporadically with NiO nanoparticles. The use of semiconductor/co-catalyst in a particle format provided a short diffusion path for the photogenerated electron-hole pairs enabling their fast transfer to the respective redox reaction sites. The photoelectrochemical performance of $Cu_2O$/BDD showed a current density of -0.12 $mA/cm^2$ at -0.6 V *vs* Ag/AgCl while a much higher photocurrent density of -0.51 $mA/cm^2$ was

obtained for NiO-$Cu_2O$/BDD photocathode at the same overpotential. The improvement in the photocurrent is attributable to the generation of new active sites at the photocatalyst and co-catalyst interface. Stability tests showed that the amount of NiO nanoparticles loading is a crucial parameter in this regard. From the experiments reported here, the $Cu_2O$/BDD decorated with 10 to 20 coating cycles of NiO nanoparticles seemed to be the most stable photocatalysts. XPS confirmed the electronic interaction between the photocatalyst and co-catalyst through a binding energy shift of the main Cu 2p peak for the NiO-$Cu_2O$/BDD electrode by comparison with the $Cu_2O$/BDD only. The electron transfer activity at the photocatalyst/electrolyte interface was investigated through electrochemical impedance spectroscopy (EIS). NiO-$Cu_2O$ particles as photocathode with enhanced photocurrent density supported on diamond electrodes provides a route to low-cost solar hydrogen production.

# 6.3 Experimental section

## 6.3.1 Chemical reagents

Chemical reagents were purchased from Sigma-Aldrich and used as received without any further purification. These were: copper (II) sulfate pentahydrate ($CuSO_4 \cdot 5H_2O$); sodium hydroxide (NaOH); L-(+)-lactic acid; nickel (II) acetate tetrahydrate; ethanolamine; 2-methoxyethanol ($CH_3OCH_2CH_2OH$), nickel sulfamate [$Ni(SO_3NH_2)_2 \cdot 4H_2O$], boric acid ($H_3BO_3$), nickel bromide ($NiBr_2$), sodium sulfate ($Na_2SO_4$) and potassium bicarbonate ($KHCO_3$). All aqueous solutions were freshly prepared, using milli-Q water (18 MΩ cm).

## 6.3.2 Equipment and experimental set-up

BDD solid wafers ([B]>$10^{20}$ $cm^{-3}$) of 10 x 10 x 0.6 mm were obtained from Element Six Co (UK) with an area of 1 $cm^2$ exposed to the electrolyte. The photo-electrochemical

measurements were performed with an Autolab PGSTAT 128N potentiostat/galvanostat and with a LCS-100 solar simulator of 100 mW/cm$^2$ lamp power. The electrochemical depositions were conducted at room temperature (24 ± 1.0°C), using a standard three electrode cell with a Pt counter electrode and a Ag/AgCl reference electrodes. The dip-coating depositions were carried out with a dip-coating unit with a precision servo motor controlled linear axis. The analysis was done with OriginPro 8.5 software (OriginLab Ltd.). The morphology of the deposits was characterised by a FEI Helios Nanolab 600i field emission scanning electron microscope with an attached Oxford Instruments Aztech X-Max-80 energy dispersive X-ray spectroscopy unit for elemental mapping. All the images were taken at 400K magnification with an acceleration voltage of 20 kV and a working distance (WD) of around 4 mm. The composition of the deposits was determined by XPS using an Al Kα (1486.6 eV) X-ray source. XPS spectra were curve-fitted with CasaXPS software[47] and a Shirley background[48]. The C 1s peak was calibrated to 285 eV with the following relative sensitivity factors (R.S.F.): C 1s (1.0), O 1s (2.93), Cu 2p (16.7) and Ni 2p (22.2).

## 6.3.3 Fabrication and working electrodes

$Cu_2O$ catalyst was electrodeposited onto BDD from a freshly prepared bath of 1.5M lactic acid and 1.9M NaOH solution containing 0.2M $CuSO_4 \cdot 5H_2O$ by a potentiostatic method. The deposition current was held at -6.6 mA (vs Ag/AgCl) for 60 seconds at 65 °C. The $Cu_2O$/BDD electrode was then removed, rinsed with ultrapure water and dried with $N_2$.

The second electrode consisted of NiO-$Cu_2O$/BDD on which the $Cu_2O$ had been electrodeposited onto BDD from a 1.5M lactic acid and 1.9M NaOH solution with 0.2M $CuSO_4 \cdot 5H_2O$ by means of the potentiostatic method described above. The $Cu_2O$/BDD electrode was then removed from the solution/electrochemical cell, rinsed with ultrapure water and dried with $N_2$ after which a dip-coating unit was then used for the deposition of the

electrocatalytic Ni particles. The operator involvement was minimized so that variables like speed, duration etc as well as movements were achieved accurately by a precision- servo-motor-controlled linear stage. Fifteen dip-coating cycles were accomplished under 0.35 cm/min motor movement 0.5M $Ni(AC)_2$, 0.5M ethanolamine and 2-methyloxyethanol solution. The electrodes dried in a pre-heated oven for 5 min between the dip-coating. At the end, the Ni- $Cu_2O$/BDD electrodes were put in a tube oven at 200 °C for 3 hours.

A two-step electrodeposition method was followed for the $CO_2RR$. $Cu_2O$ catalyst was electrodeposited onto BDD as previously described in the first paragraph of this section 6.3.3. A second electrodeposition onto the freshly prepared $Cu_2O$/BDD electrode from a nickel sulfamate bath using 0.37M nickel sulfamate, 0.64M boric acid, 0.18M nickel bromide and wetting agent ANKOR (R) (10 ml $L^{-1}$) was then accomplished by a potentiostatic method. The pH of the solution was adjusted to 3.8 by adding 1M sulfonic acid at room temperature. The deposition current was held at -20 mA (two electrode system, without reference electrode) from 10 to 50 seconds at 45 °C under mild stirring. The Ni-$Cu_2O$/BDD electrode was then removed, rinsed with ultrapure water and dried with $N_2$.

# 6.4 Results and discussion

## 6.4.1 Solar hydrogen generation using $Cu_2O$ cubical particles coated with NiO

### 6.4.1.1 Structural and XPS characterisation of the deposits on BDD

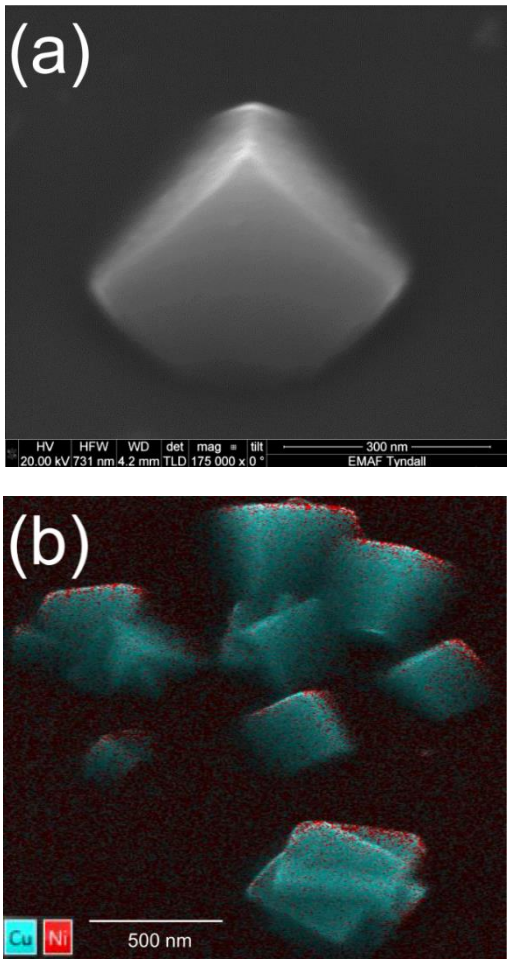


**Figure 6-1** SEM images of (a) $Cu_2O$ modified BDD and (b) Ni(15)-$Cu_2O$/BDD electrode under the preparation conditions described in the experimental section.

Structural and morphology information are shown by SEM images in figure 6-1. Figure 6-1 (a) illustrates $Cu_2O$ nanoparticles supported on the BDD substrate. The $Cu_2O$ particles were found to be cubic in shape and randomly deposited on the diamond surface. The random distribution is probably due to the variation of the B dopant distribution on the surface, which

makes the diamond more conductive in some areas than other areas. Therefore, electrochemical deposition of $Cu_2O$ particles mostly occur at the electrochemically active sites with a greater B concentration. The elemental mapping of $Cu_2O$ particles after NiO coating is shown in figure 6-1(b). The SEM image shows that NiO nanoparticles are deposited onto cubic shaped $Cu_2O$ particles and are not concealed under the excessive NiO deposits. However, a layer of NiO nanoparticles are seen on the underlying BDD surface. The NiO coating does not cover all the $Cu_2O$ nanoparticles, which is further proved by the XPS spectra. If NiO particles had excessively cover the cubic $Cu_2O$ particles the photocurrent responses would have decreased due to increase in the shell thickness that is proportional to the travel length for electron-hole pairs to the reaction interface of $Cu_2O$-NiO. Additionally, due to the large band gap (~ 3.6 eV) of NiO[45], an increased thickness in the outer shell would hinder photo absorption by the inner $Cu_2O$ particles.

XPS spectra of the deposits on BDD is presented in figure 6-2. Figure 6-2 (a) shows the wide scan of the contaminant-free $Cu_2O$/BDD and indicates the presence of C 1s peak calibrated at 285 eV, O 1s peak and Cu 2p peak. The inset of figure 6-2 (a) shows the Cu 2p peak of the $Cu_2O$ deposit. In Cu (I) oxide, there main peak is at 932.4 eV and a secondary peak at 952.3 eV. A tiny weak satellite appears at 943 eV, which is attributed to $Cu_2O$ nanoparticles. Figure 6-2 (b) illustrates the survey of the NiO- $Cu_2O$/BDD electrode. The inset of figure 6-2 (b) represents the Ni 2p peak. The two binding energy peaks located at 853.9 and 871.5 eV were respectively assigned to Ni $2p_{3/2}$ and Ni $2p_{1/2}$ of NiO of the NiO-$Cu_2O$/BDD and two smaller fitting peaks at 859.6 and 878 eV were assigned to NiO. A comparison of Cu 2p peaks of the $Cu_2O$ and NiO-$Cu_2O$ modified BDD is shown in figure 6-2 (c). The main photoelectron peaks of $Cu_2O$ were obtained at 932.3 and 952.2 eV, respectively.

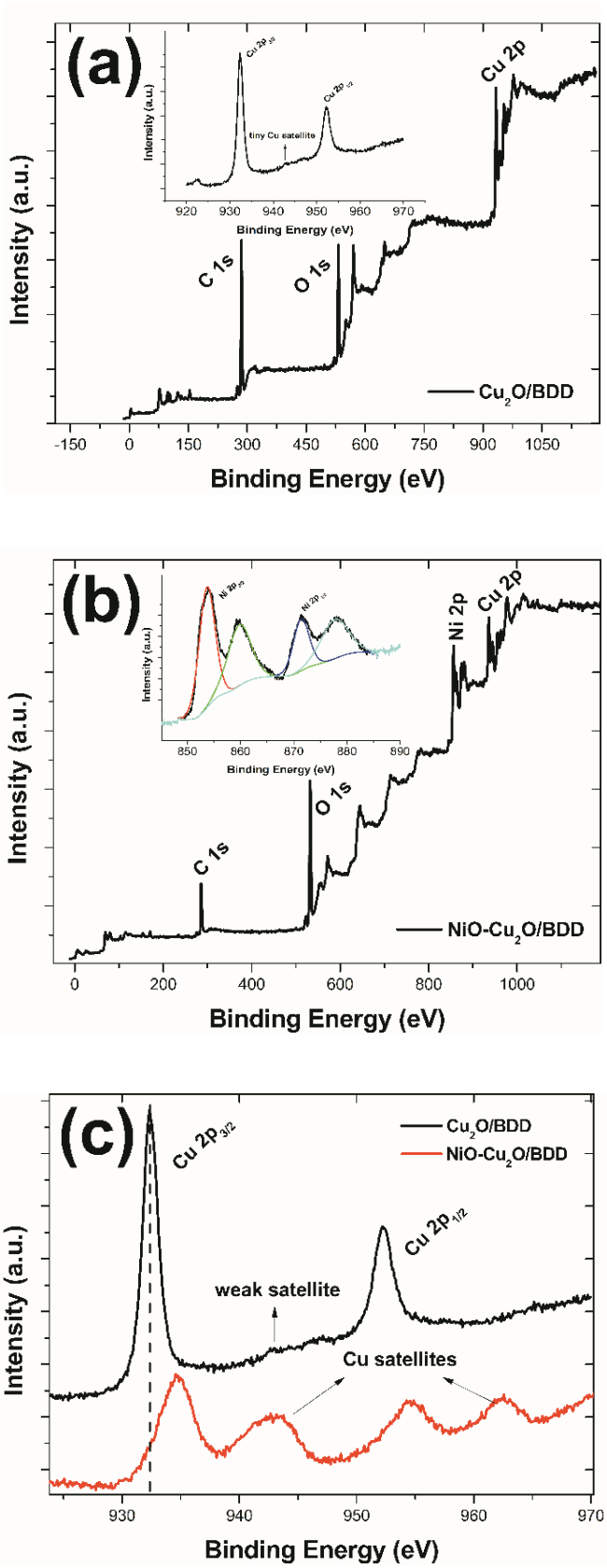


**Figure 6-2** (a) XPS spectrum of survey of the $Cu_2O$/BDD (Inset: typical Cu 2p peak). (b) XPS spectrum of wide scan of the NiO-$Cu_2O$/BDD (Inset: typical Ni 2p peak). (c) Typical Cu 2p peaks of the $Cu_2O$ and NiO-$Cu_2O$ modified BDD, respectively.

The second spectrum shows the two main peaks of Cu 2p peak at a binding energy that is shifted compared to its counterpart at 934.7 and 954.6 eV, respectively. The presence of two extra satellite peaks at relatively higher binding energies, 942.9 and 962.4 eV, also indicate the potential existence of CuO on the surface. The latter is likely to arise due to the thermal treatment and therefore oxidation of the catalysts in oven at 200 °C for 3 hours. Also, the binding energy shift indicates some electronic effects between the interfaces of the two metals, which will play a crucial role to the overall photocatalytic performance as discussed in the next section.

### 6.4.1.2 Photoelectrochemical measurements of different photocathodes

The PEC performances of the photocatalysts was characterised by linear sweep voltammetry under 0.2 Hz chopped light illumination with an intensity of 100 mW/cm$^2$ at scan rate of 10 mV/s in 0.5M $Na_2SO_4$ buffered at pH 6.1. Figure 6-3 shows the photocurrent-potential curves of various photocathodes. The potential sweep started from 0V and ended at -0.65V. Figure 6-3 (a) illustrates the comparison of the photoelectrochemical response of bare BDD versus the NiO coated and uncoated $Cu_2O$/BDD electrodes. For the sake of simplicity, parentheses are referring to the number of NiO coatings. There is no photoelectrochemical response for the unmodified BDD whereas there is a photocurrent response for the $Cu_2O$ modified BDD. The current started to increase gradually for $Cu_2O$/BDD electrode and reached a maximum of -0.12 mA/cm$^2$ at -0.6 V. The same behaviour is seen for the NiO(3)-$Cu_2O$/BDD and NiO(6)-$Cu_2O$/BDD electrodes. The photocurrent density of -0.33 mA/cm$^2$ is obtained at -0.6V for the NiO modified BDD electrodes with three and six coatings respectively. The photocurrents increased slowly for low applied potential between 0V and -0.2V and increased rapidly above -0.25V. The latter is confirmed by the inset of figure 6-3 (a), which shows the PEC performance of the same electrodes under light illumination but without chopping. In

order to find the best photocathode, more NiO coatings were applied and their PEC activities are shown in figure 6-3 (b). The photocurrent density of the NiO(10)-$Cu_2O$/BDD and NiO(15)-$Cu_2O$/BDD is 0.42 mA/cm$^2$ and 0.39 mA/cm$^2$, respectively, as acquired at -0.6V, which is obviously higher than all the other photocathodes. When the numbers of coating were increased further, the current decreased drastically. The photocurrent NiO(20)-$Cu_2O$/BDD and NiO(25)-$Cu_2O$/BDD electrodes diminished to about 0.25 and 0.35 mA/cm$^2$, respectively when measured at -0.6V. The latter is likely to arise from the fact that more coatings increases the thickness in the outer shell with higher amount of NiO nanoparticles which hinders the photo absorptions since NiO with a large band gap (~ 3.6 eV) is not photoactive in the visible region[45]. The inset of the figure 6-3 (b) shows the same photocathodes without chopped light. In the case of more than 10 coatings is that the dark current is increased due to non-photocatalytic reactions of NiO such as static charge storage. Figure 6-3 (c) compares the PEC performances of NiO(15)-$Cu_2O$/BDD and $Cu_2O$/BDD electrode. As shown previously, the unmodified diamond clearly gives no photoelectrochemical response in contrast with the $Cu_2O$ particles modified diamond electrode. Thus, photoelectrochemical responses of the $Cu_2O$ and NiO-$Cu_2O$ modified BDD electrodes are assigned to the visible light absorption by $Cu_2O$ nanoparticles. The modification of $Cu_2O$ nanoparticles by NiO(15) coating enhances the photocurrent by approximately two to four times at potential more negative than -0.4V (see figure 6-3 (c)). The enhancement in the PEC activity is due to the band energy offset made by the edge potential of $Cu_2O$ coated with NiO. This facilitates the fast transfer of the photogenerated electrons to the reaction interface and therefore delays the undesired recombination losses of electron and hole pairs.

The photoconversion efficiency ($\eta$) of photoenergy to hydrogen energy in terms of photocurrent density *versus* applied potential of $Cu_2O$/BDD, NiO(3)- $Cu_2O$/BDD, NiO(6)-$Cu_2O$/BDD, NiO(10)- $Cu_2O$/BDD, NiO(15)- $Cu_2O$/BDD, NiO(20)- $Cu_2O$/BDD and NiO(25)-

$Cu_2O$/BDD was measured under simulated sun illumination and is calculated using the following equation[47,48]:

$$\eta\ (\%) = \left[\frac{\left|J_{ph}\right|\ (mA\ cm^{-1}) \times (1.23 - \ |V_b|)(V)}{P_{total}\ (mW\ cm^{-2})}\right]$$

where $J_{ph}$ is the photocurrent density obtained under an applied potential $V_b$ between the working and the counter electrode, 1.23V is the standard water splitting reaction potential and $P_{total}$ is the incident light intensity (100 mW $cm^{-2}$). As expected, the minimum conversion efficiency was obtained for the $Cu_2O$/BDD and was 0.07%. In contrast, a maximum conversion efficiency of 0.29% was obtained for both the NiO(10)-$Cu_2O$/BDD and NiO(15)-$Cu_2O$/BDD electrodes. The photoconversion efficiency obtained for the NiO(20)-$Cu_2O$/BDD and NiO(25)-$Cu_2O$/BDD was 0.18% and 0.22%, respectively. Likewise, the electrodes with three and six Ni coatings both had a 0.23% efficiency. From the aforementioned efficiencies we can see that the optimised NiO coating generates more active sites for hydrogen evolution, these active sites act as trap sites for photogenerated electrons, which delay charge recombination losses.

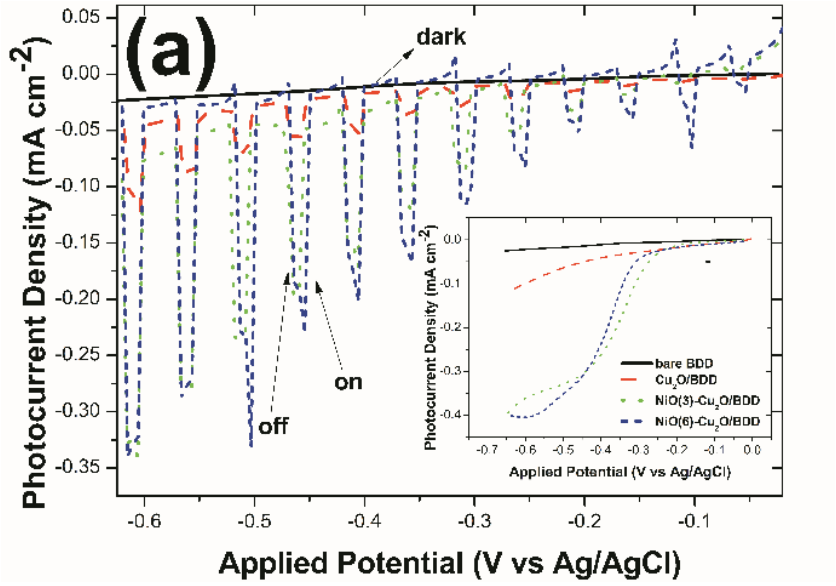

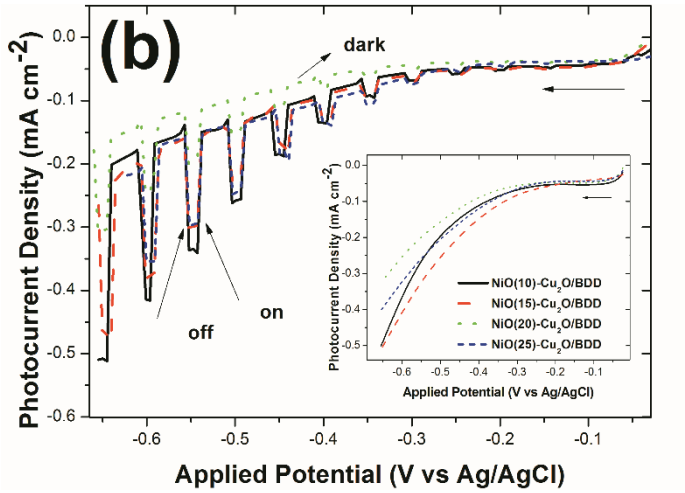


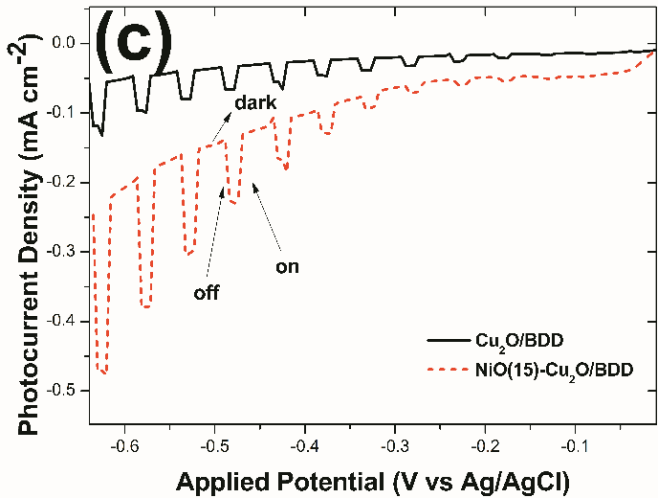


**Figure 6-3** Photoelectrochemical responses of (a) bare BDD, $Cu_2O$, NiO(3)- $Cu_2O$ and NiO(6)- $Cu_2O$ modified BDD, respectively (Inset: PEC performances under non-chopped light), (b) NiO(10)- $Cu_2O$, NiO(15)- $Cu_2O$, NiO(20)- $Cu_2O$ and NiO(20)- $Cu_2O$ modified BDD, respectively (Inset: PEC performances under non-chopped light) and (c) $Cu_2O$/BDD and NiO(15)- $Cu_2O$/BDD. All the linear sweep voltammograms were conducted in 0.1M $Na_2SO_4$ electrolyte at 10 mV/s buffered at pH 6.1 under chopped AM 1.5G light illumination.

## 6.4.1.3 Stability tests of different photocathodes

Linear sweep voltammetry (LSV) was performed to investigate the stability of the photoelectrodes under chopped light illumination at 10 mV/s at a fixed and constant frequency 0.2 Hz in a 0.1M $Na_2SO_4$ electrolyte (pH 6.1) and the results are presented in figure 6-4. Initially, all the photocathode materials were swept for 5 scans under these conditions. The electrodes were then held at a fixed potential -0.5V and for 1800 seconds. The common

denominator is that the dark current decayed quite sharply for all the photoelectrodes. Figure 6-4 (a) shows that the photocurrent decreased slightly from -0.42 mA/cm$^2$ to -0.40 mA/cm$^2$ after 5 scans for the NiO(10)-$Cu_2O$/BDD. Likewise, there was a current drop for the NiO(15)-$Cu_2O$/BDD from -0.48 mA/cm$^2$ to -0.41 mA/cm$^2$. Similarly, the NiO(10)-$Cu_2O$/BDD chronoamperogram shows that the light current decreased as well as the dark current. On the other hand, the stability of the deposits changed completely when the $Cu_2O$/BDD was coated 20 and 25 times. The PEC performance showed an overall current drop in section 3.2, but in terms of stability the NiO(20) modified $Cu_2O$/BDD showed better stability. In particular, the photocurrent density of NiO(10)-$Cu_2O$/BDD was obtained at -0.31 mA/cm$^2$ and remained almost constant after 5 scans in 0.1M $Na_2SO_4$ at -0.30 mA/cm$^2$. Conversely, the photocurrent density of NiO(25)-$Cu_2O$/BDD was acquired at -0.36 mA/cm$^2$ and -0.34 mA/cm$^2$, respectively.

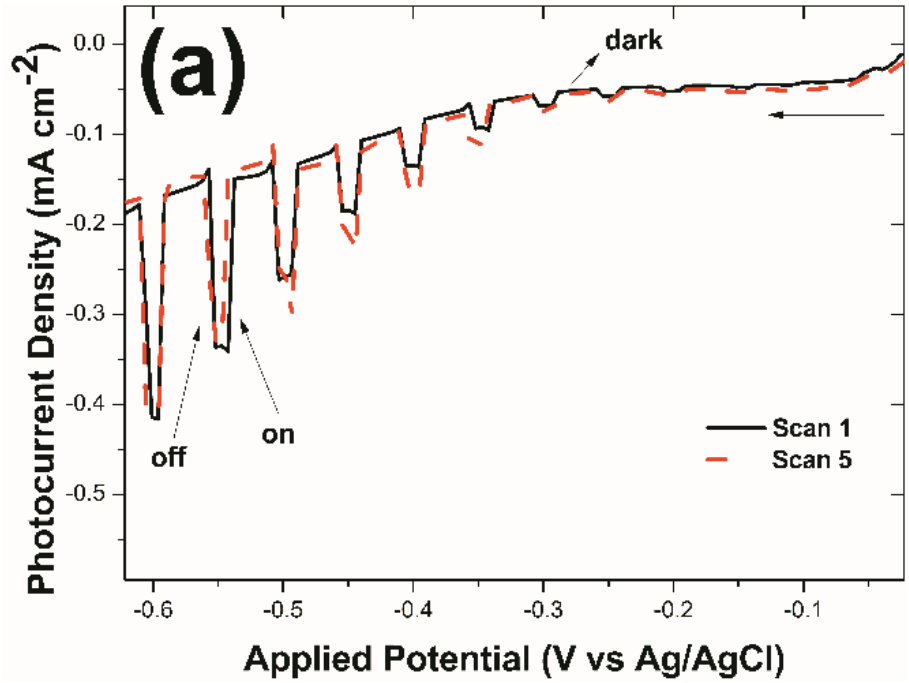

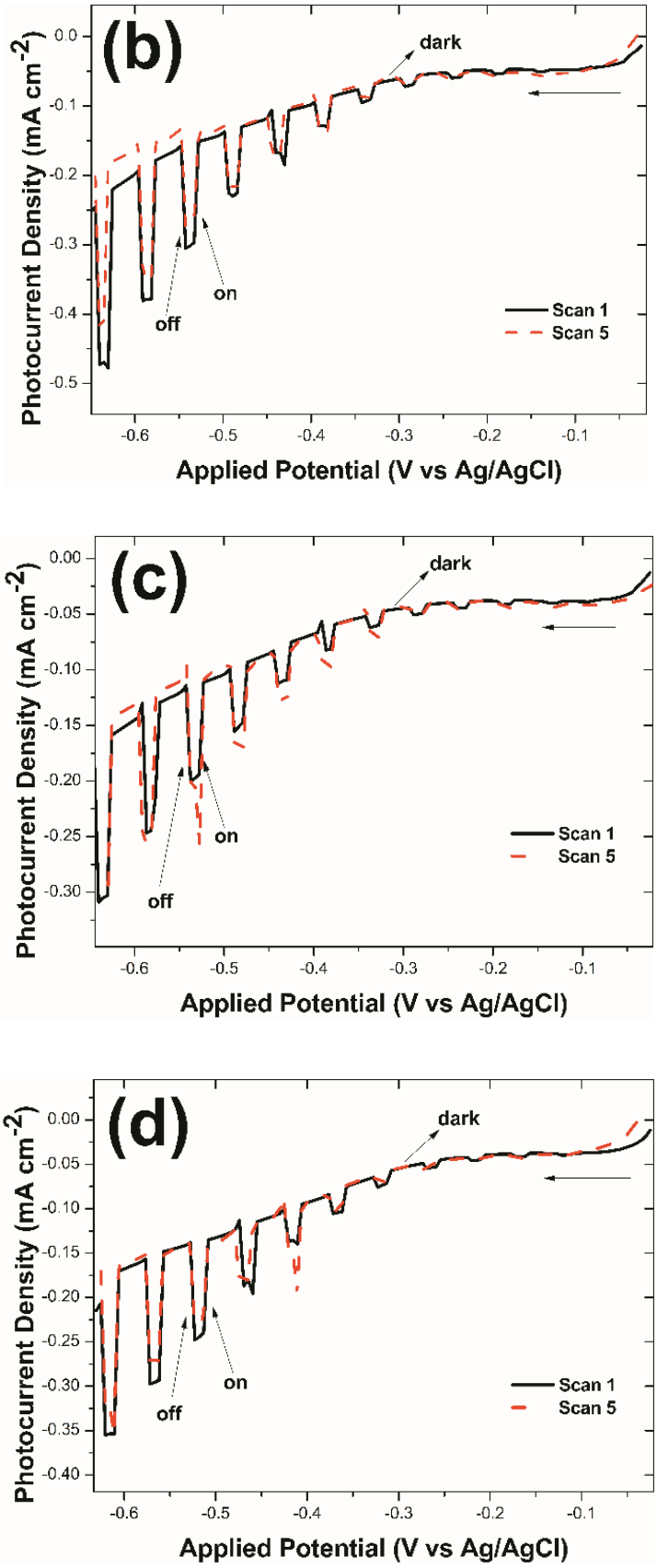


**Figure 6-4** Photoelectrochemical repsonses of different photoelectrodes: (a) NiO(10)-$Cu_2O$/BDD, (b) NiO(15)-$Cu_2O$/BDD, (c) NiO(20)-$Cu_2O$/BDD and (d) NiO(25)-$Cu_2O$/BDD under chopped AM 1.5G light illumination at 0.2 Hz at scan rate of 10 mV/s.

### 6.4.1.4 Amperometric photostability of different photocathodes

Figure 6-5 shows chronoamperometric features related to the photocatalytic stability of different photocathodes under 0.2Hz chopped light illumination at -0.5V. Figure 6-5 (a) exhibits only the $Cu_2O$/BDD electrode without NiO coating. As shown in the figure, the uncoated $Cu_2O$/BDD photoelectrode was quite stable with a dark current about 0.01 mA/cm$^2$ and a photocurrent that increased under chopped illumination before it stabilised at -0.07 mA/cm$^2$. The NiO(10)-$Cu_2O$/BDD showed a photocurrent density of -0.3 mA/cm$^2$ for the first few seconds, which slightly decreased for a period of 30 minutes to -0.18 mA/cm$^2$ i.e., 60% of the initial photocurrent retained in figure 6-5 (b). A more obvious photocurrent drop is shown in figure 6-5(c) of NiO(15)-$Cu_2O$/BDD electrode where both under dark and illumination photocurrent responses diminished before they stabilised at 70% of this photocurrent remained only after 30 minutes. There is a small photocurrent drop for the NiO(20)-$Cu_2O$/BDD electrode as shown in figure 6-5 (d). During the first few minutes the photocurrent drops from -0.15 mA/cm$^2$ to -0.13 mA/cm$^2$ after which stabilises at -0.11 mA/cm$^2$ after 30 seconds. The dark current is close to zero in the chronoamperogram of figure 6-5 (d) and 73% of this current remains after an operational period of 30 minutes, which shows a relatively stable photoelectrode. The same behaviour is also observed for the NiO(25)-$Cu_2O$/BDD photoelectrode in figure 6-5 (e) that has a retention photocurrent of 75%. Overall, NiO coated photoelectrodes gave higher photocurrent responses and better stability than that of the $Cu_2O$ itself. The latter confirms that the effect of the NiO co-catalyst increased the overall photocurrent density in addition to which if helped the electron-holes recombination to occur slower than that of $Cu_2O$ alone.

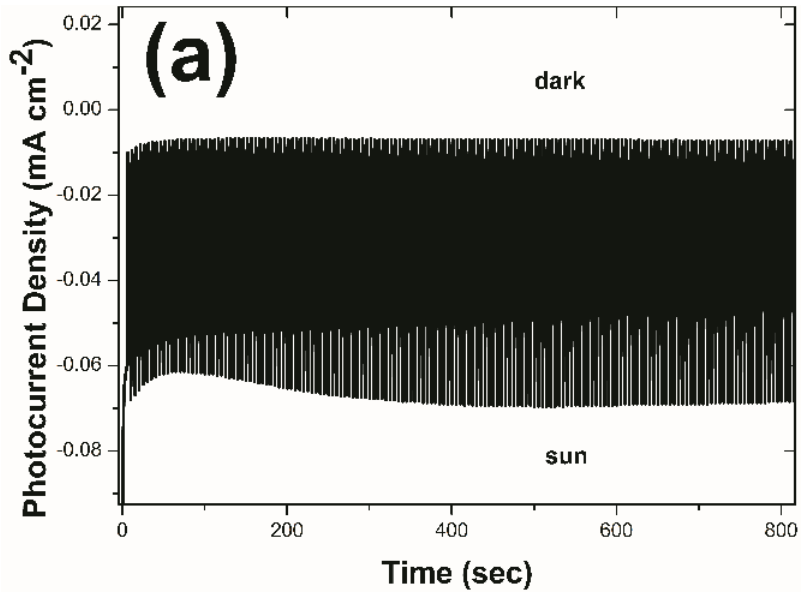
(a)
dark
sun
Photocurrent Density (mA cm-2)
Time (sec)

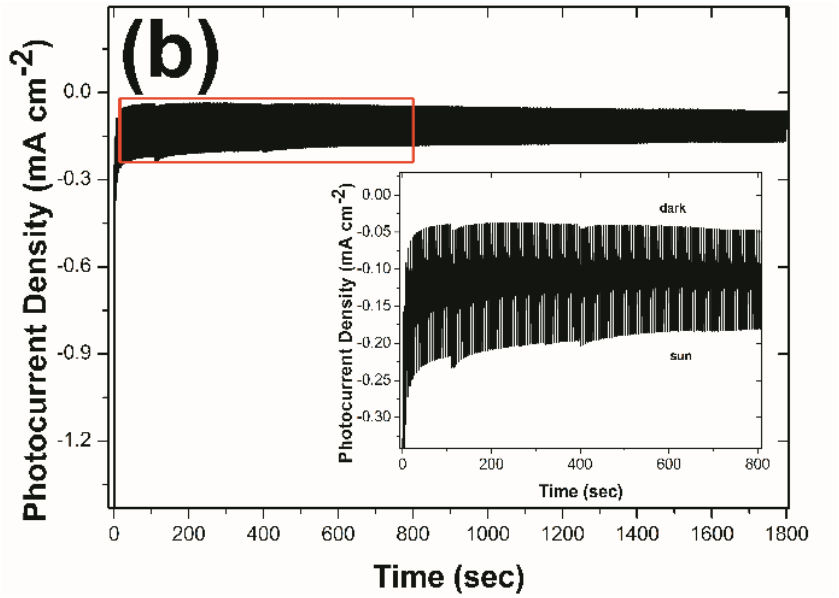
(b)
Photocurrent Density (mA cm-2)
Time (sec)
dark
sun

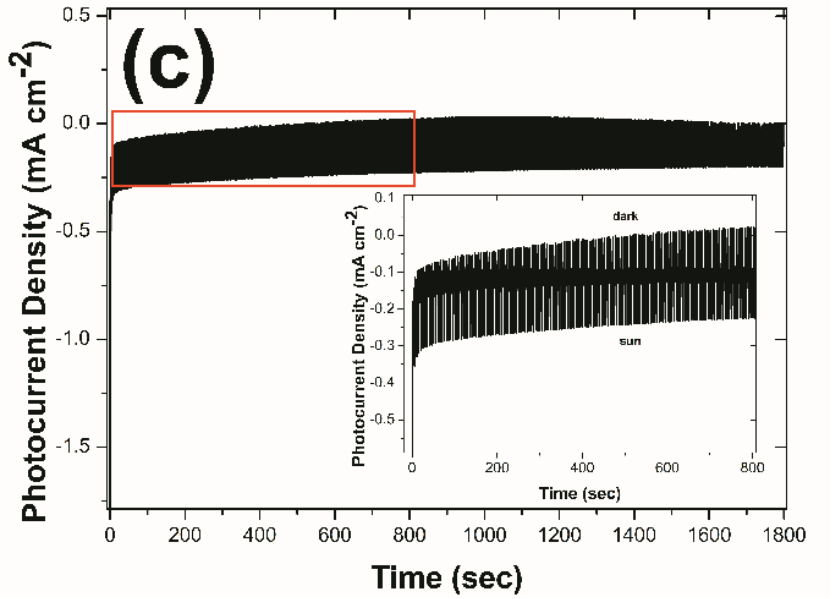
(c)
Photocurrent Density (mA cm-2)
Time (sec)
dark
sun

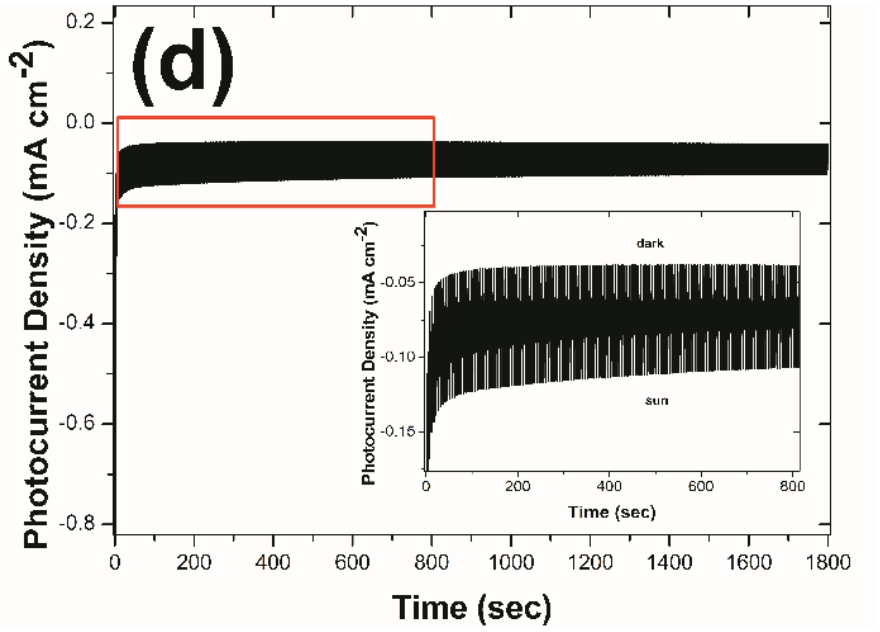


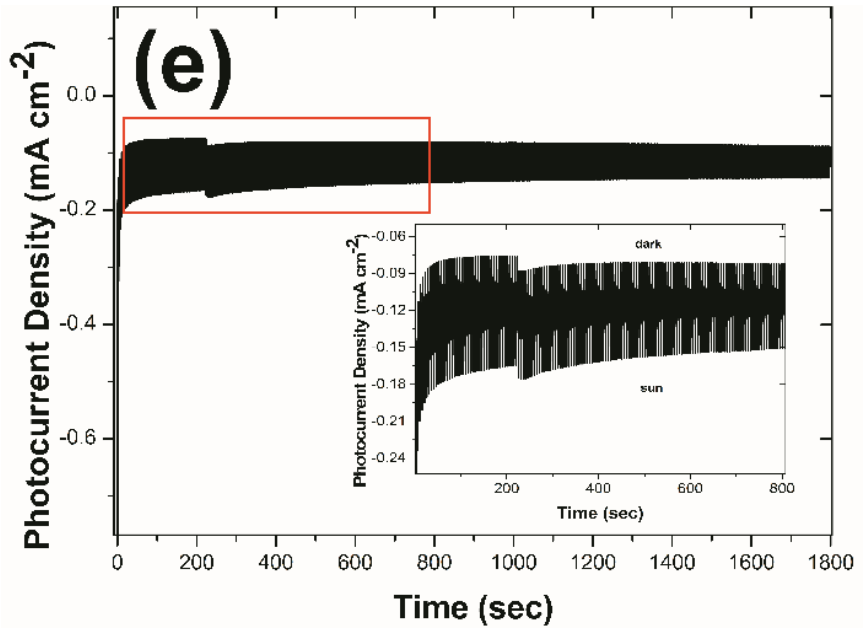


**Figure 6-5** Chronoamperograms of the photoelectrochemical response of the different photoelectrodes (a) $Cu_2O$/BDD, (b) NiO(10)-$Cu_2O$/BDD, (c) NiO(15)-$Cu_2O$/BDD, (d) NiO(20)-$Cu_2O$/BDD and (e) NiO(25)-$Cu_2O$/BDD in an aqueous $Na_2SO_4$ electrolyte (0.5 M, pH 6.1) under AM 1.5 chopped light illumination held at -0.5V for 30 min (light on-off interval of 5s).

## 6.4.1.5 Electrochemical impedance

The electron transfer activity at the photocathode/solution interface was investigated through electrochemical impedance spectra (EIS) as shown in Figure 5. The Nyquist plots of figure 6-6 (a) were used to analyse the interfacial charge transfer process of the NiO coated $Cu_2O$/BDD electrodes with the electrolyte. The measurements were carried out in the frequency range of 1 MHz to 0.1 Hz at a potential of -0.5V under dark and light conditions. The semicircular features of the Nyquist plots (Figure 6-6 (a)) at high frequencies defines the charge transfer resistance[49]. Figure 6-6 (a) shows the semicircular features of the EIS measurements both in dark and light conditions which suggests that charge transfer resistance controls the kinetics across the electrode/electrolyte interface[50,51]. The arc radii of the photoelectrodes under illumination was much smaller than their dark counterparts. The latter is attributed to the increase of the electrode conductivity when irradiated by light. This phenomenon suggests that the NiO coating on the $Cu_2O$ modified BDD facilitates the transfer of the photo-induced electrons to the reaction interfaces. Albery *et al.* interpreted the Mott-Schottky plots in 1996[52]. The capacitive behaviour of the semiconductor is combined with that of the Helmholtz layer to provide a complete description of the potential distribution in the electrolyte and in the semiconductor for all applied potentials including accumulation, the flat-band transition and depletion. Therefore, Mott-Schottky plots were used for the measurements in the depletion region when the potential is even across the Helmholtz layer. The plot with $1/C^2$ *vs*. applied potential at a fixed frequency of 1 kHz was obtained according to the Mott-Schottky equation[53]:

$$\frac{1}{C^2} = \left(\frac{2}{e\varepsilon\varepsilon_0 N_A A^2}\right)\left[V - V_{fb} - \frac{k_B T}{e}\right] \qquad (6\text{-}1)$$

where $e$ is the electronic charge (1.602 x $10^{-19}$ C), $\varepsilon$ is the relative permittivity ($\varepsilon \sim 7.5$ for the $Cu_2O$)[56], $\varepsilon_0$ is the permittivity of vacuum (8.854 x $10^{-12}$ F/m), $k_B$ is Boltzmann's constant (1.38

x $10^{-23}$ J/K), *T* is the absolute temperature (298 K), $N_A$ is the carrier density, $V_{fb}$ is the flatband potential, V is the applied potential and A is the area of the electrode. The active areas of all electrodes were considered as the geometric surface area. From the linear fit of $1/C^2$ vs. V in figure 6-6 (b), $V_{fb}$ for Cu2O were measured to be +0.11V for NiO(10)-$Cu_2O$/BDD, +0.1V for NiO(15)-$Cu_2O$/BDD, +0.03V for NiO(20)-$Cu_2O$/BDD and +0.05V for NiO(25)-$Cu_2O$/BDD electrodes. The flatband potential, as indicated by the name, is the potential at which the Fermi energy level lies at the same energy as the electrolyte redox potential, and hence no charge transfer or band bending occurs at the semiconductor-liquid junction (SLJ), thus the conduction and valence bands are flat. The $V_{fb}$ is considered the close approximation of the valence band edges of the p-type semiconductors[54]. Therefore, the position of the conduction band edge can easily be calculated from the optical bandgap energies. The conduction bands are positioned at -1.48V vs. RHE for NiO(10)-$Cu_2O$/BDD, -1.49 V vs. RHE for NiO(15)-$Cu_2O$/BDD, -1.56 vs. REH NiO(20)-$Cu_2O$/BDD and -1.54V vs. RHE for NiO(25)-$Cu_2O$/BDD electrodes. The values were converted into the scale of reversible hydrogen electrode by using the equation $V_{RHE} = V_{Ag/AgCl(1\ M\ KCl)} + 0.059 \times pH + 0.22V$ (standard potential of Ag/AgCl/1 M KCl vs. RHE) for comparison purpose only. The conduction band position of our fabricated electrodes are more negative than that of the reported literature values[13,55], in which higher conduction band positions may have provided a larger electrochemical driving force for hydrogen evolution reaction. The carrier density, $N_A$, was calculated form the slopes of Mott-Schottky plots using the following equation [56]:

$$N_A = \frac{2}{e\varepsilon\varepsilon_0 S_{MS} A^2} \qquad (6\text{-}2)$$

where *e* is the electronic charge, $\varepsilon$ is the relative permittivity, $\varepsilon_0$ is the permittivity of vacuum, $S_{MS}$ is the slope which can be obtained from the Mott-Schottky plot and *A* is the surface area of the electrode (1 $cm^2$). The slopes were measured for each electrode are $14.2 \times 10^9$ for

NiO(10)-$Cu_2O$/BDD, $11.7x10^9$ NiO(15)-$Cu_2O$/BDD, $22.3x10^9$ for NiO(20)-$Cu_2O$/BDD and $11.7x10^9$ for NiO(25)-$Cu_2O$/BDD. Hence, the charge carrier was found to be $1.32x10^{21}$ $cm^{-3}$ for NiO(10)-$Cu_2O$/BDD, $1.60x10^{21}$ $cm^{-3}$ for NiO(15)-$Cu_2O$/BDD, $8.43x10^{20}$ $cm^{-3}$ for NiO(20)-$Cu_2O$/BDD and $1.60x10^{21}$ $cm^{-3}$ for NiO(25)-$Cu_2O$/BDD, respectively. From the last calculations the NiO(15)-$Cu_2O$/BDD and NiO(25)-$Cu_2O$/BDD electrodes showed the highest charge carrier. Nevertheless, it is noted that the amount of charge carrier is not proportional to the number of NiO coating cycles. Moreover, the charge carrier is disproportionate to the photocatalytic performance of each photoelectrode. This can be attributed to the uneven dispersion of the NiO layer onto the $Cu_2O$ particles as shown through the SEM images and thus rather a preferential photoelectrochemical process takes place on the photoactive deposits on BDD. The latter is a result of the NiO coating that is difficult to control and reproduce on the diamond surface. This difficulty arises form the fact that diamond has not only an uneven distribution of the B dopant that assists the conductivity, but also a slightly varying B dopant concentration with each individual BDD wafer that subsequently causes reproducibility problems. The carrier densities in the fabricated NiO-$Cu_2O$ particles compared well with literature values with higher values than those of the $Cu_2O$ films fabricated by electrodeposition, namely higher than $5x10^{17}$ $cm^{-3}$ and $3.5x10^{20}$ $cm^{-3}$, respectively[56,57].

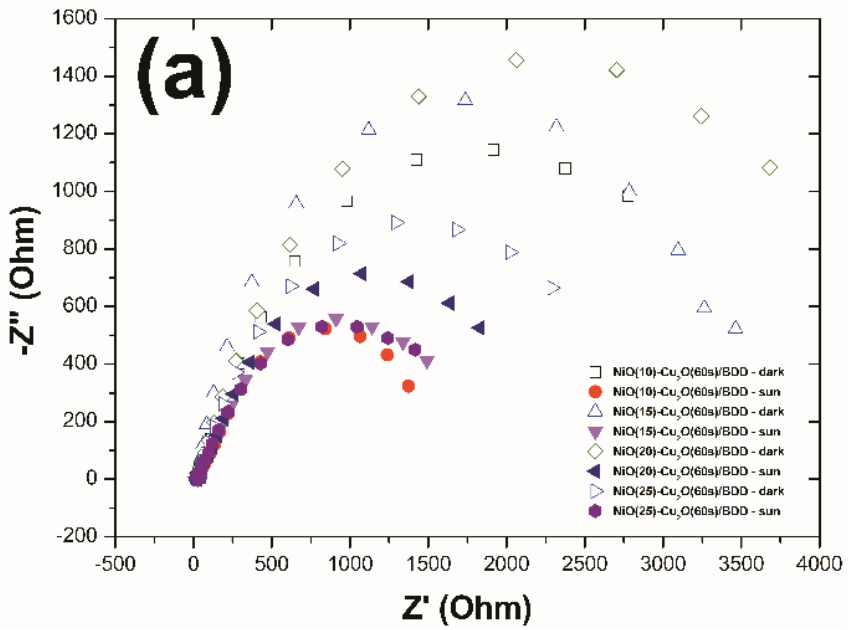


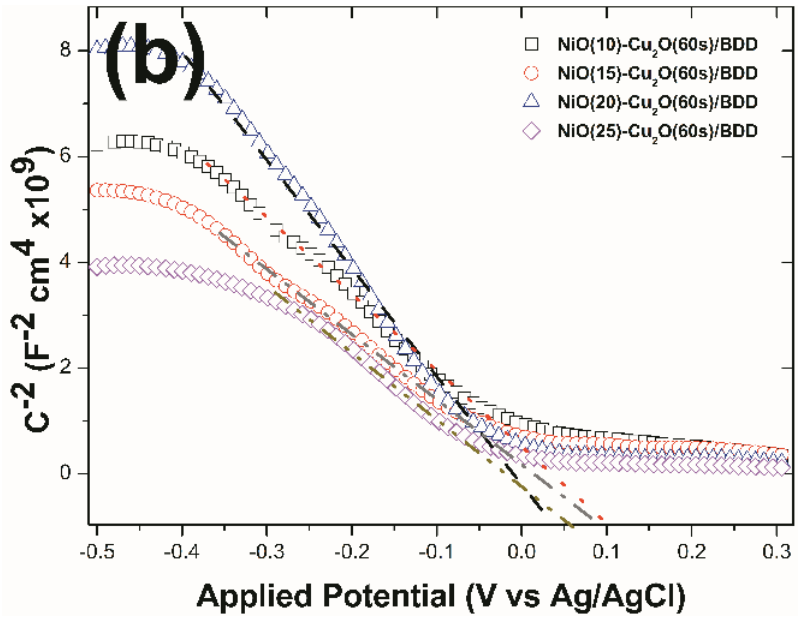


**Figure 6-6** (a) Nyquist plots of NiO(10)-$Cu_2O$/BDD, NiO(15)-$Cu_2O$/BDD, NiO(20)-$Cu_2O$/BDD and NiO(25)-$Cu_2O$/BDD photoelectrodes in dark and under AM 1.5G light illumination in 0.1M $Na_2SO_4$ electrolyte buffered at pH 6.1. (b) Mott-Schottkly plots of NiO(10)-$Cu_2O$/BDD, NiO(15)-$Cu_2O$/BDD, NiO(20)-$Cu_2O$/BDD and NiO(25)-$Cu_2O$/BDD photoelectrodes in dark in 0.1M $Na_2SO_4$ electrolyte buffered at pH 6.1.

## 6.4.2 $CO_2$ reduction using electrodeposited Ni and $Cu_2O$ nanoparticles

### 6.4.2.1 Structural and XPS characterisation of the deposits on BDD

SEM images of $Cu_2O$ modified BDD electrodes after 60 seconds of deposition at the current described in the previous section are shown in figure 6-7 (a) and (b) in 100 μm and 20 μm scale, respectively. The image with the wide scale clearly shows that the particles tend to be deposited mostly at the edges of the diamond due to the lateral conductivity of diamond electrodes as reported in previous chapters. The areas are not covered with $Cu_2O$ nanoparticles are areas with less or no B dopant concentrations that are therefore less conductive and consequently experiences inhibited $Cu_2O$ deposition. Figure 6-7 (b) illustrates $Cu_2O$ nanoparticles on BDD at the 20 μm scale. The deposition seems to be dense with a high level of particles agglomeration due to the long deposition time. The agglomeration makes it difficult to estimate the NPs size. Ni nanoparticles modified $Cu_2O$/BDD electrode is seen in figure 6-7 (c). Ni-$Cu_2O$ deposits in a non-uniform manner with visible agglomeration at the diamond edges as shown in figure 6-7. Sequential deposition tended to produce more discrete particles at some areas on the surface but as noted previously, the non-uniform nature of the deposition sensitively reflects the variations in the lateral conductivity of the diamond as a result of the non-uniform distribution of the B dopant.

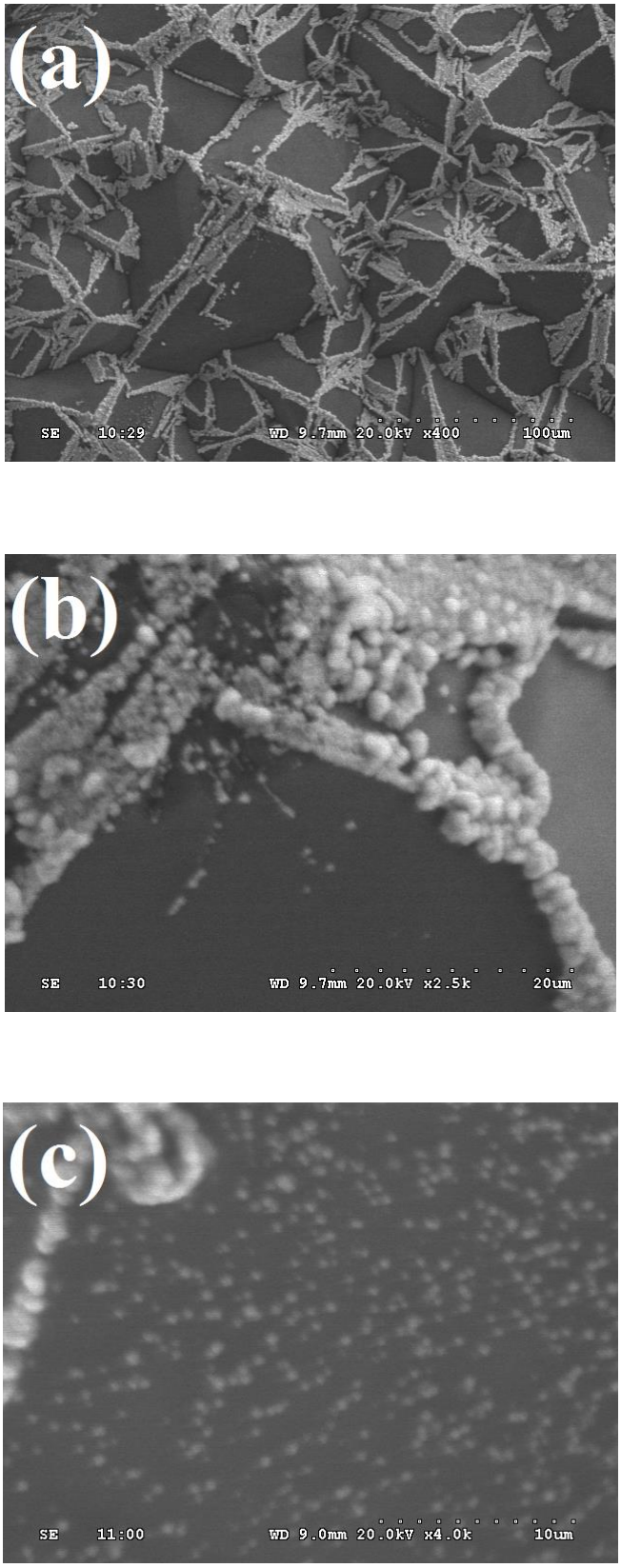


**Figure 6-7** SEM images of (a) $Cu_2O$ deposited on BDD electrodes (100 μm), (b) $Cu_2O$ on BDD (20 μm) and (c) Ni deposited on $Cu_2O$/BDD, respectively through potentiostatic method at -6.6 mA for the $Cu_2O$ and -20 mA for the Ni, respectively.

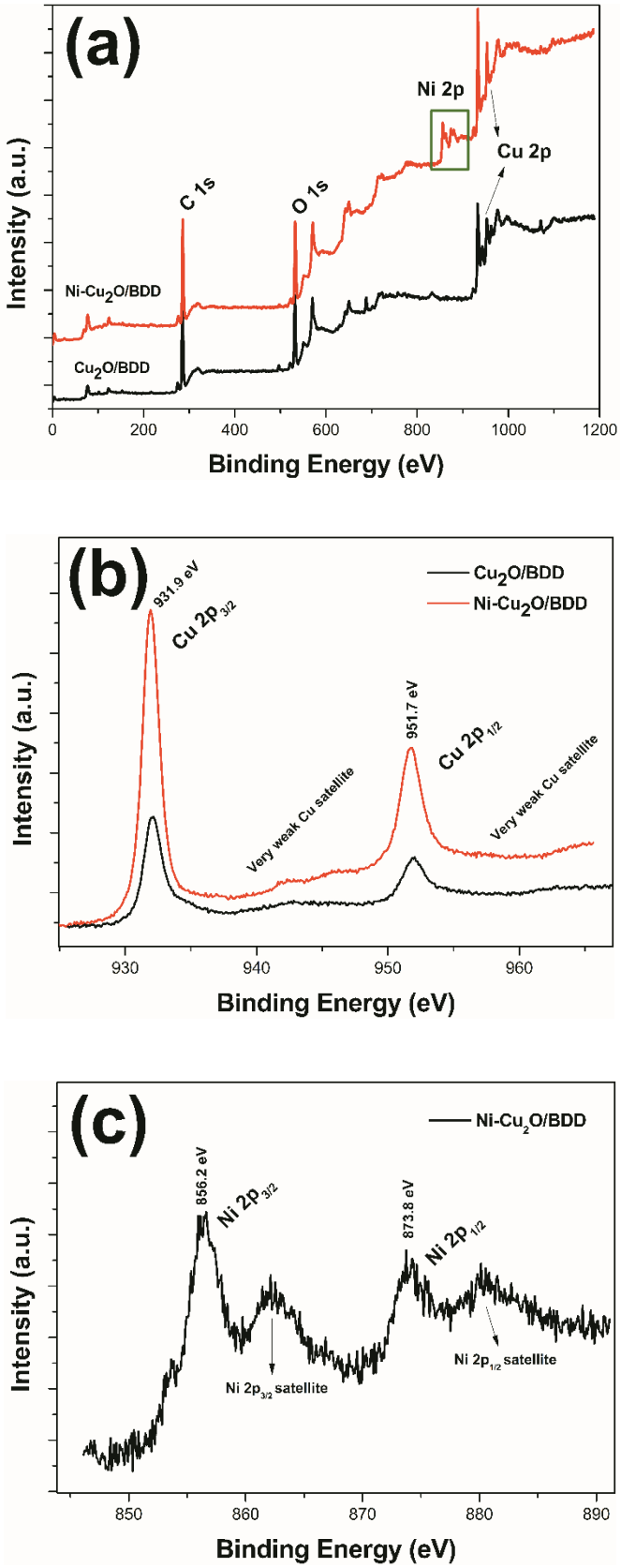


**Figure 6-8** (a) XPS spectrum of survey of the $Cu_2O$/BDD and Ni-$Cu_2O$/BDD. (b) Typical Cu 2p peaks of the $Cu_2O$ and Ni-$Cu_2O$ modified BDD electrodes respectively. (c) Typical Ni 2p peak of the Ni-$Cu_2O$ modified BDD.

XPS was conducted for the samples in figure 6-8. Figure 6-8 (a) shows the wide scans of the modified diamond electrodes with the relevant elements of $Cu_2O$ and Ni-$Cu_2O$ modified BDDs, respectively. The survey scans indicate that these electrodes contain O, C and photoelectron peaks of the relevant elements, which is consistent with the modification of contaminant-free diamond electrode with either $Cu_2O$ or Ni- $Cu_2O$ nanoparticles. Figure 6-8 (b) shows typical Cu 2p peaks of $Cu_2O$ and Ni- $Cu_2O$ modified BDDs, respectively. From the Cu 2p photoelectron peaks there is no binding energy shift, attributed to the fact that the $Cu_2O$ loading is much higher than the Ni loading and for that reason the Ni content was not adequate to cover the whole $Cu_2O$ surface and thus an electronic contribution to be seen at the XPS spectra. Both electrodes have Cu $2p_{3/2}$ and Cu $2p_{1/2}$ at 931.9 eV and 951.7 eV, respectively. Also, the two main Cu 2p peaks are accompanied by two very weak satellite peaks that suggest the existence of $Cu_2O$ instead of CuO. A typical Ni 2p peak is displayed in figure 6-8 (c). Ni peak has a Ni $2p_{3/2}$ and Ni $2p_{1/2}$ peaks at 856.2 eV and 873.8 eV, respectively. The Ni 2p peaks are also accompanied by two small satellite peaks at 862.1 eV and 880.2 eV, respectively.

### 6.4.2.2 Photoelectrochemical measurements of different photoelectrodes

The electrochemical and photoelectrochemical activities of the photocatalysts towards $CO_2$ reduction were characterised by cyclic voltammetry in 0.5M $KHCO_3$ at scan rate of 20 mV/s in the presence of $CO_2$ and/or under non-chopped AM 1.5G light illumination. Figure 6-9 (a) shows the cyclic voltammograms of the $Cu_2O$ and Ni(20s)-$Cu_2O$ modified BDD electrodes in the presence of $CO_2$ and/or under light illumination. Initially, the bare BDD was scanned between 0V and -1.6V. The current response on the unmodified surface was zero. The modification of BDD with $Cu_2O$ nanoparticles gave a strong current density peak (-12.07 $mA/cm^2$) at the cathodic scan at around -1.27V. This peak suggests on the one hand

the electroreduction of $Cu_2O$, due to the surface exposure in the PEC cell that changed colour and that confirmed the instability of $Cu_2O$ in aqueous solutions and on the other hand the reduction of the $CO_2$ present in the electrolyte. After the modification of $Cu_2O$/BDD with Ni nanoparticles the current density increased more, which resulted in another strong peak of current density -19.07 mA/cm$^2$ at -1.20V. The current peak of the Ni(20s)-$Cu_2O$/BDD shifted positively indicating the electronic interaction of the two metals at the interface of diamond and therefore the higher current response towards the $CO_2$ reduction. The last diamond electrode in figure 6-9 (a) consisted of Ni(20s)- $Cu_2O$. Light illumination was applied at the latter and then the strongest photocurrent density was obtained (-23.44 mA/cm$^2$) at -1.14V. The cyclic voltammogram of the Ni(20s)- $Cu_2O$/BDD was also shifted positively in relationship with the former $Cu_2O$/BDD as well as the Ni(20s)- $Cu_2O$/BDD in the presence of $CO_2$ but without light illumination. The onset overpotential shift in the positive direction is also noteworthy. The highest onset overpotential was -0.42V for the Ni(20s)-$Cu_2O$/BDD photocatalyst under non-chopped light illumination.

The purpose of the cyclic voltammograms in figure 6-9 (b) was the optimisation of the conditions of the Ni electrodeposition and discovery of the catalyst with the best performance. Hence, the Ni(20s)-$Cu_2O$/BDD electrode reduced the $CO_2$ giving the highest current density than its counterparts -19.07 mA/cm$^2$. As shown in the figure 6-9 (b), longer deposition time of Ni, 30 and 50 seconds respectively, does not facilitate the electronic interaction of the two metals with the diamond. Rather, the Ni(20s)-$Cu_2O$/BDD electrode reflects in part the particular properties of the metals, but also the interaction with the underlying diamond. Furthermore, a potential shift between the Ni(20s)-$Cu_2O$/BDD electrode and the electrodes of 30 and 50 seconds of Ni deposition is likely due to a combination of the amount of the deposited Ni with the underlying $Cu_2O$, the instability of the $Cu_2O$ nanoparticles and the reduction of $Cu_2O$ in the aqueous electrolyte and the reduction of $CO_2$.

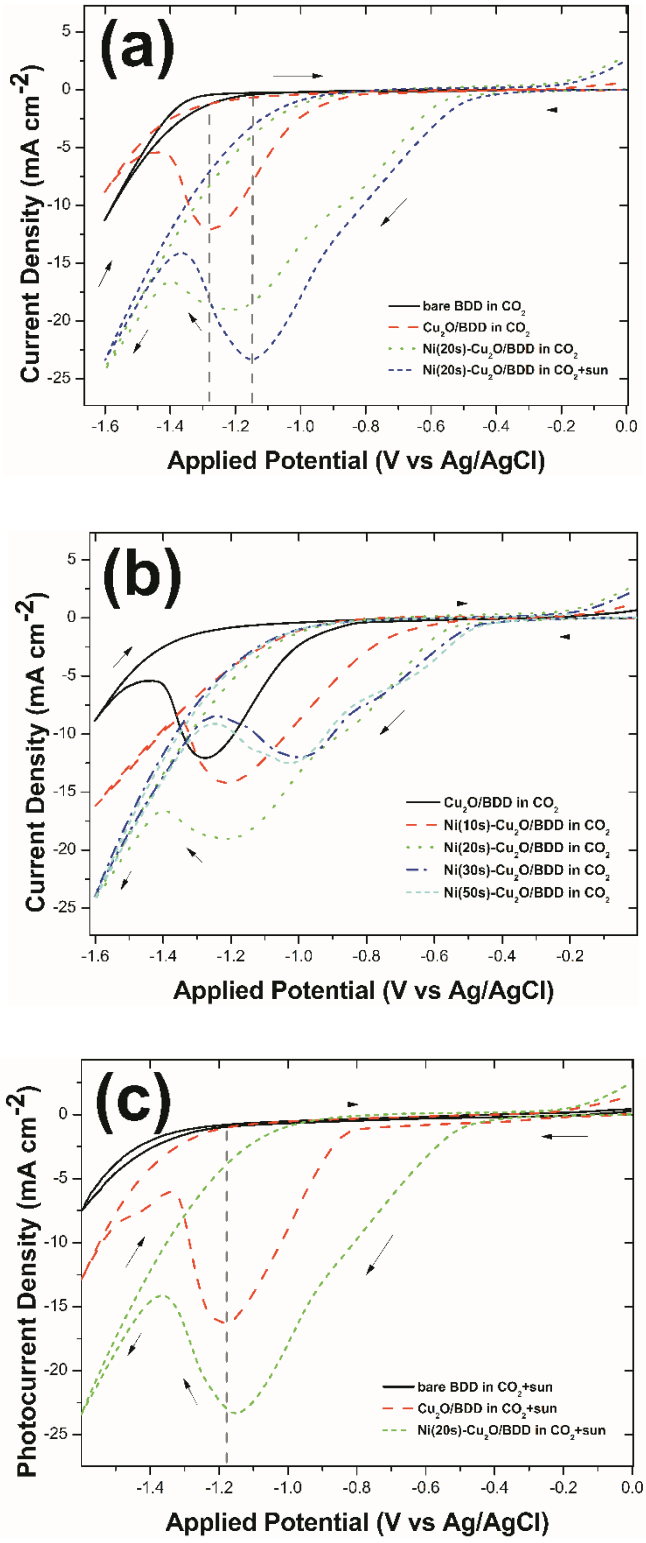


**Figure 6-9** Electrochemical and photoelectrochemical responses of (a) bare BDD, $Cu_2O$ and Ni(20s)-$Cu_2O$ in the presence of $CO_2$ and Ni(20s)-$Cu_2O$ modified BDD in the presence of $CO_2$ under non-chopped light, respectively. (b) $Cu_2O$, Ni(10s)-$Cu_2O$, Ni(20s)-$Cu_2O$, NiO(30s)- $Cu_2O$ and NiO(50s)-$Cu_2O$ modified BDD, respectively in the presence of $CO_2$ under non-chopped light. (c) Bare BDD, $Cu_2O$/BDD and Ni(20s)-$Cu_2O$/BDD in the presence of $CO_2$ under non-chopped light. All the cyclic voltammograms were conducted in 0.5M $KHCO_3$ electrolyte at 20 mV/s buffered at pH 6.1 under non-chopped AM 1.5G light illumination.

Figure 6-9 (c) shows the photocurrent density of the bare BDD, $Cu_2O$ and Ni(20s)-$Cu_2O$ modified BDDs, respectively in the presence of $CO_2$ under AM1.5G light illumination. The cyclic voltammograms were scanned between the potential window of 0V and -1.6V at scan rate of 20 mV/s. The unmodified diamond electrode is inactive whilst after its modification with $Cu_2O$ nanoparticles gives a strong sharp peak of -16.3 mA/cm$^2$ at -1.18V which represents the $CO_2$ reduction. However, the highest photocurrent response was obtained from the Ni(20s)-$Cu_2O$ modified BDD giving a greater peak (-23.36 mA/cm$^2$) in the cathodic scan at -1.14V. The tiny potential shift of 0.04V shows the contribution due to the light source as well as the electronic effects of the two metals at the interface with the diamond electrode.

At this point the fundamental aspect for photocatalytic reduction of $CO_2$ needs to be discussed. In principle, the semiconductor-based photocatalysis for the reduction of $CO_2$ with $H_2O$ involves three main steps (Figure 6-10). In the first step, electron-hole pairs are generated when a semiconductor photocatalyst is illuminated by an appropriate light source with its energy and equal to, or greater than the band energy ($E_g$) of the semiconductor (Figure 6-10 (i)). Then the generated electrons and holes migrate to the surface of the semiconductor in the second step (Figure 6-10 (iia)). Only a fraction of the carriers actually reach the surface of the semiconductor or co-catalyst. A large fraction of electron-hole pairs recombine (Figure 6-10 (iib)), with the energy being released in the form of heat or photons. In the third step, the photogenerated electrons reduce $CO_2$, which is adsorbed on catalyst surfaces, into CO, HCOOH, $CH_3OH$ or $CH_4$, whereas the holes oxidise $H_2O$ to $O_2$. The first and second steps are the same as those in the splitting of $H_2O$. The third step is peculiar to the reduction of $CO_2$. The reduction of $H_2O$ could also proceed in competition of that of $CO_2$.

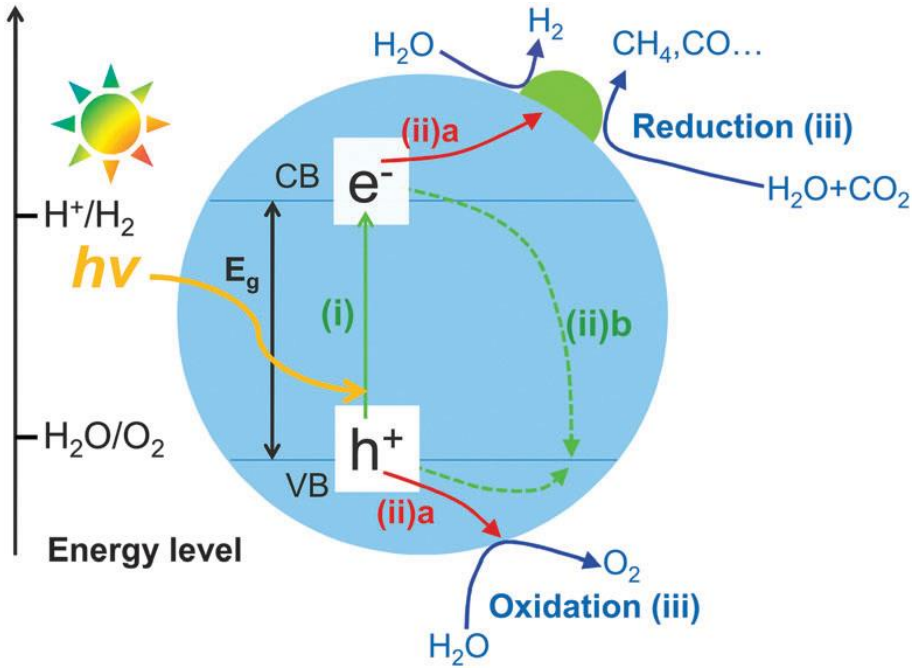


**Figure 6-10** Schematic illustration of the basic mechanism of photocatalytic reduction of $CO_2$ with $H_2O$ on a semiconductor photocatalyst[18].

# 6.5 Conclusions

In summary, a novel and low-cost photocathode material was fabricated by electrochemical methods. The method involved the electrodeposition of $Cu_2O$ nanoparticles on BDD electrodes from a surfactant-free "green" electrolyte followed by a thin coating of NiO onto the freshly prepared $Cu_2O$ nanoparticles for use in water splitting. Photocatalysts for $CO_2$ reduction were fabricated by a two-step electrochemical method involving the electrodeposition of $Cu_2O$ followed by Ni. SEM data revealed that $Cu_2O$ nanoparticles are cubical in shape and NiO deposited sporadically as nanoparticles around the $Cu_2O$ cubical particles as well as unoccupied surrounding area of the BDD substrate. The semiconductor/co-catalyst ($Cu_2O$-NiO) photocatalyst presented higher photocatalytic activity in relation to the unmodified $Cu_2O$/BDD alone. XPS data suggests electronic interaction at the interfacial surface between the two metals and therefore co-catalysts effects of the NiO-$Cu_2O$/BDD leading to the generation of more active sites for hydrogen evolution reaction compared to

$Cu_2O$/BDD itself. The best current densities were obtained at -0.51 mA/cm$^2$ and -0.13 mA/cm$^2$ for the NiO(10)- $Cu_2O$/BDD and $Cu_2O$/BDD respectively for the application of water splitting. Stability tests showed only 0.02 mA/cm$^2$ current drop (4.76% drop of the initial current) after 5 scans through linear sweep voltammetry for the NiO(10)- $Cu_2O$/BDD. Chronoamperometric response showed also a steady state current over a period of 30 minutes for the latter photoelectrode. The best current densities for the $CO_2$ reduction reaction was obtained by the Ni(20s)-$Cu_2O$/BDD at -19.07 mA/cm$^2$ only in the presence of $CO_2$ and at -23.36 mA/cm$^2$ in the presence of $CO_2$ and under light illumination. Finally, the semicircular features of EIS measurements both in dark and under illumination exhibited higher transfer of the photo-induced electrons from the NiO(10)- $Cu_2O$/BDD to the reaction interfaces. Overall, a very promising system is reported in this work; however, the effects of structural aspects of semiconductors, such as crystalline phases, particle sizes, morphologies, exposed facets and heterojunctions on their catalytic behaviours are highly significant and should be investigated in product analysis. Furthermore, other concepts like increasing the surface area of the catalyst (e.g. metal foams), use of bimetallic catalysts and use of organometallic complexes might become more important for either $H_2O$ splitting and $CO_2$ reduction reactions.

# 6.6 Bibliography

1. Parida KM, Biswal N, Das DP, Martha S. Visible light response photocatalytic water splitting over CdS-pillared zirconium-titanium phosphate (ZTP). *Int. J. Hydrogen Energy*. 2010;35(11):5262–5269. doi:10.1016/j.ijhydene.2010.03.017.

2. Biswal N, Das DP, Martha S, Parida KM. Efficient hydrogen production by composite photocatalyst CdS-ZnS/Zirconium-titanium phosphate (ZTP) under visible light illumination. *Int. J. Hydrogen Energy*. 2011;36(21):13452–13460. doi:10.1016/j.ijhydene.2011.07.106.

3. Martha S, Das DP, Biswal N, Parida KM. Facile synthesis of visible light responsive $V_2O_5$/N,S–$TiO_2$ composite photocatalyst: enhanced hydrogen production and phenol

degradation. *J. Mater. Chem*. 2012;22(21):10695. doi:10.1039/c2jm30462g.

4. Hsu YK, Lin YG, Chen YC. Polarity-dependent photoelectrochemical activity in ZnO nanostructures for solar water splitting. *Electrochem. commun*. 2011;13(12):1383–1386. doi:10.1016/j.elecom.2011.08.016.

5. Khaselev O, Turner JA. A Monolithic Photovoltaic-Photoelectrochemical Device for Hydrogen Production via Water Splitting Reports A Monolithic Photovoltaic-Photoelectrochemical Device for Hydrogen Production via Water Splitting. *Science*. 2013;425(1998). doi:10.1126/science.280.5362.425.

6. Conte M. Energy and the Hydrogen Economy. 2009:232–254 (Switzerland).

7. Warren EL, McKone JR, Boettcher SW, Mi Q, Santori EA, Lewis NS. Solar water splitting cells. *Chem. Rev*. 2010;110:6446–6473. doi:10.1021/cr1002326.

8. Turner JA. A Realizable Renewable Energy Future. *Science*. 1999;285(5428):687–689. doi:10.1126/science.285.5428.687.

9. Chen X, Shen S, Guo L, Mao SS. Semiconductor-based Photocatalytic Hydrogen Generation. *Chem. Rev. (Washington, DC, United States)*. 2010;110(11):6503–6570. doi:10.1021/cr1001645.

10. Barreca D, Carraro G, Gombac V, Gasparotto A, Maccato C, Fornasiero P, Tondello E. Supported metal oxide nanosystems for hydrogen photogeneration: Quo vadis? *Adv. Funct. Mater*. 2011;21(14):2611–2623. doi:10.1002/adfm.201100242.

11. Conte M, Iacobazzi A, Ronchetti M, Vellone R. Hydrogen economy for a sustainable development: State-of-the-art and technological perspectives. *J. Power. Sources*. 2001;100(1-2):171–187. doi:10.1016/S0378-7753(01)00893-X.

12. Kelly NA, Gibson TL. Design and characterization of a robust photoelectrochemical device to generate hydrogen using solar water splitting. *Int. J. Hydrogen Energy*. 2006;31(12):1658–1673. doi:10.1016/j.ijhydene.2005.12.014.

13. Nocera DG, Nash MP. Powering the planet: Chemical challenges in solar energy utilization. *PNAS*. 2006;103(43):15729-15735. doi:pnas.0603395103.

14. Angamuthu R, Byers P, Lutz M, Spek AL, Bouwman E. Electrocatalytic $CO_2$ Conversion to Oxalate by a Copper Complex. *Science*. 2010;327(5963):313–315. doi:10.1126/science.1177981.

15. Boot-Handford ME, Abanades JC, Anthony EJ, Blubt MJ, Brandani S, Mac Dowell N, Fernandez JR, Ferrarin MC, Gross R, Hallett JP, Haszeldine RS, Heptonstall P, Lyngfelt A, Makuch Z, Mangano E, Porter RTJ, Pourkashanian M, Rochelle GT, Shah N, Yao JG, Fennell. Carbon capture and storage update. *Energy Environ. Sci*. 2014;7(1):130–189. doi:10.1039/C3EE42350F.

16. He M, Sun Y, Han B. Green carbon science: Scientific basis for integrating carbon resource processing, utilization, and recycling. *Angew. Chemie - Int. Ed*. 2013;52(37):9620–9633. doi:10.1002/anie.201209384.

17. Centi G, Quadrelli EA, Perathoner S. Catalysis for $CO_2$ conversion: a key technology for rapid introduction of renewable energy in the value chain of chemical industries. *Energy Environ. Sci*. 2013;6(6):1711–1731. doi:10.1039/C3EE00056G.

18. Xie S, Zhang Q, Liu G, Wang Y. reduction of $CO_2$ using heterogeneous catalysts with controlled nanostructures. *Chem. Commun*. 2015;52:35–59. doi:10.1039/C5CC07613G.

19. Paracchino A, Mathews N, Hisatomi T, Stefik M, Tilley SD, Grätzel M. Ultrathin films on copper(i) oxide water splitting photocathodes: a study on performance and stability. *Energy Environ. Sci*. 2012;5(9):8673. doi:10.1039/c2ee22063f.

20. Somasundaram S, Raman Nair Chenthamarakshan C, de Tacconi NR, Rajeshwar K. Photocatalytic production of hydrogen from electrodeposited p-type $Cu_2O$ film and sacrificial electron donors. *Int. J. Hydrogen Energy*. 2007;32(18):4661–4669. doi:10.1016/j.ijhydene.2007.06.028.

21. Nian JN, Hu CC, Teng H. Electrodeposited p-type $Cu_2O$ for $H_2$ evolution from photoelectrolysis of water under visible light illumination. *Int. J. Hydrogen Energy*. 2008;33(12):2897–2903. doi:10.1016/j.ijhydene.2008.03.052.

22. Mahmoud MA, Qian W, El-Sayed MA. Following charge separation on the nanoscale in $Cu_2O$-Au nanoframe hollow nanoparticles. *Nano Lett*. 2011;11(8):3285–3289. doi:10.1021/nl201642r.

23. Barreca D, Fornasiero P, Gasparotto A, Gombac V, Maccato C, Montini T, Tondello E. The potential of supported $Cu_2O$ and CuO nanosystems in photocatalytic H2 production. *ChemSusChem*. 2009;2(3):230–233. doi:10.1002/cssc.200900032.

24. Paracchino A, Laporte V, Sivula K, Grätzel M, Thimsen E. Highly active oxide photocathode for photoelectrochemical water reduction. *Nat. Mater*. 2011;10(6):456–461. doi:10.1038/nmat3017.

25. Radi A, Pradhan D, Sohn Y, Leung KT. Nanoscale Shape and Size Control of Cubic, Cuboctahedral, and Octahedral Cu-$Cu_2O$ Core-Shell Nanoparticles on Si(100) by One-Step, Templateless, Capping-Agent-Free Electrodeposition. *ACS Nano* 2010;4(3):1553–1560.

26. Gerischer H. On the stability of semiconductor electrodes against photodecomposition. *J. Electroanal. Chem. Interfacial Electrochem*. 1977;82(1-2):133–143. doi:10.1016/S0022-0728(77)80253-2.

27. Deki S, Yano T, Mizuhata M, Kajinami A. Preparation and characterization of copper(. 1998;750(8):1865–1868.

28. Jin WM, Kang JH, Moon JH. Fabrication of 3D copper oxide structure by holographic lithography for photoelectrochemical electrodes. *ACS Appl. Mater. Interfaces*. 2010;2(11):2982–2986. doi:10.1021/am100773h.

29. Yoon KH, Choi WJ, Kang DH. Photoelectrochemical properties of copper oxide thin films coated on an n-Si substrate. *Thin Solid Films*. 2000;372(1):250–256. doi:10.1016/S0040-6090(00)01058-0.

30. Al-Kuhaili MF. Characterization of copper oxide thin films deposited by the thermal evaporation of cuprous oxide ($Cu_2O$). *Vacuum*. 2008;82(6):623–629. doi:10.1016/j.vacuum.2007.10.004.

31. Liu XM, Zhou YC. Electrochemical deposition and characterization of Cu2O nanowires. *Appl. Phys. A Mater. Sci. Process*. 2005;81(4):685–689. doi:10.1007/s00339-005-3243-z.

32. Chen L, Shet S, Tang H, Wang H, Deutsch T, Yan Y, Turner J, Al-Jassim M. Electrochemical deposition of copper oxide nanowires for photoelectrochemical applications. *J. Mater. Chem*. 2010;20(33):6962–6967. doi:10.1039/c0jm01228a.

33. Singh DP, Neti NR, Sinha ASK, Srivastava ON. Growth of different nanostructures of $Cu_2O$ (nanothreads, nanowires, and nanocubes) by simple electrolysis based oxidation of copper. *J. Phys. Chem. C*. 2007;111(4):1638–1645. doi:10.1021/jp0657179.

34. Le M, Ren M, Zhang Z, Sprunger PT, Kurtz RL, Flake JC. Electrochemical Reduction of $CO_2$ to $CH_3OH$ at Copper Oxide Surfaces. *J. Electrochem. Soc*. 2011;158(5):E45. doi:10.1149/1.3561636.

35. Cui J, Gibson UJ. A Simple Two-Step Electrodeposition of $Cu_2O$/ZnO Nanopillar Solar Cells. *J. Phys. Chem. C*. 2010;114(14):6408–6412. doi:10.1021/jp1004314.

36. Zhang S, Zhang S, Peng F, Zhang H, Liu H, Zhao H. Electrodeposition of polyhedral $Cu_2O$ on $TiO_2$ nanotube arrays for enhancing visible light photocatalytic performance. *Electrochem commun*. 2011;13(8):861–864. doi:10.1016/j.elecom.2011.05.022.

37. Siripala W, Ivanovskaya A, Jaramillo TF, Baeck SH, McFarland EW. A $Cu_2O/TiO_2$ heterojunction thin film cathode for photoelectrocatalysis. *Sol. Energy Mater. Sol. Cells*. 2003;77(3):229–237. doi:10.1016/S0927-0248(02)00343-4.

38. Ran J, Yu J, Jaroniec M. $Ni(OH)_2$ modified CdS nanorods for highly efficient visible-light-driven photocatalytic $H_2$ generation. *Green Chem*. 2011;13(10):2708. doi:10.1039/c1gc15465f.

39. Yu J, Hai Y, Cheng B. Enhanced photocatalytic $H_2$-production activity of $TiO_2$ by Ni(OH)2 cluster modification. *J. Phys. Chem. C*. 2011;115(11):4953–4958. doi:10.1021/jp111562d.

40. Subbaraman R, Tripkovic D, Strmcnik D, Chang KC, Uchimura M, Paulikas AP, Stamenkovic V, Markovic N. Enhancing Hydrogen Evolution Activity in Water Splitting by Tailoring $Li^+$-$Ni(OH)_2$-Pt Interfaces. 2011;334:1256–1260.

41. Jang JS, Choi SH, Kim DH, Jang JW, Lee KS, Lee JS. Enhanced photocatalytic hydrogen production from water-methanol solution by nickel intercalated into titanate nanotube. *J. Phys. Chem. C*. 2009;113(20):8990–8996. doi:Doi 10.1021/Jp900653r.

42. Shrestha NK, Yang M, Nah YC, Paramasivam I, Schmuki P. Self-organized $TiO_2$ nanotubes: Visible light activation by Ni oxide nanoparticle decoration. *Electrochem. commun*. 2010;12(2):254–257. doi:10.1016/j.elecom.2009.12.007.

43. Sreethawong T, Suzuki Y, Yoshikawa S. Photocatalytic evolution of hydrogen over mesoporous $TiO_2$ supported NiO photocatalyst prepared by single-step sol-gel process with surfactant template. *Int. J. Hydrogen Energy*. 2005;30(10):1053–1062. doi:10.1016/j.ijhydene.2004.09.007.

44. Mavrokefalos CK, Nelson GW, Poll CG, Compton RG, Foord JS. Electrochemical aspects of Pt–Cu and Cu modified boron-doped diamond. *Phys. Status Solidi Appl. Mater. Sci.* 2015;2567(11):1–9. doi:10.1002/pssa.201532163.

45. Shpilevaya I, Smirnov W, Hirsz S, Yang N, Nebel CE, Foord JS. Nanostructured diamond decorated with Pt particles: preparation and electrochemistry. *RSC Adv*. 2014;4(2):531. doi:10.1039/c3ra43763a.

46. Svanberg-Larsson J, Nelson GW, Escobar Steinvall S, Leo BF, Brooke E, Payne DJ, Foord JS. A Comparison of Explicitly-terminated Diamond Electrodes Decorated with Gold Nanoparticles. *Electroanalysis*. 2016;28(1):88–95. doi:10.1002/elan.201500442.

47. http://www.casaxps.com/.

48. Taylor RI. X-Ray Photoemission Spectra of Crystalline and Amorphous Si and Ge Valence Bands. *Phys. Rev. Lett*. 1972;29(16):1088–1092.

49. http://xpssimplified.com/elements/copper.php.

50. Lin C, Lai YH, Mersch D, Reisner E. $Cu_2O|NiO_x$ nanocomposite as an inexpensive photocathode in photoelectrochemical water splitting. *Thin Solid Films*. 2014;8(3):252–257. doi:10.1016/j.tsf.2013.10.122.

51. De Los Santos Valladares L, Ionescu A, Holmes S, Barnes CHW. Characterization of Ni thin films following thermal oxidation in air. *J. Vac. Sci. Technol. B, Nanotechnol. Microelectron Mater. Process Meas. Phenom*. 2014;32(5):051808. doi:10.1116/1.4895846.

52. Zhang Z, Dua R, Zhang L, Zhu H, Zhang H, Wang P. Carbon-layer-protected cuprous oxide nanowire arrays for efficient water reduction. *ACS Nano*. 2013;7(2):1709–1717. doi:10.1021/nn3057092.

53. Yang C, Tran PD, Boix PP, Bassi PP, Yantara N, Wong LH, Barber J. Engineering a

$Cu_2O/NiO/Cu_2MoS_4$ hybrid photocathode for $H_2$ generation in water. *Nanoscale*. 2014;6(12):6506–10. doi:10.1039/c4nr00386a.

54. Tamirat AG, Su WN, Dubale AA, Chen HM, Hwang B-J. Photoelectrochemical water splitting at low applied potential using a NiOOH coated codoped (Sn, Zr) α-$Fe_2O_3$ photoanode. *J. Mater. Chem. A*. 2015;3:5949–5961. doi:10.1039/C4TA06915C.

55. Albery WJ, O'Shea GJ, Smith AL. Interpretation and use of Mott Schottky plots at the semiconductor/electrolyte interface. *J. Chem. Soc. Faraday Trans*. 1996;92(20):4083. doi:10.1039/ft9969204083.

56. Cardon F, Gomees WP. On the determination of the flat-band potential of a semiconductor in contact with a metal or an electrolyte from the Mott-Schottky plot. *J. Phys. D: Appl. Phys*. 1978;11:L63-L67.

# Chapter 7

## 7.1 Thesis conclusions

In this thesis, electrochemically modified diamond and Au (111) electrodes with metal nanoparticles were investigated in regards to sustainable "green" energy applications and chemical sensors. In particular, either single nanoparticles or core-shell nanoarchitectures supported on diamond and gold substrates were evaluated towards alcohol electrolytes, glucose and illuminated under solar light for the production of valuable fuels and/or chemicals.

The main findings of this work are highlighted in the following paragraphs. Core-shell nanostructures are very advantageous anode materials in relevance to fuel cells because of their electronic interaction and metallic properties with the underlying substrate. More specifically, the latter can offer higher current densities compared to pure metal nanoparticles and less poisoning effect towards alcohol electrolytes. Furthermore, by tuning the loading of the shell metal, the metallic interaction can be maintained while reducing the overall cost of the electrocatalyst since expensive noble metals, such as Pt are needed. For reactions like water splitting and $CO_2$ reduction, the loading of the outer (shell) metal is also important because this layer protects the semiconductor (inner, core metal in this study) from self-photo corrosion in aqueous solutions. The synthesis of nanoparticles by overpotential control are extremely important since they influence nanoparticle size distribution, crystal structure and surface morphology, which in turn determines the electrocatalytic properties of the nanoparticles. Diamond is known for its stable chemical terminations, a fact utilized in this thesis to show that the hydrogen-terminated surface is more conductive than the oxygen terminated one. This subsequently affects the size of the particles and eventually the overall electrocalatalytic performance of the electrocatalyst. Similarly to the fuel cell application, bimetallic

photocatalysts displayed higher photoactivity in comparison with pure semiconductor materials. However, crystalline phases, particle sizes and morphologies are significant not only for the water splitting reaction but also for $CO_2$ reduction reaction. The next paragraphs describe the main findings of each chapter in more detail.

*Chapter 3* investigates the benefits of the electrodeposited Pt-Cu core-shell structures on diamond electrodes compared to pure Cu nanoparticles. Due to electronic modifications of the Pt through the interaction with the underlying Cu, higher current responses and with less electrode fouling were observed. Particularly important was the observation that spontaneous galvanic replacement of Cu by Pt made the deposition control of Pt onto Cu more difficult. A simple and cost-effective method of glucose sensing was also accomplished. Pure Cu nanoparticles on BDD presented high sensitivity and current density to glucose oxidation in KOH rather than in PBS solution were a surface passivation was occurred. This robust sensor showed good reproducibility and ability to separate the target analyte from any interfering species which are also exist in the biological system.

*Chapter 4* explains the effects of the applied overpotential and deposition duration on nucleation, growth, size and morphology of Pd nanoparticles. The results debunked the classical theories for electrochemical nucleation and growth and suggested that Pd nanoparticles experience overpotential dependent deposition. Clusters of nuclei grow either by the fresh reduction of ions at lower overpotential or by aggregative growth mechanisms at higher overpotentials. The particles size was found to be between 3.5 and 5 nm, the density of which increases with the overpotential. The high dispersibility and small particle size of the resulting Pd NPs resulted in the largest specific surface area (4 times of commercial Pd-C) and demonstrated high electrocatalytic activity towards ethanol electrooxidation processes. The mass activity ($\approx$ 10,000 mA $mg^{-1}$) for ethanol electrooxidation on the electrochemically deposited Pd NPs is about 35 times higher than the corresponding activity on commercial Pd-

C (286 mA $mg^{-1}$) reported to date[1]. Chapter 4 also explains how the hydrogen-terminated diamond electrodes are more conductive than the oxygen terminated ones, a fact which led to enhanced particles distribution on the surface as well as larger metal loading due to the increased conductivity. The latter reasons played a crucial role during the evaluation of the electrocatalysts towards ethanol electrooxidation showing that Pd NPs supported on hydrogen-terminated BDD demonstrated higher current densities and more tolerance towards the by-products of the ethanol oxidation. The Pd/HBDD catalysts also revealed better performance over a long operational time of 2 hours.

*Chapter 5* further extents the work on core-shell structures of Chapter 3 along with the effects of surface pre-treatment of diamond electrodes. Sn nanoparticles were found to disperse better on the hydrogen-terminated surface where the Sn NPs then served as reactive centres for the deposition of Pd, which improved the electrocatalytic performance towards ethanol electrooxidation compared to Pd nanoparticles themselves. Similarly, bimetallic core-shell Pd-Ni particles showed better catalytic performance than Pd itself. The Pd-Sn/HBDD catalysts displayed notably less electrode fouling than Pd-Ni/BDD, but the latter catalyst was more stable than the Pd-Sn/HBDD. As reported in previous chapters, the proper tuning of the Pd shell thickness on a second transition metal along with surface termination effects on diamond electrode played a significant role in achieving high mass activity and specific electrocatalytic activity.

The remaining chapter, *Chapter 6*, describes a novel and low-cost fabrication of photocathode materials for solar hydrogen production and $CO_2$ reduction. In this study, $Cu_2O$ cubic particles were electrodeposited and Ni was coated and electrodeposited onto the freshly prepared $Cu_2O$ forming a semiconductor/co-catalyst which its main purpose was to protect $Cu_2O$ from self-photo corrosion in aqueous solution. Metallic properties and electronic effects of the two metals led to high photocurrent densities compared to $Cu_2O$ itself for both

applications. The main approach of this work was the fabrication of a stable catalytic system rather than a system which will give an adequate hydrogen production or more useful fuels and chemicals for water splitting and $CO_2$ reduction. Hence, regardless of the application, the effects of structural aspects of semiconductors, such as crystalline phases, particle sizes, morphologies, exposed facets and heterojunctions on their catalytic behaviours are highly significant and should be investigated further. Other concepts like increasing the surface area of the catalyst (e.g. metal foams), use of bimetallic catalysts and use of organometallic complexes might become more important for either $H_2O$ splitting and $CO_2$ reduction reactions[2].

# 7.2 Bibliography

1. Sawangphruk M, Krittayavathananon A, Chinwipas N, Ultraporous palladium supported on graphene-coated carbon fiber paper as a highly active catalyst electrode for the oxidation of methanol. *Fuel Cells*. 2013;13(5):881–888. doi:10.1002/fuce.201200159.

2. Durst J, Rudnev A, Dutta A, Fu Y, Herranz J, Kaliginedi V, Kuzume A, Permyakova AA, Paratcha Y, Broekmann P, Schmidt TJ. Electrochemical $CO_2$ Reduction - A Critical View on Fundamentals, Materials and Applications. *Chim. Int. J. Chem*. 2015;69(12):769–776. doi:doi:10.2533/chimia.2015.769.